Metal nanoparticles tunable nanostructuring in glasses and glass ceramics : solid state chemistry, optical properties and nanostructure

Jan Baborák

ÉCOLE DOCTORALE Énergie - Matériaux - Sciences de la Terre et de l'Univers

Conditions Extrêmes et Matériaux : Haute Température et Irradiation

Materials for Photonics Laboratory

THÈSE EN COTUTELLE INTERNATIONALE présentée par :

Jan BABORÁK

soutenue le : 21 décembre 2023

pour obtenir le grade de :

Docteur de Université d'Orléans
et de l'Université de chimie et de technologie chimique de Prague

Discipline/ Spécialité : Chemistry

Metal nanoparticles tunable nanostructuring in glasses and glass ceramics : solid state chemistry, optical properties and nanostructures

THÈSE dirigée par :

Mme NEKVINDOVÁ Pavla	doc. Ing., Ph.D., UCT Prague
M. ALLIX Mathieu	HDR, Ph.D, Université d'Orléans
M. VÉRON Emmanuel	Ph.D, CEMHTI CNRS Orléans

RAPPORTEURS :

M. DEUBENER Joachim	Prof. Dr.-Ing. habil., TU Clausthal
M. KRÁTKÝ Rostislav	Ph.D., Preciosa a.s.

JURY :

M. SEDMIDUBSKÝ David	prof. Dr. Ing., UCT Prague, **President of the jury**
M. DEUBENER Joachim	Prof. Dr.-Ing. habil., TU Clausthal
M. KRÁTKÝ Rostislav	Ph.D., Preciosa a.s.
M. BLONDEAU Jean-Phillipe	prof., HDR, Université d'Orléans
Mme MACKOVÁ Anna	prof. RNDr., Ph.D., Nuclear Physics Institute of the CAS
Mme RUBEŠOVÁ Kateřina	doc. Ing., Ph.D., UCT Prague

ÉCOLE DOCTORALE Énergie - Matériaux - Sciences de la Terre et de l'Univers

Conditions Extrêmes et Matériaux : Haute Température et Irradiation

Materials for Photonics Laboratory

THÈSE EN COTUTELLE INTERNATIONALE présentée par :

Jan BABORÁK

soutenue le : 21 décembre 2023

pour obtenir le grade de :

Docteur de Université d'Orléans
et de l'Université de chimie et de technologie chimique de Prague

Discipline/ Spécialité : Chimie

NANOPARTICULES MÉTALLIQUES À NANOSTRUCTURATION AJUSTABLE DANS LES VERRES ET LES VITROCÉRAMIQUES : CHIMIE DE L'ÉTAT SOLIDE, PROPRIÉTÉS OPTIQUES ET NANOSTRUCTURE

THÈSE dirigée par :

Mme NEKVINDOVÁ Pavla	doc. Ing., Ph.D., UCT Prague
M. ALLIX Mathieu	HDR, Ph.D, Université d'Orléans
M. VÉRON Emmanuel	Ph.D, CEMHTI CNRS Orléans

RAPPORTEURS :

M. DEUBENER Joachim	Prof. Dr.-Ing. habil., TU Clausthal
M. KRÁTKÝ Rostislav	Ph.D., Preciosa a.s.

JURY :

M. SEDMIDUBSKÝ David	prof. Dr. Ing., UCT Prague, **Président du jury**
M. DEUBENER Joachim	Prof. Dr.-Ing. habil., TU Clausthal
M. KRÁTKÝ Rostislav	Ph.D., Preciosa a.s.
M. BLONDEAU Jean-Phillipe	prof., HDR, Université d'Orléans
Mme MACKOVÁ Anna	prof. RNDr., Ph.D., Nuclear Physics Institute of the CAS
Mme RUBEŠOVÁ Kateřina	doc. Ing., Ph.D., UCT Prague

ACKNOWLEDGEMENT

First of all, I would like to thank my supervisors doc. MSc. Pavla Nekvindová, Ph.D., MSc. Mathieu Allix, HDR, Ph.D. and MSc. Emmanuel Véron, Ph.D., who led me through my doctoral studies from the beginning to the end.

I would also like to thank all the people from UCT Prague, CEMHTI and others who contributed to this work, especially MSc. Alessio Zandonà, Ph.D., MSc. Petr Vařák, Ph.D., Lenka Turková, MSc. Miroslav Rada, Ph.D., doc. MSc. Alena Michalcová, Ph.D., MSc. Zuzana Zlámalová Cílová, Ph.D., MSc. Libor Mastný, Ph.D., MSc. Radka Kalousková, Ph.D., doc. MSc. Kateřina Rubešová, Ph.D., MSc. Vít Jakeš, Ph.D., MSc. Michael Pitcher, Ph.D., MSc. Cécile Genevois, Ph.D., Sandra Ory, prof. MSc. Jean-Phillipe Blondeau, Ph.D., MSc. Aurélien Canizarès, Ph.D., MSc. Severine Brassamin, Ph.D.

Finally, I would also like to thank my parents and my brother who have always stood by my side.

This work was supported by the following grants and institutions:

Barrande fellowship – French Institute in Prague (IFP), Czech Ministry of Education, Youth and Sports (MYES) and Campus France
ERASMUS+
Czech Science Foundation (GAČR), project number GAP23-05507S

SUMMARY

The long history of glass containing gold nanoparticles, which is appreciated especially for its beautiful red colour, is now facing modern applications. They are used in photonics, sensing, catalysis, biomedicine and jewellery. These applications motivate further research to gain detailed understanding of the links between the preparation technology, the composition and properties of the glass matrix and the parameters of the gold nanoparticles.

The subject of this work was to compare the possibility of preparing glass containing gold nanoparticles by the conventional melt-quenching technique with an innovative technology, aerodynamic levitation coupled to laser heating (ADL). In terms of glass formation, this technique shows unrivalled versatility: (1) containerless melting suppresses heterogeneous nucleation of crystal phases during cooling and avoids contamination from crucible and refractory materials; (2) laser heating can attain up to ~3000 °C, which is above the melting temperature of any stable oxide material; (3) the technique allows rapid cooling on the order of several hundred °C per second, facilitating cooling of melts prone to devitrification.

This work covers the search for a glassy oxide system suitable for ADL technology and, at the same time, a general model for determining the most suitable precursors. Furthermore, the possibility of preparing YAS (Y_2O_3-Al_2O_3-SiO_2) glass by the ADL method was experimentally investigated. Previously unexplored high temperature region of this ternary system was newly experimentally described. Transparent, opalescent and white glasses were prepared in this system, which differed in their nanostructure. Furthermore, the work presents the possibility of preparation of gold nanoparticles in YAS, LS (Li_2O-SiO_2) and LYAS (Li_2O-Y_2O_3-Al_2O_3-SiO_2) glass systems with different Au and SnO_2 contents using ADL technology. In particular, the optical absorption and parameters of gold nanoparticles were investigated for the prepared glasses by transmission electron microscopy (TEM). It was found that the absorption, and thus the colour of the material, can be controlled not only by the size and distribution of the nanoparticles but also by the composition of the surrounding glass, and that it is also advisable to use nanoscale phase separation to achieve better colour homogeneity.

SOUHRN

Na dlouhou historii skel s nanočásticemi zlata, která jsou ceněna především pro svou krásnou červenou barvu, navazují dnes nové moderní aplikace. Nachází uplatnění ve fotonice, při výrobě sensorů, katalyzátorů, biomedicíně a bižuterii. Uvedené aplikace jsou motivací pro další výzkum, který je zaměřen na detailní pochopení souvislostí mezi technologií přípravy, složením a vlastnostmi skelné matrice a parametry nanočástic zlata.

Obsahem této práce bylo porovnání možnosti přípravy skla obohaceného zlatými nanočásticemi tradiční metodou přípravy skelných materiálů tavením ve vysokoteplotní peci s novou technologií aerodynamické levitace spojené s laserovým tavením (ADL). Z hlediska tvorby skla vykazuje tato technika jedinečnou všestrannost: (1) tavení bez kelímku–nádoby potlačuje heterogenní nukleaci krystalových fází a zabraňují kontaminaci materiálem tavicího kelímku a žáruvzdorných materiálů; (2) laserový ohřev může dosáhnout až ~ 3000 °C, což je nad teplotou tání jakéhokoli stabilního oxidového materiálu; (3) technika umožňuje rychlé ochlazování v řádu několika stovek °C za sekundu, což usnadňuje ochlazování tavenin náchylných k devitrifikaci.

Práce se zabývala hledáním skelného oxidového systému vhodného pro ADL technologii a současně obecným modelem pro určení nejvhodnějších vstupních surovin. Dále byla experimentálně zkoumána možnost přípravy YAS skla metodou ADL, kdy byla nově experimentálně popsána málo známá vysokoteplotní oblast tohoto ternárního systému. V tomto systému byla připravena průhledná, opalescentní a bílá skla, která se lišila svou nanostrukturou. Dále práce prezentuje možnost přípravy zlatých nanočástic ve skelných systémech YAS, LS a LYAS, s různým obsahem Au a SnO_2 s využitím technologie ADL. U připravených skel byla zkoumána především optická absorpce a parametry nanočástic zlata pomocí TEM. Bylo zjištěno, že absorpci, a tedy také barvu materiálu, je možné ovládat nejen velikostí a distribucí nanočástic, ale také složením okolní skloviny, a že je pro dosažení lepší homogenity barevnosti vhodné využívat separace fází v nano-měřítku.

RÉSUMÉ

La longue histoire du verre contenant des nanoparticules d'or, apprécié notamment pour sa belle couleur rouge, trouve aujourd'hui des applications modernes. Il est notamment utilisé dans les domaines de la photonique, de la détection, de la catalyse, de la biomédecine et des bijoux . Ces applications motivent la poursuite de recherches afin de comprendre en détail les liens entre les méthodes de préparation, la composition et les propriétés de la matrice vitreuse et les paramètres des nanoparticules d'or.

L'objet de ce travail était de comparer la possibilité de préparer du verre contenant des nanoparticules d'or par la technique conventionnelle de trempe par fusion avec une technologie innovante, la lévitation aérodynamique couplée au chauffage laser (ADL). En termes de formation de verre, cette technique présente une polyvalence inégalée : (1) la fusion sans creuset supprime la nucléation hétérogène des phases cristallines pendant le refroidissement et évite la contamination par le creuset et les matériaux réfractaires ; (2) le chauffage laser peut atteindre jusqu'à ~3000 °C, ce qui est supérieur à la température de fusion de tout matériau oxyde stable ; (3) la technique permet un refroidissement rapide de l'ordre de plusieurs centaines de °C par seconde, ce qui facilite le refroidissement des matières fondues sujettes à la dévitrification.

Ce travail porte sur la recherche d'un système d'oxyde vitreux adapté à la technologie ADL et, en même temps, sur un modèle général permettant de déterminer les précurseurs les plus appropriés. En outre, la possibilité de préparer le verre YAS (Y_2O_3-Al_2O_3-SiO_2) par la méthode ADL a été étudiée expérimentalement. La région nécessitant de hautes températures de fusion de ce système ternaire, jusqu'alors inexplorée, a été décrite expérimentalement. Des verres transparents, opalescents et blancs ont été préparés dans ce système, qui diffèrent par leur nanostructure. En outre, ce travail présente la possibilité de préparer des nanoparticules d'or dans les systèmes de verre YAS, LS (Li_2O-SiO_2) et LYAS (Li_2O-Y_2O_3-Al_2O_3-SiO_2) avec différentes teneurs en Au et SnO_2 à l'aide de la technologie ADL. En particulier, l'absorption optique et les paramètres des nanoparticules d'or ont été étudiés par microscopie électronique en transmission MET pour les verres préparés. Il a été constaté que l'absorption, et donc la couleur du matériau, peut être contrôlée non seulement par la taille et la distribution des nanoparticules, mais aussi par la composition du verre environnant, et qu'il est également préférable d'utiliser une séparation de phase à l'échelle nanométrique pour obtenir une meilleure homogénéité de la couleur.

TABLE OF CONTENTS

1 INTRODUCTION

Glass coloured with metal nanoparticles has a long history. The first evidence of red (opaque) glass containing Cu NPs was found in Egypt and is dated 1400-1300 BC. Another well-known artefact containing metal nanoparticles is the Lycurgus cup, which contains nanoparticles of gold and silver, and is on display in the British National Museum in London, UK. In everyday life, glass containing metal nanoparticles can be found in stained glass windows in churches.

Even though glass containing metal nanoparticles has been produced for a very long time, the consensus is that ancient glassmakers had no idea of their presence in glass. The mechanism by which precious metals cause the colour of glass was only described with the development of scientific understanding in the early 20th century.

Glass containing nanoparticles of copper or gold is particularly valued for its red colour. It is technologically very challenging to prepare. In the past, the method for producing red-coloured glass was jealously guarded and only a few people mastered it. The red glass with gold metal nanoparticles was (and still is) used mainly for decorative purposes.

The long history of glass containing metal nanoparticles, which was particularly valued for its beauty, is now being followed by modern applications. It finds use in photonics, sensing, catalysis, biomedicine and jewellery. This provides the motivation for further research, which is focused on a detailed understanding of the connection between the technology, glass composition, glass structure and the parameters and properties of metal nanoparticles.

The thesis explores the possibility of using a new technology of containerless melting for the preparation of gold nanoparticles in glass. We assume that the beauty of the prepared glass could be used for decorative purposes or in jewellery and the change of physical properties in e.g. photonics.

The dissertation is the result of a collaboration between two laboratories: the Materials for Photonics Laboratory at the University of Chemistry and Technology Prague (UCT) in Czechia and the Extreme Conditions and Materials: High Temperature and Irradiation (CEMHTI) laboratory at The French National Centre for Scientific Research (CNRS) in Orléans, France. In the laboratory of photonics at UCT Prague the conventional technology of glass preparation

by melt-quenching was used. At the CEMHTI laboratory in Orléans, the sample preparation technique of aerodynamic levitation coupled to laser heating, which was realised and is being developed further at this institution, was used.

The dissertation is structured in a conventional way. First, a theoretical part is presented with a literature review focusing on glass, glass-ceramics and gold nanoparticles. Next, an experimental part is presented, describing the sample preparation and characterization methods, followed by the research objectives. The core of the thesis are the results and discussion chapter, which is divided into four subsections. The first one deals with the problem of volatilisation of the raw materials during sample preparation by aerodynamic levitation coupled to laser heating and the homogeneity of the prepared samples. The second subchapter is focused on the possibility of preparation of yttrium aluminosilicate glass using aerodynamic levitation coupled to laser heating. The third subchapter is about the preparation of gold nanoparticles in yttrium aluminosilicate and lithium silicate glass and their characterization. The fourth subchapter focuses on the preparation of gold nanoparticles in newly designed glass matrices. Finally, a summary of the most important results of this dissertation is presented.

2 THEORETICAL PART

2.1 Glass - glass-ceramic generalities

2.1.1 Structure and composition of glass

The definition of the glassy state has evolved over the years. Examples of older definitions include: "*In the glassy state, there are solid non-crystalline materials*" [1], or , "*Glass is an inorganic product of fusion which has been cooled to a rigid condition without crystallization*" [2–4]. However, these definitions are inaccurate today due to advances in technology and scientific knowledge. Recently, not all non-crystalline solids are classified as glasses (e.g. xerogels). In addition to inorganic glasses, there are also organic glasses. Also, the formation of glass by cooling without crystallization is by no means the only way to prepare glass. In addition to this traditional approach, glasses can also be prepared by polymerisation, by changes of pressure, or by precipitation from the gas phase.

Conradt [5] has proposed an updated definition that had been designed to be free of the above shortcomings and reads as follows, "*Glasses are dense (non-fractal) isotropic and homogeneous non-crystalline solids characterized by the absence of any internal phase boundaries. At the atomic scale, glasses are characterized by the absence of any translational symmetry*." This definition is based on work by Zachariasen [6] and Greaves [7]. Glass is most often formed by rapid cooling (quenching) of a molten form. Another, rather poetic definition of glassy state has been lately published by Zanotto and Mauro [8]: "*Glass is a nonequilibrium, non-crystalline condensed state of matter that exhibits a glass transition. The structure of glasses is similar to that of their parent supercooled liquids (SCL), and they spontaneously relax toward the SCL state. Their ultimate fate, in the limit of infinite time, is to crystallize.*"

The glasses prepared in this work are, with few exceptions, silicate glasses, which have always been prepared by rapid cooling from the melt. One of the characteristic features of the glasses is the so-called glass transition. When the cooling rate from the melt is sufficiently rapid, the glasses do not undergo a sudden change in molar volume and form crystals, but the substance enters a metastable state of a supercooled liquid. With further quenching and reaching a viscosity of the order of 10^{13} Pa s, the substance transitions from a formable state to a

mechanically solid state and a shift away from linear dependence occurs. From this point on, we no longer speak of a supercooled liquid, but of a glass. The transformation between these two states is called the glass transition and the temperature at which this change occurs is called the transformation temperature. This temperature is dependent on the cooling rate, as can be seen from the **Figure 1**. At higher cooling rates the transformation temperature is higher and vice versa. The interval between the lowest and highest achievable cooling rate is called the transformation interval. For practical purposes, the transformation temperature T_g has been defined as the transformation temperature for a cooling rate of 10 °C min^{-1}. Instead of the molar volume, the same dependence can be derived for the molar enthalpy [2,4,9].

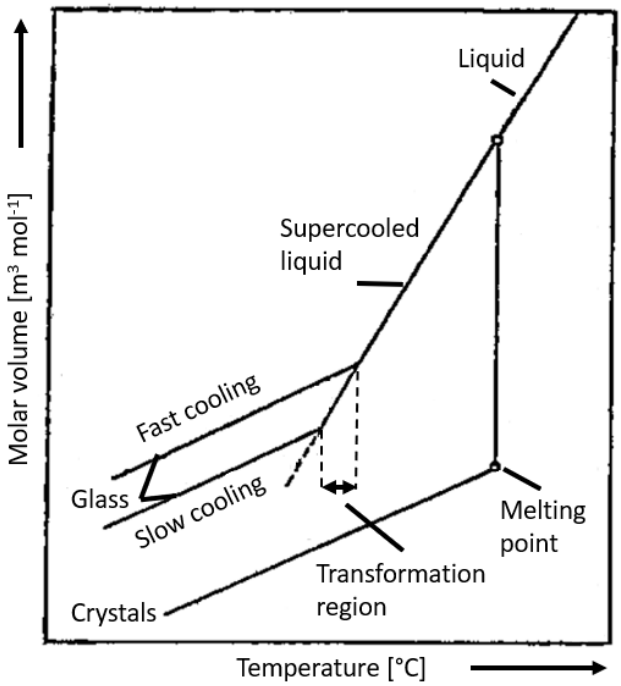

Figure 1 *Dependence of molar volume on temperature for liquid, glass and crystals [2]*

Therefore, the latest definition of the glassy state is: "*Glasses are undercooled frozen-in liquids*" [10], which is thermodynamically correct and still valid today [9]. This definition does not mention the composition of the glass. This is because glasses can theoretically be prepared from any material, we are limited only by the parameters of the technology of their preparation. In the case of glass preparation by melt quenching, the key constraint is the maximum cooling rate we are able to achieve [2].

In terms of chemical composition, glasses can be formed from a wide variety of atoms - for example, glasses composed only of carbon or metal atoms are known. Oxide glasses can only be composed of oxides of elements that meet the so-called criteria for random arrangement, i.e. a) the coordination number of the main element is 3 or 4 b) only one oxygen atom is shared by two non-oxide atoms c) the X-O-X bonding angle must be an adjustable angle of about 150° d) free rotation around the X-O bond must be possible. For these reasons, only a few oxides form the glass i.e. B_2O_3, Al_2O_3, SiO_2, GeO_2, P_2O_5 and As_2O_5.

Silicate glasses are the most common and also historically the oldest. The basis of quartz glass is silica, which occurs in nature in various forms and is based on the tetrahedral structural unit SiO_4. Zachariasen in 1932 published one of the most famous sketches of the structure of silicate glasses [6]. 80 years after the publication of Zachariasen's image, almost the same structure was actually observed by STM [11] - see **Figure 2**.

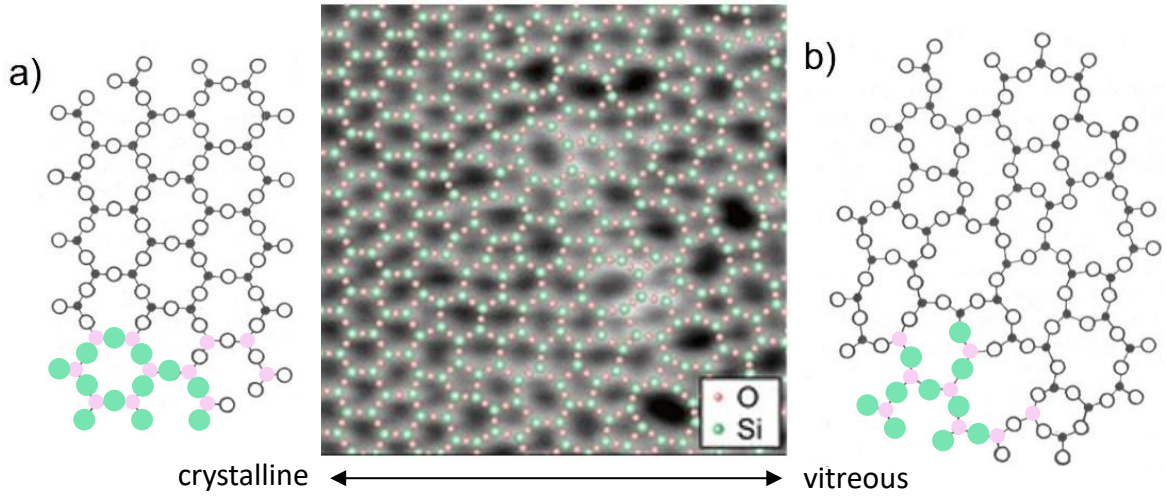

Figure 2 *Planar Zachariasen representation of a) crystalline SiO_2 b) amorphous SiO_2 and [6] in the middle the STM image of silica network is shown [11]; pink is oxygen atoms, green is silica atoms, for illustration, the original Zachariasen structure is only partially coloured*

However, pure silicate glasses are difficult to melt, so the glasses are usually a mixture of silica and other oxides. In silicate glasses, there are three types of building blocks of the glass structure: 1) **glass network formers** (B_2O_3, P_2O_5, SiO_2 and GeO_2) which form polyhedra in the glass structure, which are interconnected by their vertices, edges or, in exceptional cases, faces.

Oxygen species in the vertices of these polyhedra that are connected to others are referred to as bridging oxygens (BO_x); 2) **glass network modifiers (**Li_2O, Na_2O, K_2O, CaO, MgO, ZnO and SnO_2**)** which are situated as cations in cavities in the glass network and breakdown the bonds between individual glass network formers. When such bonds are broken, terminal or also non-bridging oxygens (NBO_x) are formed; 3) **intermediates** (Al_2O_3) - can be incorporated into the structure either as a network forming element or as a modifier.

In terms of strength of chemical bond between oxygen and an element X in the glass, the elements can also be divided as follows: if bonding energy E_b per single bond is higher than 334 kJ mol^{-1}, the element X is considered a glass network former. If E_b is less than 251 kJ mol^{-1}, the element X is a glass network modifier. When the energy E_b is in between these two values, the element is an intermediate [12].

It is not easy to describe the structure of the glass because of its irregular nature. For this reason, the precise description of the structure of various types of oxide glasses is nowadays receiving a lot of attention and spectroscopic methods are usually combined with theoretical models. Experimentally, the structure and properties of glasses have been investigated by the following techniques: Nuclear magnetic resonance (NMR), Raman spectroscopy, neutron diffraction, x-ray diffraction (XRD), x-ray absorption fine structure (XAFS), extended x-ray absorption fine structure (EXAFS), and magic angle spinning nuclear magnetic resonance (MAS-NMR) [7,13–15].

One of the best known and feasible methods for the analysis of glasses is the Raman spectroscopy, which can describe the degree of glass network crosslinking in simple silicate-alkaline glasses by means of the so-called Q_n motifs. If the glass structure/composition is not too complex, it is then also possible to evaluate the percentage of individual Q_n motifs from the deconvolution of the spectra. An example of a Raman spectrum from approximately 900-1250 cm^{-1} together with formula for percentage amount of Q_n that belongs to a soda-silicate glass is shown in **Figure 3**.

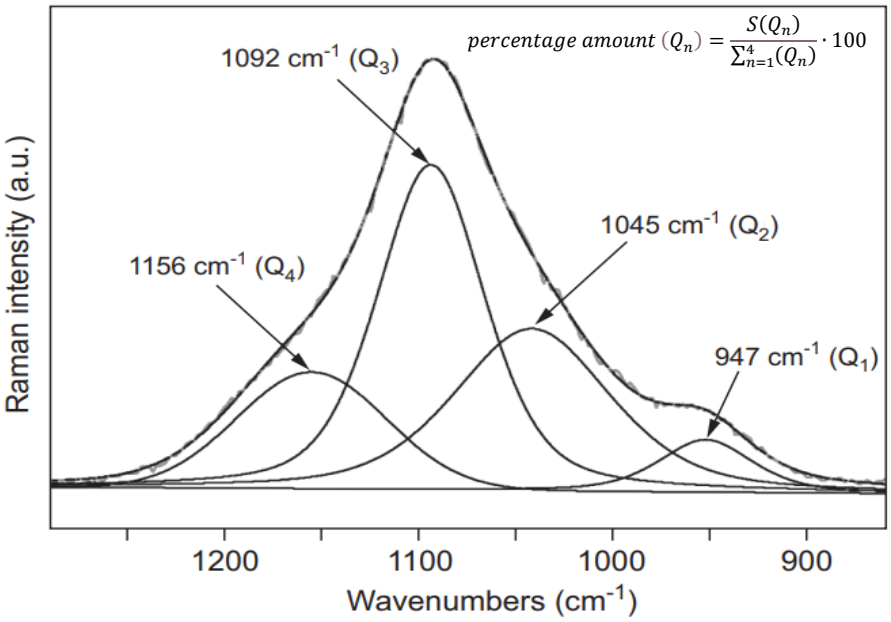

Figure 3 *Deconvolution of Q-motives in a soda-silicate glass [10]*

Other relatively experimentally demanding techniques used to investigate the structure of glass are MAS-NMR and EXAFS, which provide a much more accurate description of the environment - they detect the connection of individual elements of the glass network. However, they cannot characterise all the elements contained in the glass and are particularly suitable for Na, B, Si, Al, Pb and O.

Even with this plethora of intense studies on glass, the exact local structures due to the presence of network modifiers and the variations with the doping concentration remain unclear. The lack of long-range order in amorphous solid always imposes additional difficulties in experimental characterization making the precise structural determination far more challenging than in crystalline solids. Thus, computer simulation is a powerful complementary tool to probe the details of short-range order and medium range order in order to provide further insights on amorphous solids [16,17]. **Figure 4** shows a geometrically optimized 3D structural model of a silicate glass containing different amounts of sodium as a modifying element as an example. The dependence of the electronic structure on the composition and physical properties such as density, refractive index and Young's modulus of simple silicate glasses was calculated using the accurate ab initio molecular dynamics (AIMD) for structural modelling and the ab initio orthogonalized linear combination of atomic orbitals (OLCAO) method [17].

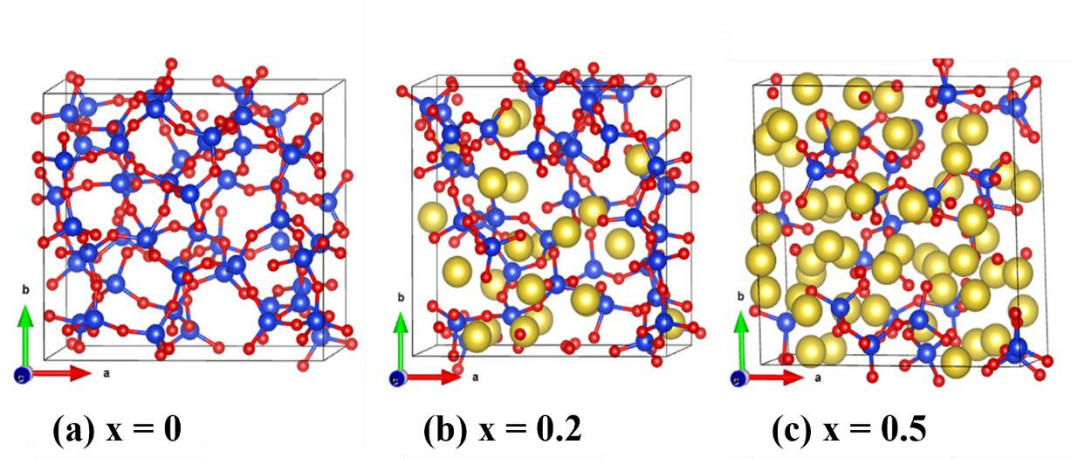

Figure 4 *The ball models of structure of sodium silicate glass* $(Na_2O)_x(SiO_2)_{1-x}$ *with x 0.2 and 0.5 modelled using ab initio molecular dynamics (AIMD) based on the density functional theory (DFT) – edited [17]*

2.1.2 Structure and composition of glass-ceramics

Glass-ceramics were first discovered by Stookey [18] and defined as "*a material formed by the controlled nucleation and crystallization of glass*". Recently, an updated definition of glass-ceramics has been proposed [19]. It consists of the following three main points: 1) glass-ceramics are prepared by controlled crystallization of glasses by various processing methods, 2) glass-ceramics contain at least one type of functional crystalline phase and residual glass, 3) the volume fraction of crystallized glass in glass-ceramics can range from ppm to nearly 100% [19]. As mentioned in definition, glass-ceramics are formed by controlled crystallization from a base glass. The course of such nucleation, which can start either in the volume of the glass (internal nucleation) or on its surface (surface nucleation) is shown in **Figure 5 a, b, c**. First, the crystalline phase nucleates, later the crystalline phase grows and finally the ceramic microstructure forms.

The nucleation and controlled crystallization of the initial glass material is essential to achieve the desired properties of glass-ceramic materials. By nucleation is meant the formation of submicroscopic seeds (nuclei), which is followed by their growth into macroscopic crystals - controlled crystallization. The rate of these two processes depends, among other things, on temperature; this relation was first described for glass crystallization by Tammann and later developed by Stookey - see **Figure 5d**. The rate of these processes is non-zero in the region between the values of approximately 2/3 of the glass transformation temperature T_g and the

liquidus temperature T_l. Over a relatively wide temperature interval, however, these processes can occur simultaneously.

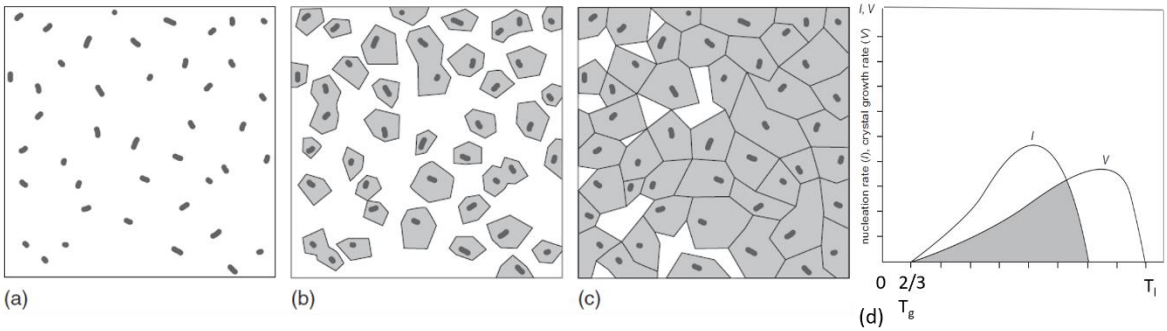

Figure 5 *Changing glass to glass-ceramics by internal nucleation. a) formation of nuclei, b) crystal growth on nuclei, c) glass-ceramic microstructure. In (d) The nucleation rate I and crystal growth rate V as function of reduced temperature T/T_l. Tg represents glass transition temperature, T_l is liquidus temperature [20].*

If we focus on the composition, its variability is enormous. The crystalline phase can be formed in many different glass systems, but oxide glass-ceramics are the most well-known and studied. As an example, the spinel glass-ceramics may be mentioned, which contain, in addition to the basic silicate glass phase, various crystalline phases of different compositions ranging from gahnite ($ZnAl_2O_4$) to spinel ($MgAl_2O_4$). These phases can be crystallized using ZrO_2 and/or TiO_2 as nucleating agents. **Figure 6** shows the microstructure of several different oxide ceramics, the structure and composition of which are mostly studied by electron microscopy.

The key to producing glass-ceramics with the desired properties is a) selection of crystalline phases with suitable properties and b) proper design of the initial glass composition so that preferential crystallization of the selected phases occurs and c) appropriate nucleation method and temperature regime to produce the desired microstructure.

Glass-ceramics have, in principle, several advantages over glass or ceramic materials alone: 1) they can be mass produced by any glass-forming technique, 2) it is possible to design their nanostructure or microstructure for a given application, 3) they have zero or very low porosity, 4) it is possible for them to combine a variety of desired properties.

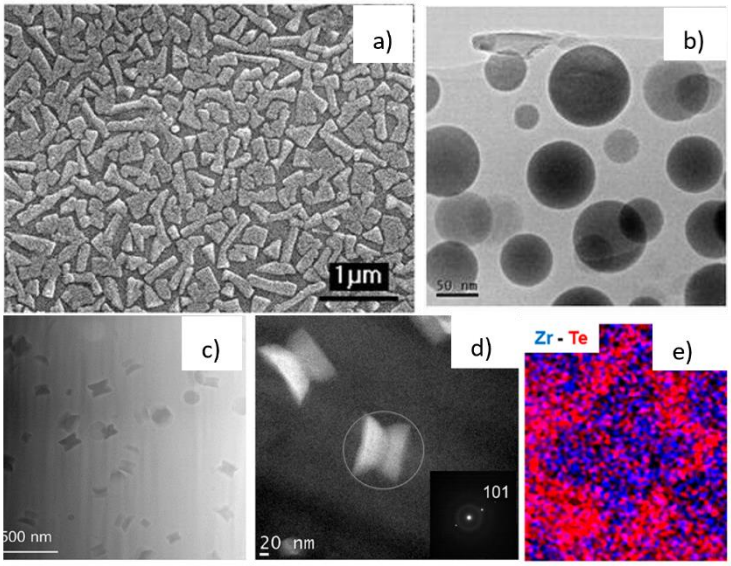

Figure 6 *Microstructure of various glass-ceramics* ***a)*** *($K_{0.5}Na_{0.5}NbO_3$) glass-ceramics [21]* ***b)*** *$SiO_2/Lu_2Si_2O_7$ nanocomposite as scintillation materials [22]* ***c) and d)*** *fluorotellurite glass-ceramics with luminescence properties* ***e)*** *EDX-STEM analyses of sample in image* ***d)****: Te a and Zr [23].*

Due to the wide range of crystalline phases with different characteristics, glass-ceramic materials can be divided into several categories, its microstructure is closely linked to its properties: glass-ceramics for **thermal utilisation** - the crystalline phase usually has a negative thermal expansion coefficient (TEC), the TEC of the glass matrix is positive. The overall TEC of the material can be therefore finely tuned, zero or even negative values can be achieved; **transparent glass-ceramics** (fine nanostructure), **bioactive and dental glass-ceramics**, **electrically conducting and insulating glass-ceramics** insulate - act as ion conductor or a superconductor; **machinable glass-ceramics** (entangled microstructure); **construction glass-ceramics**; **high-strength glass-ceramics; glass-ceramic armour** [20,24].A special type of glass-ceramics are metal crystals in a glass matrix, which are usually used to colour glass.

2.1.3 Technology of glass and glass-ceramics preparation

Nowadays there are a few different glass preparation technologies. **Melt-quenching** is the oldest technology and in terms of the volume of glass produced still the most important one. Over 90% of the world's glass production is produced by this technology. The main basis of this technology is the glass batch - a mixture of input raw materials - that is melted in a gas or electric furnace, the resulting glass is shaped by machines or by hand into products that can be further processed, e.g. by grinding or polishing, after controlled cooling in an annealing furnace.

The **float technology**, which is now used to produce the vast majority of plate glass worldwide, is worthy of special mention. This technology consists of pouring glass from a melting furnace onto a molten tin surface to form a ribbon of flat glass, which is then annealed and cut into glass panes used, for example, in the architecture and automotive industries The key to this technology is the input raw materials, their preparation and later the melting process itself. Both natural and synthetic raw materials are used to melt glass. In terms of function, they can be divided into several groups: 1) *glass network formers* - form the basic glass network. These include e.g., SiO_2, B_2O_3, P_2O_5; 2) *fluxes* - their purpose is to reduce the high melting temperature of glass network formers. For example, to melt pure silica glass, a temperature higher than 2000 °C is required, which cannot be achieved in conventional melting equipment. The most known fluxes include the alkaline oxides Li_2O, Na_2O, K_2O, which are most often added to the glass batch in the form of carbonates. The disadvantage of using these fluxes is that they degrade much the mechanical, chemical and optical properties of glass. They increase the tendency of glasses to crystallise, reduce chemical resistance, the elastic modulus, density or change the refractive index; 3) *colourants* - substances added to glass in small quantities that change its colour. The colour may be caused by a) ions e.g. rare earth ions, Ni^{2+}, Co^{3+}, b) non-metals and their compounds (e.g. Se, CdS) or c) metal nanoparticles (e.g. Cu, Ag, Au). In some cases, colourants are added to glasses to remove unwanted colouration due to impurities (especially Fe compounds) in the major raw materials; 4*) fining agents* - substances that help remove small bubbles from molten glass. During the melting process, the fining agents decompose into gaseous products that form a large number of larger bubbles, which are connected to smaller bubbles and together escape from the melt more easily due to the buoyant force [25].

This technology is very energy intensive, but its advantages include, for example, that a certain proportion of the glass batch may also consist of cullet from the same production. This achieves utilization of waste material, saving raw materials and also increases the efficiency of the melting process. In some productions (e.g. glass bottle production) this proportion can be up to 40% of the weight of the glass batch [25].

Other developed techniques for the preparation of glass materials are **the chemical vapour deposition method (CVD)** and **the sol-gel method. CVD** involves the deposition of a gaseous

substance on a substrate. A glass layer is gradually formed on the surface of the substrate. It is used for the production of optical fibre preforms or for the production of high purity chalcogenide glasses. The disadvantages of this method are the high purity requirements of the precursors and the need to convert the precursors into a gaseous state. **The sol-gel method** is based on the mixing of liquid precursors which, by a gradual condensation reaction, crosslink to form a gel and finally a solid sample. Heating the resulting sample to 100-120 °C removes organic residues and water, densifies the sample and forms a glass. The advantage of this method is that the low temperatures used allow the preparation of samples that cannot be prepared at high temperatures (e.g. due to thermal decomposition). The disadvantages of this method are that the preparation of monolith samples is very slow. Glass prepared by this technique is most often used in biomedical applications [26].

Among the modern technologies for the preparation of glass or glass-ceramics, of the most diverse properties and compositions are techniques such as aerodynamic levitation coupled to laser heating (ADL) [27,28]. It has been used in order to study the properties of melts at high temperature (e.g. by X-ray or neutron scattering [29]) but also as a response to the ever-growing push towards new materials discovery [30]. Next, glass preparation technology using 3D printing is now being intensively investigated [31–34]. Both of these techniques, however, have not yet had much commercial application because the dimensions of the glass or glass products prepared in this way are small. Technology Spark Plasma Sintering (SPS) is a material processing method, through the production of spark plasma applying pressure, temperature, and current, simultaneously. This method reduces considerably the sintering temperature, provides very fast heating rates, very short holding times, and allows highly transparent materials to be obtained. There is a wide literature available on SPS applied to get ceramic materials with desired properties, as well as other materials like metals, alloys, cements, intermetallic compounds, composites, and amorphous structures [35].

2.1.4 Glass system Y_2O_3-Al_2O_3-SiO_2 (YAS)

The glass system Y_2O_3-Al_2O_3-SiO_2 (YAS) has been the subject of intensive investigation over the past decade due to the combination of excellent mechanical properties, low thermal expansion, high glass transition temperatures, refractive indices, and thermo-chemical stability of its members [36–39]. Moreover, since yttrium ions can be replaced by rare earth or transition

metal dopants of similar ionic radii and charge states, such glasses have garnered attention as in vivo drug delivery vehicles for cancer treatments [40], nuclear waste vitrification [41], and, due to their high glass transition temperatures and low thermal expansion coefficients, they are used as seals between glass-to-metal / ceramic components [42]. YAS glasses in the form of optical fibres have been shown to exhibit intrinsically low Brillouin and Raman scattering [43], which are important features critical to the continued scaling of high power/energy amplifiers and lasers.

Such a diverse range of applications, hence enabling properties, benefits from a broad range of compositions in the Y_2O_3-Al_2O_3-SiO_2 system and processes to realize them in glassy form. According to the available experimental studies [44,45], it could be assumed that glass formation occurs for compositions in the middle of the diagram – see **Figure 7** [46].

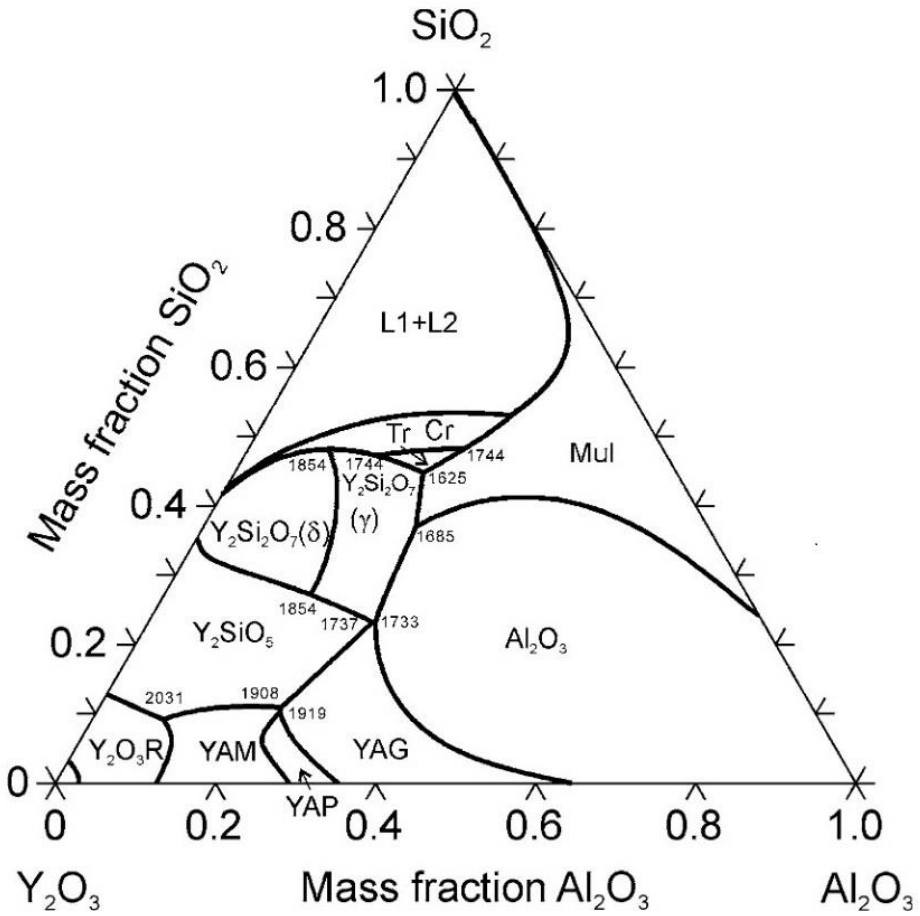

Figure 7 *Calculated liquidus surface of the YAS system. Temperatures are in K, fractions are mass fractions [46]. Tr, Cr, Mul, YAM, YAP and YAG stand for tridymite, cristobalite, mullite, yttrium aluminium monoclinic, yttrium aluminium perovskite and yttrium aluminium garnet respectively.*

Based on the available phase diagrams [45–50], crystalline phases such as Y_2O_3, Al_2O_3, SiO_2, yttrium-aluminium garnet (YAG), yttrium-aluminium perovskite (YAP), Y_2SiO_5, $Y_2Si_2O_7$ or mullite occur in areas of high concentration of one of the oxides. So far, glass crystallization has been examined in this system [51–57], but the SiO_2-rich portion of the ternary phase diagram has not been thoroughly explored. The reason is the difficult preparation of materials with melting temperatures above 1700 °C and relatively high viscosity, which makes it impossible to use the melt-quenching method in a conventional furnace and to cast homogeneous samples.

Yttrium alumino-silicate glass compositions have been studied using different forming methods ranging from conventional melt and quench to laser-induced melting (levitation method) followed by very rapid quenching and the molten core method of (optical) fibre formation. The compositions also cover a wide range of silica concentrations from as low as 12 mol% to as high as 90 mol% [39,58].

Since the usability of these YAS glasses depends on their composition and thermal history, it is crucial to understand and reveal their structure well and to optimize it for different applications. Existing investigations using methods such as Raman spectroscopy [59] and NMR [60,61] suggest that the structure of YAS glasses is formed by the sharing of [SiO_4] and [AlO_4] tetrahedra, which are linked by common oxygen (bonding oxygen) as crosslinking elements. At moderate concentrations, Y^{3+} cations form modifiers of the glass network bound by ionic bonding to the terminal oxygen. When alkali metals or alkaline earth metals are added to the system, they are incorporated into aluminosilicate structures and behave as network modifiers by forming non-bridging oxygens (NBOx) or they can behave as charge network modifiers i.e. as charge compensators for the [AlO_4] units depending on the glass composition.

In a previous NMR study, it has been shown that aluminium predominantly exists as four-coordinated Al species as network former, and significant fractions of five- and six-coordinated Al species are present, depending on the Al/Y ratio [59,62]. Several experimental studies confirmed the existence of substantial proportions of five-coordinated Al in these glasses and the correlation of the rare-earth network modifier’s nature and concentration [63]. The role of yttrium in these glasses is still not well understood, therefore recently a density-functional theory (DFT) simulation of the glass system has been created, which by means of calculations

confirms the above-mentioned coordination numbers of aluminium and suggests the formation of 2-member Al rings, which overall strengthen the glass structure. For the yttrium ion surroundings, it proposes a coordination of oxygen of 5,6 or 7 depending on its ratio to Si [64].

2.2 Metal nanoparticles in glass

Nanoparticles are crystalline or amorphous particles of various shapes with dimensions of 1-100 nm [65,66]. Compared to bulk materials, they exhibit significantly different properties, which are mainly caused by the increased proportion of surface atoms with the decrease of particle size. The difference between the properties of bulk materials and nanomaterials caused by an increase in the ratio of surface atoms is referred to as "surface effects". Surface atoms have less coordination with adjacent atoms, which is reflected in a decrease in the overall binding energy of the nanostructure. This effect has a large influence on changes in physical properties such as density or phase transition temperatures. Phenomena affecting the band structure of energy levels due to the manifestation of quantum constraints are referred to as "quantum size effects". The splitting and formation of new energy levels and forbidden bands has a major effect on the optical and electrical properties of nanomaterials. Due to the collective oscillation of electrons, characteristic absorption bands of plasmon resonance are formed in their optical spectrum. The formation of forbidden energy bands can lead to low-temperature semiconducting behaviour in materials that are good conductors in bulk form [67,68].

2.2.1 Au nanoparticles and their optical properties

The band structure of energy states and the decreasing density of energy states of nanoparticles are closely related to the optical properties of nanostructures. The Surface Plasmon Resonance (SPR) phenomenon has a great influence on these properties. Plasmons are energy states characterized by the collective oscillation of delocalized electrons in the crystal structure of metals. Electrons can be excited to these energy levels by absorbing a quantum of energy from external electromagnetic radiation. Plasmons in bulk metals appear in a wide range of wavelengths and determine their typical optical properties (colour, lustre). They occur throughout the bulk of metallic materials, but those at the interface between the material and the surrounding environment (surface plasmons) are particularly important in terms of optical properties. The oscillations of the electrons of the surface plasmon give rise to electromagnetic

fields which can propagate into the surroundings at distances of tens to hundreds of nanometres from the surface. There is significant absorption of light at a specific wavelength.

Plasmons in the nanostructure do not propagate into the surroundings but are confined to the limited space provided by the nanostructure; these are localised plasmons. If the electrons in a localised plasmon are excited (depending on the type of material and size of the nanostructure) by radiation at the frequency of visible light, the LSPR will manifest itself by changing the colour of the material. In the case of spherical Au nanoparticles, the radiation frequency corresponding to the plasmon energy level is ca. 520-580 nm (depending on the size of the nanoparticles) and absorption occurs for nanoparticles with a size of ca. 2-100 nm. For this reason, colloidal solutions of spherical Au nanoparticles have a typical red colour and show a characteristic shift in the absorption spectrum – **Figure 8.**

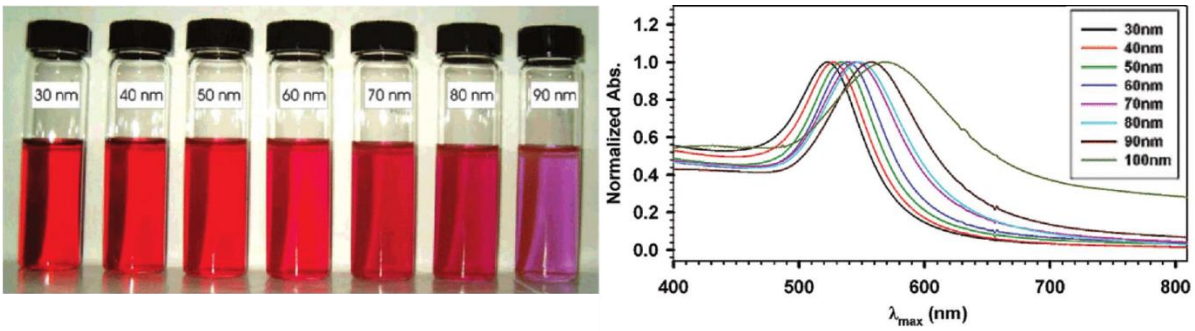

Figure 8 *Colour and absorption spectra of colloidal solutions of gold nanoparticles - the influence of size [58]*

This phenomenon was first described by Gustav Mie and it as known as Mie theory [69,70]. In short, light interacts with metal nanoparticles that are an order of magnitude smaller than the wavelength of the incident light. The electromagnetic wave (light) causes a collective resonant oscillation across the free electrons of the metal nanoparticle. This leads to the characteristic absorption and scattering of the incident light, which is macroscopically manifested by the distinctive colour of the sample containing the metal nanoparticles [71]. The extinction occurs for the incident beam, which can be calculated as the sum of absorption and scattering.

The proportion of absorption and scattering depends strongly on the nature of the element forming the nanoparticle and the size of the nanoparticle. Nanoparticles smaller than two nanometres lose their metallic character and do not exhibit plasmon behaviour. For spherical

particles with a diameter of 20 nm the effect of scattering is zero, for particles with a diameter of 40 nm the scattering is very small, but for particles with a diameter of 80 nm the effect of scattering is already very significant - see **Figure 9** [72]. It is fascinating that Mie's explanation of the colour of solutions based on the content of metal nanoparticles was given 25 years before the first electron microscope was built and enabled to observe these particles [73].

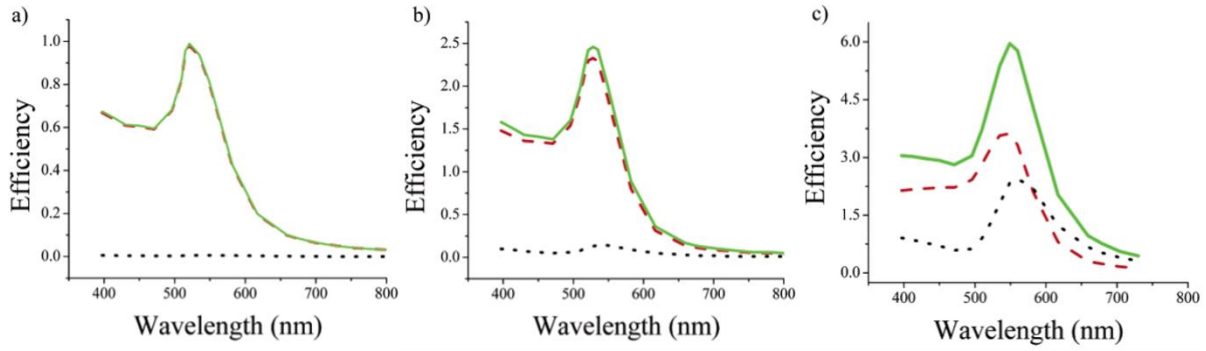

Figure 9 *Calculated spectra of the efficiency of absorption Q_{abs} (red dashed), scattering Q_{sca} (black dotted), and extinction Q_{ext} (green solid) for gold nanospheres (a) D = 20 nm, (b)D = 40 nm, (c) D = 80 nm [72]*

Based on Mie theory, knowledge of the refractive index of the medium, dielectric function and size of the nanoparticles, the position and shape of the LSPR peak can be calculated. The position of the peak agrees very well with the experimental data for aqueous solutions; however, the peak shape is not completely accurate. Experimentally measured data generally has a broader peak than calculated data – see **Figure 10**. This may be partly due to the boundary conditions of the calculation, which assume uniform spherical particles that are evenly distributed in the surrounding environment and do not interact with each other.

The synthesis of AuNPs in aqueous solutions is nowadays very well experimentally mastered. It is possible to prepare AuNPs of precisely chosen size with a narrow size distribution, NPs covered with different surface functional groups or nanoparticles of different shapes. In addition to basic nanospheres [74], these are for example nanoshells, nanorods, nanotriangles [75], nanostars [76] or nanocubes [77] – see **Figure 11**. One of the first and most well-known techniques for the preparation of monodisperse spherical gold nanoparticles with a diameter of approximately 10-20 nm in aqueous solutions is the Turkevich method. It consists in the

reduction of gold from $[AuCl_4]^-$ solution by sodium citrate. The citrate then also acts as a surface protecting agent for the produced nanoparticles [53].

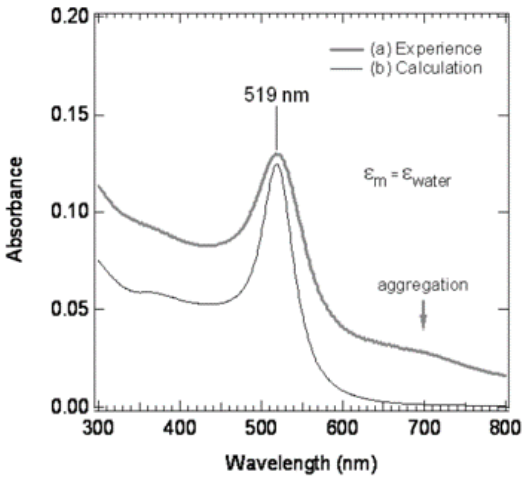

Figure 10 *Comparison of measured and calculated absorbance for 14.2 nm gold nanoparticles in water [71]*

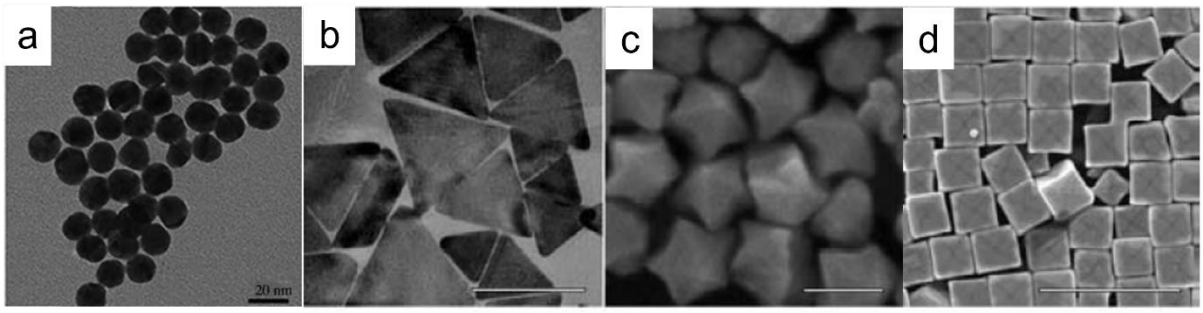

Figure 11 *Gold nanoparticles of different shapes. a) spheres b) triangles; scalebar=166 nm c) stars; scalebar=100 nm d) cubes; scalebar=500 nm*

The position of the LSPR, which is critical for many potential applications of nanoparticles, is also influenced by the shape of the nanoparticles. The absorption band for spherical nanoparticles with a diameter of 30-100 nm is a single band (due to the symmetry of the NPs) with maximum between 520 and 570 nm. For cylindrical particles (nanorods), however, the maximum splits into 2 bands corresponding to the oscillation of the electron density along the transversal and longitudinal axis of the cylinder. The absorption corresponding to the

longitudinal axis is at a higher wavelength and the intensity and position of the absorption bands depend on the ratio of the axis lengths of the cylinder (

***Figure* 12**). Similarly, different absorption maxima can be assigned to more complex nanoparticle shapes according to the shape factor and the corresponding plasmon resonance. In these cases, the absorption maximum of the band can extend to the NIR region of the spectrum i.e. 650 -900 nm.

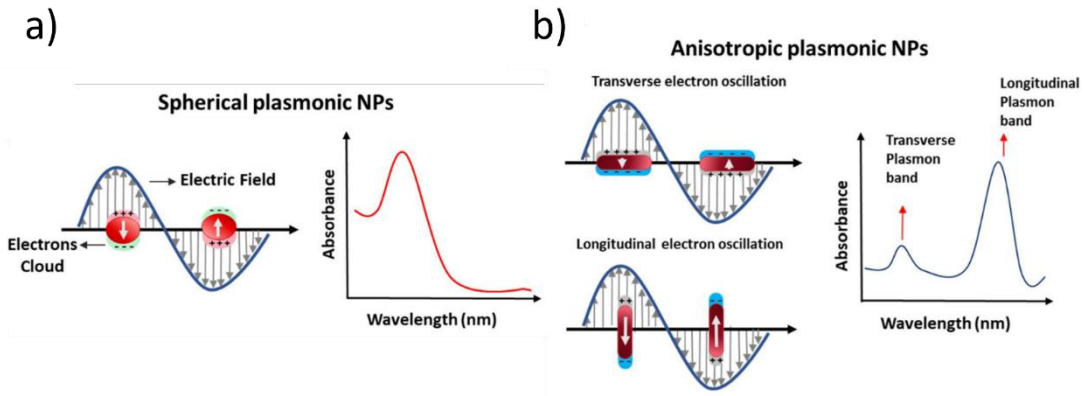

Figure 12 *Schematic representation of Surface Plasmon Resonance (SPR) band in (A) spherical and (B) rod-shaped plasmonic NPs [78].*

Moreover, the position and intensity of the LSPR band can be affected by a change in the environment surrounding the nanoparticle, as it depends on the refractive index of the glass

matrix. The higher the refractive index is, the more intense and more shifted the plasmon resonance is to higher wavelengths. Examples are provided in **Figure 13** [71].

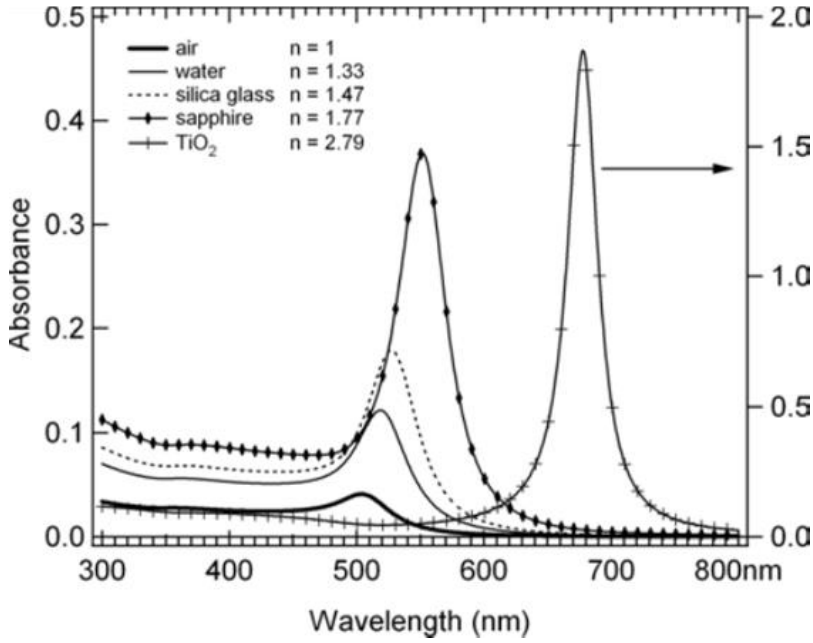

Figure 13 *Dependence of absorbance of AuNPs on refractive index of surrounding medium [71]*

In summary, a shift of the LSPR peak can be caused by:

1) a change in the size of the nanoparticles [71,79]. Gold nanoparticles smaller than 2 nm in diameter do not absorb. For slightly larger nanoparticles (~2.5 nm), the typical LSPR peak appears and redshifts (i.e. increases its wavelength) with increasing nanoparticle size;
2) a change of the shape of the nanoparticles [80] – spherical nanoparticles have are the most blueshifted (shifted to lower wavelengths), with decreasing symmetry of the nanoparticles a redshift in LSPR occurs;
3) a change in temperature. Decreasing temperature a minor blueshift of the LSPR occurs [81];

4) using nanoparticles with different shell and core structure [71];
5) aggregation of the AuNPs [82];
6) the value of refractive index of the surrounding environment [71].

2.2.2 Gold nanoparticles in glasses and glass-ceramics

The preparation of gold nanoparticles in glasses is not nearly as technologically advanced as in solutions. Paradoxically, however, the first gold nanoparticles were created in glass. The oldest artifact containing AgAuNPs is the Lycurgus cup, a Roman opaque glass cup from the 4th century AD (see **Figure 14**). The figure shows that the cup exhibits a strong dichroism. When the cup is illuminated from the outside (i.e. when the incident radiation is reflected) it appears green, whereas when illuminated from the inside (when the radiation is transmitted) it appears deep red. In addition, in the area of the torso of King Lycurgus the red colour changes to purple. These colour changes are caused by the presence of metal nanoparticles. So far, it has been found that the cup is made of ordinary soda-lime silicate glass, with a relatively high iron content, and the colour changes are caused by gold and probably colloidal Cu -Ag -Au particles, which are, moreover, not evenly distributed [83].

This amazing phenomenon is still not fully explained, and some studies claim that the red colour is caused by the absorption of gold of about 10 nm at wavelengths of about 520 nm, while the purple colour is caused by larger gold particles (about 20-30 nm). The green colouration is caused by light scattering on silver particles > 40 nm in size [84]. Recent studies suggest that surface phase separation of α-quartz could be present in the cup and that the red colour in transmitted light is due to light absorption by metal nanoparticles, while the olive green colour of the glass in reflected light is mainly due to Fe^{2+} and Fe^{3+} ions and Rayleigh scattering on SiO_2 droplets on the surface. [85]

The process of using gold in the glass industry was rediscovered and described in detail not until the 17th century. It is associated with the names Andreas Cassius of Leyden and Johann Kunckel. Cassius discovered the pigment that is now known as the Purple of Cassius. It is a pigment formed from gold that is dissolved in aqua regia and then precipitated by a mixture of stannous chloride and stannic chloride. Kunckel used this pigment in the preparation of the so-called gold ruby glass. However, Kunckel kept the exact details of how this type of glass

was prepared secret. After his death, the secret of preparing gold ruby glass was lost again. It was not rediscovered until the 19th century [71].

Figure 14 *Lycurgus cup in reflected and transmitted light [86]*

Nowadays, the enrichment of glass with gold is not only used for decorative purposes such as the preparation of glass vessels and jewellery, but with the development of diagnostic methods capable of detecting nanoparticles in glass and thus controlling their distribution and size, it is also used in the following industries:

1) **Optoelectronics** – Because the non-linearity in glasses (as main optics material) is generally quite small, the non-linear response can be improved by several orders of magnitude by embedding NPs. Particularly, all-optical switching devices based on NLO glasses with embedded NPs can potentially overcome the speed limitation imposed by electrical switching devices [87–90].
2) **Photonics -** Enrichment of rare earth doped glasses with metal nanoparticles can be used to improve the luminescent properties of the glasses, leading to the preparation of high-performance photonic devices [91–93].
3) **Sensing -** Surface-enhanced Raman spectroscopy (SERS) is now a well-known analytical technique that allows sensitive detection of a single chemically specific molecule [94–96].

4) **Heterogeneous catalysis** - A current trend is the use of porous glasses as supports for suitably distributed metal nanoparticles, which, due to their large surface area, enable a variety of catalytic processes [97,98].

5) **Biomedicine** - Incorporation of metal nanoparticles into biocompatible enamels (for example Cu NPs) improves their healing properties, their bioadhesion, and increases their anti-cancer potential [99]. In addition, such enamels also have antibacterial effects [100].

6) **Art and jewellery** – Red ruby glass, especially that coloured with gold, still finds its application in the field of decoration and art.

2.2.3 Preparation of metal nanoparticles in glass - technology

Several possible ways of creating glass containing crystalline metal NPs have been described in the literature. In addition to the classical glassmaking method of forming nanoparticles over the entire volume of the glass in-situ, glasses containing metal NPs can be created by ion exchange, ion implantation, localized irradiation. There are also several ways to incorporate pre-fabricated metal NPs into the glass. Since the melting temperature of bulk gold is 1064 °C (and significantly lower for nanoparticles), simply mixing the pre-prepared nanoparticles directly into glass that is melted at a higher temperature is not an option. These techniques are sol-gel doping, glass powder doping [101]. A summary of the methods with their advantages and disadvantages is given in **Table 1**. It should be noted that there is a significant disadvantage of using a high-temperature synthesis. Gold is quite volatile and some part (or most of it) might be lost during melting at high-temperatures.

Table 1 *Methods of metal nanoparticles preparation*

Method	Advantage	Disadvantage	Ref.
Melt-quenching	-simple and long standing -short processing times -continuous processing -NPs throughout the volume high variability of glass composition -inexpensive	-high temperature processing -no control of NP size, distribution and location within the glass during melt process	[102–130]
Ion-exchange	-simple -possibility to control of NP location	-for metals subject to ion exchange -concentration limit of	[91,131–141]

	-no damage virgin glass -co-embedding various metal NPs -inexpensive	NPs in the surface thin film	
Ion-implantation	-short processing times, -low temperature processing -control of NP location within the glass -high concentration of NPs -uneven distribution of NPs near the surface high variability combination NPs vs. substrate	-no control of NPs size and distribution -damage of glass -may generate impurities- -expensive	[106,142–150]
Localized irradiation	-simple -possibility to control of NP location -short processing times	-damage of glass -expensive	[151–155]
Sol-gel doping	-low temperature processing -inexpensive	-long processing times -discontinuous processing -no control of NP location within the glass	[156–160]

Melt-quenching (conventional method)

This method is widely used primarily to prepare coloured glasses in their entire volume. The basic technology involves two steps. In the first step, a transparent colourless glass is prepared by melt-quenching. Gold is mixed directly into the glass batch (ca 0.003-0.05 wt. % [103]), most often in the form of a solution of $H[AuCl_4]$ or purple of Cassius (purple pigment, mixture of $H[AuCl_4]$ and tin (II) chloride). Polyvalent ions (e.g. compounds Sn, Sb, Se, Pb, As) are in fact an important component of the base glass, as they facilitate the dissolution of Au in the glass, increase its solubility at lower temperatures and in the second step ensure easier and uniform colouring of the glass. In the second step, most commonly referred to as "striking", the glass is heated for ~1-20 h to a temperature close to the T_g of the glass. A typical coloration occurs, which is caused by the formation of AuNPs in the glass volume.

The colour of the glass may be pink, red, blue, purple or brown for glasses containing AuNPs depending on the number, size, internal structure and shape of the dispersed particles. It may

also be different depending on whether the glass is observed in reflected or transmitted light. This phenomenon is called colour dichroism [102].

A model has been developed to control the colour of glass containing gold nanoparticles. Weyl [102] proposed several distinct different types of gold containing glasses in order to simplify the discussion about their properties and transitions. The different types are shown schematically in **Figure 15**. **Type I** (**colourless glass**) exists only in molten glass. Gold is dissolved in the glass in the form of Au ions. Cooling of gold-containing glass leads to supersaturation and spontaneous crystallization. Two extreme cases can occur:

1) First, if the temperature dependence of the solubility of Au in the glass is steep, then virtually all the gold precipitates as crystals that cannot move in the glass due to its high viscosity (**type II-weak coloured reflection**). Importantly, virtually no gold remains dissolved in the glass. If this glass is heated to a high enough temperature for a long enough time, the existing clusters are allowed to precipitate, and the glass turns brown (**type III - brown colour**).

2) The second extreme case during cooling is that some of the gold precipitates out as tiny nuclei and the rest remains dissolved in the glass (**type IV-no colour**). For this to happen, the temperature dependence of the solubility of Au in glass must be less steep. This can be achieved by the addition of metallophilic elements as Sn, Sb, Pb, which increase the solubility of gold in molten glass. By heating such glass to a sufficiently high temperature to allow the movement of Au ions in the glass and the growth of nuclei. Spherical (**type V- red colour**) or anisometric particles (**type VI- purple colour**) are formed. By careful heating and recrystallization of **Type VI** glass, **Type V** can be achieved. **Type V** glass is referred to as gold ruby glass - a desirable product of glass production.

Further heating of **type III, V, VI** glass will result in the growth of large Au particles at the expense of small ones and their coagulation, forming large spherical crystals. The resulting glass (**type VII – blue colour**) has a distinctive brown colour in reflected light and blue in transmitted light. It is referred to as saphirin glass.

The optimal route for the preparation of gold ruby glass is I→ IV→(VI)→V (highlighted with thicker green arrows in **Figure 15**). If the glass gets to the right side of the diagram (types II, III, VII) during production, the desired red colour is no longer achieved. In other words, for

glasses with a steep temperature dependence of the Au solubility in the glass, the desired red colour cannot be achieved.

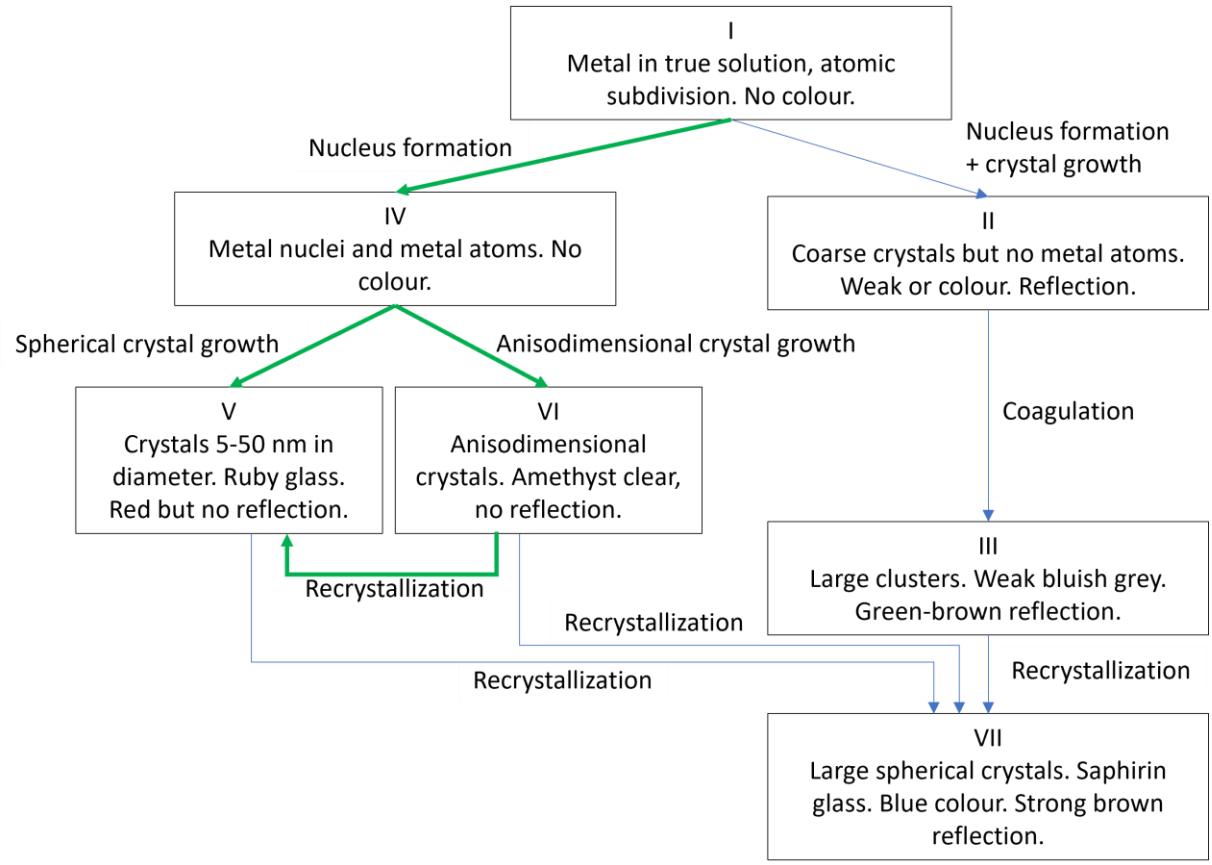

Figure 15 *Different types of gold-containing glasses according Weyl [102] (edited).*

Generally, the colour of the glass corresponds to the size of the AuNPs nanoparticles as follows: size below 3-5 nm = colourless glass, no contribution to the absorption; size 5-60 nm = good ruby glass, light absorption does not depend on AuNPs size, but on the amount of Au in the glass, when only particles from 5-60 nm are present; size 70-100 nm = brown colour, livery; size 200-500 nm = little contribution to absorption or scattering, strong reflection [102].

Several authors report that the colour of glass containing Au nanoparticles can be influenced by the addition of metal oxides such as tin, antimony, bismuth and lead [102,103]. The mechanism is not precisely elucidated, but as in solutions, the formation of a weak metallophilic

interaction between gold and metal ions can be assumed. This interaction prevents the growth of large gold crystals and rather promotes the formation of many small gold nanoparticles that absorb light in the visible part of the spectrum. The most common metallophilic element is tin [104,105] (in glasses mostly in the form of SnO_2). However, the solubility of SnO_2 in glass can also be influenced by the composition of the whole glass, e.g. by the content of alkali metals or aluminium oxide [102].

The relationship between glass composition and nanoparticle formation is not systematically described in the literature [106]. Most of the current publications that investigate the link between glass colour and the presence of Au nanoparticles focus on the description and explanation of archaeological findings [107,108]. Relatively few articles describe the formation of gold nanoparticles for the purpose of glass colouring. Usually relatively complex oxide or chalcogenide systems containing e.g. more than 5 glass components are studied. Alternatively, there are publications focused on special types of bismuth, zirconia or lead glass. An overview of the glass systems containing AuNPs that have been published in the literature in recent years can be found in the **Table 2**.

In general, it can be said that the reproducible preparation of uniformly coloured glasses is extremely challenging from a technological point of view. The resulting colour of the glass depends on many factors, and precise control of the entire melting process is important, from the correct homogenisation of the glass, through uniform and sufficiently fast cooling, to a suitably selected subsequent striking regime. For this reason, only a few companies produced gold ruby glass by MQ, the others then purchased it in the form of coloured glass rods or glass cullet [102].

Table 2 *Overview of glass systems doped with AuNPs*

Glass matrix [mol%]	**Reference**
xK_2O-xB_2O_3-$(100-2x)Sb_2O_3$, x = (10, 15, 20, 25)	[109]
$60Bi_2O_3$-$30B_2O_3$-$10SiO_2$	[110]
Li_2O-CaF_2-$20ZnO$-B_2O_3	[111]
$35Bi_2O_3$-$65B_2O_3$	[112,113]
$25Na_2O$-$2Sb_2O_3$-$73B_2O_3$	[114,115]
$30Na_2O$-$10ZnO$-$60B_2O_3$	[116]
$25Na_2O$-$0.5Eu_2O_3$-$5Sb_2O_3$-$69.5B_2O_3$	[117,118]
$1.4Na_2O$-$10.8ZnO$-$10MgO$-$19.7Al_2O_3$-$48.4SiO_2$-$5TiO_2$-$4ZrO_2$-$0.7SnO_2$	[119,120]

$20Na_2O$-$10CaO$-$1Sb_2O_3$-$70SiO_2$	[121]
$12.6Na_2O$-$0.3K_2O$-$6.3MgO$-$9.2\ CaO$-$0.3Al_2O_3$-$71.3SiO_2$	[122]
$9.3Na_2O$-$10.8CaO$-$4.8MgO$-$63.6SiO_2$-$0.6Al_2O_3$-$0.5ZrO_2$-$0.2Sb_2O_3$-$10.2B_2O_3$	[123]
$60SiO_2$-$32CaO$-$8P_2O_5$ (sol-gel)	[124,125]
$6.7Na_2O$-$18.3B_2O_3$-$0.1Al_2O_3$-$74.9\ SiO_2$	[126]
$10Na_2O$-$20ZnO$-xEr_2O_3-$70TeO_2$ (x = 0.1)	[127]
20Ge-5Sn-75S	[105]
$60PbO$-$40GeO_2$	[128]

Glass powder doping

This method is very similar to conventional melt-quenching and consists of three steps: 1) preparing and crushing the base glass, 2) mixing the pre-prepared NPs and crushed glass, and 3) fusing the powder mixture together and casting into a mould. The main challenge of this method is to find a compromise between good dispersion of the NPs, complete bonding of the powder mixture and at the same time not ruining the original properties of the NPs. High melting temperatures and/or long melting times promote good homogeneity of the prepared samples, but at the same time they lead to a change in the size and shape of the introduced NPs [129,130].

Ion exchange

Ion exchange is currently a relatively mature technology for fabricating optical waveguides in glass substrates and, due to the low optical signal loss and robustness of the process, it appears to be the most suitable approach for developing a range of passive integrated optical devices [131–134]. The process is usually carried out by immersing a glass substrate in a bath of molten salt containing the desired metal ion, which is exchanged with the alkaline ions of the glass to produce a diffusion profile whose shape and depth depend on the diffusion coefficients of the ions and the temperature. In some cases, an external electric field can be used to control the shape of the profile more precisely. In other approaches, diffusion of metal ions is carried out from a metal layer deposited on the glass surface; in this case, migration is promoted by an external voltage applied between the two sides of the glass slide [135].

If the ion-exchange technique is used for noble metals (Au, Ag or Cu), it focuses mainly on the exchange of $Ag^+ \leftrightarrow Na^+$ or Cu^+ or $Cu^{2+} \leftrightarrow Na^+$ [91,136–138]. Ion exchange of gold for alkaline ions is very rarely performed. Besides the fact that the presence of metal ions increases the

refractive index, the metal nanoparticles use a large third-order nonlinear susceptibility with ultrafast response suitable for applications also in nonlinear optics [139–141]. Although it is possible to achieve a suitable coloration of the glass after annealing (e.g. yellow-brown colouration in the case of Ag NPs) this technique is not widely used for large-scale production of coloured glass.

Ion implantation

Ion implantation in glasses requires by which ions of Au^{+} are accelerated into a glass target, thereby create the nanoparticles and simultaneously changing the physical, chemical, or electrical properties of the target. Ion implantation is the most versatile method of preparing metal nanoparticles especially in silicon or silicate glasses [142–145]. This method allows easy control of the layer depth and concentration of implanted ions as well as the formation of nanoparticles. Commonly are used energies range from 50 keV to 3 MeV and fluences between 10^{16}-10^{18} ions.cm^{-2}. It has been found that increasing the fluence and energy of ion implantation leads to the formation of nanoparticles and facilitates their growth. A similar effect, especially for gold nanoparticles, is achieved by annealing after implantation [146] The disadvantage of the high energy ion implantation process is the damage to the matrix in the ion impact area and the formation of defects. These defects can also cause absorption of optical radiation in the range of 5-7 eV [147], but can be removed by post-implantation annealing.

Unlike ion exchange technology, any various kind of glass can be used as a substrate for this method. Most often gold particles were implanted into silica and usually had a size from 3 nm to 40 nm and a spherical shape after ion implantation [106,148]. Rarely gold nanoparticles of other shapes were found. Previous results from our group have shown that the range of implanted ions depends mainly on the density of the glass and, to a lesser extent, on the structure of the glass. Moreover, the shape, size and distribution of nanoparticles are strongly influenced by the actual annealing temperature in the sense that the larger the deviation of the annealing temperature from the transformation temperature of a given glass, the smaller the nanoparticles formed and vice versa [149,150].

Formation of nanoparticles in glass by localised irradiation

If a photosensitiser (most commonly Ce^{3+} for Au) is contained in the glass together with noble metal ions, the glass becomes sensitive to short wavelength ionising radiation, such as UV light

or X-ray [151,152]. By covering part of the glass with a photomask and then irradiating it, this photosensitized glass can be used as a photographic medium [153]. This technology has recently been further developed, using a femtosecond laser it is possible to generate 3D patterns in glass on a similar principle [154]. Gold ruby glass was made by irradiation technology into soda-lime-silicate glass using gamma rays and further heating instead of using a reducing agent such as stannous oxide. Different colours were obtained by controlling the temperature and heating times [155].

Sol-gel doping

Pre-prepared nanoparticles with suitable surface ligands are added to the liquid sol of the prepared glass. The mixture is homogenized using a mixer or ultrasound and cast into a mould or deposited onto a substrate. Subsequently, as with glass preparation using sol gel technology, the matrix is cross-linked to form a gel containing NPs. By careful drying of the gel, a bulk sample can be formed [156–159]. The advantage of this technique is that we have full control over the properties of the nanoparticles (shape, size) that are incorporated into the glass. However, this technology carries all the disadvantages of sol-gel technology such as high time consumption, imperfect sample densification and poor mechanical properties [160].

2.2.4. Current research- new trends

In recent years, research on AuNPs in glasses has been very prominent, especially in the connection with their optical properties. Most often these glasses are prepared by classical melt-quenching technology, in a few cases by sol-gel or ion implantation. The most commonly used gold precursor is $H[AuCl_4]\cdot xH_2O$, other variants are Au_2O_3, AuCl, $AuCl_3$ or metallic Au. In the vast majority of papers, only one of the ways in which the properties of AuNPs can be influenced, and thus the overall optical properties of the studied material, is always investigated. The most frequently reported ways of changing optical properties of glass samples doped with gold are the secondary heat treatment (and the effect of its length or temperature), the concentration of Au in the glass or the change of the refractive index of the glass matrix [161]. Jagannathan research group have also published papers on the effect of changing the local refractive index by using nucleating agents (TiO_2, ZrO_2) or by nanoscale phase separation in the glass matrix [119].

Potential applications often reported include the possibility of using AuNPs in solid state lasers, colour displays (LCDs), ultrafast optical switches, photonic devices, new optical glasses and glass-ceramics, optical limiting, bio-imaging, harmonic generation, and data storage. However, original potential applications are also emerging. Takebe [123] proposed a way to recycle retired solar panels. Gold ruby glasses with a characteristic LSPR peak between 521-544 nm were prepared from the cullet of these panels, which can be used for decorative purposes. Bioactive glass in combination with AuNPs prepared by sol-gel method is another unique idea. When ground and mixed with Vaseline, it can be used to regenerate skin wounds [124,125]. Germanate-lead glasses doped with Eu and Au could be used to optimize the performance of photovoltaic devices [128]. Lebedev [126] published a procedure to prepare porous borosilicate glass, with AuNPs incorporated into the pores by liquid state chemical deposition. Such a glass could serve as a membrane with selective ion transport.

There are also theses on AuNPs in glass. Bring [162] addressed this subject with the aim of (re)inventing an alternative to the toxic CdS and CdSe pigments that are used to achieve the red colouration of glasses. Saiyasombat [163] investigated in detail a sodium silicate glass containing Au and SnO_2. In his work he describes in detail the role of SnO_2 to achieve the coloration of the samples and based on the measured data he proposes a model describing the behaviour of gold ions and nanoparticles in the glass. Wei [101] described a new method for preparing glasses containing nanoparticles. He describes this method, called the "powder reheating technique," as suitable for preparing noble metal nanoparticles in a wide variety of different types of glasses.

3 MOTIVATION AND RESEARCH OBJECTIVES

Although gold nanoparticles have been in practical use for thousands of years, they still find applications both in solutions and as part of the solid phase in traditional and modern industries, as shown in the theoretical part of the thesis. Also, with the development of electron microscopy, there is a much greater opportunity to investigate their shape, distribution and structure in the context of optical and biocatalytic applications. Their nucleation and growth in glasses is relatively rarely described in the current literature, as it is difficult to achieve a pre-specified and desirable distribution and size of gold nanoparticles in glass substrates. For bulk doping of glasses, which has mainly decorative applications, MQ technology is used exclusively. According to the literature research, containerless technologies such as ADL have not yet been tried and offer a unique opportunity to dope materials with a relatively high melting temperature with gold.

The presented dissertation aims to investigate a completely new containerless ADL technology for melting glass containing gold nanoparticles, to investigate the influence of ADL technological parameters on their distribution and shape by means of absorption and transmission electron microscopy.

The sub-objectives were set as follows:

1) To find which glass oxide systems are suitable for ADL technology and to try to generalize the findings.
2) To test the influence of ADL setup parameters on the formation of glass or other phases in the Y_2O_3-Al_2O_3-SiO_2 oxide system and to make a basic comparison with conventional melting.
3) To design and test a technological procedure for the preparation of gold nanoparticles in glass using ADL technology - i.e. 1) to describe the homogeneity of the samples and the distribution of the nanoparticles; 2) to compare the influence of the chemical composition in the two basic systems YAS and LS; 3) to evaluate the suitability and influence of the addition of tin(IV) oxide to the glass during ADL technology; 4) to compare the results, especially the absorption and distribution of nanoparticles, with the glasses of the same composition prepared by MQ.

4) To propose a suitable chemical composition of the glass for the preparation of Au NPs by ADL and to investigate how the composition can be used to influence the formation, size and distribution of gold nanoparticles.

4 EXPERIMENTAL PART

Two different experimental techniques have been used to prepare the samples. The main technique used was the aerodynamic levitation coupled to CO_2 laser heating (ADL), available at the CEMHTI laboratory in France. The second technique was conventional melt-quenching (MQ) in a high-temperature furnace, which was carried out at UCT Prague. A comparison of the two technologies is shown in **Figure 16** and **Table 3**. It is evident that the advantages of ADL are its higher maximum melting temperature, higher cooling rate, non-contact melting (and therefore reduced surface/heterogeneous crystallization) or a higher sample preparation speed (regarding the number of different samples, not their mass). The main disadvantage of this technology is its very small size of prepared samples and volatilization of certain elements from the melt.

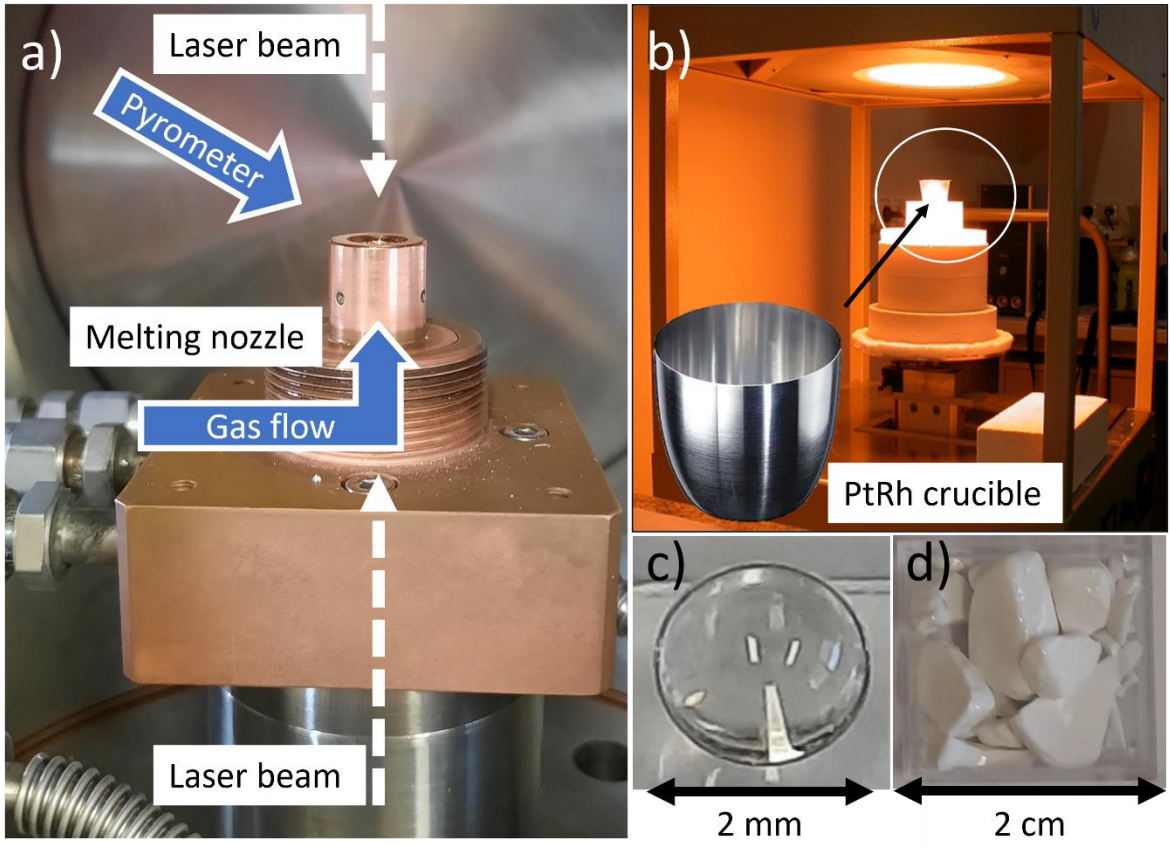

Figure 16 *Comparison of melt-quenching and ADL techniques. a) melting nozzle of the ADL device, b) high-temperature laboratory furnace with an enlarged image of a PtRh crucible, c) glass bead prepared by ADL d) glass sample prepared by MQ.*

Table 3 *Comparison of ADL and MQ*

	ADL	**MQ**
Max. temperature	3000 °C	1700 °C
Melting time	~ s	~ h
Cooling rate	~300 °C s^{-1}	~100 °C s^{-1}
Sample mass	~ mg	~ g
Sample shape	Sphere	Free (mould)
Contactless	Yes	No

Generally, silicate glasses containing systematically varying contents of modifiers such as Li, Na and K or intermediate elements such as Y and Al were chosen as the basis for the glass systems fabricated by both methods. The Y_2O_3-Al_2O_3-SiO_2 (YAS) system was studied first as the base of the glass matrix because of its advantageous optical and mechanical properties. The second base glass was $Li_2O{\cdot}2SiO_2$ (LS), which was chosen for its simple chemical composition, low melting temperature and which proved to be suitable for both preparation methods. These glasses were doped with varying gold and tin (IV) oxide contents. At the end of the work, several glasses were prepared in the Li_2O-Y_2O_3-Al_2O_3-SiO_2 (LYAS) system, which combine the advantages of both YAS and LS compositions that had been investigated in detail.

4.1 Aerodynamic levitation coupled to laser heating (ADL)

4.1.1 Chemicals used

Yttrium oxide, Y_2O_3 (99.9%, Strem chemicals)

Aluminium oxide, Al_2O_3 (99.997%, Alfa Aesar)

Silicon oxide, SiO_2 (99.5%, Alfa Aesar)

Hydrogen tetrachloroaurate (III) trihydrate, $H[AuCl_4]{\cdot}3H_2O$ (99.99%, Thermo Scientific, Germany)

Lithium carbonate, Li_2CO_3 (99%, Aldrich)

Sodium carbonate Na_2CO_3 (99.5+%, Strem chemicals)

Potassium carbonate K_2CO_3 (99%, Fluka)

Tin (IV) oxide, SnO_2 (99.9%, JMC Puratonic)

Argon gas, Ar (99.999%, Air Liquide)

Oxygen gas, O_2 (99.995 mol%, Air Liquide)

Epoxy resin EpoFix (Struers, Denmark)

Corn flour (Maizena)

Distilled water

Ethanol (denatured)

SiC polishing papers (P320-P4000, Presi, France)

Diamond polishing suspension (1 μm, Escil, France)

SiO_2 non-crystallizing polishing suspension (0.03 μm, Presi, France)

Wenol metal polishing cream

4.1.2 Description of pellet preparation

During the preparation of the samples using the ADL technology, it was first necessary to prepare the so-called tablet or pellet from mixed and compacted precursors (see **Figure 17a**), which would then be either melted in parts. A typical procedure for preparing the tablet was as follows: first, chemicals with a total weight of 1 g were carefully weighed using analytical balance based on a glass batch calculation. These were then mixed with a small amount of ethanol in an agate mortar and homogenized until most of the alcohol had evaporated. The mixture was then transferred to a steel die in which it was compressed into a coin-shaped tablet using a laboratory hydraulic press. Subsequently, small pieces of compact material weighing several tens of mg were broken off from this tablet and melted in the ADL device. If the above procedure was used, glass beads of irregular size were formed, which led to significant heterogeneities especially when doped with gold.

In order to improve the reproducibility of the experiments carried out, an alternative procedure was developed during the course of this work to prepare individual small pellets of approximately the same weight and a suitable spherical cap shape (see **Figure 17b**). The newly proposed procedure consists of mixing the powdered chemicals with a slurry of corn starch and then dispensing the resulting suspension with a precision repetitive pipette.

First, the chemicals were carefully weighed into an agate mortar according to the glass batch calculation. Then, 2 g of Maizena corn flour was added to a beaker containing 25 ml demineralized water under constant stirring with a magnetic stirrer. The mixture was heated for 7 minutes on an electric stove set at 200°C with constant stirring. The mixture was then transferred to a cold magnetic stirrer where it was allowed to cool for 4 minutes. The resulting slurry was mixed with the powder chemicals in the agate mortar in a weight ratio of

approximately 1:1 (the ratio varied for different glass compositions) and dispensed in 50 µl drops onto a non-stick pad using a Distrimann brand repetitive pipette. The resulting pellets were left on the pad overnight to dry. The next day, the pellets were annealed in an electric furnace for 30 min at 200 °C (ramp 5 °C/min from RT) and then for another 30 min at temperature close to the glass transition temperature T_g of prepared glass (ramp 5 °C/min). The pellets annealed this way were approximately the same weight and shape, mechanically robust and free of majority of the starch from the corn flour.

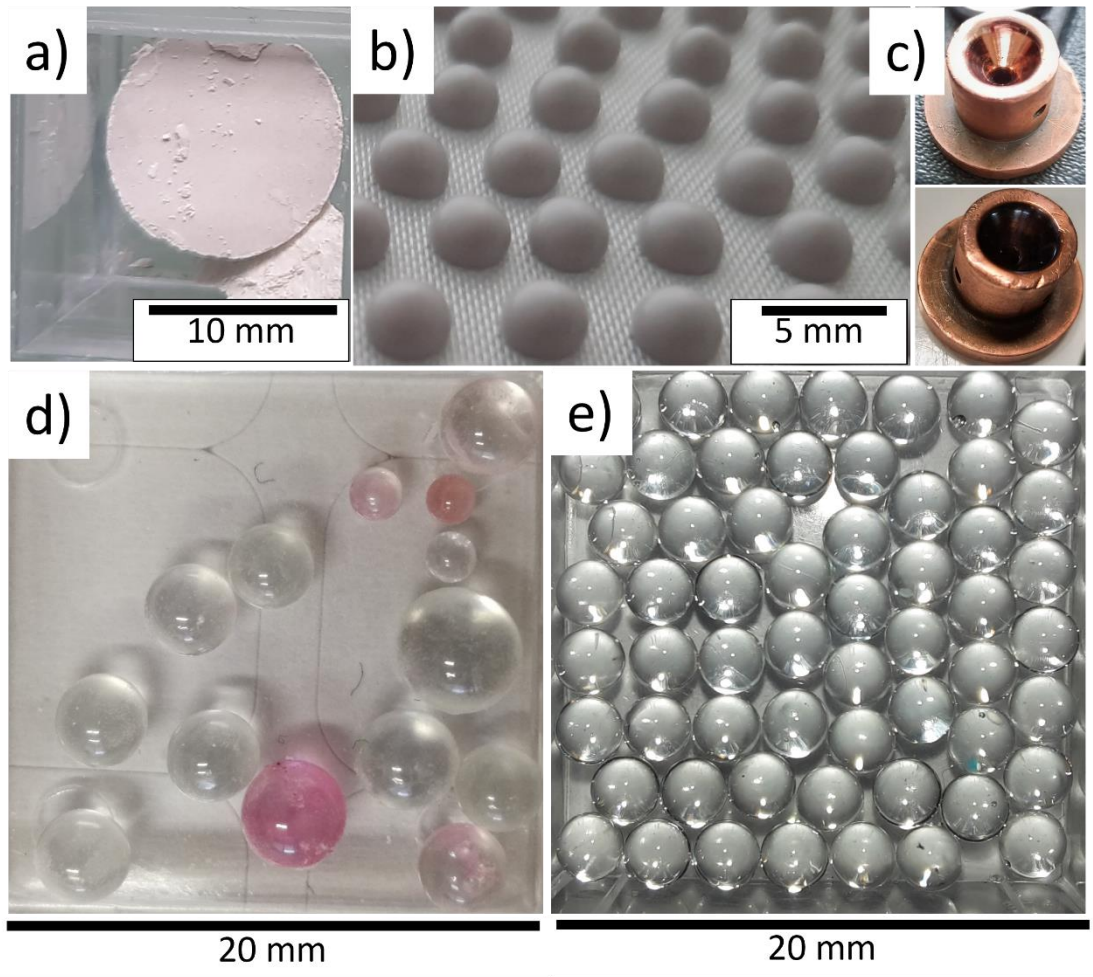

Figure 17 *a) A pellet for ADL melting prepared by pressing raw precursors b) Pellets for ADL melting prepared using cornstarch slurry and a repetitive pipette. c) Clean (top) and contaminated (bottom) Cu melting nozzle d) LS glass beads prepared by using the "old" approach e) LS glass beads prepared by using Maizena slurry and repetitive pipette.*

The pellets containing gold were prepared by a more complex process, which was developed during the course of this work to achieve maximum sample homogeneity in the shortest possible

melting time using the lowest possible melting temperature. The last two conditions (which are contradictory to achieving good sample homogeneity) are necessary in order to minimize gold volatilization during sample preparation. This can be observed with the naked eye as purple vapour escaping from the sample during melting, or as a black-purple layer that gradually accumulates on the melting nozzle. Photographs of the just-cleaned melting nozzle and the contaminated nozzle are shown in **Figure 17c**. The results of the EDS analysis of the contaminated nozzle indicate that a layer of $AuCl_3$ has formed on its surface.

For the preparation of pellets with gold content, the raw materials for the preparation of the base glass matrix without gold and tin were first calculated. These were milled, dried and the base glass was melted and milled again. Gold, in the form of a solution of $H[AuCl_4]$ and SnO_2, was added to the glass powder, and everything was carefully mixed. From this step forward, the procedure of preparation pellets doped with gold was the same as for pellets without gold described above. The mixed chemicals were combined with Maizena slurry and dispensed in form of small drops using Distrimann pipette onto a non-stick surface. The gold-containing pellets were easily distinguishable at first sight from the others. The higher the gold content, the pinker the pellets were after formation. This process of pellet preparation evolved during the course of the dissertation. This procedure was used to prepare samples with the designation **JB50** and higher.

The pellets prepared by this technique are shown in **Figure 17 b**. In **Figure 17d and e** one can see a comparison of beads prepared with the original and new techniques. The original beads are different in size at first sight, while the new samples are the same size. The weight of the samples prepared by the new method was tested on 60 beads prepared from 50 μl pellets. The average mass of a bead was (15.84±0.24) mg, the standard deviation of mass was 1.54 %.

4.1.3 Description of technology

The aerodynamic levitation device (see **Figure 18**) consists of several key parts. The heart of the device is a conical melting nozzle into which the pellet was placed. The pellet was levitated in a stream of gas which was coming from a gas bottle and whose flow was controlled by a computer. During the aerodynamic levitation, the sample was heated by a pair of pulse CO_2 lasers (Coherent Diamond K series, 670 nm visible and 10.6 μm radiation, 400 W max average,

900 mJ max 1ms pulse) whose beams were brought to the sample from above and below by mirrors. The actual power of the lasers was also controlled by the computer. An Impac ISR 320 pyrometer (two channels, spectral range 0.9 and 1.05 μm) was pointed at the sample in the melting chamber to monitor the temperature and a video camera with a suitable filter was used to monitor the melting process in real time.

The actual sample preparation was carried out as follows: a piece of the prepared pellet of the sample was inserted into the conical melting nozzle. Then the gas flow was adjusted so that the sample levitated in the nozzle. The lasers were then started, and the sample was melted within a few seconds. The result of the ADL melting was a glass sphere with a diameter of about 2 mm, which contained bubbles in some of the samples. By using pellets of the same mass, it was possible to semi-automate the melting process, i.e., to always maintain a constant gas flow and to set an identical melting program for all samples of the same composition.

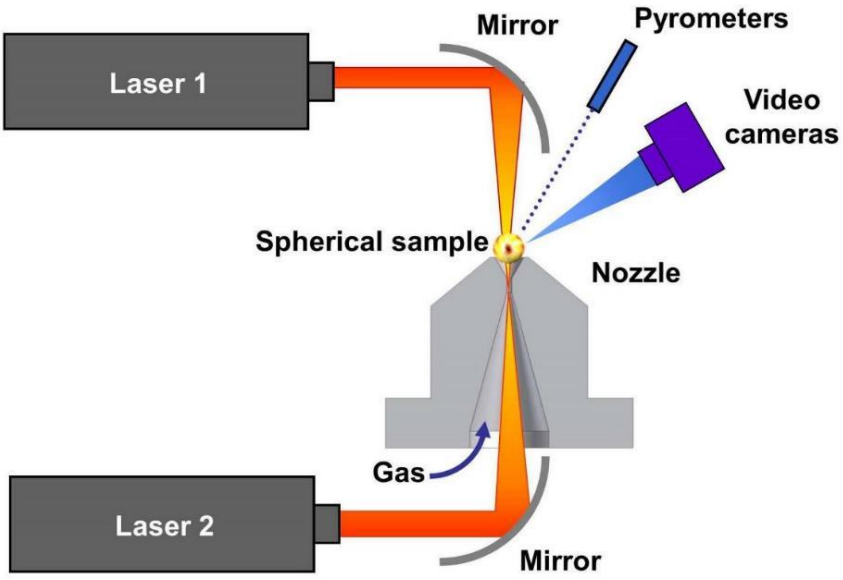

Figure 18 *Aerodynamic levitation coupled to laser heating - basic experimental setup [164]*

Multiple input parameters can be set during sample preparation with ADL technology. To improve the reproducibility of the experiments performed, it was essential to keep the melting parameters constant. These parameters can be divided into several groups:

First, the initial condition of the melting device - these parameters include the shape of the melting nozzle and the reflectivity (cleanliness) of its inner surface, the cleanliness and

correct alignment of all optical components in the laser beam path (optical mirrors, ZnSe or NaCl windows), the type of gas used for levitation

Second, the initial characteristics of the prepared sample - for good reproducibility of the experiments, it was necessary to load the device with pellets of approximately the same mass with a suitable shape.

Third, the parameters controlled by the computer during melting - although the laser power and gas flow in the melting device could be controlled with great real-time precision, for reproducibility of the experiments it was preferable to find a suitable melting programme for each sample composition and to keep this constant. These melting parameters, i.e., the time-dependent laser power value, the total time, and the gas flow rate, were designed so that samples of different compositions underwent approximately the same thermal history.

During the experiments carried out in this work, a copper melting nozzle was used and polished at regular intervals with Wenol metal polishing cream. The cleanliness of the optical elements in the melting device, which could be stained by volatile components of the prepared samples, was also checked at regular intervals. The gas used was initially argon because of its good ability to levitate the sample. Later, oxygen was used to provide an oxidizing atmosphere during melting. For melting, Coherent Diamond K250 CO_2 lasers with a maximum average power of 400 W were used, emitting radiation at wavelengths of 670 nm and 10.6 μm; 900 mJ max 1 ms pulse. For sample preparation, 15% of the maximum power of the lasers was used at most and the average melting time was 40 s. The temperature readings from the pyrometer were always below 2000 °C for YAS samples and below 1800 °C for all samples containing gold and also for all other samples of different base composition. Sample preparation by ADL is summarized in a diagram in **Figure 19**.

More than 100 compositions were melted using this procedure. From each sample 5-100 beads were prepared. The full list of samples is given in the **Appendix**, or the relevant samples are always listed in the introduction of each chapter in the **Results** section of the thesis.

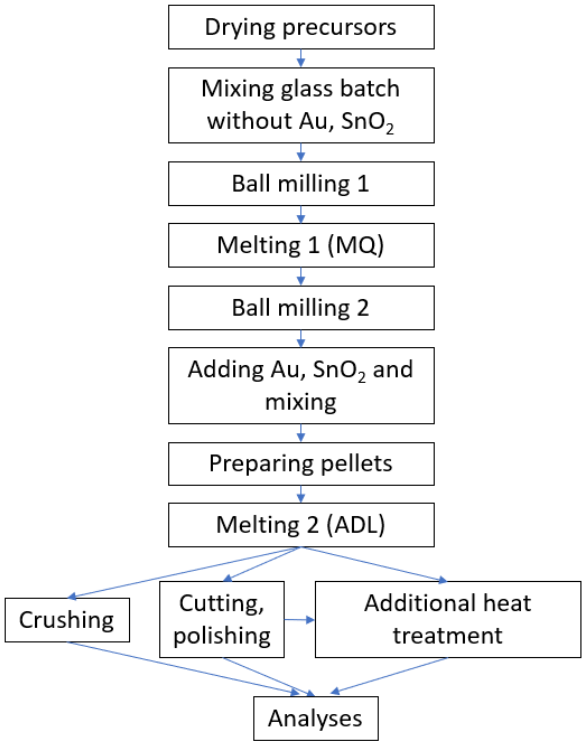

Figure 19 *ADL sample preparation protocol.*

4.2 Melt-quenching (MQ)

4.2.1 Chemicals used

Distilled water

Ethanol (denatured)

Isopropyl alcohol, $CH_3CH(OH)CH_3$ (p.p., 99.7%, Lach-Ner s.r.o., Czech Republic)

SiC polishing papers (P320-P2500, Hermes WS Flex 16, Germany)

Cerium oxide, CeO_2

Yttrium oxide, Y_2O_3 (99.9% by XRF analysis)

Aluminium hydroxide, $Al(OH)_3$ (p.a., Lach-Ner s.r.o., Czech Republic)

Silica gel, SiO_2 (high-purity grade, Sigma-Aldrich)

Hydrogen tetrachloroaurate(III) trihydrate, $H[AuCl_4]\cdot 3H_2O$ (99.99%, Thermo Scientific, Germany)

Lithium carbonate, Li_2CO_3 (99%, Aldrich)

Tin (IV) oxide, SnO_2 (Grade 1, JMC Puratonic)

4.2.2 Description of technology

Before starting the experiments, all hygroscopic precursors were put into a laboratory dryer at 100 °C overnight. A Clasic commercial melting furnace, heated by an electric resistance and capable of reaching temperatures of up to 1700 °C, was used to melt the glass. Two main series of glasses were prepared - glasses with a lithium silicate matrix Li_2O-SiO_2 (LS) and with yttria-alumina-silica matrix Y_2O_3-Al_2O_3-SiO_2 (YAS). First, only the basic matrices were prepared. Next, additional glass samples were prepared with different additions of Au and SnO_2 to those matrices.

After calculation, all precursors were carefully weighted using analytical balance, mixed, and homogenized by mortar and pestle for 10 min. Then, the first part of the glass batch was put in a platinum rhodium (PtRh) crucible with a lid into the melting furnace. At regular intervals of 15 minutes, the rest of the glass batch was cautiously added to the crucible to avoid foaming and overflowing of the melt. After the first hour from the start of the melting, the stirring of the melt began by circular movements of the melting crucible while holding it in steel tongs. Stirring was carried out 7 times each 10 minutes. After 3.5 hours from the start of melting, the sample was cast either into a steel mould with stops or into a steel die and immediately transferred to a pre-heated annealing furnace where the internal stress in the sample was removed overnight. The remaining glass in the PtRh crucible was rapidly cooled by immersing the crucible in water. The resulting cullet was also subsequently transferred to the annealing furnace.

In later experiments, a different sample preparation procedure was used in an attempt to improve sample homogeneity. First, the chemicals were weighed to make the glass matrix free of gold and a tin (IV) oxide. These were finely ground in an agate grinding vessel containing 30 g of chemicals, 30 g of demineralised water and 60 g of agate spheres using a ball mill. The mill was run for 10 minutes at 500 rpm and the direction of rotation was changed every 3 minutes. The resulting suspension was then vacuum filtered and dried in a laboratory dryer overnight. The dried ground chemicals were homogenized by a mortar and pestle and a base glass was prepared as described in the previous paragraph, except that all glass was rapidly cooled in the PtRh submerged in water to make cullet. This cullet was then crushed in a steel mortar, ground again in the agate mill (500 rpm, 30 min), filtered and dried. The cullet was

further thoroughly mixed by a mortar and pestle with gold precursor ($H[AuCl_4]\cdot 3H_2O$ solution), and SnO_2, and melted a second time in the electric resistance furnace, but this time only for 1.5 h. The entire melting protocol is summarized in **Figure 20** below.

The samples were cut using a diamond cutter and polished to optical quality using commercially available SiC sandpaper and CeO_2 suspension. The results were glass slices polished from both sided in the shape of a circular section with a radius of approximately 1 cm, a central angle of approximately 90° and a thickness of approximately 1 mm.

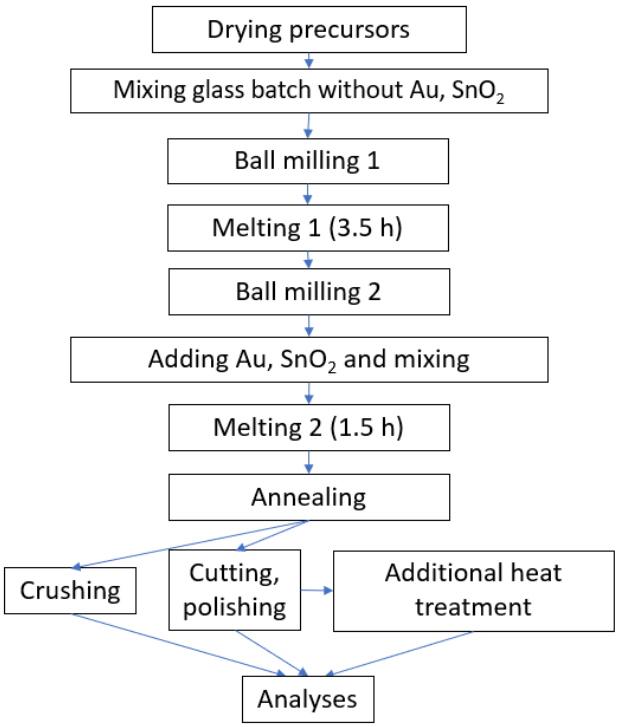

Figure 20 *Melt-quenching experimental protocol*

Immediately after melting, all samples prepared by melt-quenching were tempered in an annealing furnace to remove internal stresses. This process consisted of heating the sample at a constant temperature close to the T_g of the prepared glass for 1 h followed by controlled cooling at a rate of 1°C per minute to room temperature.

More than 40 samples of different compositions were prepared by this method. A detailed overview of the sample labelling and composition is given in the **Appendix**. A summary table of the relevant samples is always given at the beginning of the chapters in the **Results** section.

4.3 Additional heat treatment - striking

For the samples containing gold, the additional heat treatment after melting – striking – was of another key importance. This is because at temperatures around T_g, nucleation and subsequent growth of gold nanoparticles in the sample occurred, causing the typical coloration of the prepared glasses. The colour of the glasses ranged from pink to red to purple, depending on the temperature and the duration of the annealing.

Striking experiments were performed at constant temperature in the range of 300-1050 °C for 5 min up to 72 h. Typical parameters for YAS samples: 900°C, 15-120 min. Typical parameters for LS samples: 500 °C, 15-45 min. The annealing temperatures used for each glass system were based on the DSC analysis of the glass matrix. The main guideline was the temperature T_g, near which the optimal temperatures for nucleation and growth of nanoparticles were located. The upper limit for the annealing temperature was then the temperature of the first crystallization peak $T_{x,1}$. Crystallization of the glass matrix was undesirable in our experiments because it caused opaque zones in the prepared samples.

Annealing took place in refractory moulds or on unglazed ceramic tiles in Clasic or Nabertherm furnaces.

4.4 Characterization of prepared samples (instrumentation)

X-Ray fluorescence spectroscopy (XRF)

In order to determine the chemical composition of the prepared glass samples, X-ray fluorescence spectroscopy analyses were conducted in the Central Laboratories of UCT Prague using spectrometer ARL 9400. Approx. 1 g of sample was crushed into fine powder in an agate mortar before analyses. For samples containing lithium, the amount of Li_2O was input directly into the software according to its amount in the glass batch.

Laser ablation inductively coupled plasma atomic emission spectroscopy (LA-ICP-AES)

This technique was used to determine the local chemical composition of our samples. One of its major advantages for this work was, that LA-ICP-AES is able to quantify the amount of lithium oxide in the sample. Polished samples embedded in epoxy resin were used for the analysis. One bead of each studied composition was then analysed by Laser Ablation Inductively Coupled Plasma Mass Spectrometry (LA-ICP-MS) by adapting the analytical protocol developed at the IRAMAT-CEB for glass matrices [165]. On average, the beads had a diameter of 2 mm and were polished to study a cross section of the core of the bead. The laser ablated circular spots with a diameter of 0.1 mm. The measurements were performed at the IRAMAT laboratory of the CNRS Orléans.

Differential scanning calorimetry (DSC)

Differential scanning calorimetry (DSC) was used to obtain information about glass transition temperature T_g, crystallization temperature(s) $T_{x,n}$ and melting temperature T_m. Many beads or pieces of bulk glass were crushed into fine powder in an agate mortar before analyses. The measurements of most samples were performed at the CEMHTI laboratory of the CNRS Orléans. Approx. 400 mg of each sample was analysed by Setaram MHTC96 instrument. A 700 µl Pt crucible and Ar atmosphere were used for the DSC analyses. Heating rate of the samples was 10°C min^{-1}, the analyses were conducted in the temperature range 100–1400°C.

Thermal behaviour of samples LYAS 2, 5 and 8MQ was analysed by Simultaneous thermal analysis (STA). The DTA and TG curves were recorded simultaneously on a Linseis STA PT1600 apparatus with a heating rate of 10 °C min^{-1} in a dynamic air atmosphere (50 ml min^{-1}). 50 mg of samples were measured in 120 µl alumina crucibles.

X-Ray diffraction (XRD)

Room temperature XRD analysis was used to verify the glassy state of prepared samples and to determine the composition of present crystalline phases. For samples containing gold it was also used to estimate the average size of Au nanoparticles according to the Scherrer equation

$$D = \frac{k\lambda}{\beta \cos\theta} \tag{3.1}$$

where D is the diameter of the particle, k is Scherrer's constant (K=0.94), λ is the X-ray wavelength (1.5406 Å), β is full width at half maximum (FWHM) of the diffraction peak, and θ is the diffraction angle.

Several (1-3) beads or small pieces of bulk glass were crushed into fine powder in an agate mortar. Then the samples were dispersed on low-background flat Si holders with the help of some ethanol droplets. Room temperature powder X-ray diffraction was performed using a Bruker D8 Advance laboratory diffractometer (Cu Kα1,2 radiation) equipped with a LynxEye XE detector in Bragg-Brentano geometry. The crystalline phases were identified using the ICDD PDF-4 edition 2021 database. The measurements were performed at the CEMHTI laboratory of the CNRS Orléans.

Variable temperature X-ray diffraction (VT-XRD)

Variable temperature X-ray diffraction was performed on selected samples to determine their crystallization behaviour at high temperatures. These analyses were conducted using a D8 Advance Bruker Bragg-Brentano (CuKα1,2 radiation) diffractometer equipped with a linear Vantec detector and an Anton Paar oven chamber (HTK1200N model). Fine granular powder of the sample was deposited on a platinum disk in an alumina crucible. The temperature behaviour and the thermal expansion of the setup had previously been calibrated using the corundum reference [166]. The measurements were performed at the CEMHTI laboratory of the CNRS Orléans.

Raman spectroscopy

Raman spectroscopy was used to provide information about the structure of the glass matrix of prepared samples. Selected beads or glass shards were cast into epoxy pellets, which were then cut and polished using conventional SiC papers (P300-P4000) and diamond particle suspensions. Subsequently samples were characterized at room temperature by Raman spectroscopy on a Renishaw InVia Qontor spectrometer mounting a green laser (514 nm) operated at 50 mW, although the power was occasionally reduced to avoid detector saturation in highly crystalline samples. The signal was collected in the range 80–2000 cm^{-1} (low-wavenumber cut-off of the edge filter: ~100 cm^{-1}) using an 1800 lines/mm holographic grating, with 15 s acquisition time and 6 repetitions. Only visually homogeneous, not fully opaque

samples were measured, focusing 20-40 μm below the surface with a 50x objective and acquiring spectra from several beads/locations to ensure reproducibility. The measurements were performed at the CEMHTI laboratory of the CNRS Orléans.

M-line spectroscopy

An m-line spectroscopy performed on a Metricon Prism Coupler (2010) device in the Laboratory of Photonics at the department of Inorganic Chemistry at UCT Prague was used to determine the value of refractive indices of our glasses. Samples with 2 polished parallel surfaces were used for the measurements. The measurements were performed at the Department of inorganic chemistry at the UCT Prague.

Optical microscopy (OM)

Quality of sample surface during the polishing process as well as macroscopic defects in the sample (e.g., bubbles) were evaluated by means of optical microscopy. An Olympus BX51 microscope was used.

UV-VIS spectroscopy

An AVANTES AvaSpec Starline spectrometer was used to measure absorption spectra in the range of 250-1100 nm. Samples with 2 polished parallel surfaces were used for the measurements, thickness of each sample was subsequently used to normalize the obtained spectra. The following parameters were used for the measurements: integration time 40 ms, averaging 200. Each sample was measured at least three times at three different points, the final result was calculated as the arithmetic mean of the measured values. The measurements were performed at the Department of inorganic chemistry at the UCT Prague.

Electron probe micro-analysis (EPMA)

EMPA was used to perform analyses of the chemical composition of prepared samples and also to view the number and size of larger gold particles. Prior to analyses with an EPMA, sample beads or chips were embedded in epoxy resin, polished, and carbon coated (15–20 nm) under vacuum. The analyses were performed at the Institute of Geology of the Czech Academy of Sciences in Prague using electron probe microanalyzer (microprobe) JEOL JXA-8230 with five

wave dispersive X-ray spectrometers (WDS), energy dispersive X-ray spectrometer (EDS) and panchromatic cathodoluminescence detector.

Scanning electron microscopy (SEM)

SEM was used to characterize the microstructure of prepared samples. Prior to analyses with a SEM, sample chips were embedded in Epoxy resin, polished, and carbon coated (15–20 nm) under vacuum. Microstructural analysis was carried out with a IT800SHL JEOL Scanning Electron Microscope (FEG SEM) equipped with SSD Ultim Max 100mm^2 detector (EDS Oxford system) – CNRS Orléans. A Hitachi S-4700 scanning electron microscope with a cold cathode was used at UCT Prague.

Transmission electron microscopy (TEM)

TEM was used to provide detailed information about the nanostructure of prepared specimens.

Powder sample: Samples for transmission electron microscopy (TEM) were prepared from powder dispersed in absolute ethanol and deposited onto a holey carbon film supported by a copper grid. Bright field images were carried out with a TEM (Philips CM20 – CNRS Orléans; EFTEM Jeol 2200 FS – UCT Prague) operating at 200 kV and equipped with an Oxford energy dispersive spectrometry (EDS) analyser.

Thin foil sample: TEM on thin foils of a few selected samples was performed to obtain high-quality images of nanostructure of those samples. First, a 50 μm slice polished on both parallel sides of the sample was obtained by careful mechanical polishing. Then the slice was glued onto a copper grid and a thin wedge was created on the sample by precision ion polishing system (PIPS). Sample was then observed by a TEM (see details above).

5 RESULTS AND DISCUSSION

This part of the thesis is organized in 4 chapters. In **Chapter 5.1**, the suitability of different glass systems for melting using ADL technology is discussed. In **Chapter 5.2**, the YAS system is investigated in detail using ADL technology. Special emphasis is given to the region with SiO_2 content > 80mol%, which had not been experimentally investigated previously to this work. **Chapter 5.3** presents the preparation of gold nanoparticles in glasses in the LS and YAS system using ADL and MQ technologies. **Chapter 5.4** proposes the composition of glasses containing AuNPs in the LYAS system based on the previous findings of this thesis.

The samples in this chapter are labelled with an alphanumeric code. The letter in the name corresponds to an oxide - see **Table 4** below. The number after the letter corresponds to the content of that oxide in the sample in mol% (rounded mathematically), or relative concentration to other oxides. For example, *L33-S67* indicates that the sample contains 33 mol% Li_2O and 67% SiO_2. The same sample may also be labelled *LS2* because the ratio of Li_2O:SiO_2 is 1:2.

Table 4 *Oxide abbreviations in this chapter*

Letter	**A**	**B**	**G**	**K**	**L**	**N**	**P**	**S**	**T**	**Y**
Oxide	Al_2O_3	B_2O_3	GeO_2	K_2O	Li_2O	Na_2O	P_2O_5	SiO_2	TeO_2	Y_2O_3

5.1 Glass systems and ADL technique

The initial experiments described in this chapter were focused on the search for key parameters affecting the quality of the prepared glass. The basic aim was to create a homogeneous glass bead free of bubbles and to look for a relation between the composition and properties of the glass and the variable parameters of the ADL technology.

Binary silicate glasses were selected for this work to investigate the challenges of synthesizing glasses by ADL over a broad range of melt viscosities and evaporation tendencies, thereby focusing on simple compositions. In the following, the synthesis of nine compositions of glass by conventional melt-quenching and/or ADL is studied: three lithium silicates: **LS2** (*L33-S67*), **LS4** (*L25S75*) and **LS8** (*L11-S89*); three sodium silicates: **NS2** (*N33-S67*), **NS4** (*N25-S75*) and **NS8** (*N11-S89*), and three potassium silicates: **KS2** (*K33-S67*), **KS4** (*K25-S75*) and **KS8** (*K11-S89*). An overview of the prepared samples is given in **Table 5**.

Table 5 *Composition of the silicate glass (mol% of oxides) and used technology*

Glass	Li_2O	Na_2O	K_2O	SiO_2	B_2O_3	P_2O_5	Technology
LS2 (*L33-S67*)	33.3			66.7			ADL, MQ
LS4 (*L25S75)*	20.0			80.0			ADL
LS8 (*L11-S89*)	11.1			89.9			ADL
NS2 (*N33-S67*)		33.3		66.7			ADL, MQ
NS4 (*N25-S75*)		20.0		80.0			ADL
NS8 (*N11-S89*)		11.1		89.9			ADL
KS2 (*K33-S67*)			33.3	66.7			ADL, MQ
KS4 (*K25-S75*)			20.0	80.0			ADL
KS8 (*K11-S89*)			11.1	89.9			ADL
LB2 (*L33-B67*)	33.3				66.7		ADL
NP (*N50-P50*)		50.0				50.0	ADL

ADL was used to prepare beads of the listed nine compositions. To facilitate the analysis of the ADL method, 3 g of **LS2, NS**2 and **KS2** were additionally synthesized as reference materials by conventional melt-quenching.

The expected increasing temperature sensitivity (i.e., tendency toward high-temperature vaporization 48–50) of the samples along the series **LSX-NSX-KSX** (X = 2, 4,or 8) was tackled using the following synthesis strategy: **LSX** samples were invariably prepared first, optimizing the melting parameters (temperature reading, time) to minimize their high-temperature dwell while still obtaining good-quality glass beads with (possibly) no bubbles visible to the naked eye. Then, the exact same procedure was applied to the corresponding **NSX** and **KSX** samples, as visualized on **Figure 21**; note that the same temperature readings as for **LSX** could be achieved for **NSX** and **KSX** samples using an equal or lower laser power, supporting the reliability of the results concerning high-temperature evaporation (see below). More specifically, we performed the syntheses at maximum pyrometer readings of ∼1500 °C for **MS2**, ∼1700 °C for **MS4** and ∼1800 °C for **MS8** (where M is Li, Na or K) Samples prepared in this way were glassy and transparent, with a variable bubble content.

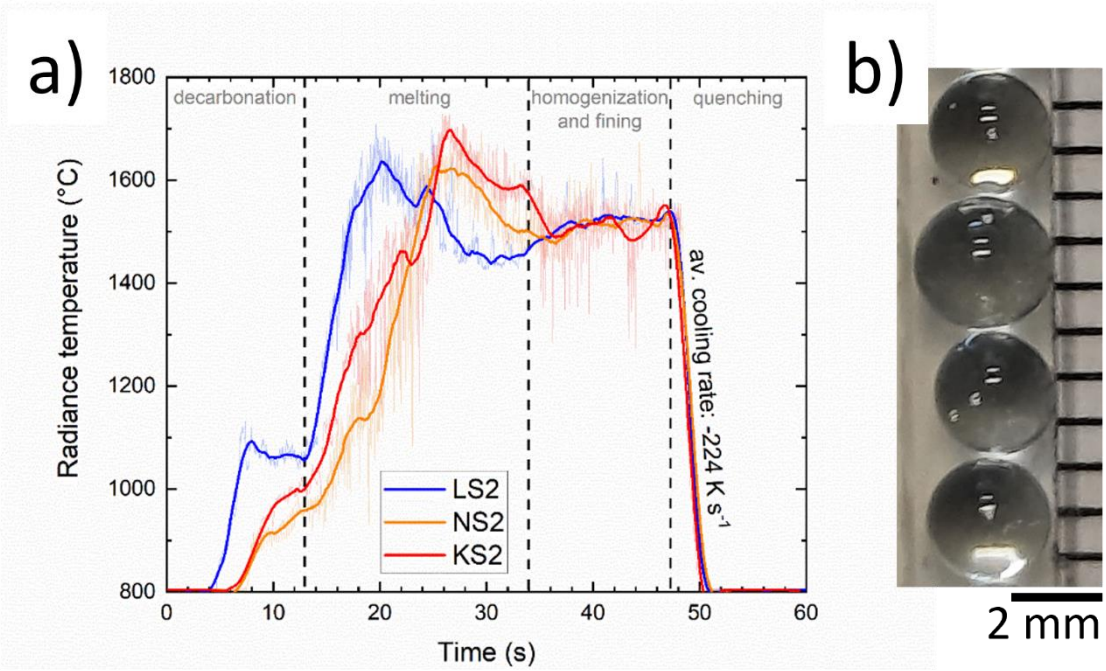

Figure 21 *a) Example of time-temperature curves acquired during the ADL synthesis of* ***LS2****,* ***NS2*** *and* ***KS2*** *glass beads, schematically separated in four main stages: decarbonation, melting, temperature homogenization and fining, quenching. b)example of glass beads* ***LS2****. The distance between 2 horizontal lines is 1 mm.*

In order to test the validity of our approach over a wider compositional range, we melted two additional samples according to the same procedure: a lithium borate **LB2** (*L33-B67*) and a sodium phosphate **NP** (*N50-P50*). In both cases, glass beads could be easily obtained without any signs of evaporation loss, at readings of 1050 and 1125 °C, respectively. Sample **LB2** was subsequently intentionally heated to higher temperature (up to 1200 °C) to induce high temperature volatilization and mass loss.

4.1.1. Preliminary estimation and calculation using DSC measurement

The three compositions synthesized by conventional melt-quenching (**LS2, NS2,** and **KS2**) were characterized by differential scanning calorimetry (DSC) to investigate their glass stability and glass transition temperature T_g, using a SETARAM Multi HTC 1600 and loading ~500 mg of powder in the Pt crucibles for each measurement. First, simple upscans were performed up to 1173 K and used to estimate glass stability according to the Hrubý method [167].

$$K_{gl} = \frac{T_c - T_g}{T_m - T_c} \quad \text{Eq 4.1}$$

where T_c stands for the crystallization onset, T_g for the glass transition temperature, and T_m for the melting temperature. The real T_g of the samples (viscosity $\eta \approx 10^{12}$ Pa s) was obtained by rate-matching measurements at 10 K min^{-1}: the glass samples were heated beyond their glass transition to achieve melt relaxation, subsequently cooled at 10 K min^{-1} to constrain their thermal history and then measured during a second upscan at 10 K min^{-1}.

During this segment, the glass transition onset (T_{onset}) was extracted from the heat flow curve using the double tangent method. As demonstrated in previous works [168–172], rate-matching DSC measurements can be associated with viscosity η through the relation:

$$\log_{10} \eta\,(T_{onset}) = -\log_{10}|q_{c,h}| + K_{onset} \quad \text{Eq 4.2}$$

where $q_{c,h}$ is the heating and cooling rate applied during DSC measurements, and K_{onset} is a constant, calibrated at 11.20 (±.15) Pa s. For $q_{c,h}$ = 10 K min^{-1} , one obtains log 10η(T_{onset}) = 11.98 Pa s ≈ 12 Pa s. Based on T_g values obtained from DSC and data from the literature [170,173], full viscosity curves were fitted for the three compositions **LS2, NS2** and **KS2**, using the Waterton-Mauro-Yue-Ellison-Gupta-Allan (w- MYEGA) equation [174].

$$log_{10}\eta = log_{10}\eta_\infty + (12 - log_{10}\eta_\infty)\frac{T_g}{T} exp\left[\left(\frac{m}{12 - log_{10}\eta_\infty} - 1\right)\left(\frac{T_g}{T} - 1\right)\right] \quad \text{Eq. 4.3}$$

in which $\log_{10}\eta_\infty$ defines viscosity at the limit of infinite temperature and m the melt fragility. For the fits, only these two parameters were varied, while T_g was fixed to the values obtained from DSC. The calculated parameters of glasses **LS2, NS2** and **KS2** are summarized in **Table 6**: the temperature difference between glass transition and crystallization (and therefore similarly K_{gl}) increased substantially going from **LS2** to **NS2** and **KS2** (**Figure 22- a**). Based on the results of previous authors [175], we assumed that this higher glass stability also corresponds to a higher glass-forming ability of the respective melts.

T_g values (at which viscosity $\eta = 10^{11.98\pm0.15}$ Pa s) were obtained using rate-matching DSC measurements[168–172]: they enabled to fit full viscosity curves for the three glass-forming

melts (**Figure 22- b**), using high-temperature viscosity data from literature[170,173]. While T_g increased going from **LS2** to **NS2** and **KS2**, fragility indices *m* exhibited an opposite trend (**Table 6**), eventually making **KS2** the most viscous and LS2 the least viscous liquid among the three samples. At the melting temperature T_m, we calculated a viscosity of $10^{1.51}$ Pa s for **LS2**, $10^{2.94}$ Pa s for **NS2** and $10^{2.38}$ Pa s for **KS2**.

Table 6 *Parameters obtained from DSC measurements and viscosity fits of the reference samples synthesized by conventional melt-quenching: T_g stands for the glass transition temperature (from rate-matching DSC measurements at 10 K min^{-1}), T_c for the onset of crystallization (on simple DSC upscans at 10 K min^{-1}), T_m for the liquidus temperature (from literature[176–178]), K_{gl} for the glass stability parameter after Hrubý[167], m for the fragility index and $\log_{10}\eta_\infty$ for the logarithmic viscosity at infinite temperature (from viscosity fits using the w-MYEGA model, Eq. 2). $\log_{10}\eta(T_m)$ provides the viscosity at the melting temperature, calculated through the w-MYEGA fits.*

Sample	Composition	T_g [K]	T_c [K]	T_m [K]	K_{gl}	m	$\log_{10}\eta_\infty$ (η in Pa s)	$\log_{10}\eta[T_m]$ (η in Pa s)
LS2	*L33-S67*	726±5	837±5	1306	0.24±0.02	41.4±0.7	-1.5±0.1	1.5
NS2	*N33-S67*)	728±5	916±5	1148	0.81±0.03	37.1±0.9	-1.8±0.2	2.9
KS2	*K33-S67*)	768±5	1043±5	1309	1.03±0.03	34.6±0.9	-2.2±0.3	2.4

Concerning ADL synthesis, high-temperature evaporation was monitored by measuring the mass of each dried pellet (still including only the inorganic precursors and the corn starch, assuming all H_2O was lost during drying at 200 °C) and of the respective resulting glass bead; the mass of the pellets allowed to calculate the expected bead mass (after subtracting the mass of the corn starch and of CO_2 removed during melting) and compare it to the measured one, estimating mass losses due to high-temperature evaporation. For each composition, ten pellets/beads were considered for statistics. One bead of each composition was then analysed by laser ablation inductively coupled plasma mass spectrometry (LA-ICP-MS) by adapting the analytical protocol developed at the institute IRAMAT- CEB for glass matrices [165]. On average, the beads had a diameter of 2 mm and were polished to study a cross section of the core of the bead. The laser ablated circular spots with a diameter of 0.1 mm; four acquisitions were per- formed (one in the centre and three near the edges) to confirm sample homogeneity and quantify compositional drifts due to evaporation. Due to their expected higher hygroscopicity, **LB2** and **NP** beads were measured without any polishing step, shortly after the synthesis; two subsequent ablations at the same spot were used to confirm the homogeneity of the beads between surface region and interior.

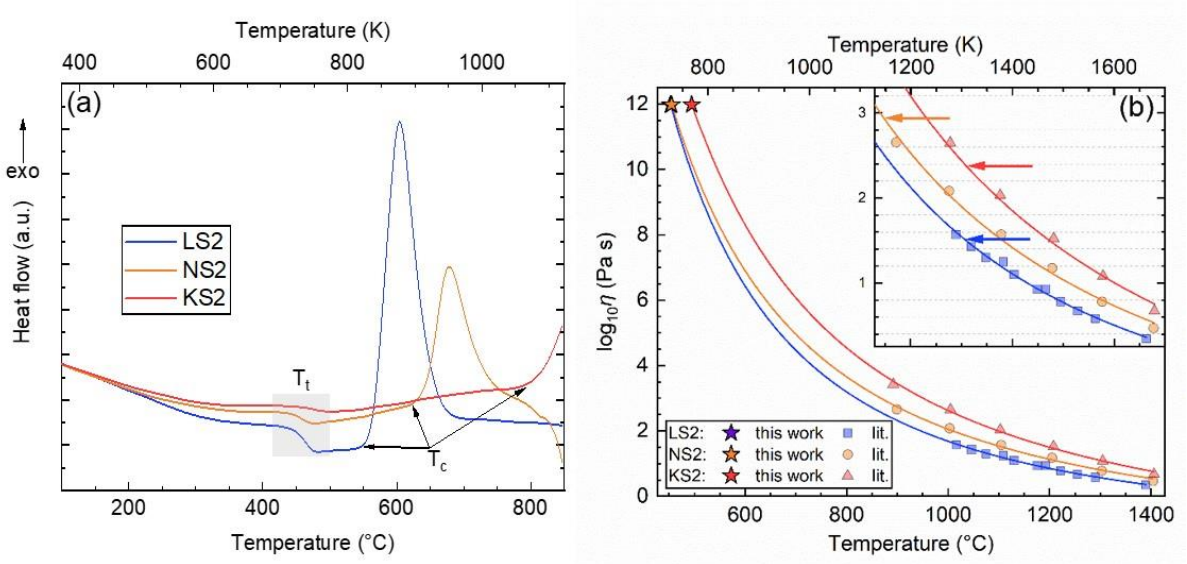

Figure 22 *a) Heat flow curves obtained during DSC upscans at 10 K min^{-1} applied to samples* ***LS2, NS2*** *and* ***KS2*** *synthesized by conventional melt-quenching; a shaded area labelled as T_t marks the glass transition region, while T_c labels the onset of crystallization. b) w-MYEGA fits (fit parameters in* ***Table 6****) of the full viscosity curves of* ***LS2****,* ***NS2*** *and* ***KS2****, based on the T_g values determined within this work and high-temperature viscosity data from literature[170,173]. Horizontal arrows signal the viscosity at T_m for each composition.*

To obtain a crude prediction of the tendency towards high-temperature volatilization of the nine samples to be synthesized by ADL (**LS2, LS4, LS8, NS2, NS4, NS8, KS2, KS4** and **KS8**), the two parameters r_{evap} (Eq. 4) and Δ_{evap} (Eq. 5) are here defined as:

$$r_{evap} = \frac{T_{m,\Sigma}}{T_m} \qquad \text{Eq. 4.4}$$

$$\Delta_{evap} = r_{evap,max} - r_{evap,min} \qquad \text{Eq. 4.5}$$

where T_m is the melting point of a given oxide component and $T_{m,\Sigma}$ the melting point of the target multicomponent glass (both obtainable from phase diagrams, see

Table 7; $r_{evap,max}$ and $r_{evap,min}$ respectively stand for the highest and lowest r_{evap} values among all components of the target glass. As demonstrated below, a higher r_{evap} indicates an increasing

tendency of a given oxide component to evaporate from the respective multicomponent melt at high temperature.

Table 7 *Melting points T_m from literature [176–178] and resulting r_{evap} and Δ_{evap} parameters for the nine samples analysed within this work.*

Sample	T_m	r_{evap}		Δ_{evap}
	[K]	M_2O	SiO_2	
LS2	1306	0.76	0.66	0.11
LS4	1633	0.95	0.82	0.13
LS8	1788	1.04	0.90	0.14
NS2	1148	0.82	0.58	0.24
NS4	1738	1.24	0.88	0.36
NS8	1808	1.29	0.91	0.38
KS2	1309	1.10	0.66	0.44
KS4	1248	1.05	0.63	0.42
KS8	1553	1.31	0.78	0.52

Especially if one of the melt components exhibits $r_{evap} > 0.8$ (indicative threshold based on the results of this work), Δ_{evap} can then be used to estimate the risk of evaporation-driven compositional drifts: increasing Δ_{evap} manifest an increasing risk of uneven high-temperature losses. The values for the melts analysed within this work are summarized in **Figure 23**: r_{evap} was observed to generally increase with a higher SiO_2 content in these binary glasses, due to the rising T_m of the mixtures. Alkali oxides invariably exhibited higher values as compared to SiO_2, with Li_2O plotting between 0.7 and 1.1, Na_2O between 0.8 and 1.3 and K_2O between 1.0 and 1.3. The observed trends mirrored those expectable based on previous literature sources analysing the high-temperature vaporization of simple oxides[179–181]**.** Also, Δ_{evap} slightly increased proportionally to the SiO_2 content of the glasses, reaching the highest values in K_2O-containing samples (up to ~0.5) and the lowest in those containing Li_2O (~0.1).

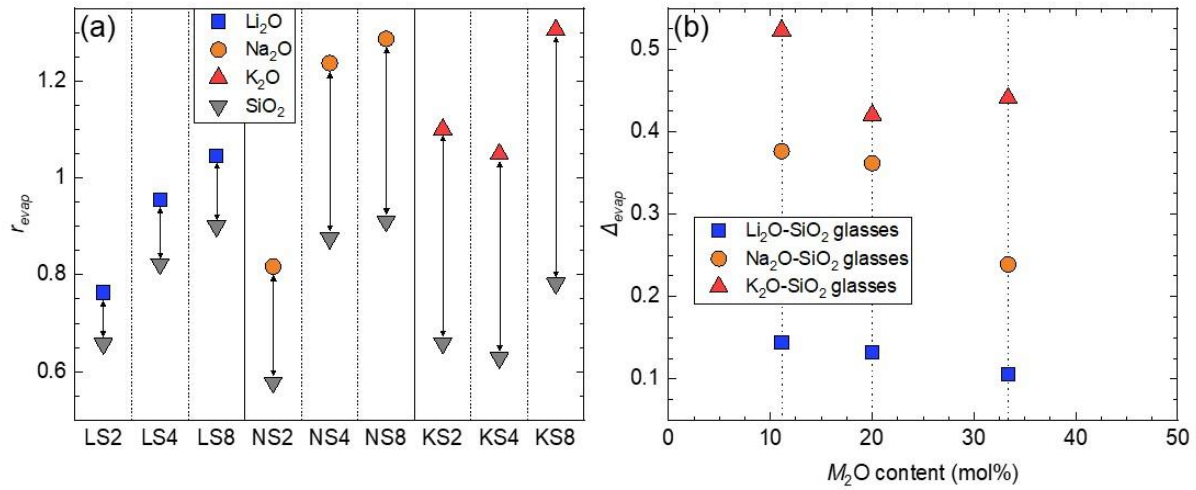

Figure 23 *(a) r_{evap} (Eq. 4.4) and (b) Δ_{evap} (Eq. 4.5) parameters computed for the compositions analysed within this work, using data from literature[176–178]. Vertical arrows in the (a) panel correspond to the Δ_{evap} values plotted in (b).*

4.1.2. Verification experiment

After this preliminary examination, ADL was used to synthesize glass beads of these nine target compositions. Due to the increasing melt viscosity inferred above, obtaining perfect bubble-free beads proved increasingly difficult moving from Li_2O- to Na_2O- and K_2O-bearing melts, as already inferable from a visual inspection of the samples (**Figure 24**); a similar effect was noticed in the case of increasing SiO_2 content (e.g. in the series **LS2-LS4-LS8**).

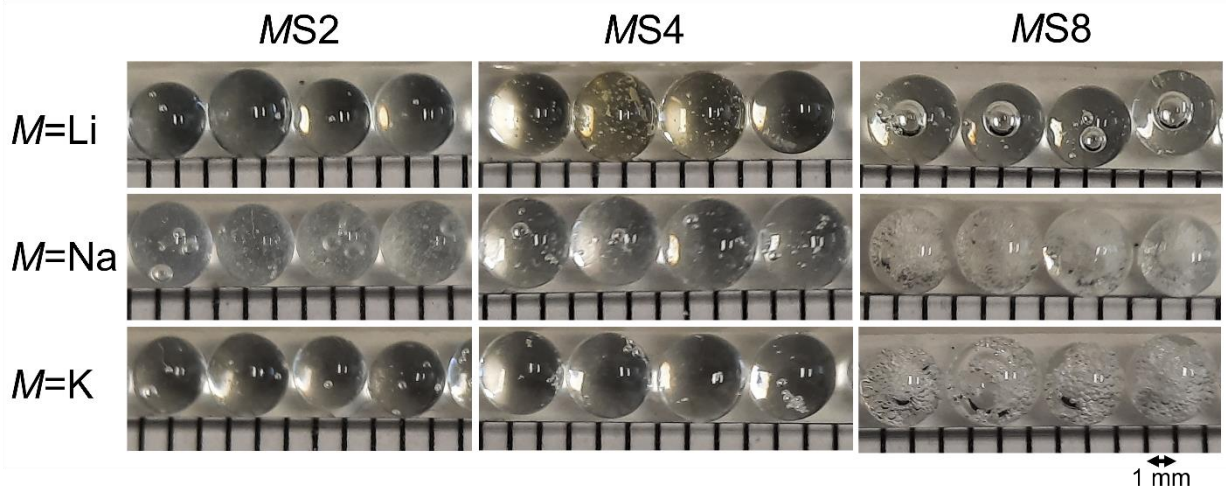

Figure 24 *Pictures of beads synthesized by ADL. Visible influence of silica content and different alkali oxides. The distance between the vertical black bars is 1 mm.*

Despite the complexity of these phenomena, previous experiments performed both in a space laboratory and in normal gravity conditions suggest that the rotation of the droplet renders bubble escape even more challenging than in conventional melting, favouring bubble migration towards an axial position, with buoyancy playing a lesser role[182–184]. Bubbles are expected to originate from the decomposition of corn starch and carbonate precursors, as well as from direct injection of the levitation gas jet during the initial melting stage, when the droplet has not yet achieved a stable spherical shape.

The bead mass expected after decarbonation of the pellets and that of the synthesized glass beads was compared to quantify losses due to evaporation during ADL melting (**Figure 25-**a); error bars on the graph are plotted according to the standard deviation of the data over ten measured beads. Note that the samples with lower content of silica were melted at lower temperatures (1800 K), while a higher melting temperature (up to 2100 K) was required to prepare samples with lower M_2O content. Li_2O-bearing samples invariably plotted closer to the expected mass, while Na_2O- and especially K_2O-containing beads exhibited mass losses up to roughly 20%. In all cases, a lower initial content in alkali oxide (or alternatively a higher SiO_2 content) led to more noticeable mass losses.

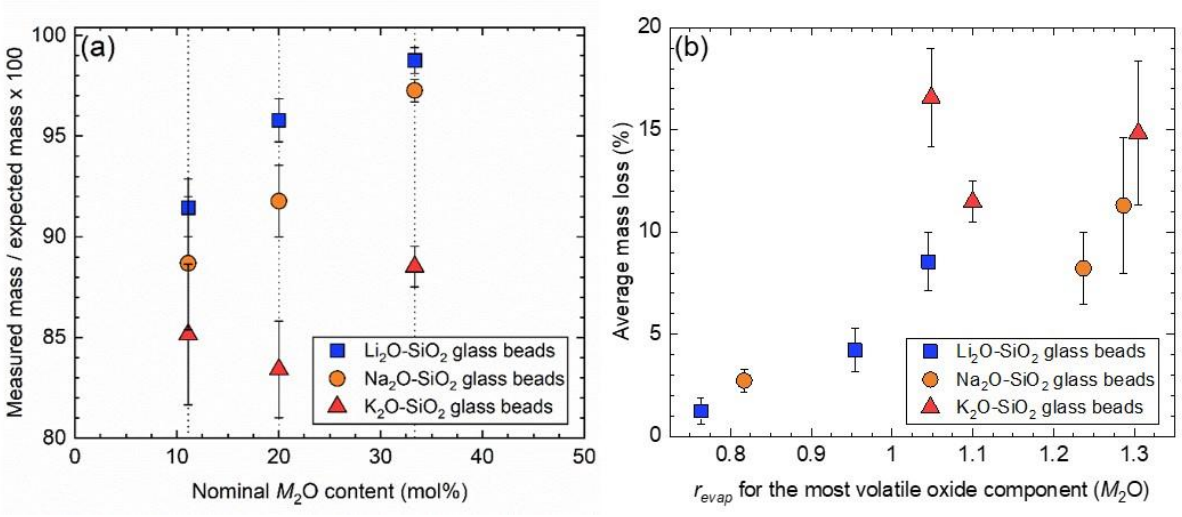

Figure 25 *a) Comparison between measured and expected masses of glass beads synthesized by ADL, as a function of their nominal M_2O (M = Li, Na, K) content; error bars correspond to the standard deviation over 10 measured beads. b) correlation between the average mass loss of each target composition and the r_{evap} value of its most volatile component (alkali oxide M_2O).*

As demonstrated in **Figure 25**-b, the average mass losses determined for the nine target compositions exhibited a clear correlation to the r_{evap} value of the most volatile components, i.e. the alkali oxides Li_2O, Na_2O or K_2O (as expectable from previous studies on the vaporization behaviour of oxides[179–181]).

LA-ICP-MS measurements performed on one representative bead for each composition confirmed these observations (**Figure 26**): Li_2O-containing beads plotted very close to the 1:1 diagonal, i.e. their measured composition was very close to the nominal one. On the contrary, those containing Na_2O and K_2O were invariably found to plot lower, signalling a non-negligible alkali loss during melting. SiO_2-rich matrices such as **NS8** and **KS8** lost up to 80% of their initial alkali oxide content; these losses exhibited a correlation to the values of Δ_{evap} for the respective composition.

All in all, the samples exhibiting the highest mass losses and chemical drifts corresponded to those richer in bubbles (**Figure 24**): considering that a better fining could have only been achieved at higher temperatures (i.e. at lower viscosity) or with longer high-temperature dwells (which would have aggravated high-temperature vaporization), it is easy to see that certain compositions are intrinsically unsuitable for the synthesis of glass beads by ADL. This concept is developed and specified in the following.

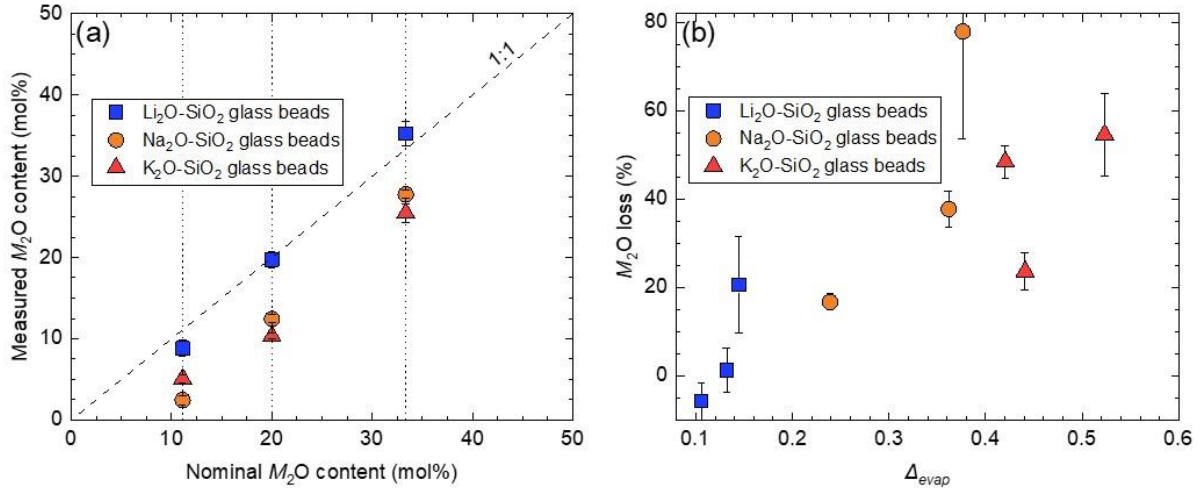

Figure 26 *a) Comparison between nominal M_2O content (M = Li, Na, K) of the nine samples synthesized by ADL and the values measured by LA-ICP-MS on representative beads; b) correlation between the M_2O loss in each of the measured beads and the Δ_{evap} value of the respective target composition.*

5.1.4 Summary and discussion

As known from conventional glass production[185], fining and bubble removal can only be accomplished if the melt viscosity allows for bubble escape[186]. More specifically to ADL synthesis, sufficient melt fluidity is also necessary to form a sufficiently spherical droplet and obtain stable levitation on the gas jet. It is therefore apparent that melt viscosity plays a major role in determining successful ADL synthesis of bubble-free glass beads. An evaluation of viscosity at the melting temperature T_m is thereby particularly revealing, since it represents the lowest temperature at which a liquid droplet can be obtained during heating, minimizing evaporation risks that could affect the sample at higher temperatures. The comparison among some representative glass formers (**Figure 27**, melting temperatures[176–178,187–194] and viscosity estimations[170,172,191,195–197] from previous literature) emphasizes how the lowest viscosity possibly obtainable in a stable melt can vary substantially according to composition: while less polymerized or less strongly bonded aluminate and tellurate melts are immediately very fluid after melting ($\log_{10}\eta(T_m) < 1$), (alumino)silicate melts plot at noticeably higher viscosities. In the case of fully polymerized SiO_2 and GeO_2, $\log_{10}\eta(T_m)$ values exceed 4 and sufficiently low viscosity for bubble removal can only be achieved at very high temperature after substantial mass losses, which could explain the virtually complete absence of literature on the reproducible ADL synthesis of transparent bubble-free beads of these yet very good glass formers.

Obviously, high viscosity at T_m will force the ADL operator to increase laser power until sufficient fluidity can be achieved for homogenization and bubble escape. When dealing with viscous melts ($\log_{10}\eta(T_m) > 1$ on **Figure 27)**, it is therefore necessary to take into account their susceptibility towards differential high-temperature evaporation of their chemical components (i.e. Δ_{evap}), which could cause compositional drifts. As also supported by the results of this work, alkali oxides are for instance more volatile than SiO_2 and tend to be lost during high temperature melting[198–200], leading to an overall SiO_2 enrichment. Although quantitative estimations of the tendency of simple oxides towards thermal vaporization are available in the literature[179–181], they are difficult to apply to multicomponent systems. Moreover, numerous studies analysed high-temperature evaporation in melts of geological relevance[201–203], but no overarching understanding of these processes has been offered yet, especially in the case of exotic compositions. Here, the empirical parameters r_{evap} and Δ_{evap} have been shown

to predict with satisfactory reliability the risk of compositional drifts during ADL synthesis, empirically identifying the most sensitive component(s) with an alternative method to the consultation of high-temperature vaporization rates of simple oxides[179–181].

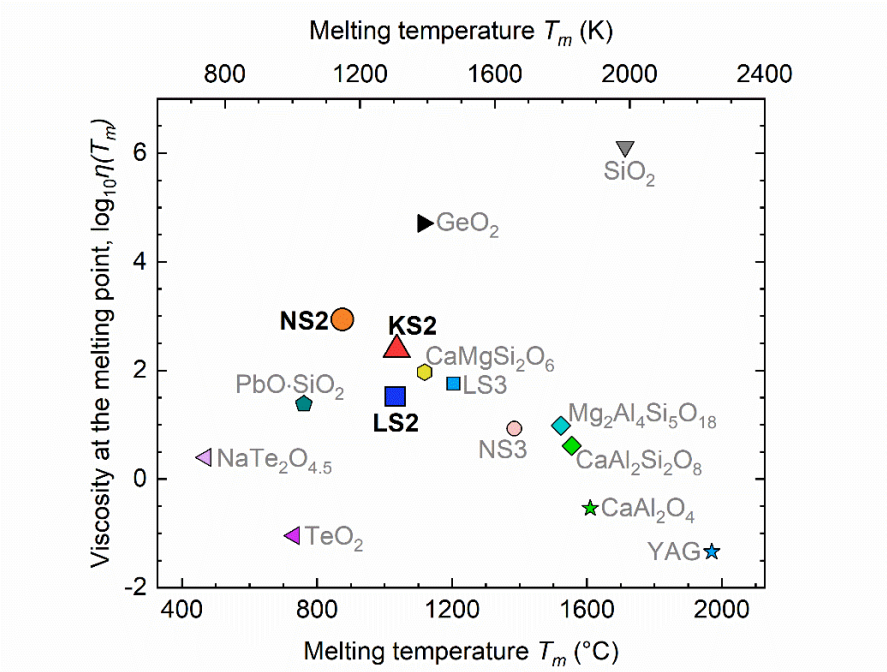

Figure 27 *Correlation between melting temperatures T_m and viscosity at T_m $\log_{10}\eta(T_m)$ for a range of representative glass-forming melts, based on viscosity data from this work (LS2, NS2 and KS2) and reliable literature sources (see related text for references).*

Particularly, when the achievement of low viscosity for bubble removal requires heating above the T_m of the target glass by hundreds of kelvins, the results of this work suggest that non-negligible high-temperature evaporation should be expected for r_{evap} values significantly exceeding ~0.8, although this threshold may vary according to the chosen composition, ADL setup, levitation gas, desired final bead size and melting procedure. For instance, a shorter high-temperature dwell may limit vaporization, though possibly preventing satisfactory homogenization and fining. Similarly, Δ_{evap} values above ~0.2 signalled a high risk of compositional drift for the Na_2O- and K_2O-bearing samples synthesized within this work, stressing the general need to minimize this parameter during compositional design. Incidentally, Δ_{evap} minimization can be obtained through the choice of (near-)eutectic compositions, which are also typically known to represent the most favourable regions for glass formation in a phase diagram.

Extending this treatment to other compositions of possible interest for glass scientists (**Figure 28**), it is easy to see that r_{evap} values are able to reproduce the comparatively high volatility[179–181] of glass former oxides such as B_2O_3 or TeO_2. As for aluminates such as $CaAl_2O_4$ and $Y_3Al_5O_{12}$, their high melting temperature brings the r_{evap} of their constituting oxides to relatively high values (0.8-1): indeed, previous authors reported non-negligible mass loss from SrO-Al_2O_3 melts during ADL synthesis [204], although no significant compositional drifts should be expected due to the low Δ_{evap} (vertical arrows). Note that the calculation of r_{evap} is expected to estimate less precisely the evaporation behaviour of elements prone to oxyreduction such as transition metals, since melting or decomposition temperatures of the respective oxides can strongly depend on the oxidation state.

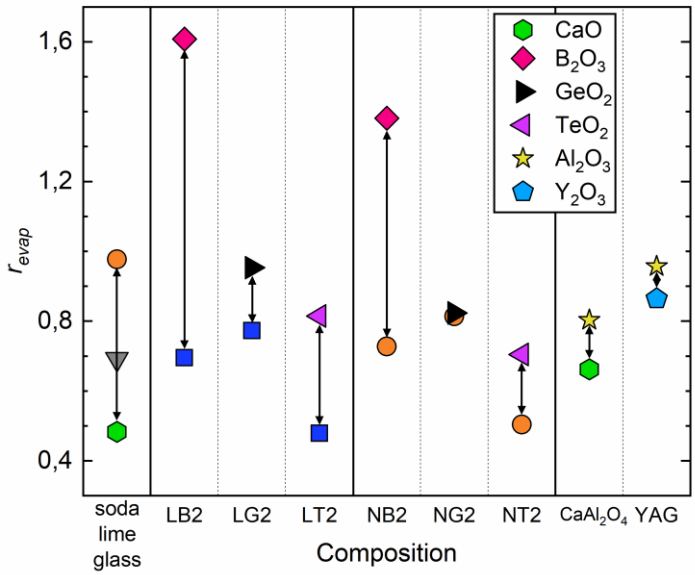

Figure 28 *r_{evap} parameters computed for some representative glass-forming substances (LB2: $Li_2O{\cdot}2B_2O_3$, LG2: $Li_2O{\cdot}2GeO_2$, LT2: $Li_2O{\cdot}2TeO_2$, NB2: $Na_2O{\cdot}2B_2O_3$, NG2: $Na_2O{\cdot}2GeO_2$, NT2: $Na_2O{\cdot}2TeO_2$, YAG: $3Y_2O_3{\cdot}5Al_2O_3$); vertical arrows are a graphical representation of Δ_{evap}. Melting temperatures were obtained from previous literature[176–178,190–192,205–210]. See also* ***Figure 23****-a for a complete symbol legend.*

To finally test the outlined approach and demonstrate the applicability of ADL synthesis to compositions including volatile components, two additional samples were prepared: **LB2** ($Li_2O{\cdot}2B_2O_3$) and **NP** ($Na_2O{\cdot}P_2O_5$), whose key melt properties are summarized in **Table 8**. Due

to their comparatively low melting temperature and low viscosity, both glasses could easily be prepared in the form of bubble-free beads (**Figure 29**); their measured composition closely corresponded to the nominal one, ruling out the occurrence of major volatilization during laser heating. Intentional melting of **LB2** at higher temperatures (~1200 °C on the pyrometer reading) led instead to mass losses up to 45% and to a general enrichment of the melt in B_2O_3, which made evident the merely qualitative character of the estimation of volatilization tendencies using r_{evap} and Δ_{evap}. Although the molar loss in B_2O_3 from the samples was substantially higher than that in Li_2O (**Figure 29**-b), the difference was clearly not as pronounced as expectable from the values plotted in **Figure 28**. As such, ADL users approaching the synthesis of a new composition should consider these empirical parameters as a valuable indicative tool, though being aware of their inability to quantitatively capture the subtleties of evaporation mechanism and kinetics.

Table 8 *Key melt parameters for samples LB2 and NP: melting temperatures[206,211,212] T_m, approximate viscosity[213,214] at the melting temperature $log_{10}\eta(T_m)$, r_{evap} for the respective oxide components and Δ_{evap}.*

Sample	**Composition**	T_m **[K]**	$log_{10}\eta[T_m]$ (η in Pa s)	r_{evap} Li_2O	r_{evap} Na_2O	r_{evap} B_2O_3	r_{evap} P_2O_5	Δ_{evap}
LB2	(*L33-B67*)	1190	< 0	0.69	-	1.61	-	0.92
NP	(*N50-P50*)	900	0.3	-	0.64	-	1.06	0.42

From the results of this chapter it appears that

1) Aerodynamic levitation coupled to laser heating represents a highly prized method for glass synthesis, new materials discovery and high-temperature in-situ melt characterization.
2) Evaporation of volatile components during laser melting has however noticeably limited its applicability over an extended compositional landscape.
3) Viscosity at the melting temperature $log_{10}\eta(T_m)$ should be critically evaluated before the synthesis: for $log_{10}\eta(T_m) < 1$, glass-forming melts will be easily obtained as bubble-free beads without major volatilization concerns. viscosity of the melt and consequently on the homogeneity of the prepared glass beads by ADL technique.

4) When comparing the addition of known glass modifiers Li, Na and K, the results show a positive effect of decreasing the radius and ionicity of the modifier on the viscosity of the melt and consequently on the homogeneity of the prepared glass beads by ADL technique.

5) In case of more viscous melts, the empirical parameters r_{evap} and Δ_{evap} can support a smart compositional design minimizing high-temperature mass loss and chemical drifts.

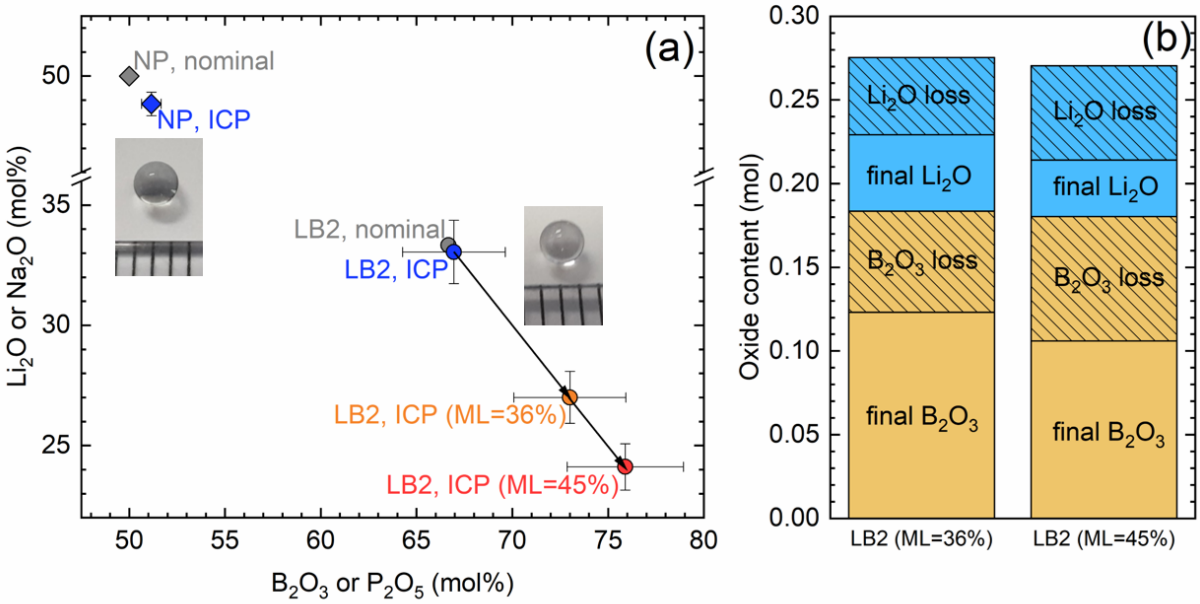

Figure 29 *(a) Results of LA-ICP-MS measurements performed on glass beads synthesized by the ADL method for $Na_2O{\cdot}P_2O_5$ (NP) and $Li_2O{\cdot}2B_2O_3$ (LB2) compositions. The data points labelled as "NP, ICP" and "LB2, ICP" correspond to the average of several beads synthesized without evident signs of evaporation (pictures are provided as onsets). In the case of LB2, two beads were intentionally melted at higher temperatures to induce volatilization, with mass losses (ML) up to 45% of the expected mass. (b) LA-ICP-MS results for the beads that underwent mass losses up to 45%, recalculated in terms of the actual molar Li_2O and B_2O_3 content of the two samples.*

5.2 Y_2O_3-Al_2O_3-SiO_2 system synthesis using ADL

In this chapter, the preparation of samples of the Y_2O_3 - Al_2O_3 - SiO_2 system using the ADL technique was investigated. In addition to the eutectic composition(Y13-A19-S68, sample **9**), we focused on a relatively wide range of system composition, the SiO_2 content was varied in

the range of 35 to 95 mol%. In addition, the region with SiO_2 content above 80 mol%, varying the Y/Al ratio, which due to the high temperatures required for sample preparation is a virtually experimentally unexplored region in the YAS phase diagram, was systematically investigated. The occurrence of phase separation in this region was observed and described. The possibility of influencing size and distribution of phase separated droplets, by the choice of a suitable composition, was also investigated.

For these experiments, glasses of general composition $xY_2O_3.yAl_2O_3.zSiO_2$ (mol%) were prepared. In addition to the studied ADL technology, the common melt-quenching procedure was used as a standard comparison technique for a few compositions. The nominal glass compositions as well as sample names are summarised in **Table 9**. Moreover, the glass compositions are also plotted in the ternary phase diagram in **Figure 30**.

Table 9 *– A summary of the nominal compositions (mol%) of the prepared glasses. The sample code column summarizes chemical composition of the glass batch in mol %, rounded mathematically.*

Sample no.	Sample code	x (Y_2O_3)	y (Al_2O_3)	z (SiO_2)
1	*Y15-A50-S35*	15.0	49.8	35.2
2	*Y11-A35-S54*	10.7	35.4	53.9
3	*Y07-A24-S68*	7.3	24.2	68.5
4	*Y05-A15-S80*	4.6	15.3	80.1
5	*Y02-A08-S90*	2.4	7.9	89.7
6	*Y22-A32-S46*	21.9	32.4	45.7
7	*Y24-A22-S54*	23.5	22.3	54.2
8	*Y24-A14-S62*	24.5	13.5	62.0
9	*Y13-A19-S68*	12.6	19.2	68.2
10	*Y14-A11-S75*	14.0	10.6	75.4
11	*Y08-A12-S80*	7.9	12.1	80.0
12	*Y06-A09-S85*	6.0	9.0	85.0
13	*Y04-A06-S90*	4.0	6.0	90.0
14	*Y02-A03-S95*	2.0	3.0	95.0
16	*Y15-A05-S80*	15.0	5.0	80.0
18	*Y18-A03-S80*	17.5	2.5	80.0
22	*Y10-A10-S80*	10.0	10.0	80.0
23	*Y03-A18-S80*	2.5	17.5	80.0
33	*Y12-A22-S66*	12.2	22.0	65.8
34	*Y01-A25-S74*	1.0	25.0	74.0
35	*Y03-A25-S72*	3.0	25.0	72.0
36	*Y01-A15-S84*	1.0	15.0	84.0

4.2.1 General description of the prepared samples

Glasses of various compositions were prepared by the ADL technique and already differed in their optical appearance. All glasses with SiO_2 content below 70 mol% as well as some glasses with SiO_2 content above 70 mol% and simultaneously containing high amounts of Al_2O_3 were transparent (yellow circles in **Figure 30**). Glasses containing high amount of SiO_2 and Y_2O_3 were opaque-white in appearance (red symbols in the **Figure 30**). Two glass compositions, samples **22**(*Y10-A10-S80*) and **14**(*Y02-A03-S95*), showed distinct opalescence and are marked in orange.

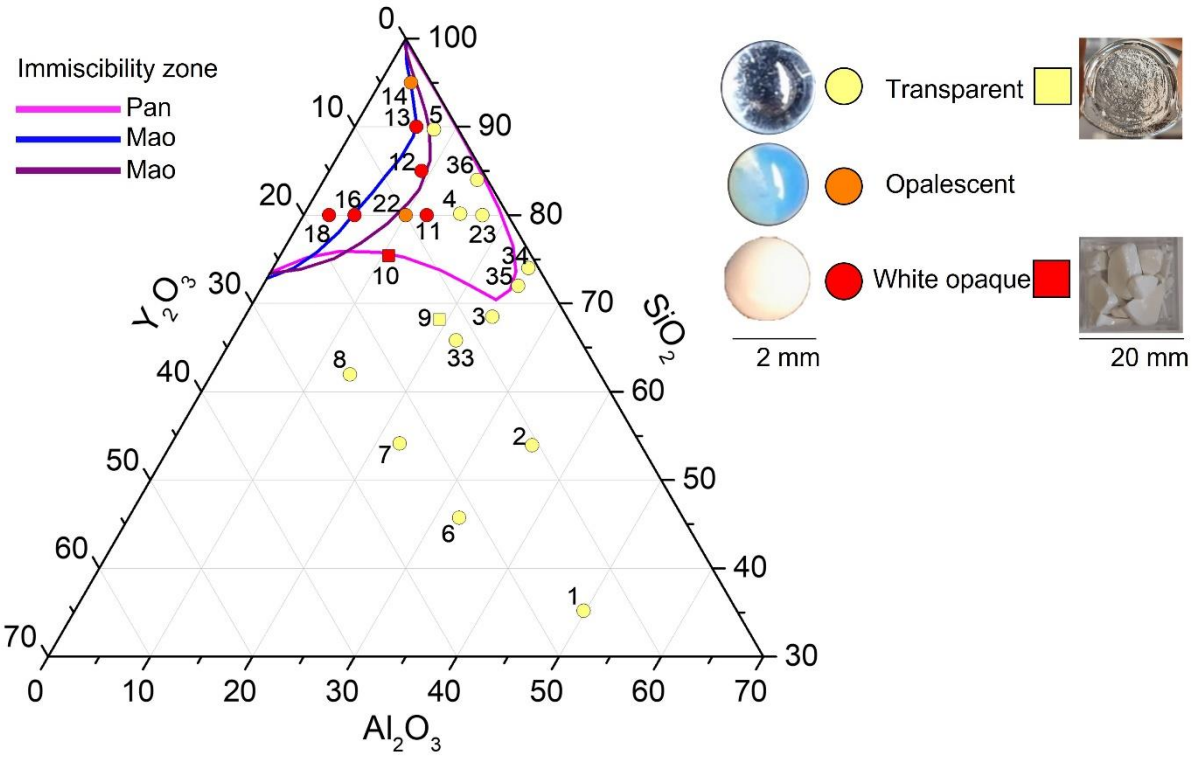

Figure 30 *Part of YAS ternary diagram with highlighted stable liquid-liquid immiscibility fields, that were published by Pan et al. [26] and Mao et al. [30]. Samples prepared in this work by the ADL technique are represented as circles: yellow = transparent, orange = opalescent, red = opaque white. Samples prepared both by melt-quenching and ADL are represented with squares. The diagram is accompanied by photographs of samples prepared by both techniques.*

For comparison, a transparent sample (composition **9**(*Y13-A19-S68*)) and a white opaque one (composition **10**(*Y14-A11-S75*)) were also prepared by conventional melt-quenching technique, obtaining the same optical appearance as by ADL. These glasses are marked by squares with

the colour corresponding to the appearance. In addition, the theoretically calculated liquid-liquid immiscibility regions by Pan et al. [46] and Mao et al. [50] are added to the figure.

4.2.2. Investigation of thermal properties and glass structure

The properties of transparent glasses labelled **1-9** prepared by the ADL technique were analysed by DSC. The glass transition temperature (T_g) and temperature at which the maximum of the first crystallization peak occurs (T_c) were determined. One illustrative DSC curve (sample 1(Y15-A50-S35)) is shown in **Figure 31a**. In **Table 10**, the determined values of T_g and T_c are shown for all individual glasses. The T_g values range from 899 to 922 °C, with only 25 °C difference, and no observable trends. More differences could be observed in the case of T_c. After plotting the obtained values of T_c on a colour map, it is clear that its value increases with the addition of silica as expected (**Figure 31b**). The effect of the Y_2O_3 and Al_2O_3 addition was negligible.

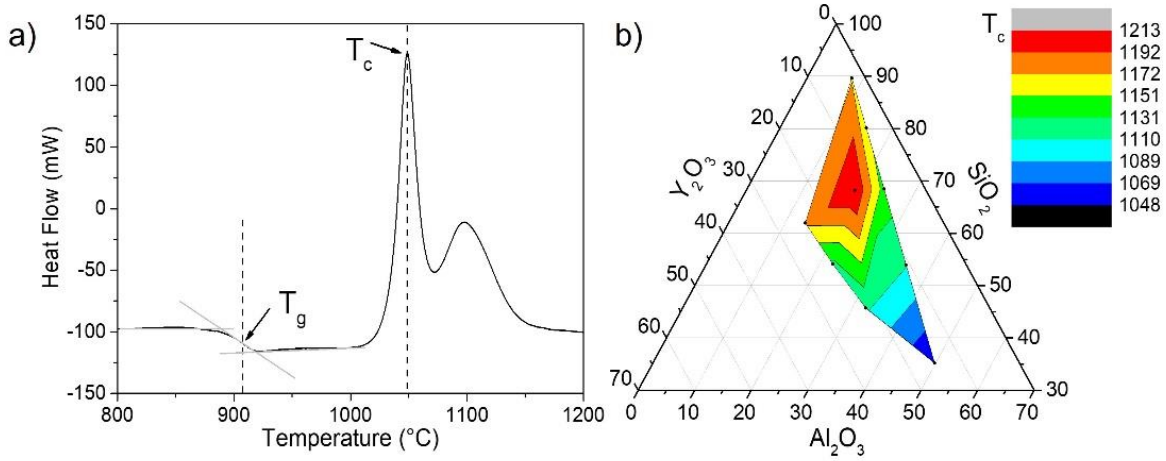

Figure 31 *Thermal behaviour of the glasses determined by DSC analyses – (a) DSC curve measured for sample 1(Y15-A50-S35) as an example; (b) colour map showing the dependence of T_c on glass composition.*

To check for the possible formation of crystalline phases during quenching, glasses with composition **1-10** were characterized using powder XRD. The observations focused mainly on the comparison between transparent and white opaque samples prepared by both methods. **Figure 32** shows the XRD pattern comparison for samples with composition **9**(*Y13-A19-S68*) and **10**(*Y14-A11-S75*) (other measurements are not shown). From the patterns it is obvious that,

regardless of their appearance, the samples were confirmed to be amorphous showing only the broad diffraction band that is characteristic for silicate amorphous structures.

Table 10 *Values of transformation and crystallization temperatures. Estimated uncertainty: ± 5 °C.*

Glass		**T_g [°C]**	**T_c [°C]**
1	*Y15-A50-S35*	908	1048
2	*Y11-A35-S54*	903	1111
3	*Y07-A24-S68*	922	1142
4	*Y05-A15-S80*	919	1157
5	*Y02-A08-S90*	904	1170
6	*Y22-A32-S46*	899	1113
7	*Y24-A22-S54*	907	1126
8	*Y24-A14-S62*	918	1175
9	*Y13-A19-S68*	917	1213

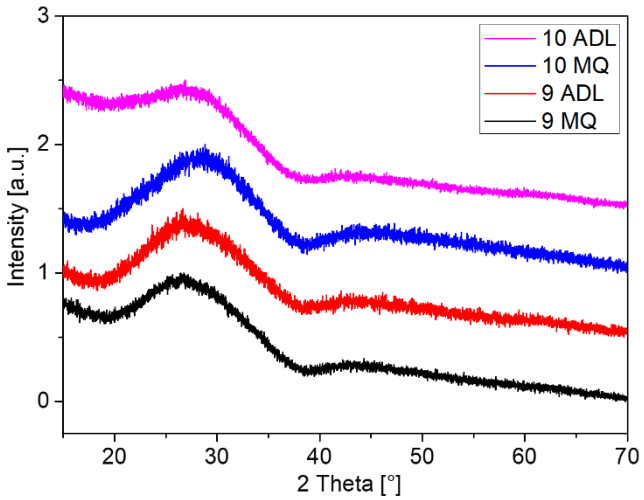

Figure 32 *The XRD pattern of samples* ***9*** *(Y13-A19-S68) and* ***10*** *(Y14-A11-S75) prepared by melt-quenching (MQ) as well by aerodynamic levitation coupled to laser heating technique (ADL).*

The structure of the YAS glass and network polymerization is expected to be strongly dependent on the composition, due to the variable role of the three oxide components. According to [40], the structure of YAS glass is that of a disordered glass network containing silicon and aluminium as network-forming cations and yttrium as a network-modifying cation. While silicon is almost entirely four-coordinated, aluminium ranges from four- to six-

coordinated (NMR studies in [62]), and yttrium can have a wider range of coordination numbers, with six and seven being most common. Increasing the yttrium content increases all cation-oxygen coordination numbers and gives a greater range of oxygen environments. Most oxygen atoms have two, three, or four neighbours, depending on composition, and the concentration of non-bridging oxygen atoms increases with increasing yttrium concentration. Increasing the yttrium concentration reduces the silicate network connectivity, and reduces the clustering of the modifying yttrium atoms; both effects will promote faster glass dissolution [215].

The glass structure changes were studied by Raman spectroscopy. Figure **33a** shows the Raman spectra of the glasses **1-10** measured in the range of 200 to 1500 cm^{-1}. In the spectra, two main distinct intensity regions can be observed, which are characteristic for alumino-silicate glasses. A high-frequency contribution (A_{1000}) was observed between 800 – 1200 cm^{-1}, with main maximum in the range from 932 to 1057 cm^{-1} depending on the type of the glass. This complex intensity envelope is known to arise from asymmetric Si-O-Si stretching vibrations in Q^n units, where Q represents [SiO_4] tetrahedra and *n* represents the number of bridging oxygens (BO). The high intensity of this band is typically present in highly depolymerized silicate glasses containing network modifiers, such as alkali ions [216–218]. The position of this band and the relatively low intensity in the samples **3***(Y07-A24-S68)*, **4***(Y05-A15-S80)*, **5***(Y02-A08-S90)* (see **Figure 33**-red colour) agrees well with their high content of SiO_2. The positional shift of the band to lower wavenumbers and increase of the intensity (with maximum around 960 cm^{-1}) is due to break-up of the silica network, as well as interlinking of Si-O-Al network, and can correspond to lower content of SiO_2 and higher content of both Al_2O_3 and Y_2O_3. It means that this band can be attributed to the stretching vibration of silicon-oxygen tetrahedra with two corners shared with aluminium (also yttrium) polyhedra [219].

The broad Raman band (A_{500}) with maximum of the main peak between 394 and 477 cm^{-1} is related to the bending vibrations of the interconnected aluminosilicate network. Especially, the vibration between 391 a 650 cm^{-1} are caused by bending vibration of bridging oxygen (BO) bonds of [SiO_4] units and the band near 779 cm^{-1} could be assigned to the Si-O-Si network or to [AlO_4] units with three BO and one NBO [220]. Significantly high intensity of these bands is evident in samples **3***(Y07-A24-S68)*, **4***(Y05-A15-S80)*, **5***(Y02-A08-S90)* with a high content of

SiO_2 and thus high content of BO between [SiO_4] tetrahedra. On the contrary, samples **2** *(Y11-A35-S54)* and **6** (*Y22-A32-S46*) show a much lower relative intensity of this band, which can be ascribed to a decrease of Si-O-Si linkage due to low content of SiO_2 and high content of Y_2O_3 and Al_2O_3. This may be ascribed to the fact that Al can be also present as 5- or 6-fold coordinated in the glass matrix and act as a modifier (similarly to Y^{3+}) [221].

If we compare the spectra of glasses with composition **9** *(Y13-A19-S68***)** (transparent) and **10 (***Y14-A11-S75***)** (opaque) it is obvious that, at a first glance, the positions of their bands were not much different. However, in detailed spectra (see Figure **33b**) two new bands become visible in samples with composition **10 (***Y14-A11-S75***)**, i.e. in glasses that are opaque (due to phase separation, see below). The same peaks were observed in the samples prepared by melt-quenching (not shown). They are also hinted in the spectra of glasses with composition **4** (*Y05-A15-S80*) and **5** (*Y02-A08-S90*) with very high SiO_2 content. These bands are located at 493 and 606 cm^{-1}; they are typical for the spectrum of pure SiO_2 and have been assigned to defects in the glass structure, associated with breathing vibrations of oxygen atoms in four- and three membered tetrahedral rings [222,223].

The degree of glass polymerisation can be qualitatively evaluated as the intensity ratio of the regions associated to the Si–BO bending vibrations (A_{500}) and to the Si-O-Si stretching (A_{1000}) bands [224]. The average value of A_{500} /A_{1000} was calculated from five spectra recorded at the same spot of each glass sample. The average values of the degree of polymerisation (A_{500}/A_{1000}) of the used glasses are calculated by a standard process (see e.g. [18]). **Figure 33c** shows the change in the degree of polymerisation calculated for each glass in the ternary diagram. From this figure, it is evident that the degree of network polymerisation appears to increase with the addition of SiO_2 as expected but simultaneously also with the addition of Al_2O_3, which is an intermediary oxide and may act as both network former and network modifier. Increasing of Al_2O_3 content thus leads to incorporation of Al^{3+} in network-forming 4-fold coordination. The content of Y_2O_3 as a modifier seemed to reduce the degree of glass network polymerization.

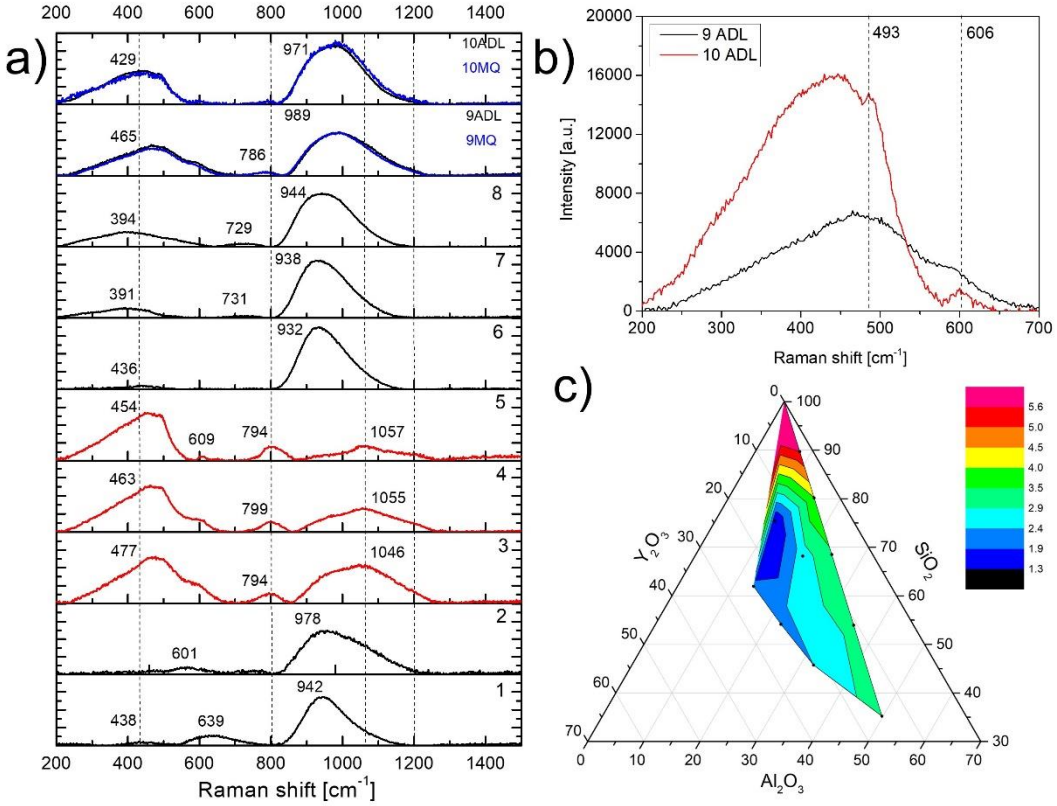

Figure 33 *Raman spectra of the samples prepared by ADL a) spectra comparison - the vertical dashed lines correspond to the 430,800,1060 and 1200cm^{-1} bands assigned to the fundamental vibrations of silicate glasses. They are added for better orientation. Small numbers indicate the maxima of measured bands; b) detail of spectra- the comparison of glasses* ***9****(Y13-A19-S68****)*** *and* ***10(****Y14-A11-S75****)*** *prepared by ADL; c) degree of glass polymerisation on a ternary diagram.*

4.2.3. Investigation of phase separation in prepared glasses

As there were no clear differences in the XRD or Raman analysis when comparing samples **9**(Y13-A19-S68) (transparent) and **10**(Y14-A11-S75) (white opaque), the characterization of samples with this composition as well as samples containing more than 65 mol% SiO_2 was done using electron microscopy. SEM images were collected using backscattered electrons, so that areas containing a higher concentration of heavy elements (such as Y^{3+}) appeared brighter. On the contrary, TEM images were acquired in bright-field mode: due to the fully amorphous state of the samples, contrast arose from density fluctuations, with denser phases appearing darker.

Sample **9**(Y13-A19-S68) appeared fully homogeneous down to the nanoscale level according to TEM examination (**Figure 34**), after both ADL and conventional melt-quenching synthesis. On the contrary, sample **10**(Y14-A11-S75) exhibited an amorphous phase separation during SEM inspection, with darker nanoparticles (SiO_2 enriched according to EDS analyses) in a brighter matrix. The nanoparticles appeared bigger in the melt-quenched sample, reaching a maximum diameter of approximately 200 nm, while they reached ca. 50 nm in the ADL sample. This size difference is likely to arise from the different melting temperature and quenching rate experienced by the materials during the synthesis [225].

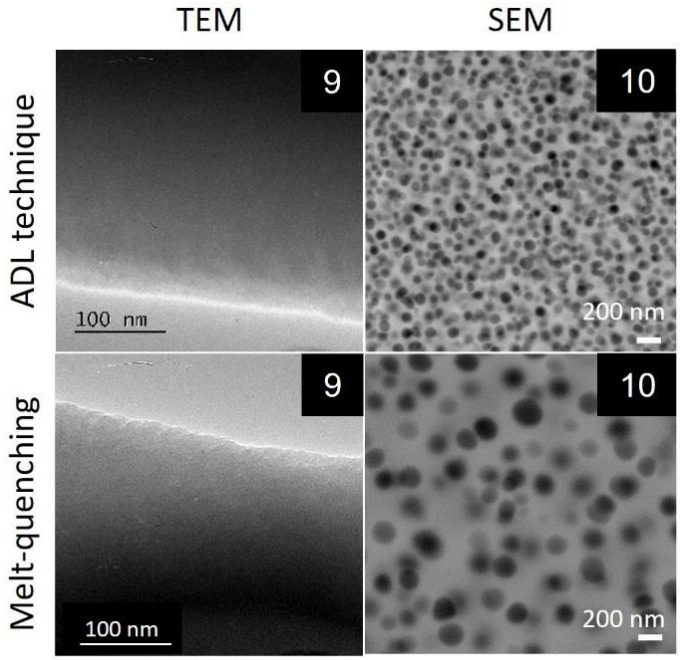

Figure 34 *Electron microscopy images (SEM and TEM) – comparison of microstructure of the samples prepared by melt-quenching and ADL*

Subsequently, samples prepared by ADL within the liquid-liquid immiscibility field [46,50] were characterized by SEM to gain more insight into the morphology of their amorphous phase separation. Samples **11**(Y08-A12-S80), **12**(Y06-A09-S85), **13**(Y04-A06-S90), **14**(Y02-A03-S95) demonstrate that an increasing content of SiO_2 leads to a decrease of the nano-nanoparticle size (**Figure 35a**). In glass **11**(Y08-A12-S80), most of the particles show a size of 50-60 nm, while in glass **14**(Y02-A03-S95) the nanoparticles exhibit a size of 30-40 nm. Decreasing imaging contrast between the particles and the matrix also possibly indicates a decreasing difference in their chemical composition.

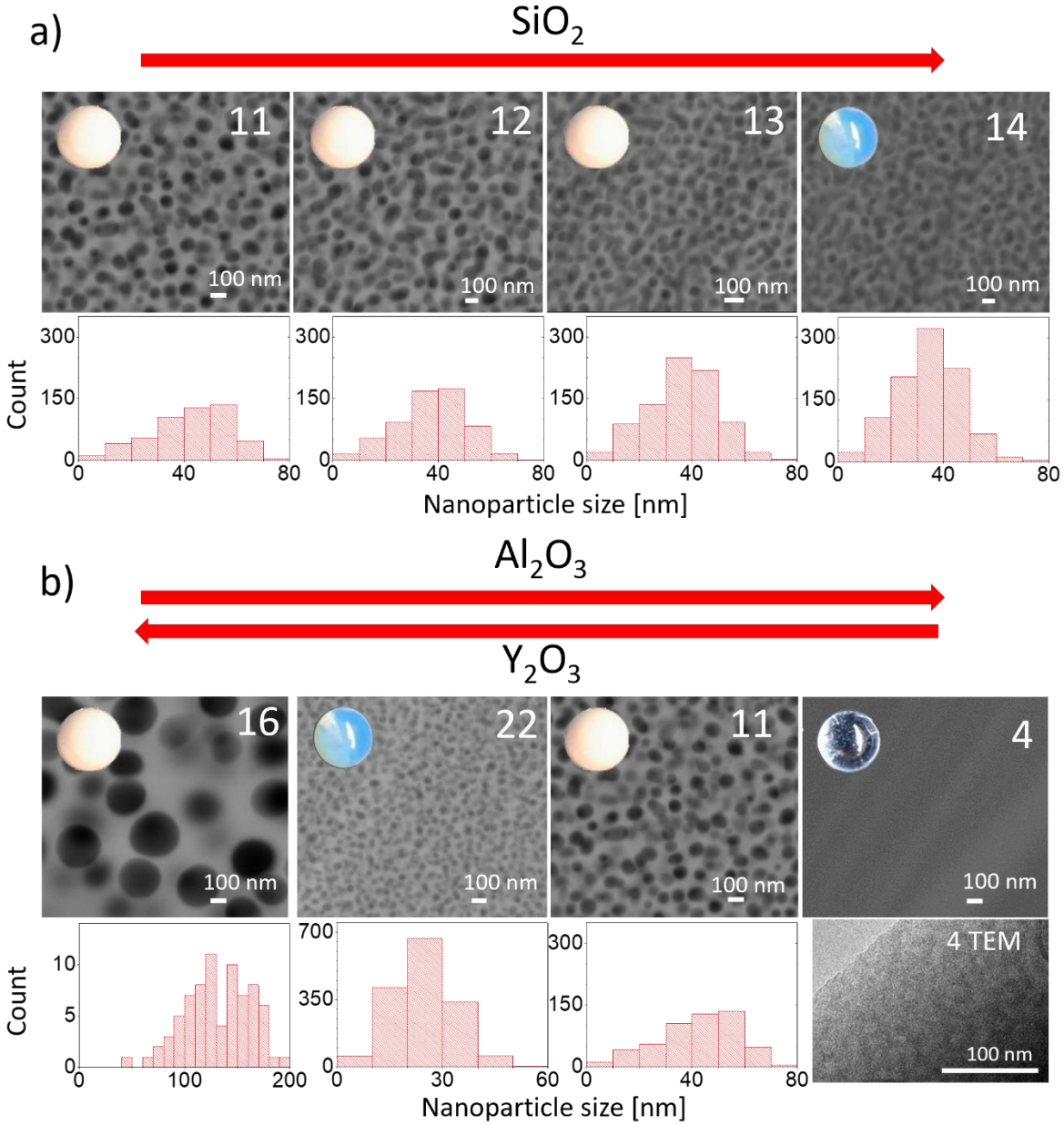

Figure 35 *The influence of chemical composition on the microstructure of phase-separated glasses - SEM images: a) increasing SiO_2 b) increasing Al_2O_3 and decreasing Y_2O_3. As there are no nanoparticles visible in the SEM image of sample 4, a TEM image of this sample is presented instead of the histogram, showing signs of spinodal decomposition. All bins in histograms represent difference in particle diameter of 10 nm. In each SEM image, an illustrative image of the sample is embedded.*

Consequently, the effect of the Al_2O_3 addition and the simultaneous reduction of Y_2O_3 content was also investigated (from left to right in the phase diagram). Glasses marked as **16**(Y15-A05-S80), **22**(Y10-A10-S80), **11**(Y08-A12-S80) and **4**(Y05-A15-S80) were prepared. SEM images are shown in **Figure 35b**. Growth or reduction of glass phase nano-nanoparticles is not as

systematic as before. Large nanoparticles (some with a diameter up to 180 nm) become small (size 30-50 nm) with addition of Al_2O_3. Good contrast is still evident, and the prepared glass exhibits opalescence. By adding higher amount of Al_2O_3, the size increased again to an average of 40-60 nm simultaneously with a decrease in contrast. After another addition of Al_2O_3, the observed glass phase separation disappears completely (sample **4**). Under TEM, signs of spinodal decomposition can be observed in this sample.

In order to study the interesting changes in the microstructure caused by Al_2O_3 addition as well as to determine the chemical composition of the nano-nanoparticles, selected samples were additionally inspected by high-resolution TEM. Compared to the SEM analysis (**Figure 35**), the nanoparticles are depicted in reverse contrast and are lighter than the matrix. The sample **22**(Y10-A10-S80) was prepared as thin lamella and samples **16**(Y15-A05-S80) and **12**(Y06-A09-S85) were analysed as powder. **Figure 36** shows the obtained images. In the first row only, the images of glass **22**(Y10-A10-S80) (opalescent sample) are shown. The glass presents a phase separation with small (average diameter is around 66 nm) brighter nanoparticles in a dark matrix. When examined in detail, the rounded nanoparticles appear partially interconnected by "channels" in between some of them (red arrows in the figure). Moreover, percolation between several nanoparticles is sometimes evident. The electron diffraction pattern does not show defined spots indicating an amorphous state. Consequently, both composition of nanoparticles and matrix were determined by EDS analyses – see **Table 11**. The absolute measurement error is less than ±1%. The error might be largely caused by the superposition of the analysed nanoparticles and the matrix.

The second row in **Figure 36** shows images of samples **12**(Y06-A09-S85) and **16**(Y15-A05-S80). The same kind of phase separation with white nanoparticles in a darker matrix is evident. The spherical nanoparticles seem to be well separated and the average diameter was 105 nm for sample **12**(Y06-A09-S85) and 327 nm for sample **16**(Y15-A05-S80). These diameters correspond well with spherical nanoparticles distribution investigated by SEM. Again, electron diffraction patterns confirmed the amorphous state of the material, with the absence of any bright spots or reflections. From the results of the EDS analysis (see **Table 11**), it is clear that the nanoparticles in all samples have the same composition close to pure SiO_2, while the glass matrix reflects very well the trend and ratios of oxides from the nominal bulk composition.

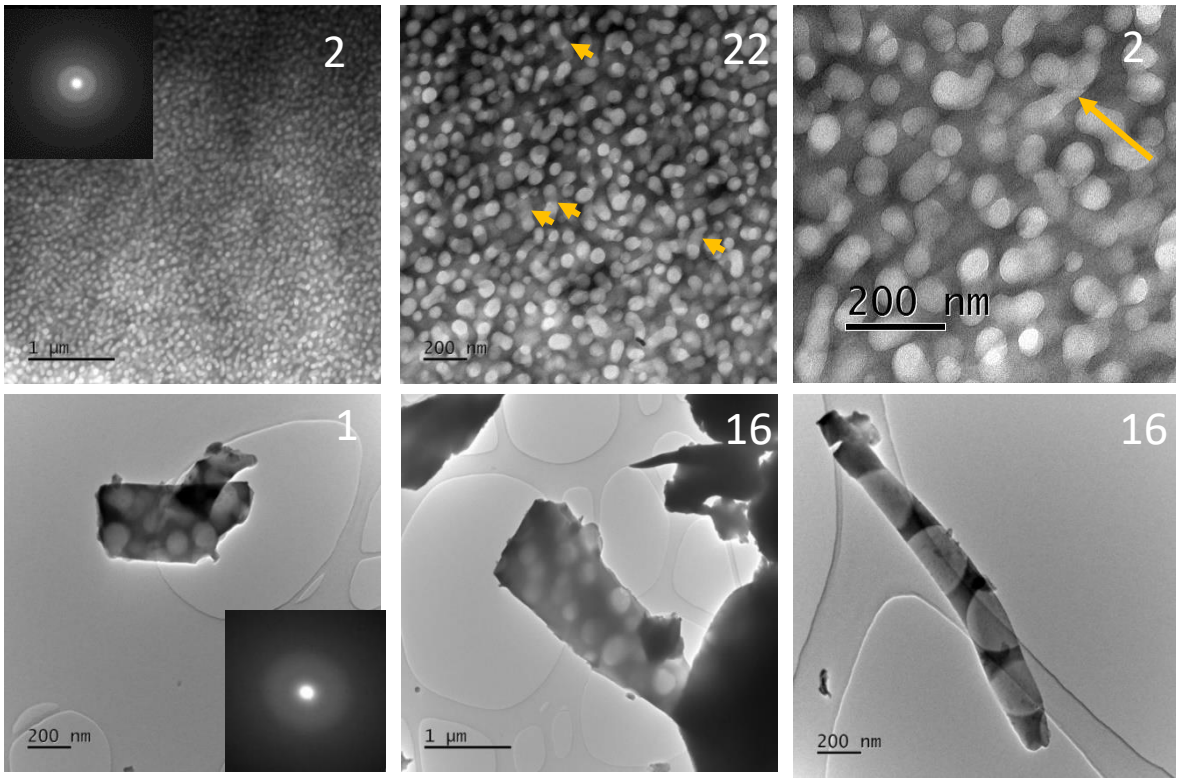

Figure 36 *TEM images of samples 22, 12, 16. Red arrows point at "channels" between white nanoparticles in the opalescent sample 22. Electron diffraction patterns indicate amorphous state.*

Table 11 *Chemical composition of samples 12, 16 and 22 in mol %. The absolute measurement error is less than ±1%.*

Sample	**Matrix**			**Nanoparticles**		
	Y_2O_3	**Al_2O_3**	**SiO_2**	**Y_2O_3**	**Al_2O_3**	**SiO_2**
12	21.0	13.5	65.5	1.0	1.5	97.5
16	28.5	7.5	64.0	1.0	1.0	98.0
22	15.5	14.0	70.5	1.0	1.5	97.5

4.2.4. Summary and Discussion

The research on nanostructured materials in the YAS system has mainly focused on the formation of crystalline nanoparticles, which are formed by subsequent annealing of the glass of a given composition [53–55]. The crystalline phases thus formed may have a great influence on the properties of YAS glass-ceramics with a number of potential applications, e.g. high temperature structural ceramics, oxidation protective coatings, environmental barrier coatings and jewellery due to their specific mechanical, thermal, tribological, dielectric and optical

properties and environmental resistance [45,54]. In the glass-forming region of the phase diagram, SiO_2, $Y_2Si_2O_7$, $3Al_2O_3{\cdot}2SiO_2$ (mullite) and Al_2O_3 [55,56] are commonly found. It is also possible to encounter other types of silicates (Y_2SiO_5) or apatite-like $Y_{4.67}(SiO_4)_3O$ [45]. These phases are mostly irregular in shape due to crystallisation. The analysis of the shape and distribution of the prepared nanoparticles shows that the shape of the particles is closely related to the crystal structure and therefore also has corresponding shapes of the crystal nuclei [229,230]. Crystalline phases rarely have a spherical shape. On the contrary, our work demonstrates the potential (and limitations) to exploit liquid-liquid phase separation to prepare nanostructured materials containing spherical nanoparticles in the YAS system. Focusing on the size, distribution and chemical composition of the formed nano-sized nanoparticles, the following facts are evident from the above-mentioned results:

1) only amorphous nano-sized nanoparticles with a composition very close to pure SiO_2 can be formed in the investigated region of the YAS system;
2) nanoparticles are formed if the melt contains 75 mol% or more of SiO_2 and simultaneously around 20 mol% of Y_2O_3 or less;
3) changes in the Y/Al ratio of the samples significantly affected the size of SiO_2-enriched nanoparticles, but the change was not directly proportional to composition;
4) changes in the SiO_2 content seemed to have a less significant effect on the size or composition of the nanoparticles. An increase in the overall SiO_2 content of the melt probably brought about a SiO_2 enrichment of the matrix, which converged towards the composition of the nanoparticles (as inferable from the lower contrast in **Figure 35**);
5) with the same content of both Y_2O_3 and Al_2O_3, opalescent glass was formed in the region above 65 mol% of SiO_2, which is characterized by a very small size of SiO_2 nanoparticles and also some interconnection between the nano-nanoparticles.

The influence of the used synthesis technology (ADL or conventional melt-quenching) is obvious. The two methods differ mainly in the maximum achievable melting temperature and cooling rate. It is a well-known fact that a higher cooling rate causes the formation of a larger number of small nanoparticles and vice versa [225]. This fact has been confirmed and is evident when comparing the preparation of glass **10**(Y14-A11-S75) (see **Figure 34**), where smaller SiO_2 nanoparticles are formed using ADL technology as compared to MQ technology.

Experimental data on the Y_2O_3-Al_2O_3-SiO_2 phase system are sparse and contradictory, for example, the phase diagrams of the Y_2O_3-Al_2O_3-SiO_2 system calculated by Groebner [57] are inconsistent with more recent data [49] on subsolidus phase relations. New calorimetric measurements and calculations especially in the near eutectic region are reported by Fabrichnaya [56]. The region of the phase diagram with SiO_2 content above 70 mol% is practically unexplored, most authors report the formation of crystalline SiO_2 (tridymite). Theoretical models are given by the previously mentioned Pan et al. [46] and Mao et al. [50], who define the phase separation region above 70 mol% SiO_2, which are in reasonable good agreement with our experimental results. The region defined by Mao et al. [50] corresponds to the region where spherical SiO_2-enriched nanoparticles form due to phase separation, according to our observations. The region defined by Mao is also characterized by obvious phase separation, which may not manifest itself as spherical SiO_2 formations but as spinodal decomposition.

Turning towards the domain of possible applications, the conditions offered by ADL synthesis appear very close to those experienced by the material during the drawing of optical fibres. The two methods match in the considerable cooling rate from temperatures as high as 2000 °C. Indeed, nanostructured optical fibres have been previously described in the YAS system especially by Paul et al., nanoparticles with a size of 5-10 nm have been reported in YAS preforms and fibres, with high content of SiO_2 (>90 mol%) [226,231–235] , where their size as well as distribution was controlled by the presence of phosphorus or fluorine. The amorphous nanoparticles or parts with spinodal decomposition were significantly enriched by Y_2O_3 and Al_2O_3 or another used dopants whereas the surrounding matrix was enriched by silica [236,237]. The shape of these nanoparticles, in agreement with our experiment, is mostly spherical or unbounded, while the nanoparticles prepared in our experiments contained practically pure SiO_2. It should be kept in mind that the experimental procedure differed significantly. The preparation of the preforms and the enrichment of fibre core by Al or Y was done by MCVD method combined with solution doping, and the mechanism of nanoparticle formation was also different; the YAG nanocrystals were crystallized in the preform and amorphized during fibre drawing, rather than created by phase separation, as in our study.

5.3 Fabrication of gold nanoparticles by ADL technique - comparison with conventional melting approach

5.3.1 Selection of melting parameters

When preparing samples using ADL, many input parameters can be selected that affect the outcome of the experiment. To ensure maximum reproducibility of the experiments and homogeneity of the prepared samples, several experiments were first performed to find the optimal set of these experimental parameters. Another requirement was to use the lowest possible temperature and the shortest possible melting time in order to minimize the volatilization of Au and SnO_2 from the samples. To achieve good homogeneity of the samples, the exact opposite conditions are suitable - high melting temperature and long melting time - so a compromise had to be found between these requirements.

It is clear from the design of the ADL technological equipment that the adjustable parameters are volume of prepared pellets, shape and material of melting nozzle, suitable gas for levitation and its pressure, melting time and melting temperature.

First, a pellet preparation procedure was designed to ensure a constant melt volume and a very stable levitation of the prepared sample from the beginning to the end of the melting process (see **Chapter 3.1.2**). The volume of the prepared pellets was 50 µl. This volume was the largest possible with which stable levitation and good homogeneity of the samples was achieved without using too high melting temperatures.

A conical copper melting nozzle was chosen for the preparation of the samples, which, in comparison to nozzles of the same shape made of aluminium or stainless steel, caused the least sticking of the samples to the nozzle wall during melting. Oxygen was chosen as the gas to levitate the samples during melting. Levitation of the samples with this gas was very stable. Another reason for using O_2 was that there was significantly more volatilization during sample melting when using Ar or the 95% Ar, 5% H_2 mixture available in the laboratory. The O_2 flow rate through the melting nozzle was chosen between 1.2 and 1.5 min^{-1} depending on the initial mass of the melted pellets. LS pellets were less dense, while YAS pellets were denser. The gas flow rate was always chosen so that before and after the lasers were switched on, i.e. in the

pellet and bead phase, there was no contact of the prepared sample with the wall of the melting nozzle.

The last two parameters that needed to be adjusted were the melting time and the melting temperature. The temperature could not be controlled directly, only the power of the melting lasers and its time dependence was controlled on the device. An Impac ISR 320 pyrometer (two channels, spectral range 0.9 and 1.05 μm) provided information about the actual temperature during melting. This temperature is referred to as the apparent temperature. This temperature can differ from the real temperature by up to ± 200°C, but it is a reliable indication for observing trends within a set of samples. To determine the real temperature, it would be necessary to know the melting temperatures and the temperature dependence of emissivity for each of the prepared compositions. Measurement of this dependence is very laborious and would be the subject of a separate thesis. The calibration of the pyrometer was done based on the melting temperature and emissivity data of Al_2O_3.

In order to determine the appropriate melting time and temperature (laser power), experiments were performed with samples **JB60** (YAS) and **JB62** (LS). A set of samples was prepared and melted by laser for 15, 30 or 45s. The minimum laser power used corresponded to the first time a bead was successfully formed from the starting material. For LS samples, the apparent temperature corresponded to 1500 °C, for YAS samples to 1600 °C. The power of the lasers was then increased so that the apparent temperature increased in 100 °C increments until a transparent sphere was prepared due to significant gold volatilization. Temperatures of 1500-1800°C were used for LS samples and 1600-1900°C for YAS samples. The laser power was 3-8% for the LS experiment and 4-8% for the YAS experiment. The results of both experiments are shown in **Figure 37**.

The YAS system samples were first evaluated by naked eye, then samples were embedded in epoxy resin, polished and the homogeneity, elemental analysis as well first inspection of Au nanoparticles presence was done by EPMA. Selected samples - systematic series with variation of melting time and temperature - were also examined by SEM. These samples are shown in yellow in **Figure 37**a.

Table 12 *Time-temperature experiment with samples YAS60 and LS62*

Sample no.	Y_2O_3	Al_2O_3	SiO_2	Li_2O	Au	SnO_2	Time [s]	Temperature [°C]
1	0	0	66.67	33.33	0.127	0.25	15	1600
2	0	0	66.67	33.33	0.127	0.25	30	1600
3	0	0	66.67	33.33	0.127	0.25	45	1600
4	0	0	66.67	33.33	0.127	0.25	15	1500
5	0	0	66.67	33.33	0.127	0.25	30	1500
6	0	0	66.67	33.33	0.127	0.25	45	1500
7	0	0	66.67	33.33	0.127	0.25	15	1700
8	0	0	66.67	33.33	0.127	0.25	30	1700
9	0	0	66.67	33.33	0.127	0.25	45	1700
10	0	0	66.67	33.33	0.127	0.25	15	1800
10.5	0	0	66.67	33.33	0.127	0.25	30	1800
11	12.62	19.21	68.17	0	0.127	0.25	15	1600
12	12.62	19.21	68.17	0	0.127	0.25	30	1600
13	12.62	19.21	68.17	0	0.127	0.25	45	1600
14	12.62	19.21	68.17	0	0.127	0.25	15	1700
15	12.62	19.21	68.17	0	0.127	0.25	30	1700
16	12.62	19.21	68.17	0	0.127	0.25	45	1700
17	12.62	19.21	68.17	0	0.127	0.25	15	1800
18	12.62	19.21	68.17	0	0.127	0.25	30	1800
19	12.62	19.21	68.17	0	0.127	0.25	45	1800
20	12.62	19.21	68.17	0	0.127	0.25	15	1850
21	12.62	19.21	68.17	0	0.127	0.25	30	1850
22	12.62	19.21	68.17	0	0.127	0.25	45	1850
23	12.62	19.21	68.17	0	0.127	0.25	15	1900
24	12.62	19.21	68.17	0	0.127	0.25	30	1900
25	12.62	19.21	68.17	0	0.127	0.25	45	1900

Figure 37a shows that most of the prepared samples were opaque, brown or brown-red. With increasing temperature and longer melting time, the samples became lighter and lighter in colour, until finally, at 1900°C and a melting time of 45 s, a completely transparent sample was prepared. Using EPMA (see **Figure 38**), firstly the images of the samples were taken to evaluate their homogeneity. Images were taken at ×40 magnification in BSE and SE mode to get a general overview of the sample quality, then images were taken at ×1700 magnification to capture the most heterogeneous area on the sample surface. Secondly a spot analysis of the chemical composition of each sample was also performed. In each sample, 3 points were analysed sequentially from the centre of the sample to the edge of the sample to verify constant chemical composition. The composition of significant heterogeneities in the sample was also analysed.

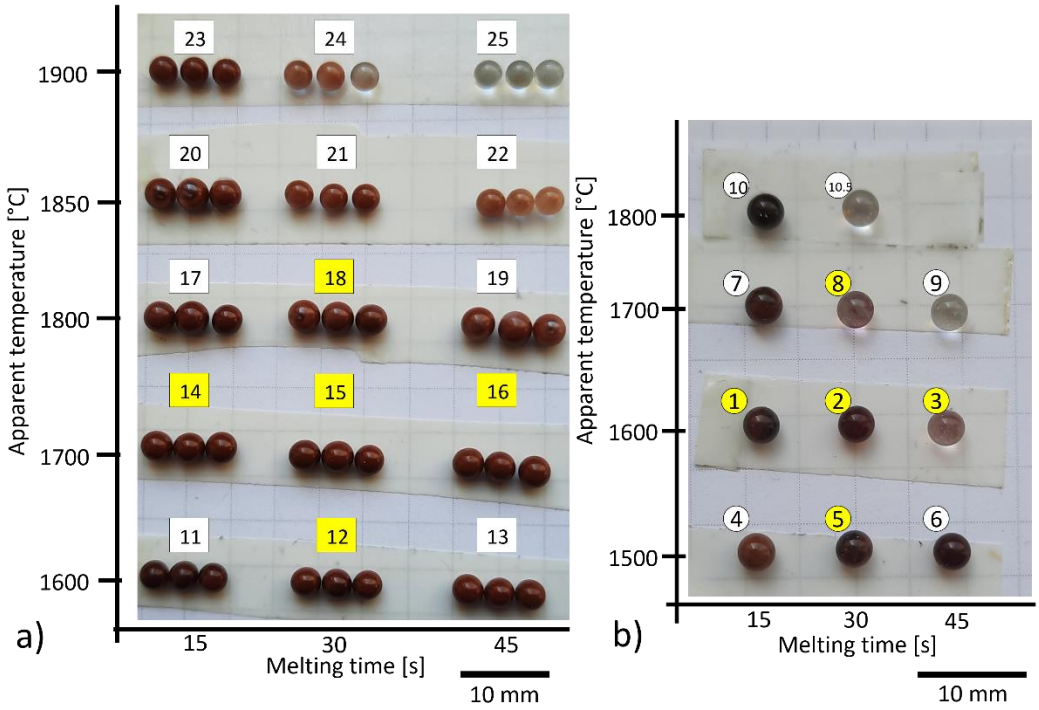

Figure 37 *ADL technology- time-temperature experiment: images of samples prepared under different conditions (x-axis time, z-axis temperature) a) using the YAS glass system JB60 b) using the LS glass system JB62*

Macroscopic images (**Figure 38**) show that 9 of the 15 tested combinations of sample preparation parameters resulted in one or more bubbles in the centre of the sample. These bubbles are a very obvious and common defect with unsuitable input conditions for ADL technology. From these results the best temperature for sample preparation appears to be around 1800 °C, where the bubbles were removed from the sample at all melting times investigated. In addition to the bubble, gold particles (chemical composition confirmed by analysis) are visible in the samples - mostly spherical in shape, distinctly white compared to the glass matrix. The gold is not evenly distributed in the glass homogeneously, there are often areas with many gold particles, chains and a large area of the sample without these particles. According to the images in **Figure 38**, the Au particle size ranged between 0.3-5 μm. In samples containing SnO_2 light grey clusters of SnO_2 particles of 5-50 μm in size were evident. These particles are very irregular in shape and are composed of many small spherical particles of about 0.3-0.6 μm in diameter.

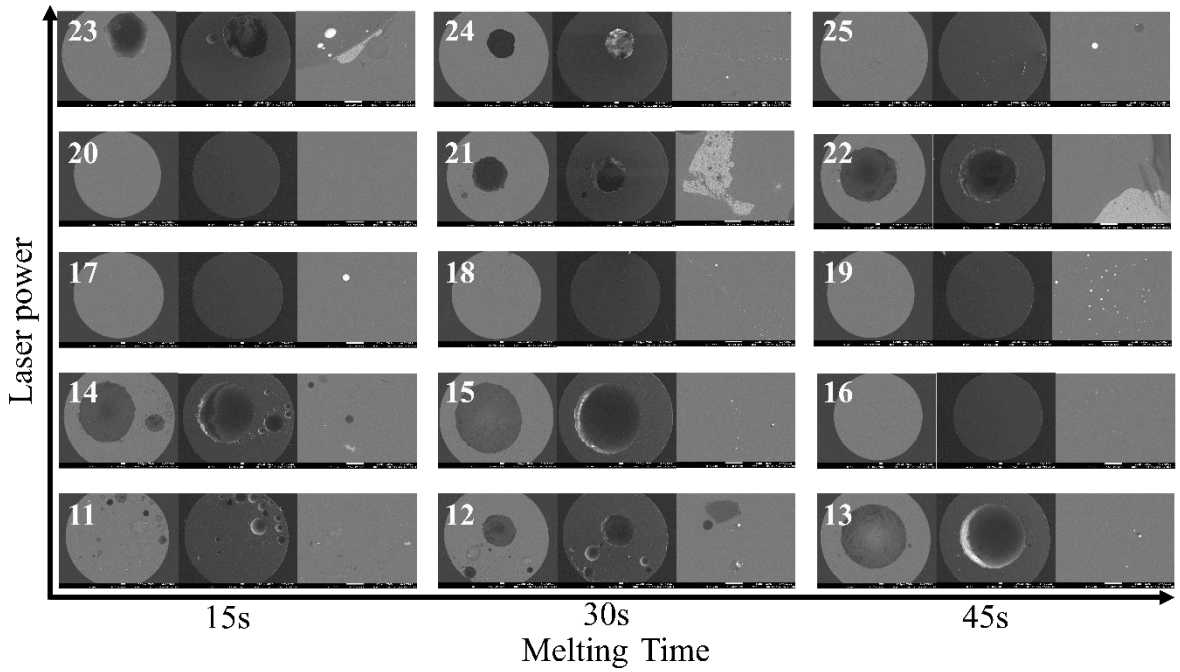

Figure 38 *Evaluation of the influence of melting time and temperature on the homogeneity of the beads, EMPA analyses of the YAS glass system, images with ×40 magnification in BSE and SE mode (first two images) and ×1700 magnification (last image)*

Based on the chemical composition analysis using EPMA, it is clear that there is no significant loss of elements during the synthesis process using the ADL technology. Measured variations in oxide concentration in wt.% never exceeded 2 %. Therefore, it is obvious that the composition of the glass of the whole bead corresponds to the weighed amount of input oxides in YAS system. For the content of Au and SnO_2, a similar observation cannot be done because the measurements of its content are subject to too large of a measurement error due to its low concentration in the samples.

SEM images (see **Figure 39**) were taken on samples **14**, **15** and **16**. The magnifications used ranged from x500 to x55 000. For image analysis, images were taken at ×5000 magnification. The images show different amounts of spherical Au nanoparticles with a diameter of 50-400 nm. Also, scratches on the sample surface caused by imperfect sample preparation are visible. Based on image analysis (see **Figure 39**) together with evaluation of the number and size of AuNPs, it can be seen that the number of these particles decreases with increasing melting time. Similar trend can be seen when increasing the melting temperature.

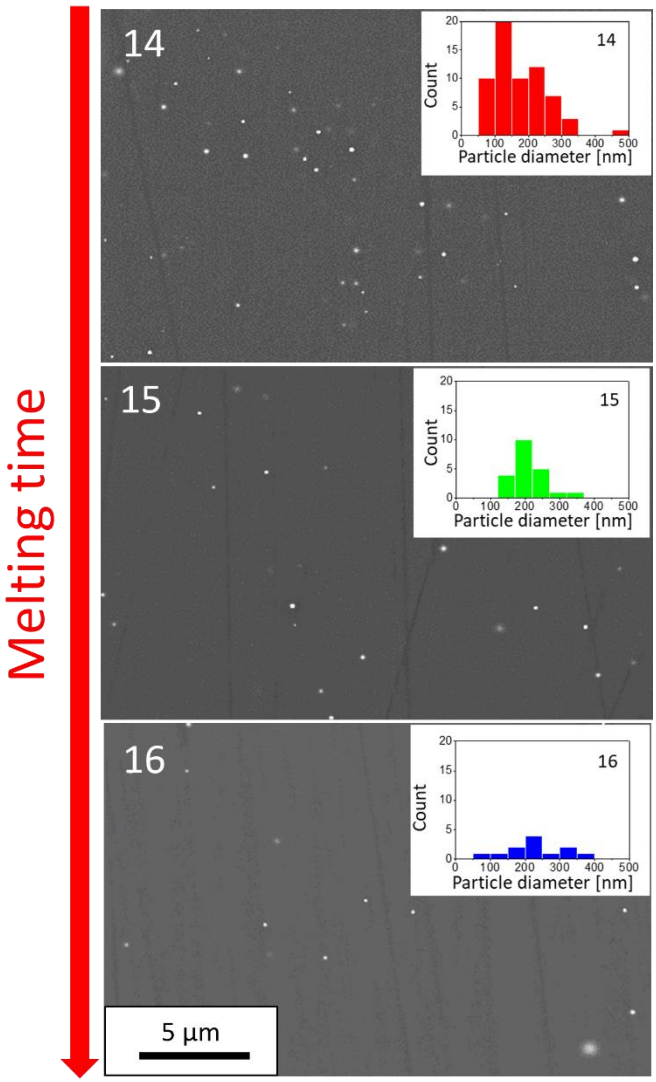

Figure 39 *SEM images of AuNPs in YAS system, ×5000 magnification, the influence of time and temperature as input parameters of ADL technology, histograms of particle size are the result of image analysis*

We evaluated the LS system in the same way as the YAS system. In the LS matrix, 8 of the 11 prepared samples were opaque, brown or brownish-red (see **Figure 37**b). With increasing temperature and longer melting time, the samples became lighter in colour, the first clear sample was prepared at 1600 °C and 45 s time, the next at 1700 °C and 30 s time. Unlike the YAS samples, more homogeneous samples were prepared, without bubbles (see **Figure 40**), which is in good agreement with the results shown in **Section 4.1**. Based on the EPMA images, we can say that sample **4**, which was melted for the shortest time at lowest temperature, is significantly more heterogeneous compared to all the others. It contains many small bubbles, SnO_2 particles of characteristic shape and spherical Au particles. The other samples do not

contain visible bubbles. We can see spherical Au particles with a size of 0.3-10 μm. The number of these particles decreases significantly with increasing melting time and temperature.

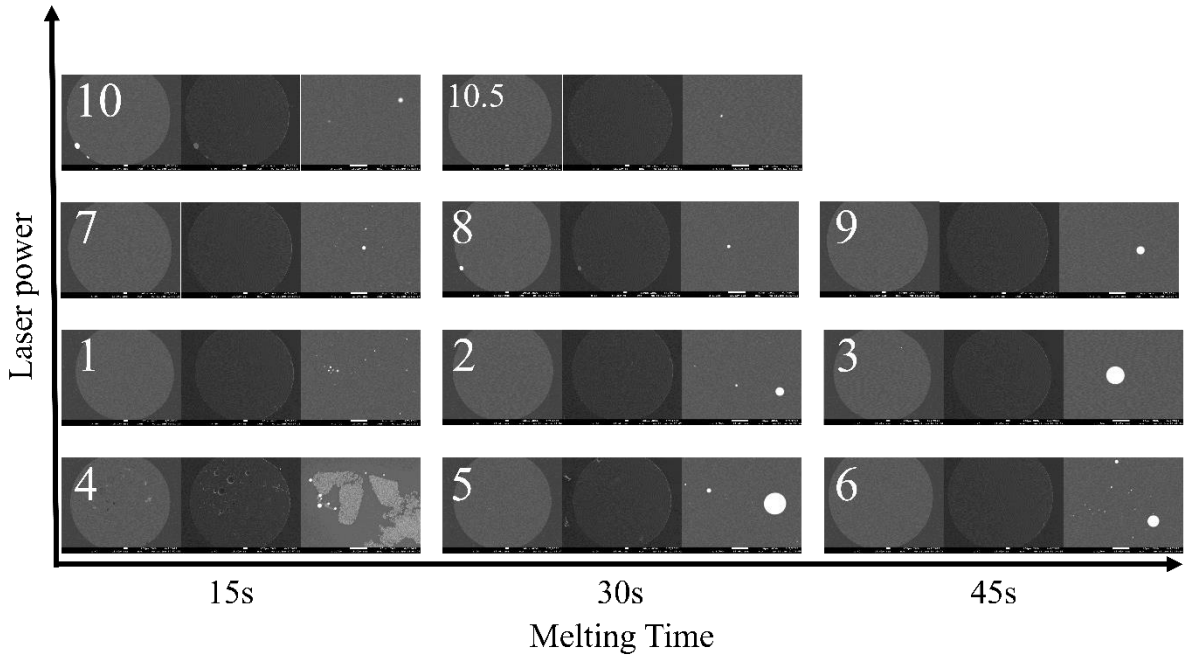

Figure 40 *Evaluation of the influence of melting time and temperature on beets homogeneity, EMPA analyses of the LS glass system, images with ×40 magnification in BSE and SE mode (first two images) and ×1700 magnification (last image)*

Based on the analysis of chemical composition by EPMA, SnO_2 and Au are volatilising from the samples, but precise quantification is difficult due to their low content. The SnO_2 content is conclusively highest at short melting time and low temperature and decreases visibly at long melting time and high temperature. The Au content cannot be evaluated in this way as it is subject to a large measurement error and the Li_2O content could not be directly determined by EPMA and was always calculated based on glass batch.

SEM images were taken on samples **1**, **2**, **3**, **5**, **8**, selected images are shown in

Figure 41. Based on image analysis of these images, it is again evident that the Au particle content decreases significantly with increasing melting time and temperature. If we focus on the sample size, then Au particles <1 μm formed irregular clusters and chains only in samples **1** and **5**. In the other samples, isolated particles of diameter from 30 nm to 5 μm were observed. In one case, a large spherical Au particle with a diameter of 100 μm was observed on the sample surface. However, the particles are very sparsely distributed in the majority of the samples,

which made image analysis not possible. Most of the nanoparticles were spherical in shape, but square or polygonal particles were found in sample **1** and **3**.

Based on experiments presented in this chapter, the following preparation conditions were selected. For all samples, an initial pellet size of 50 µl was chosen, a Cu conical melting nozzle was used, and O_2 was used as the support gas with a flow rate of 1.2-1.5 l min^{-1}. For the YAS system glasses the selected temperature was 1700 °C and time 45 s, for the LS system glasses the selected temperature was 1600 °C and time 45 s. Under these initial conditions all samples were prepared using ADL technique later on and will be described further in the thesis.

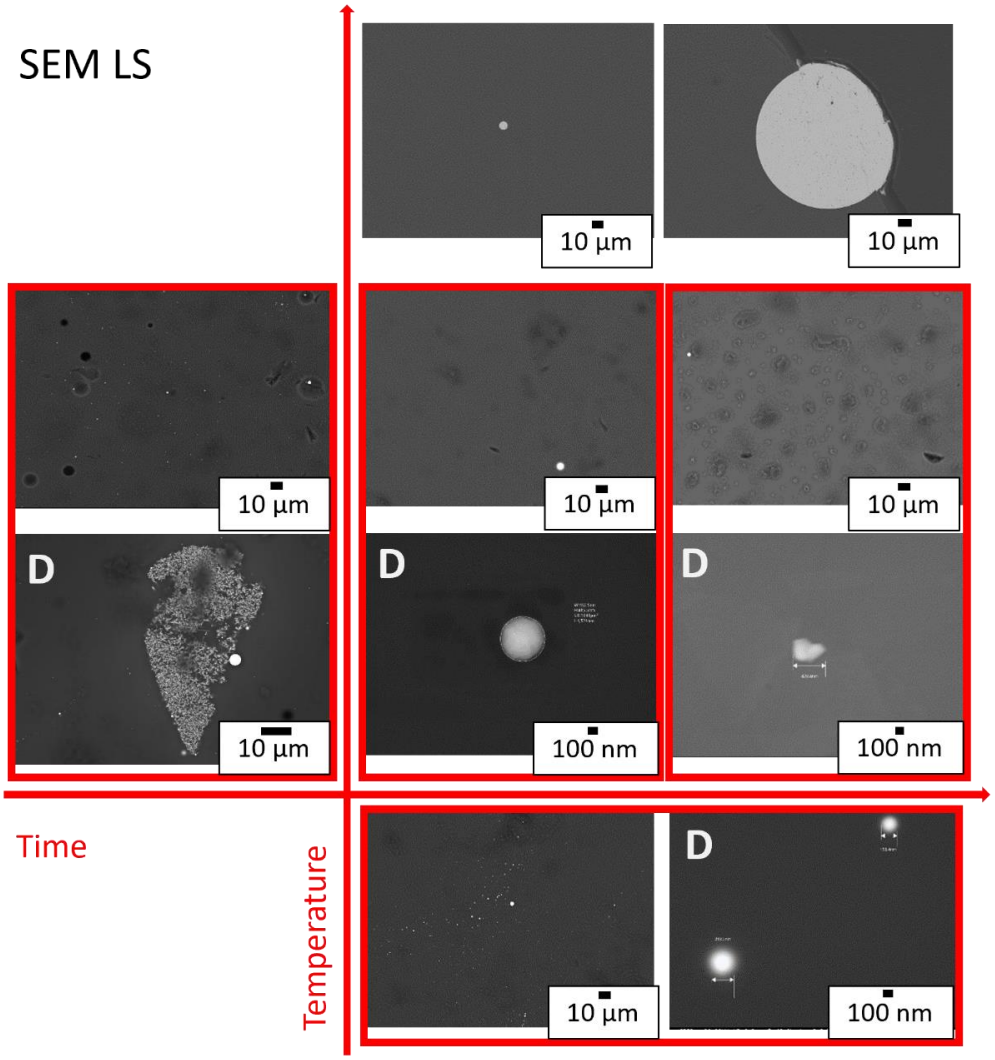

Figure 41 *SEM images of AuNPs in LS system, ×5000 magnification, influence of time and temperature as input parameters of ADL technology, images marked with D indicate detail from the image in the common frame*

5.3.2 Au nanoparticles prepared in Y_2O_3-Al_2O_3-SiO_2 system

A set of YAS glass samples were prepared by both ADL and MQ techniques. The conditions for the ADL technique were chosen based on the results presented in the previous chapter (45 s and 1700 °C) and for the MQ technique the melting temperature was set to 1650 °C. Maintaining and accurately determining the temperature is challenging, especially for the ADL technique, so a record of the temperature measurement was taken for each sample using a pyrometer (two channels, spectral range 0.9 and 1.05 μm). For ten selected beads of sample **2ADL** prepared by constant applied laser power, the temperature reading record from the pyrometer is shown in **Figure 43**. It shows the very good repeatability of the experiment.

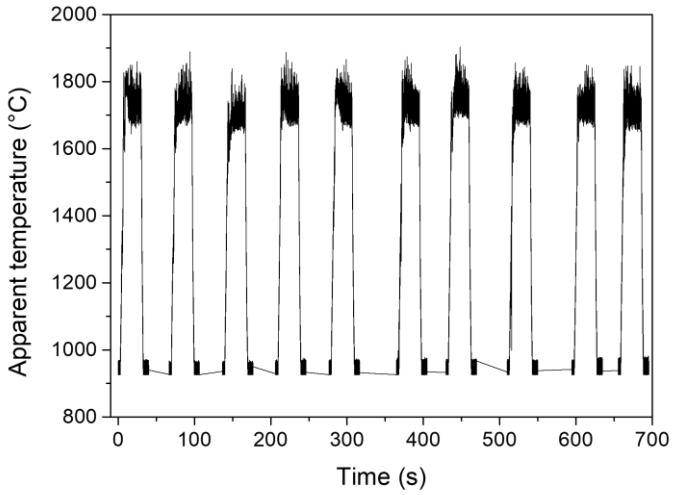

Figure 42 *Data from pyrometer in the ADL device. Each "peak" represents one bead of sample 2ADL melted.*

The composition of the prepared set of samples is summarised in **Table 13**. The composition of the base glass matrix was the eutectic: 68.2 mol% SiO_2, 19.2 mol% Al_2O_3 and 12.6 mol% Y_2O_3 (corresponding to sample number 9 in the phase diagram in **Figure 30**). Gold was added to one set of samples in three gradually decreasing concentrations. The second set contained the same concentrations of gold with the addition of 0.25 mol% SnO_2. The annealing temperature was tested on the prepared samples (not shown) and all the prepared samples, i.e., those prepared by ADL and MQ techniques, were annealed for 15, 60 and 120 min at the selected temperature of 900 °C.

Table 13 *A summary of the nominal compositions (mol%) of the prepared Au:YAS glasses using ADL and MQ technique. The sample code column summarizes chemical composition of the glass batch in mol%, rounded mathematically.*

Sample no.	Sample code	Y_2O_3	Al_2O_3	SiO_2	Au	SnO_2	Technology
1	*Au:Y13-A19-S68*	12.62	19.21	68.17	0.127		MQ, ADL
2	*Au:Y13-A19-S68*	12.62	19.21	68.17	0.013		MQ, ADL
3	*Au:Y13-A19-S68*	12.62	19.21	68.17	0.001		MQ, ADL
4	*Au,Sn:Y13-A19-S68*	12.62	19.21	68.17	0.127	0.250	MQ, ADL
5	*Au,Sn:Y13-A19-S68*	12.62	19.21	68.17	0.013	0.250	MQ, ADL
6	*Au,Sn:Y13-A19-S68*	12.62	19.21	68.17	0.001	0.250	MQ, ADL

Photographs of the prepared samples are shown in **Figure 43**. The flat samples were prepared by MQ technique and the beads by ADL technique. At first glance, it is evident that when the glasses were prepared by MQ, the samples with the highest concentration of Au were coloured immediately after quenching. Sample **1MQ** without SnO_2 was brown, sample **4MQ** with SnO_2 was light brown. The other samples with lower Au content were prepared as clear colourless glasses. At first sight, the SnO_2 content did not play any role. Its impact is only noticeable after the samples have been annealed. Only the samples with the highest and medium Au content with SnO_2 showed a visible change in appearance. Sample **4MQ** changed colour from the original light brown to dark pink and dark purple after 60 and 120 min, respectively. For the originally clear sample **5MQ**, a pink stripe appeared after 60 minutes, and after 120 minutes the colour of the sample was also dark purple.

The samples prepared by the ADL technique behaved very similarly to MQ samples as shown in the photograph. A dark brownish-red colouration was also observed only in the beads with the highest gold concentration (**4ADL**). The annealed samples containing 0.013% Au and SnO_2 (**5ADL**) showed signs of inhomogeneous red colour.

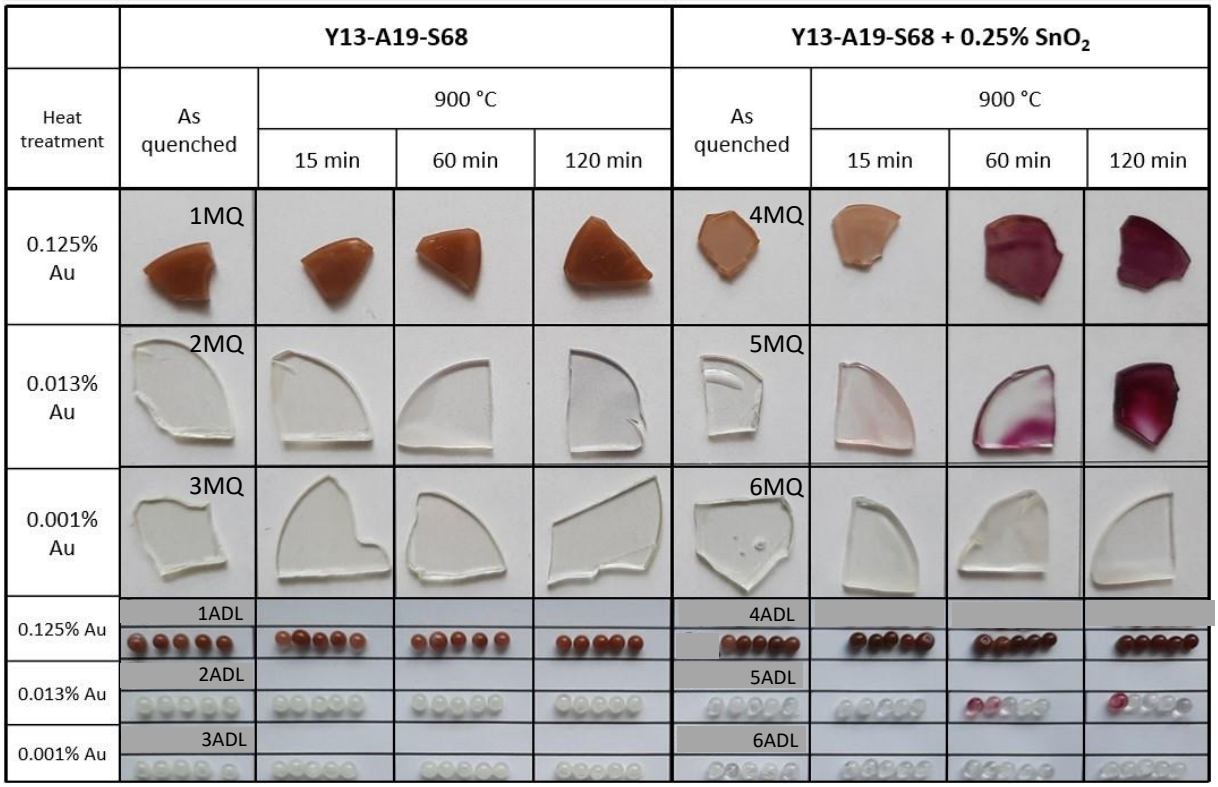

Figure 43 *Photographs of YAS glasses prepared by MQ and ADL with different concentration of Au and SnO_2*

All samples were analysed by XRF for determination of their chemical composition. Results of the YAS set are presented in **Table 14**. The results show a relatively good stability of the oxides of the basic glass composition i.e. yttrium and aluminium are stable, and a small relative loss is shown by silica. However, for both technologies there is a significant loss of SnO_2 as well as Au. Approximately 60% of the SnO_2 content is lost during melting using both technologies and Au volatilises even more. In most samples, less than 50% of the original gold content remains. This fact is evident in the samples with the highest gold content, while in samples with lower gold concentrations the determination was often already below the detection limit of the instrument. When comparing the two technologies, it can be seen that more Au volatilizes out with the ADL technology.

Table 14 *Results of XRF analysis of the chemical composition of YAS samples prepared by different techniques. The results are given in weight % and the columns marked % indicate the percentage deviation from the weighed amount (+ is the surplus compared to the weighed amount, - is the decrease compared to the original weighed amount). If * is in the column, the amount determined was below the detection limit of the analysis.*

Sample no.	Sample code	Y_2O_3	%	Al_2O_3	%	SiO_2	%	Au	%	SnO_2	%
1MQ	*Au:Y13-A19-S68*	36.98	+16	23.14	+5	39.35	-14	0.125	-55		
2MQ	*Au:Y13-A19-S68*	36.63	+14	23.39	+6	39.63	-14	0.007	-74		
3MQ	*Au:Y13-A19-S68*	37.15	+16	23.22	+6	39.35	-14	*			
4MQ	*Au,Sn:Y13-A19-S68*	37.59	+18	23.10	+6	38.77	-15	0.087	-69	0.165	-61
5MQ	*Au,Sn:Y13-A19-S68*	37.30	+17	23.05	+5	38.98	-15	0.005	-81	0.170	-59
6MQ	*Au,Sn:Y13-A19-S68*	38.07	+19	22.92	+5	38.55	-16	*		0.180	-58
1ADL	*Au:Y13-A19-S68*	34.39	+8	22.03	+0	42.86	-7	0.071	-75		
2ADL	*Au:Y13-A19-S68*	34.43	+8	22.09	+0	42.77	-7	0.006	-78		
3ADL	*Au:Y13-A19-S68*	34.49	+8	21.96	+0	42.94	-7	*			
4ADL	*Au,Sn:Y13-A19-S68*	34.27	+8	22.03	+1	42.72	-6	0.133	-52	0.234	-44
5ADL	*Au,Sn:Y13-A19-S68*	34.32	+8	22.03	+1	42.84	-6	*		0.162	-62
6ADL	*Au,Sn:Y13-A19-S68*	34.44	+8	22.00	+0	42.68	-7	*		0.135	-68

Next, SEM and TEM images of selected coloured samples were taken. The **1MQ** and **4MQ** samples that were not annealed, had the highest gold concentration and differed in the addition of tin oxide, were selected for SEM. From the series of annealed samples, samples **4MQ** and **5MQ**, which had been annealed for the longest time, were selected for analysis. Image analysis was performed using the ImageJ software. The evaluation of the results is summarized in **Table 15**. Most of the Au particles observed by SEM were very sparsely distributed. A selected representative image from the SEM is shown in **Figure 44.** Samples prepared by ADL were not analysed by SEM.

Table 15 *Results of image analysis of SEM for Au:YAS system of samples prepared by MQ.*

Sample no.	Sample code	Heating	Particles visible in SEM	SEM particle shape	SEM particles counted	SEM avg size [nm]
1MQ	*Au:Y13-A19-S68*		yes	spherical	>20	1182
4MQ	*Au,Sn:Y13-A19-S68*		yes	spherical	>20	1334
4MQ	*Au,Sn:Y13-A19-S68*	900°C 120min	yes	spherical	>20	2023
5MQ	*Au,Sn:Y13-A19-S68*	900°C 120min	no	-	-	-

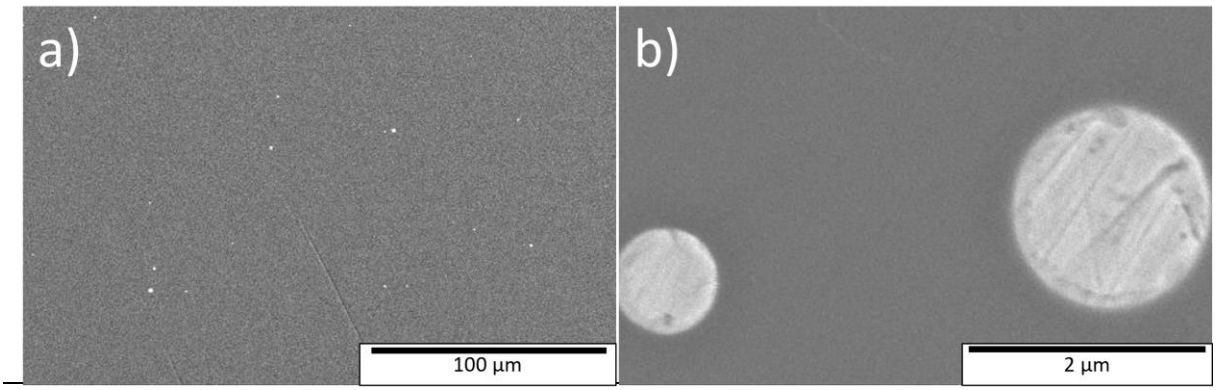

Figure 44 *Selected representative Au particles from SEM images. The figure shows (a) the distribution and (b) detail of Au particles in sample 1MQ prepared in the furnace, unannealed and containing the highest gold concentration used.*

It can be seen from **Table 15** and **Figure 43**, **Figure 44** that when the samples show a brownish red to brownish colouration, they contain large, sparsely distributed spherical gold particles. The average size of the particles in unannealed samples is 1.3 µm. The addition of tin as well as subsequent annealing probably promotes the aggregation of gold into larger particles (average diameter about 2 µm).

As we expected from the literature research that the colouration and corresponding absorption of the prepared samples would be related to the formation of much smaller nanoparticles, the samples were observed with a transmission electron microscope. For this analysis, the same samples as for the SEM of analysis were chosen. Since the effect of annealing wanted to be observed in more details, samples of **4MQ** composition were added, i.e. samples annealed at shorter times (15 and 60 min). The analysis was carried out on powdered samples which were spread on a Cu mesh. To confirm the composition of the visible nanoparticles, EDS analysis was performed on a few selected nanoparticles each time and the images were evaluated by image analysis. The results are summarized in **TEM analysis** of samples prepared by ADL show individual sparsely distributed AuNPs, similar to **Figure 45b.**

Table 16 and representative images are shown in **Figure 45**. TEM analysis of samples prepared by ADL show individual sparsely distributed AuNPs, similar to **Figure 45b**.

Table 16 *Results of image analysis of TEM images for a set of Au:YAS samples prepared by MQ and ADL.*

Sample no.	Sample code	Heating	NP shape	TEM particles counted	avg size [nm]
1MQ	*Au:Y13-A19-S68*		almost spherical, vermicular	3	20
4MQ	*Au,Sn:Y13-A19-S68*		vermicular	18	12
4MQ	*Au,Sn:Y13-A19-S68*	900°C 15min	almost spherical, vermicular, deformed polygons	9	15
4MQ	*Au,Sn:Y13-A19-S68*	900°C 60min	almost spherical	18	15
4MQ	*Au,Sn:Y13-A19-S68*	900°C 120min	vermicular, deformed polygons	18	19
5MQ	*Au,Sn:Y13-A19-S68*	900°C 120min	vermicular, deformed	16	13

It can be seen that vermicular, spherical and deformed nanoparticles were found in the unannealed samples. The size of the observed nanoparticles averaged 12-20 nm; the shortest particle dimension was always measured. When annealed for 60 and 120 min, no more vermicular particles were found, only nanoparticles with spherical or deformed polygon shape were present and their size slightly increased (**Figure 45c**). For samples annealed for 120 min, unidentified ink-like formations were observed. The described nanoparticles are shown in **Figure 45 d**. The size of these nanoparticles is not easy to determine due to their irregular shape. HRTEM analysis was performed from this image (sample with medium Au content and SnO_2 annealed for 120 min) (**5MQ-900-120**) (**Figure 46**), which showed both AuNPs (see interplanar spacing [238]) and unidentified phases.

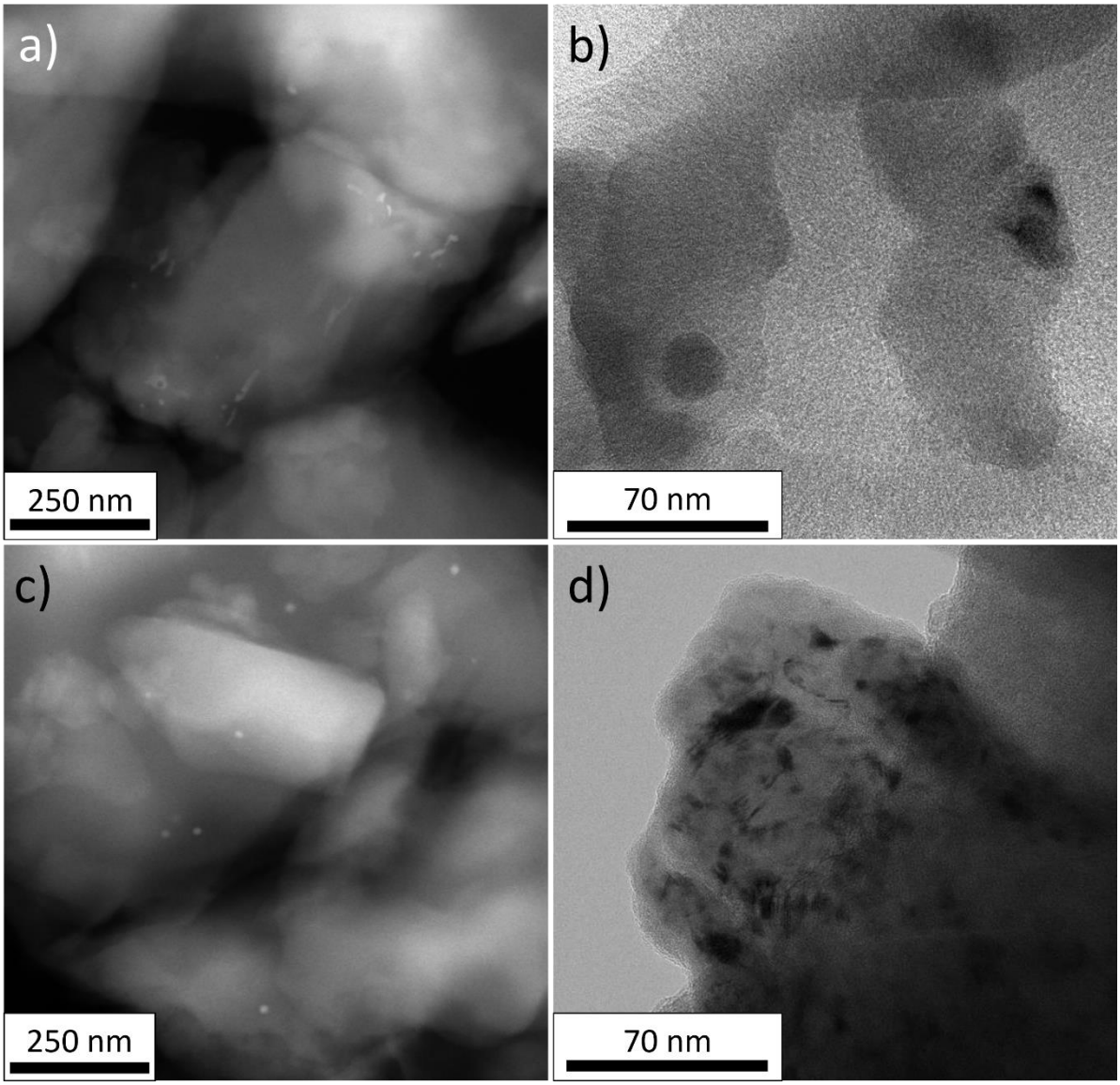

Figure 45 *Selected representative Au NPs from TEM images. a) vermicular AuNPs - sample 4MQ unannealed, b) pear-shaped AuNP - 4MQ unannealed, c) spherical AuNPs - sample 4MQ annealed 60 min., d) unidentified ink-like shaped particles - sample 5MQ annealed 120 min. Images a) and c) are HAADF images, AuNPs can be seen as the brightest spots. Images b) and d) are bright field images, AuNPs appear darker than the glass matrix.*

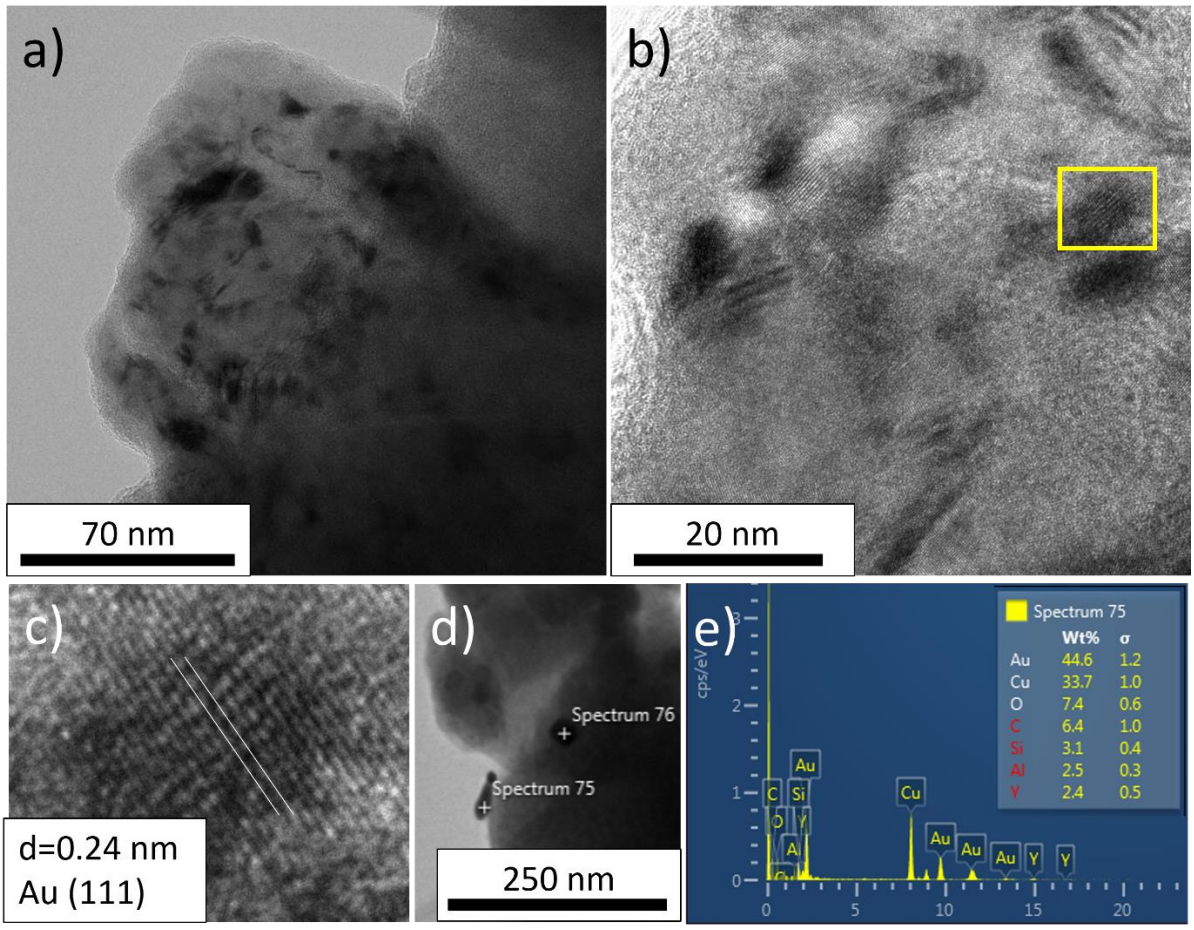

Figure 46 *Evidence of the presence of Au in the samples: a) area with ink-like particles, b) closer look at the selected area, particle in yellow box analysed by HRTEM in the next image c) by measuring the interplanar spacing on the HRTEM image, d, e) by EDS analysis*

Next, measurements of the absorption spectra were made. Samples **4MQ** and **5MQ** on which the effect of annealing was observed were measured. The change in absorbance as a function of additional heat treatment is shown in **Figure 47**. For the originally brown sample **4MQ** unannealed, the broad absorption band from about 525 to 700 nm changes to a characteristic peak at 550 nm, which corresponds to reddish coloration of the sample. The intensity of this peak further increases when the sample is annealed for 120 minutes. A similar trend of change in the absorption band was also visible in the sample **5MQ** with lower gold concentration, which was initially clear, and which did not have the described broad band (the absence of brown colour corresponds to practically zero intensity of the broad absorption band). However, as a result of annealing, a narrow band with a maximum at 550 nm appeared. The lower intensity corresponded well with lower Au content.

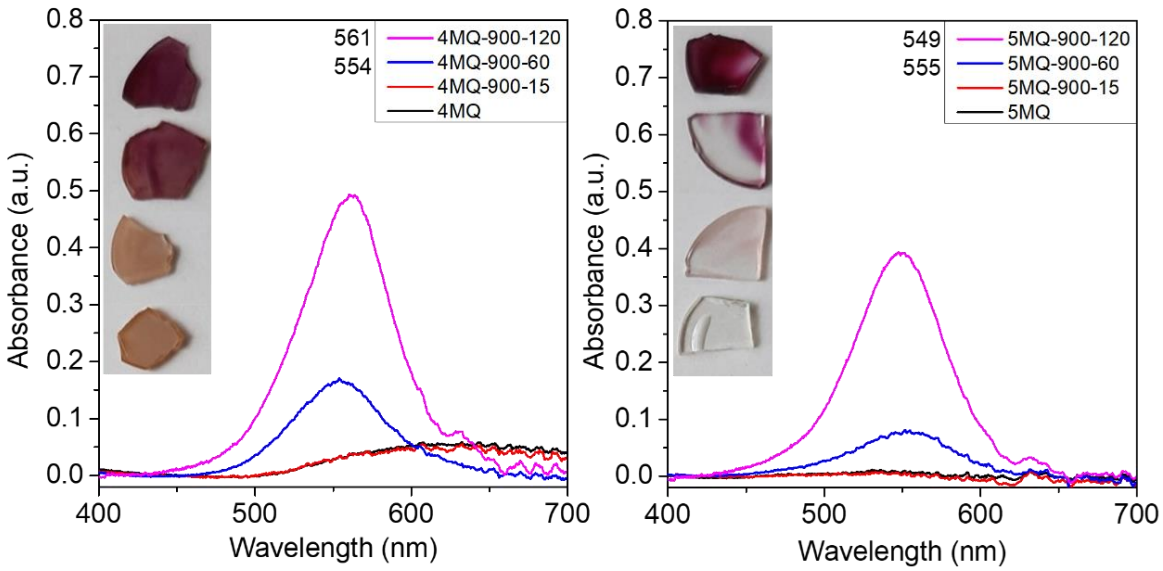

Figure 47 *The effect of annealing on the absorption spectra of samples 4MQ (highest Au content + SnO_2) and 5 MQ (medium Au content + SnO_2). Au nanoparticles prepared in Li_2O-SiO_2 system*

5.3.3 Au nanoparticles prepared in Li_2O-SiO_2 system

Since it was difficult to prepare homogeneously distributed small gold nanoparticles in the YAS system, a simple Li_2O-SiO_2 (LS) glass system was chosen for the next set of experiments. According to the results of **Chapter 4.1**, it could be assumed that this system was suitable for the ADL technique and also easier to nucleate gold nanoparticles. The experiments were performed in the same way as in the YAS system. The base matrix had a chemical composition of 66.67 mol% SiO_2, 33.33 mol% Li_2O. Again, a set of six glass samples was prepared with different gold concentrations (0.127, 0.0127 and 0.00127 mol% Au) without the addition of SnO_2 and with the addition of 0.25 mol% SnO_2 using both technologies, ADL and melt-quenching. For additional heat treatment, a temperature of 500 °C and times of 15, 30 and 45 min were chosen. These conditions were chosen based on DSC analysis of the base glass and several preliminary experiments. For the growth of AuNPs (i.e., for the diffusion of Au in the glass matrix), it is necessary to heat the sample to a temperature around the T_g of the base glass. The temperature and total time must not be too high to avoid crystallization of the glass matrix itself. An overview of the prepared samples is given in **Table 17**.

Table 17 *A summary of the nominal compositions (mol.%) of the prepared Au:LS glass samples using ADL and MQ. The sample code column summarizes chemical composition of the glass batch in mol%, rounded mathematically.*

Sample no.	Sample code	Li_2O	SiO_2	Au	SnO_2	Technology
7	*Au:L33-S67*	33.33	66.67	0.127		MQ, ADL
8	*Au: L33-S67*	33.33	66.67	0.013		MQ, ADL
9	*Au: L33-S67*	33.33	66.67	0.001		MQ, ADL
10	*Au,Sn: L33-S67*	33.33	66.67	0.127	0.250	MQ, ADL
11	*Au,Sn: L33-S67*	33.33	66.67	0.013	0.250	MQ, ADL
12	*Au,Sn: L33-S67*	33.33	66.67	0.001	0.250	MQ, ADL

A photograph of the samples after cooling and after additional heat treatment is shown in **Figure 48**. At first glance, there is a significant difference from YAS system and a much greater difference between ADL and MQ technologies. When the samples were prepared by MQ, the samples already differed significantly in appearance after quenching. The samples without SnO_2 were, from the lowest Au concentration to the highest, successively transparent (**9MQ**), light pink (**8MQ**) and light orange (**7MQ**). The sample with the lowest Au content and with SnO_2 (**12MQ**) was transparent with a light pink stain. The samples with the medium (**11MQ**) and highest (**10MQ**) Au concentration with SnO_2 were almost black in reflected light and deep red to reddish-brown in transmitted light. Samples prepared by the ADL technique were significantly different. Only the samples with the highest Au concentration showed coloration after the bead preparation. While the colour of the samples without SnO_2 addition was highly inhomogeneous and showed both orange and bluish shades (**7ADL**), the samples with the addition of tin were ruby red (**10ADL**).

The effect of additional heat treatment is shown in **Figure 48**. Samples prepared by the MQ followed by annealing changed their colour to ruby red hues, which is particularly noticeable for samples with higher Au concentrations (**7MQ** and **8MQ**) and shorter annealing times. The long annealing time has caused the noticeable partial crystallisation that is characteristic of lithium glasses. In the samples prepared by ADL technology, the annealing had a rather negative effect. For the samples without SnO_2 addition, the red colouration did not appear (the samples had rather a bluish tint, see sample **7ADL**) and for the samples containing SnO_2, the red colouration changed to a brown opaque colour after annealing.

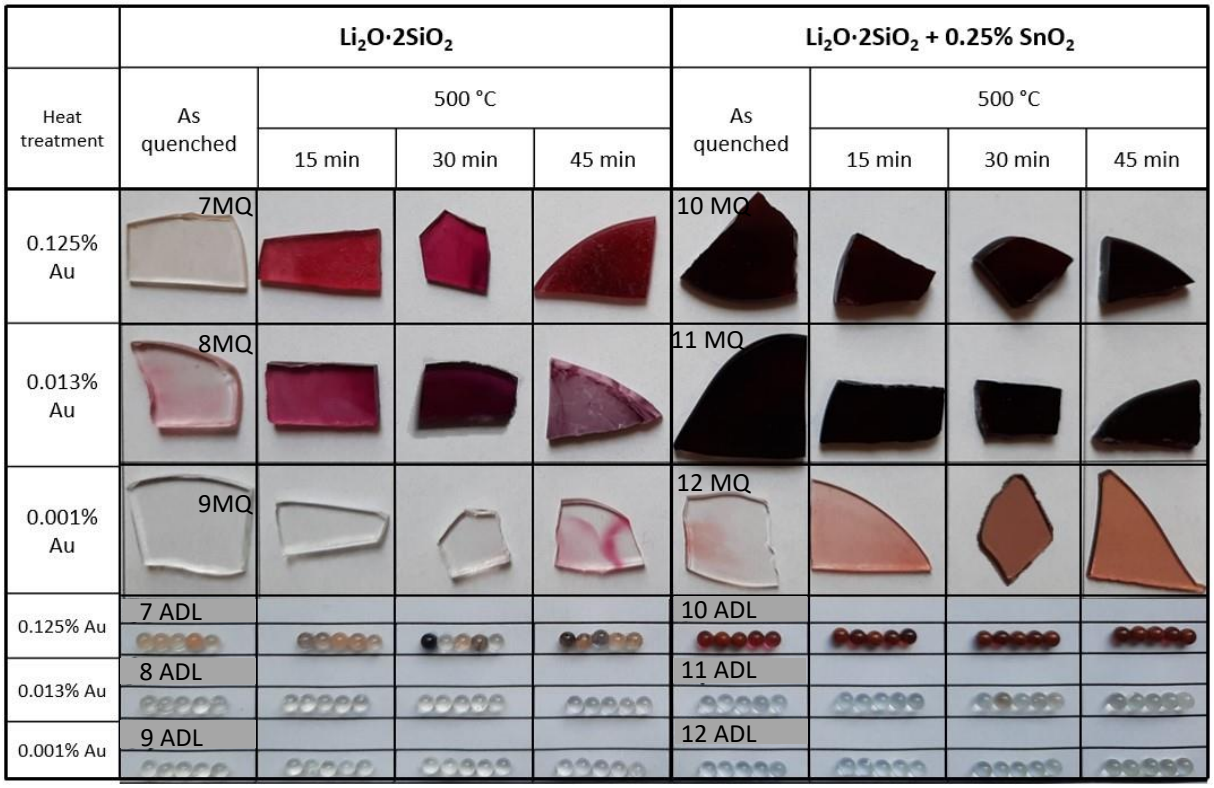

Figure 48 *Photographs of LS glass samples prepared by MQ and ADL with different concentration of Au and SnO_2*

Similar to the YAS samples, the chemical composition of the lithium silicate samples was measured by XRF. However, in this case the amount of Li_2O was always inserted into the calculations according to the batch, since the XRF method used cannot determine Li. The results of XRF analyses are shown in **Table 18**.

In this case, only tin and gold loss could be observed by XRF, the amount of SiO_2 corresponds to the batch. If we examine the Au loss, it is clear that the MQ technology results in less gold volatilisation than the ADL technology. In samples with lower gold concentrations, the determination was often already below the detection limit of the instrument. The results of the **9MQ** and **12MQ** samples show more Au than was added to the samples. This is due to the huge relative measurement error (± 50%) at such a low concentration of the analyte. SnO_2 in the samples remained only approximately 47% when using MQ and only 33% when using ADL (only 16% in the case of sample **11ADL**).

Table 18 *Results of XRF analysis of chemical composition of LS samples prepared by ADL and MQ techniques. Li amount given by weight. The results are given in weight %. The columns marked % show the percentage difference from the original weighted amount (+ is the excess over the weighted amount, - is the decrease from the original weighted amount). A * indicates that the amount determined was below the detection limit of analysis (<50 ppm).*

Sample no.	Sample code	Li_2O	%	SiO_2	%	Au	%	SnO_2	%
7MQ	*Au:L33-S67*	19.82	0	79.06	-1	0.035	-93		
8MQ	*Au: L33-S67*	19.90	0	79.51	-1	0.016	-67		
9MQ	*Au: L33-S67*	19.91	0	79.52	-1	0.006	+20		
10MQ	*Au,Sn: L33-S67*	19.67	0	78.97	+0	0.039	-92	0.354	-52
11MQ	*Au,Sn: L33-S67*	19.76	0	79.05	-1	0.016	-68	0.356	-52
12MQ	*Au,Sn: L33-S67*	19.76	0	79.12	+0	0.006	+27	0.345	-54
7ADL	*Au:L33-S67*	19.82	0	79.39	+0	0.146	-71		
8ADL	*Au: L33-S67*	19.90	0	79.37	-1	0.000	-100		
9ADL	*Au: L33-S67*	19.91	0	79.03	-1	0.000	-100		
10ADL	*Au,Sn: L33-S67*	19.67	0	79.14	+0	0.074	-85	0.247	-67
11ADL	*Au,Sn: L33-S67*	19.76	0	79.40	+0	0.000	-100	0.117	-84
12ADL	*Au,Sn: L33-S67*	19.76	0	79.35	+0	0.000	-100	0.242	-68

Scanning and transmission electron microscopy was used to observe the shape and distribution of gold nanoparticles on selected samples. First, the scanning electron microscopy results are presented in **Figure 49** for the samples containing the highest used Au concentration (**7MQ** and **10MQ**). The results of the image analysis are shown in **Table 19**. In the mentioned unannealed samples, spherical particles with a diameter of about 1.5 μm were observed (see **Figure 49 a), b)**). In samples with lower gold concentration, particles with smaller diameter (sample **11MQ** - AuNPs size 1.2 μm) or none (sample **12MQ**) were observed. After subsequent annealing, large spherical Au particles were observed in all samples except for sample **11MQ** (particles were probably not found due to their sparse distribution). Their size appeared larger than before annealing. For example, for the annealed samples containing the highest concentration of Au and tin addition (**10MQ**), spherical Au particles with a diameter of greater than 3 μm were observed (see **Figure 49 c**), in samples with lower gold concentration particles with a diameter of 2 μm appeared). In the images, we were able to capture the probable formation of large lost particles that arise from clusters of approximately 500 nm made up of several smaller Au nanoparticles (see **Figure 49 d**). Similar clusters were also observed on sample with the lowest used gold concentration that was annealed for 30 min (**12MQ**). Samples prepared by ADL have not been studied by SEM.

Table 19 *Results of image analysis of SEM images for Au:LS system of samples prepared by MQ.*

Sample no.	Sample code	Heating	Particles visible in SEM	SEM particle shape	SEM particles counted	SEM avg size [nm]
7MQ	*Au: L33-S67*		yes	spherical	22	1779
7MQ	*Au: L33-S67*	500°C 30min	yes	spherical	7	2529
8MQ	*Au: L33-S67*	500°C 30min	yes	spherical	2	982
10MQ	*Au,Sn: L33-S67*		yes	spherical	8	1536
10MQ	*Au,Sn: L33-S67*	500°C 30min	yes	spherical	3	2032
11MQ	*Au,Sn: L33-S67*		yes	spherical	1	1286
11MQ	*Au,Sn: L33-S67*	500°C 30min	no	-	0	-
12MQ	*Au,Sn: L33-S67*	500°C 30min	yes	deformed polygons	17	148

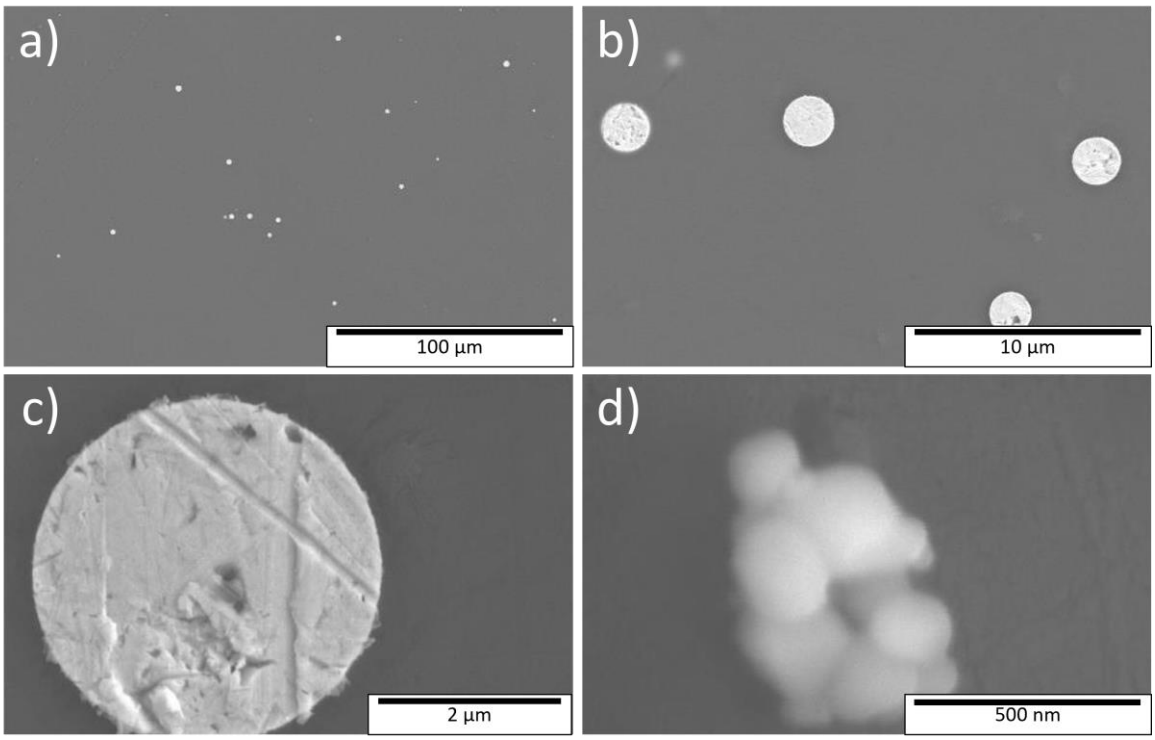

Figure 49 *SEM images of Au particles in LS glasses (a) spherical Au particles in sample 7 MQ unannealed, (b) detail of spherical Au particles in sample 7 MQ unannealed, (c) detail of spherical Au particle in sample 10MQ annealed 30 min., (d) cluster of Au nanoparticles captured in sample 10MQ annealed 30 min.*

TEM images were taken for all samples prepared by both MQ and ADL. The samples prepared in the furnace will be described first. Powder TEM samples were prepared both for samples

with increasing gold concentration with or without tin addition (**7MQ -12MQ**), and also for a sample annealed at 500 °C for 30 min each time. The samples are shown in **Figure 48**. The results of the analysis are summarized in **Table 20**, and selected images with different shapes of the nanoparticles found are shown in **Figure 50**.

Table 20 *Results of image analysis of TEM patterns for Au:LS system of samples prepared by MQ and ADL technology.*

Sample no.	Sample code	Heating	Au confirmed by EDS	NP shape	TEM particles counted	avg size [nm]
7MQ	*Au:L33-S67*	-	no	-	0	0
7MQ	*Au:L33-S67*	500°C 30min	yes	almost spherical	15	6
8MQ	*Au: L33-S67*	-	yes	triangles, vermicular	10	15
8MQ	*Au: L33-S67*	500°C 30min	yes	deformed triangles	4	6
9MQ	*Au: L33-S67*	-	no	-	0	0
9MQ	*Au: L33-S67*	500°C 30min	yes	almost spherical, triangles, vermicular	24	13
10MQ	*Au,Sn: L33-S67*	-	yes	deformed polygons, ovals, triangles	31	12
10MQ	*Au,Sn: L33-S67*	500°C 30min	yes	almost spherical, deformed polygons	15	6
11MQ	*Au,Sn: L33-S67*	-	yes	almost spherical, triangles, vermicular	13	13
11MQ	*Au,Sn: L33-S67*	500°C 30min	yes	deformed polygons, almost spherical	57	6
12MQ	*Au,Sn: L33-S67*	-	no	-	0	0
12MQ	*Au,Sn: L33-S67*	500°C 30min	yes	deformed polygons, vermicular	5	22
7ADL	*Au:L33-S67*	-	no	spherical	24	5
7ADL	*Au:L33-S67*	500°C 30min	no	spherical	60	3
10ADL	*Au,Sn: L33-S67*	-	yes	spherical	5	40

From **Table 20** it is obvious that it was easier to find AuNPs by TEM in samples with higher Au concentration. Compared to the YAS system, the observed nanoparticles showed a greater variability of shapes - often non-spherical and triangle-shaped NPs were found. The presence of SnO_2 also has a significant effect on the number of AuNPs found. In samples without SnO_2 (**7-9 MQ**) and without further annealing, fewer AuNPs were formed and had a more anisometric shape than in samples containing SnO_2 (**10-12MQ**). After annealing, the observed AuNPs had a more symmetric shape. An apparent decrease in nanoparticle size was also evident after annealing. This can be explained by recrystallization and a change in shape from the general

shape of a polyhedron to a sphere. Selected images from the TEM can be found in the **Figure 50** below. The first row presents an example of different shapes of Au nanoparticles found and the second row presents the effect of subsequent annealing on the shape of the particles.

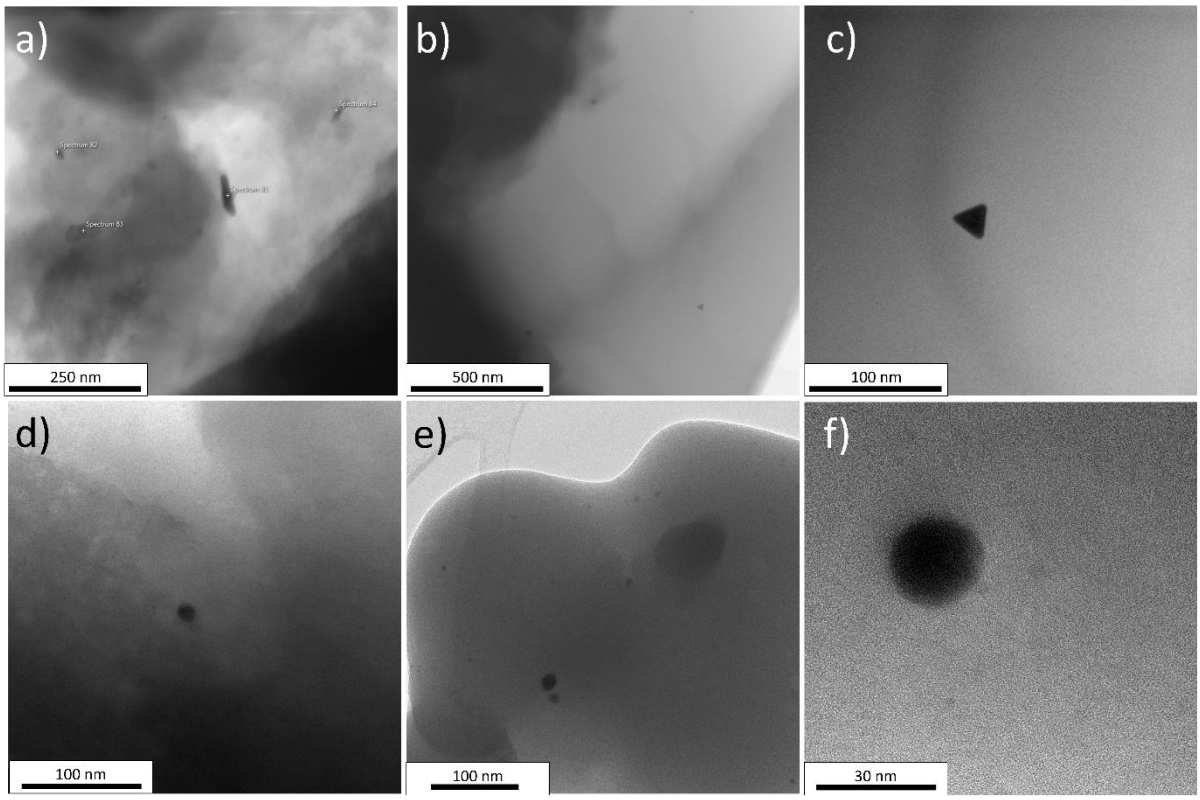

Figure 50 *Selected representative AuNPs from TEM images: a) anisometric vermicular AuNPs - sample 2MQ unannealed (b) triangular AuNPs - sample 10MQ unannealed, (c) triangular AuNPs, closer look - sample 10MQ unannealed, d) spherical AuNP - sample 7MQ, annealed 30 min (e) the influence of annealing – spherical nanoparticles – sample 10MQ annealed 30min. (f) spherical AuNP, closer look – sample 10MQ annealed 30 min.*

Figure 51 shows the HRTEM analysis of the sample containing the highest concentration of Au and no Sn (**7MQ**). The distribution of nanoparticles in the sample was calculated and also the nanoparticle in image a) was focused on and the interfacial distance was determined. This corresponded to the cubic *fcc* Au structure. The spherical shape of the nanoparticle caused by annealing of the sample is evident in the image.

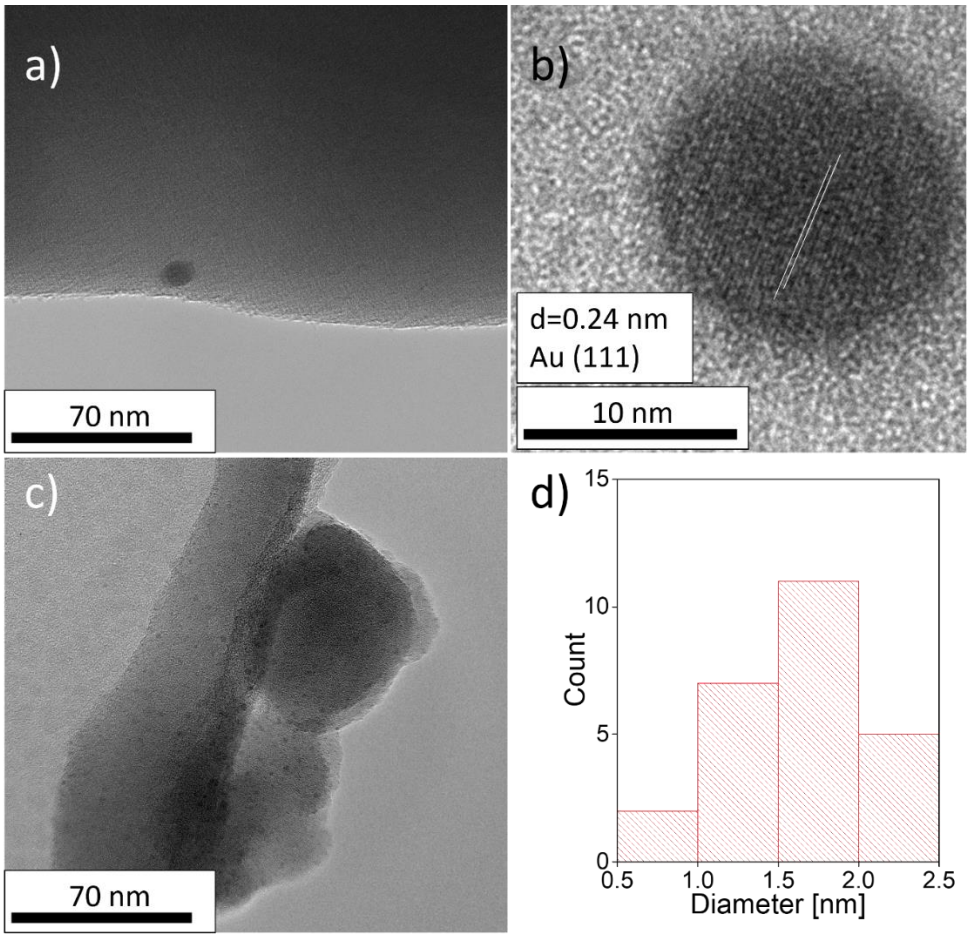

Figure 51 *TEM images of sample 7MQ after annealing at 500°C for 30 min: a) spherical AuNPs, b) detail of AuNPs, HRTEM, c) image with a large number of small AuNPs, d) particle size distribution from image c.*

Figure 52 shows the difficulty of evaluating the particle distribution from TEM images. In most of the images, the AuNPs are very sparsely distributed and are about 1 micron or more apart, which makes it practically impossible to plot the size distribution of the AuNPs. However, when a site with an increased abundance of AuNPs in the glass (inhomogeneity) is captured, the size distributions of the AuNPs have been plotted (**Figure 52 b,c**). These images also show that the diameter of small AuNPs in the glass decreased from the original 5 nm to 3 nm after annealing. Another observation in **Figure 52c** is the phase separation in the glass matrix, which is manifested by lighter and darker areas.

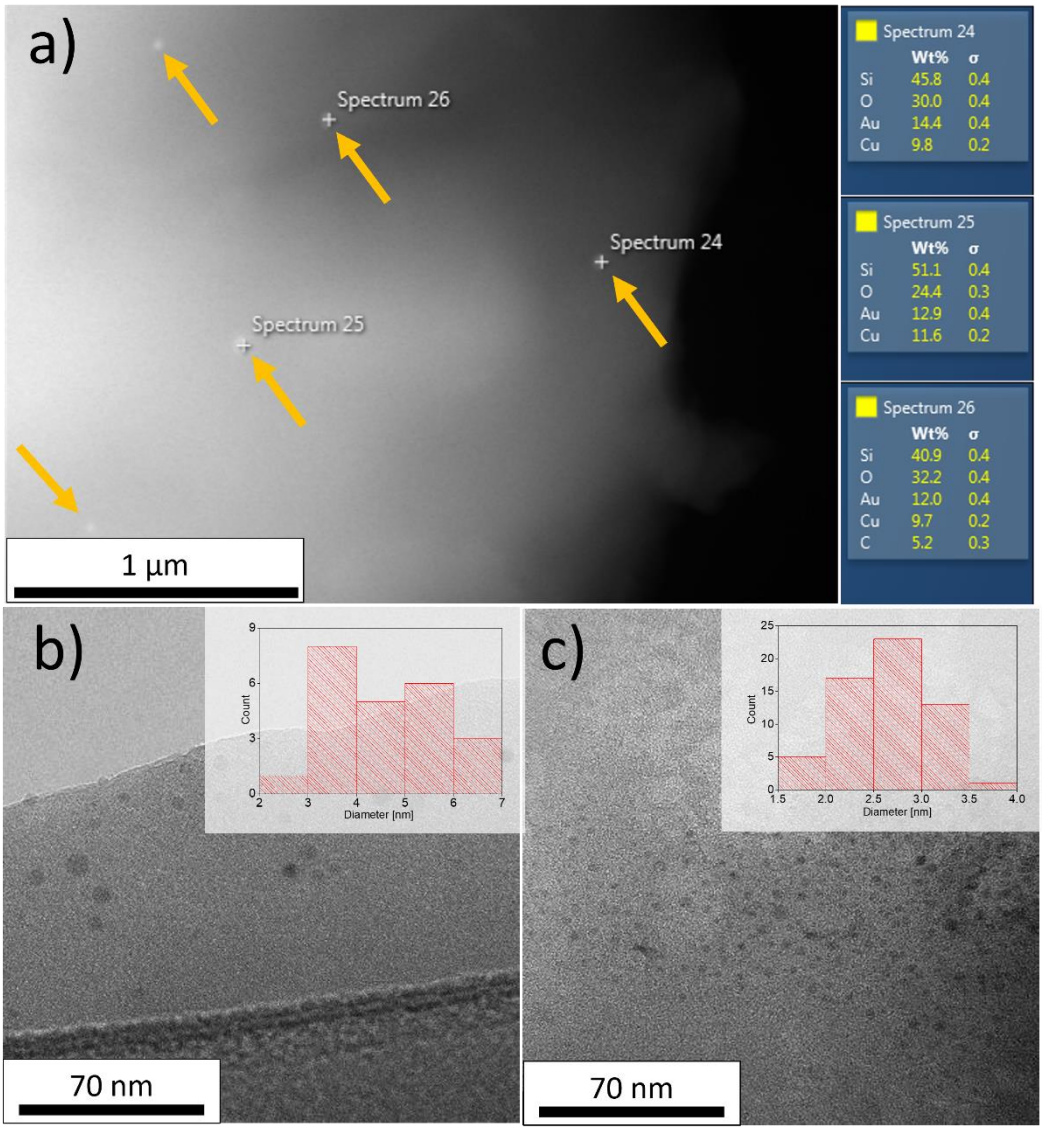

Figure 52 *TEM: a) sample 10 ADL, AuNPs highlighted with red arrows (HAADF contrast, AuNPs are the brightest points), EDS analysis b) sample 7 ADL, AuNPs with particle size distribution, BF contrast (AuNPs dark), sample 7 ADL after additional heat treatment at 500°C for 30 min, AuNPs with particle size distribution, BF contrast (AuNPs are dark).*

Due to the different colour of the prepared samples, the absorption spectra were also expected to be different. All polished samples prepared by MQ were measured by absorption spectroscopy. The change in absorbance spectra and influence of additional heat treatment on its position of the shape is shown in **Figure 53**. Samples prepared by ADL could not be analysed by spectrophotometer due to their heterogeneity.

From the results of the absorption spectra, it is as expected that a high concentration of Au or Au and Sn causes an absorption band with a maximum in the 530-560 nm range (samples **7-11MQ**). Due to annealing, the maximum of the band shifts to higher wavelengths and its intensity increases. For samples annealed for 45 min, crystallization was observed for high Au concentrations, which resulted in significant noise in the measurement. The formation of this band corresponds to the red coloration of the glass. Its intensity then follows the intensity of the colour, which is already very dark for long annealed samples. If the concentration of gold is reduced, this results in a significant reduction in the intensity of the described band, which for very low concentrations corresponds to the inhomogeneity of the red colour. The addition of tin is reflected in the absorption spectra by a very significant increase in the intensity of the band, the maximum of which does not show any significant shift in wavelength even due to subsequent annealing. The maximum is always close to 547 nm. The glasses with this band are dark red (samples **10** and **11MQ**). Significantly different after annealing was the sample with the lowest concentration of Au containing SnO_2 (**12MQ**), which was light brown and had an absorption peak maximum around 515 nm.

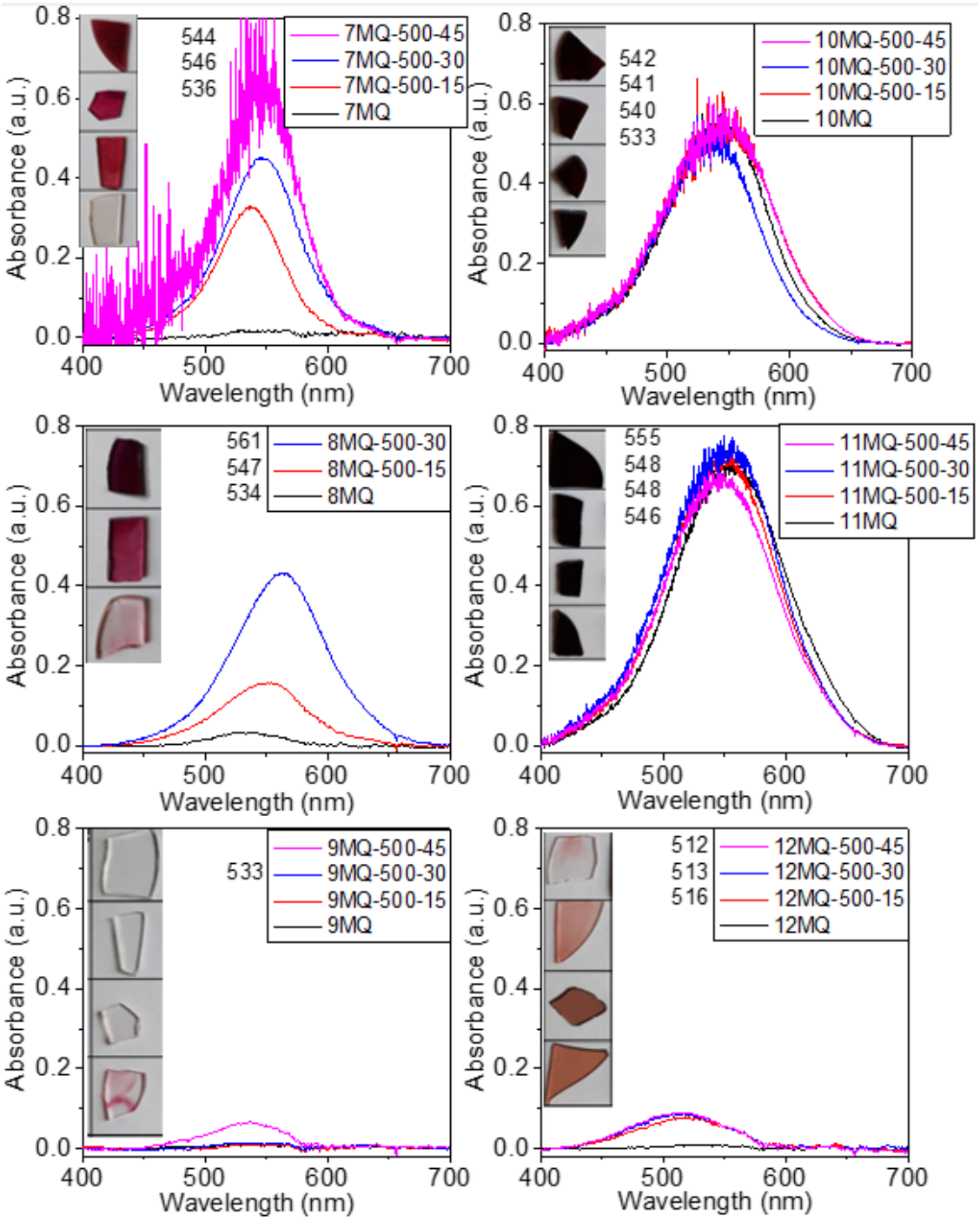

Figure 53 *Change of absorbance of LS glasses with Au and SnO_2 after additional heat treatment.*

5.3.4 Summary and discussion

From the results of this chapter, the following conclusions are drawn:

1) ADL technology can be used to prepare metallic gold particles in glass, which have dimensions of μm or nm. The common *fcc* structure of metallic gold was demonstrated for these nanoparticles. The selected conditions of the technology, as well as the subsequent annealing, can then influence their number, shape, distribution and thus the colour of the glass.
2) It has been shown that during the ADL process, gold volatilizes from the glass matrix. Its volatilisation depends on the selected conditions of the technology, and it is confirmed that the higher the temperature and preparation time, the lower the Au concentration. Comparing both used technologies, we observed greater Au loss with ADL technology than with MQ technology.
3) It is difficult to control the reproducibility of prepared samples that would show the same colour. In our work, we have already succeeded in preparing reproducibly homogeneous samples of the same size due to the new design of the pellet preparation technology and the strict control of the ADL parameters. However, a uniform colour sample could not be reproducibly prepared. An example of the best sample set so far is shown in **Figure 54**. The preparation of colourless samples whose colour can be controlled later by subsequent annealing seems to be more suitable.

Figure 54 *An example of the best homogeneity of prepared samples (10ADL).*

4) The addition of tin has been shown to significantly promote the formation of AuNPs in both technologies used. Tin shows a lower loss percentage during glass melting than gold.

5) Nanoparticle formation was strongly influenced by the composition of the glass matrix. An important factor was the addition of ions reducing the degree of glass matrix polymerization and promoting the formation of NBOs, which likely leads to the nucleation of gold nanoparticles. Due to the lower viscosity associated with the lower degree of polymerization, gold nanoparticles were formed more easily in the LS system than in the YAS system. In addition, large spherical nanoparticles, which are μm-sized and do not affect glass colour, have been observed much more frequently in YAS system. The LS samples achieved much more attractive colours due to presence of gold nanoparticles of nanometre dimensions.
6) Large spherical gold particles, a few 1-10 μm in diameter, were observed in both types of glass systems, but were distributed too sparsely for statistical image analysis. The formation of these particles was not much affected by the composition of the glass and was not related to the colour of the samples. Using ADL technology, these large particles were very heterogeneously distributed and formed 'chain-like' clusters.
7) The formation of Au nanoparticles with nanometre dimensions and different shapes (anisometric vermicular, triangular, spherical) was detected in both glass systems using TEM. In the YAS glass system, the irregular shapes corresponded to the appearance of brown or brownish-red coloration of the samples. Furthermore, the colour of these glass samples could not be easily affected by subsequent annealing. In the LS system, the irregular shapes corresponded to a red colouration of the glass.
8) Subsequent annealing of the glass with irregular nanoparticles shape caused the shape to change to spherical in both LS and YAS systems.

If we focus on the technologies that are used for the preparation of AuNPs in glass, it is clear that MQ is the most widely used and industrial technology, which is also associated with glass colour. Bulk doped glass samples are prepared by this technology. Gold nanoparticles in thin layers are probably the most prepared by sol-gel technique [124,125] or also by ion implantation technology [122]. In these cases, however, their preparation is mostly associated with their bioactivity, catalytic reactions, surface plasmon resonance or nonlinear optical phenomena or other effects. No record was found of the use of ADL technology in the preparation of glass samples containing AuNPs.

If we compare the shape, amount, size and distribution of AuNPs prepared by different technologies from the current literature, it seems that mostly spherical gold nanoparticles were prepared, their amount and distribution is related to the selected sample preparation conditions. For sol-gel, the concentration of nanoparticles in the gel is crucial and can be controlled very well. For ion implantation, it is primarily the fluence that determines the number of NPs formed and it is the energy of the ion beam that is critical for the distribution and especially the depth at which the NPs are implanted below the surface. Few images of AuNPs in systematically varying thin layers were taken by TEM.

If we focus on the chemical composition of the glass matrices in which the Au NPs were prepared, mainly studied compositions are borate [109–118], silicate [119–126,162,163] and also chalcogenide [101,105,127] glasses based on the findings of recent literature. High contents boron and chalcogenide glasses have inferior mechanical and chemical properties compared to silicate glasses and are difficult to use in practice. The procedure for preparing glass samples (especially borate and chalcogenide) by other authors differs by melting the glass at a lower temperature and for a shorter time. For example, high-boron glasses are melted at 850-1200°C, 10-60 min [109–118]. In the literature, information on the actual Au content in the sample after melting is practically never reported and the issue of Au volatilization is not discussed. This is probably due to the very low gold concentration, which is usually below the detection limit of analytical methods. The addition of uniform gold nanoparticles of defined size to the glass has also been tried in these low-melting systems (glass has a lower melting point than gold), but the nanoparticles dissolved and reassembled [112,113]. TEM images of AuNPs in glass are published very sparsely and the nanoparticles are mostly spherical in shape. Only in the Bi_2O_3-B_2O_3 system an irregular shape was found [112].The average particle size ranges from 10 to 100 nm - most commonly around 10 nm or 40 nm. However, some nanoparticles are not clear in the images and they are very densely distributed, mostly lacking XRD or EDS analysis, so it is questionable whether actually only gold NPs are presented and not a separation of other glass phases as well (e.g. [113,118]).

Much more often, technological conditions are associated with optical absorption in the VIS region corresponding to the red colour. The typical colour of glasses containing AuNPs is in some cases achieved immediately after quenching of the glass, in other cases only after

subsequent thermal annealing [102,103]. If additional heat treatment is used, the temperature used is in the vicinity of the T_g of the glass matrix [103]. From these publications it is clear that the formation of nanoparticles their shape, distribution the coloration of the samples is closely related to their thermal history.

In our case, it is possible to compare the two glasses, i.e. the YAS and LS glasses, because the temperature of the beads was recorded during the ADL melting and cooling (for the MQ technology such a comparison is not possible). The mentioned records are shown on two samples of the same mass as shown in **Figure 55**. If we average the cooling rate for the five YAS and five LS samples, we get values of 135 °C s^{-1} and 226 °C s^{-1} for YAS and LS, respectively. From these values, it is clear that the cooling of lithium glass is faster.

It is not entirely clear why the red colour is easier to develop and control in the LS system than in the YAS system. According to Weyl [102], the key parameter is the temperature dependence of gold solubility in a given glass, but this is difficult to quantify. We believe that this fact may also be related to the density of the glass network and hence the mobility of Au particles within it. Despite the fact that with ADL technology, controlled cooling of the samples directly after melting is easier compared to MQ, and therefore coloured samples can be obtained directly without additional heat treatment, in order to achieve uniform coloration in a controlled manner, it is preferable to start with transparent glass after ADL or MQ and obtain the desired colour by a secondary heat treatment of the samples. Finally, it can be noted that only a small number of authors show the appearance of samples and discuss their homogeneity and reproducibility.

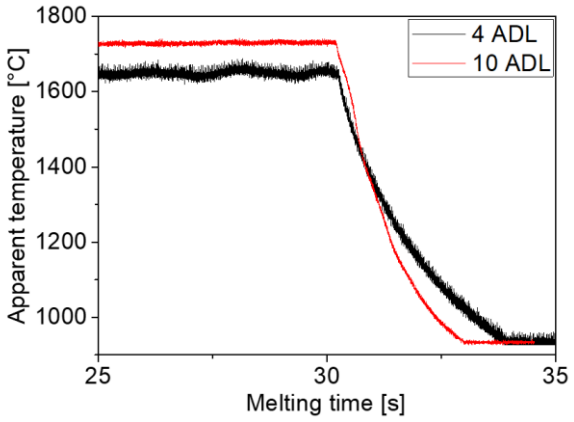

Figure 55 *Comparison of cooling rate of YAS (4ADL) and LS (10ADL) glass samples.*

5.4 Design of a new glass composition (system Li_2O-Y_2O_3-Al_2O_3-SiO_2) suitable for the preparation of Au nanoparticles using ADL

From the previous results, it is clear that the preparation of gold nanoparticles was easier and more controllable in the LS system. Therefore, in the following part, several glass compositions were proposed in the Li_2O-Y_2O_3-Al_2O_3-SiO_2 (LYAS) system. The main intention of this substitution was to benefit from the advantageous optical properties of YAS glass but reduce its viscosity and thus facilitate its preparation. Another idea behind this replacement was to combine the two previously prepared glass matrices and to take advantage of the observation that the amounts of Au and SnO_2 used in the LS matrix colour the glass too much, whereas in the YAS matrix, at lower concentrations, they hardly colour the glass at all.

The compositions were derived from already prepared samples in the YAS system by replacing 10 mol% of one of the oxides, i.e. Y_2O_3, Al_2O_3 or SiO_2, with 10 mol% of Li_2O.

5.4.1 Preparation of nanoparticles in systematically selected glass compositions

In this part, only the SnO_2-containing glasses were prepared because they showed better colouration in previous experiments. Again, the same three concentrations of Au as in the previous chapter were used for MQ technology. The set of glass samples with the lowest gold concentration was not prepared using the ADL technique. Based on the DSC analyses (not shown) and heating experiments of small glass shards, the annealing conditions for the glasses with Y_2O_3 and SiO_2 substitution were chosen as 825 °C 60 min, 850 °C 60 min and 850 °C 20h. For glasses with Al_2O_3 substitution, the annealing conditions chosen were 775 °C 60 min, 800 °C 60 min and 825 °C 60 min. A summary of the prepared samples is shown in the **Table 21** below. In **Figure 56** the appearance of the samples and their colouration can be seen.

Table 21 *A summary of the nominal compositions (mol%) of the prepared Au:LYAS glasses using ADL and MQ technique. The sample code column summarizes chemical composition of the glass batch in mol.%, rounded mathematically.*

Sample no.	Sample code	Li_2O	Y_2O_3	Al_2O_3	SiO_2	Au	SnO_2	Technology
1	*Au,Sn:L10-Y3-A19-S68*	10.00	2.52	19.21	68.17	0.127	0.250	MQ, ADL
2	*Au,Sn:L10-Y3-A19-S68*	10.00	2.52	19.21	68.17	0.013	0.250	MQ, ADL
3	*Au,Sn:L10-Y3-A19-S68*	10.00	2.52	19.21	68.17	0.001	0.250	MQ
4	*Au,Sn:L10-Y13-A19-S58*	10.00	12.62	19.21	58.17	0.127	0.250	MQ, ADL
5	*Au,Sn:L10-Y13-A19-S58*	10.00	12.62	19.21	58.17	0.013	0.250	MQ, ADL
6	*Au,Sn:L10-Y13-A19-S58*	10.00	12.62	19.21	58.17	0.001	0.250	MQ
7	*Au,Sn:L10-Y13-A9-S68*	10.00	12.62	9.21	68.17	0.127	0.250	MQ, ADL
8	*Au,Sn:L10-Y13-A9-S68*	10.00	12.62	9.21	68.17	0.013	0.250	MQ, ADL
9	*Au,Sn:L10-Y13-A9-S68*	10.00	12.62	9.21	68.17	0.001	0.250	MQ

a)

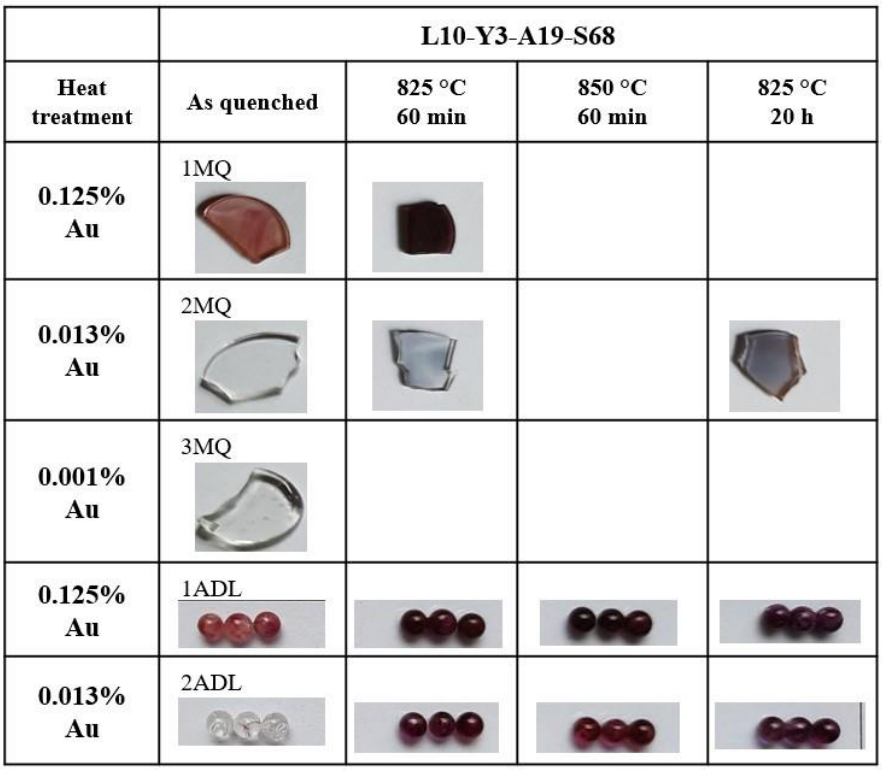

Figure 56 *Images of LYAS glasses prepared by MQ and ADL with different concentration of Au and SnO_2 (a) samples with Y→Li substitution, (b) samples with Si→Li substitution, (c) samples with Al→Li substitution.*

b)

Heat treatment	L10-Y13-A19-S58			
	As quenched	825 °C 60 min	850 °C 60 min	825 °C 20 h
0.125% Au	4MQ 	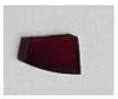		
0.013% Au	5MQ 			
0.001% Au	6MQ 			
0.125% Au	4ADL 			
0.013% Au	5ADL 			

c)

Heat treatment	L10-Y13-A9-S68			
	As quenched	775 °C 60 min	800 °C 60 min	825 °C 60 min
0.125% Au	7MQ 	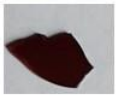	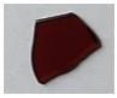	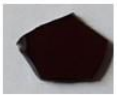
0.013% Au	8MQ 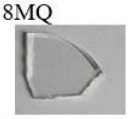	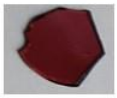		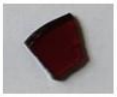
0.001% Au	9MQ 	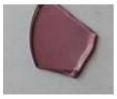		
0.125% Au	7ADL 			
0.013% Au	8ADL 			

Figure 54 - continuation *Images of LYAS glasses prepared by MQ and ADL with different concentration of Au and SnO_2 (a) samples with Y→Li substitution, (b) samples with Si→Li substitution, (c) samples with Al→Li substitution.*

When evaluating the properties of the samples with respect to the different substitutions used, it was found that in the case of the Y→Li substitution, the variability of the glass colour was low and red colour could be prepared by ADL technique. Moreover, the melt had the highest viscosity at the melting temperature used compared to the other substituted glasses. If we focus on the appearance of the prepared samples, glasses with high Au concentrations were brown in colour immediately after the MQ technique and turned darker by subsequent annealing (see **Figure 56a - 1MQ**). Glasses with lower Au concentrations were clear after preparation and turned only very slightly blue-grey by annealing (**2** and **3MQ**). When the ADL technique was used, the high Au concentration glasses behaved similarly to the furnace-prepared glasses. If a lower concentration of gold was used, the glasses were clear after melting (but often contained bubbles) and subsequent annealing caused them to turn red at first and turn purple later (using a higher annealing temperature) (see **Figure 56a - 2ADL**).

In the case of Si→Li substitution (see **Figure 56b**), the glass generally melted much more easily – its viscosity at melting temperature was lower, it was easier to mix and cast. When prepared by the MQ technology, a ruby coloration appeared much more readily after annealing and did not change its hue towards brown shades, even after a relatively long annealing time. Using the ADL technique, however, it appears that the highest gold concentration chosen caused the samples to darken rapidly after the subsequent annealing (sample **4ADL**), whereas the lower gold concentration did not cause any colour change and the glasses were still clear after annealing (sample **5ADL**).

The most diverse colour changes were observed in the Al→Li substitution (see **Figure 56c**), where samples of brown, red, purple and blue colour shades were prepared. The glasses melted very easily compared to the Y→Li substitution. After preparation by the MQ technique, the glass was mostly clear; subsequent annealing produced red to very dark red hues (see samples **7-9MQ**). At the lowest concentration of gold, while using the highest annealing temperature, a blue colour appeared in the glass. When the samples were prepared using ADL technology, the highest gold concentration was too high to produce a ruby red colour and the glass tended to turn brown. When lower gold concentrations were used, the samples were initially clear and after annealing had a purple or blue colour depending on the annealing temperature chosen (see sample **8ADL**).

XRF analysis was performed on MQ samples only, as not enough samples were prepared by ADL technology. Li_2O was again included in the analyses based on the glass batch. The results of the XRF analysis are summarized in **Table 22**. There were no significant differences between samples with different substitutions. For Y_2O_3, Al_2O_3 and SiO_2 oxides we observe the same trend as in the YAS system (see **Section 5.3.2**, **Table 14**). There is a few wt% less SiO_2 according to the analysis, which is reflected by the increased relative amount of Al_2O_3 and Y_2O_3. These results confirm the stability of the glass composition in both preparation methods. SnO_2 was determined to be 26-45 wt% of the original amount in the samples. The amount of remaining Au could only be measured in samples 1MQ, 4MQ and 7MQ with the highest Au concentration, only 24, 18 and 8 wt% of the original amount remained in the samples, respectively. The remaining samples therefore contain less than 50 ppm Au (XRF detection limit). Even so, most of the samples have a characteristic colour after annealing that confirms presence of AuNPs.

Table 22 *Analysis of the chemical composition of LYAS samples prepared by MQ technology using XRF method (Li amount given by glass batch). The results are given in wt. %. The columns marked '%' indicate the percentage deviation from the weighed amount ('+' is an excess, '-' is a loss compared to the original amount). If an '*' is in the column, the quantity determined was below the detection limit of the analysis.*

Sample no.	Sample code	Y_2O_3	%	Al_2O_3	%	SiO_2	%	Au	%	SnO_2	%
1MQ	*Au,Sn:L10-Y3-A19-S68*	9.32	+14	30.04	+7	55.71	-5	0.087	-76	0.189	-65
2MQ	*Au,Sn:L10-Y3-A19-S68*	9.34	+14	31.10	+11	54.64	-7	*	-100	0.143	-74
3MQ	*Au,Sn:L10-Y3-A19-S68*	9.20	+12	31.27	+11	54.59	-7	*	-100	0.233	-57
4MQ	*Au,Sn:L10-Y13-A19-S58*	35.14	+7	23.04	+2	37.57	-7	0.052	-82	0.196	-55
5MQ	*Au,Sn:L10-Y13-A19-S58*	37.59	+14	24.71	+9	33.49	-17	*	-100	0.194	-56
6MQ	*Au,Sn:L10-Y13-A19-S58*	37.52	+14	24.83	+10	33.53	-17	*	-100	0.191	-56
7MQ	*Au,Sn:L10-Y13-A9-S68*	37.84	+9	12.41	+9	45.46	-8	0.024	-92	0.16	-65
8MQ	*Au,Sn:L10-Y13-A9-S68*	37.97	+10	12.34	+8	45.52	-9	*	-100	0.184	-60
9MQ	*Au,Sn:L10-Y13-A9-S68*	38.04	+10	12.35	+8	45.57	-9	*	-100	0.146	-68

SEM image analysis was performed on samples prepared by MQ technique on a set of samples annealed at 825 °C for 60 min. The results are summarized in **Table 23**. SEM images were taken on two different instruments on selected samples. The first part of selected samples was analysed using a Hitachi S4700 microscope at UCT Prague. The second set of samples was analysed using the IT800SHL JEOL SEM with higher resolution at CNRS Orléans. The instrument used is indicated in the last column of the table. Selected electron microscope images are shown in **Figure 57**.

Table 23 *Results of image analysis of SEM images for Au:Sn:LYAS samples prepared by MQ*

Sample no.	Sample code	Heating	Particles visible in SEM	SEM particle shape	SEM particles counted	SEM avg size [nm]	SEM
1MQ	*Au,Sn:L10-Y3-A19-S68*	825°C 60min	yes	spherical, almost spherical	>100	68	JEOL
2MQ	*Au,Sn:L10-Y3-A19-S68*	825°C 60min	yes	spherical	7	219	JEOL
3MQ	*Au,Sn:L10-Y3-A19-S68*	825°C 60min	no	-	-	-	JEOL
4MQ	*Au,Sn:L10-Y13-A19-S58*	850°C 60min	yes	spherical	6	1764	Hitachi
4MQ	*Au,Sn:L10-Y13-A19-S58*	825°C 60min	yes	spherical, almost spherical	>20	109	JEOL
5MQ	*Au,Sn:L10-Y13-A19-S58*	825°C 60min	yes - only nano	spherical	18	31	JEOL
6MQ	*Au,Sn:L10-Y13-A19-S58*	825°C 60min	no	-	-	-	JEOL
7MQ	*Au,Sn:L10-Y13-A9-S68*	775°C 60min	yes	spherical	3	2295	Hitachi
7MQ	*Au,Sn:L10-Y13-A9-S68*	825°C 60min	yes	spherical	1	1970	Hitachi
7MQ	*Au,Sn:L10-Y13-A9-S68*	825°C 60min	yes	spherical	20	3885	JEOL
8MQ	*Au,Sn:L10-Y13-A9-S68*	825°C 60min	no	-	-	-	Hitachi
8MQ	*Au,Sn:L10-Y13-A9-S68*	825°C 60min	yes	spherical	2	cannot be measured	JEOL
9MQ	*Au,Sn:L10-Y13-A9-S68*	825°C 60min	no	-	-	-	Hitachi
9MQ	*Au,Sn:L10-Y13-A9-S68*	825°C 60min	yes - only nano	almost spherical	10	23	JEOL

Table 23 above summarises the results of the analysis of the SEM images. Selected images are shown in **Figure 57**. Using a Hitachi microscope with low resolution, Au particles of 2-3 μm were found only in the samples with the highest Au concentration (**4** and **7MQ**, annealed). A complete set of samples **1-9MQ** was observed using the microscope with better resolution at CNRS Orléans after annealing at 825 °C for 60 min. Using this microscope, micro- and nanoparticles of Au were observed in all samples except **3MQ** and **6MQ**, which contained the lowest concentration of Au.

In general, it was not easy to capture multiple nanoparticles in a single image even at low magnifications. It was easiest to find gold particles in the samples with the highest gold content when observing with the electron microscope. The particles were found in larger numbers and their size was also larger. The shape of the observed particles was spherical or approximately spherical. The largest Au particles, with a diameter of 3.9 μm (**Figure 57a**), were found in sample with where the Al→Li substitution (**7MQ**) was used. On the other hand, the smallest observed AuNPs, with an average diameter of 23±8 nm, were observed in sample with the lowest Au content and Al→Li substitution (**9MQ**). Generally, there is no apparent difference in the size or number of Au particles related to the Y/Si/Al →Li substitution performed.

An important observed difference was the creation of nanoscale phase separation in the samples with Al→Li substitution (see **Figure 57d**). At first glance, these samples show similar phase separation to the samples in the YAS system (see **Chapter 4.2.**). However, due to the nano-scale nature of this separation, these samples appear transparent.

TEM images were acquired from powder samples. Samples prepared by MQ technique containing medium and highest gold concentrations (labelled **1MQ**, **2MQ**, **4MQ**, **5MQ** and **7MQ** and **8MQ**) annealed at 825°C for 60 min were analysed. Of the samples with low gold concentration, only sample **9MQ** annealed under the same conditions was analysed. The resulting description of the shape, count and average size of nanoparticles in each sample is summarized in **Table 24**. Selected images can be found in **Figure 58**. Samples prepared by ADL were not analysed.

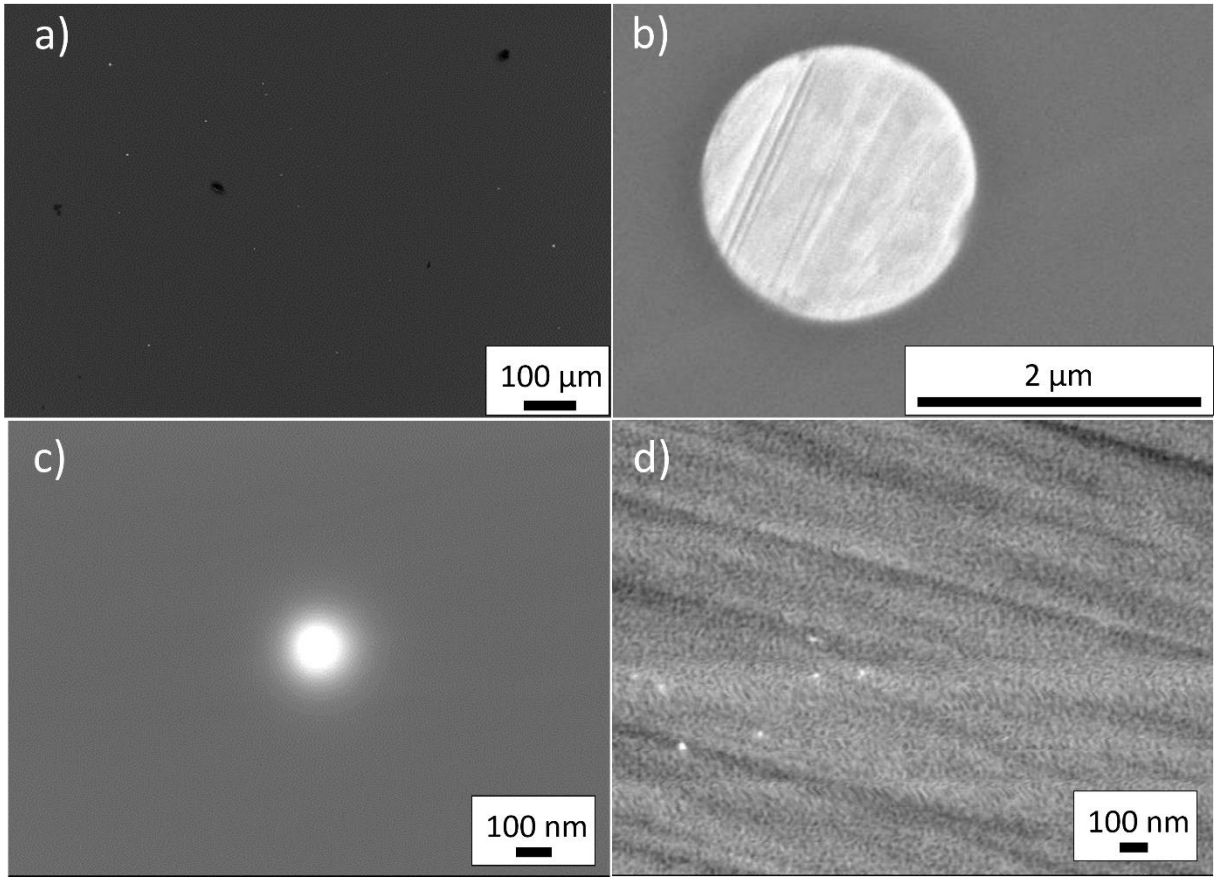

Figure 57 *Selected SEM images of LYAS samples annealed at 825°C for 60 min. a) 7MQ, gold particles, approx. 4 µm in diameter, b) 7MQ, spherical gold particle, c) 2MQ, gold nanoparticle, d) 9MQ, gold nanoparticles in phase separated glass matrix.*

Table 24 *Results of image analysis of TEM images for Au:Sn:LYAS samples prepared by MQ and ADL.*

Sample no.	Sample code	Heating	Au confirmed by EDS	NP shape	TEM particles counted	avg size [nm]
1MQ	*Au,Sn :L10-Y3-A19-S68*	825°C 60min	not measured	almost spherical	6	10
2MQ	*Au,Sn :L10-Y3-A19-S68*	825°C 60min	not measured	almost spherical	5	6
4MQ	*Au,Sn :L10-Y13-A19-S58*	825°C 60min	not measured	almost spherical	1	3
5MQ	*Au,Sn :L10-Y13-A19-S58*	825°C 60min	not measured	-	0	0
7MQ	*Au,Sn :L10-Y13-A9-S68*	825°C 60min	yes	almost spherical	1	7
8MQ	*Au,Sn :L10-Y13-A9-S68*	825°C 60min	not measured	-	0	0
9MQ	*Au,Sn :L10-Y13-A9-S68*	825°C 60min	yes	almost spherical	7	22

Observed nanoparticles are very sparsely distributed, contrary to our expectations. The average size of the AuNPs in the samples was measured using image analysis and ranged from 3 (sample with highest Au content, Si→Li substitution (**4MQ**)) to 22 nm (sample with lowest Au content, Al→Li substitution (**9MQ**)). The shape of the particles was almost spherical (see **Figure 58 a, b, d**). It is clear from the **Table 24** that in general the largest numbers of nanoparticles were found in samples with high gold content and also when Li was substituted for Y (sample **1MQ**). Surprisingly, no AuNPs were found in samples with medium gold content and Si→Li (**5MQ**) and Al→Li substitution (**8MQ**), which are strongly coloured.

The 9MQ sample is notably different from the others, as it was the only one of the samples prepared by the MQ technique to exhibit a blue colour shade. In this sample, particles with sizes up to 22 nm were found in relatively large numbers. It should be remembered, and this was also confirmed by TEM analysis, that in samples where Al→Li substitution in composition was performed (**7-9MQ**), the phase separation (spinodal decomposition) at the nanoscale (see **Figure 58 c,d**) was observed. This is consistent with the SEM observations and also with the results in the YAS chapter (see **Chapter 4.2.**).

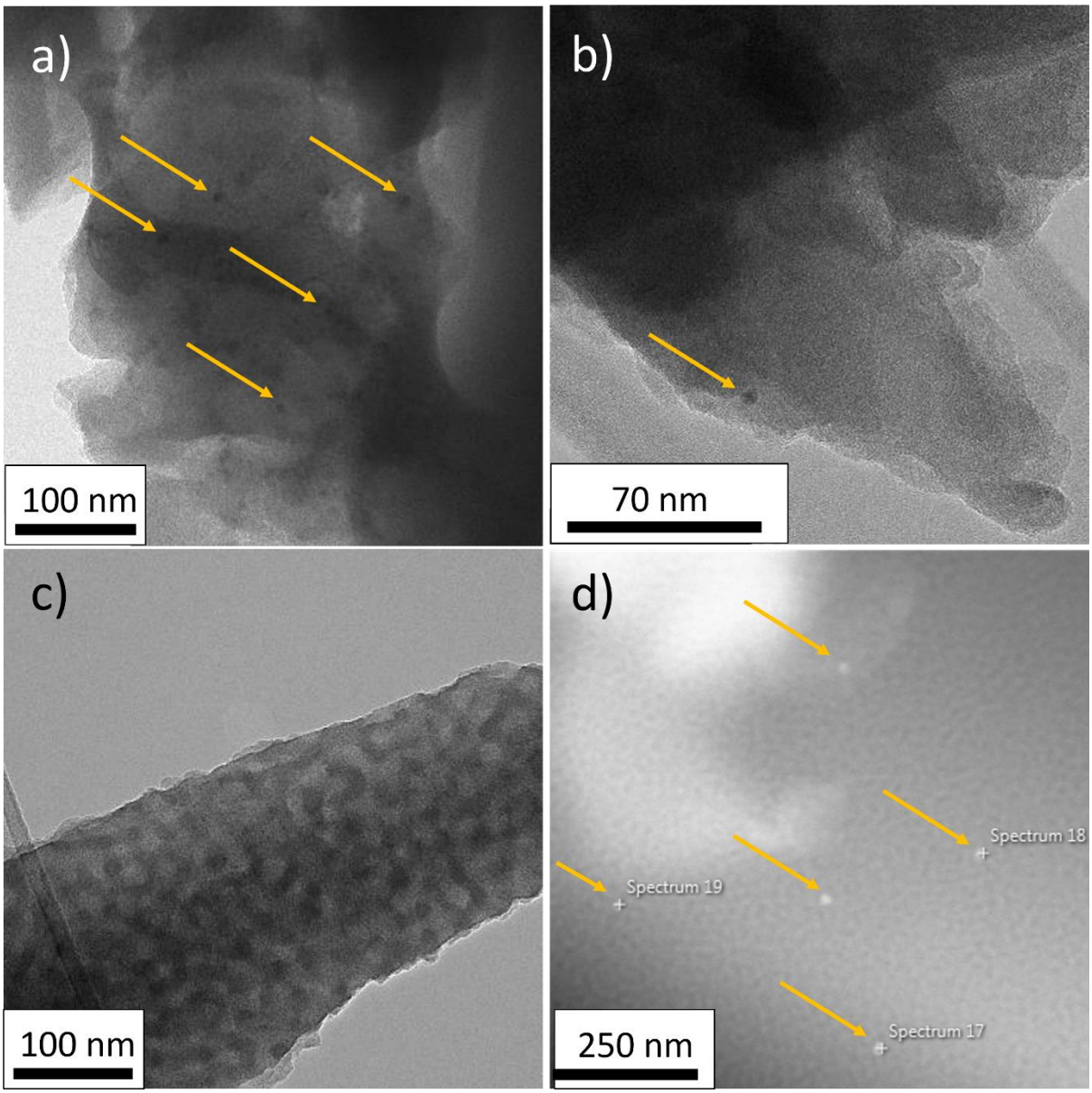

Figure 58 *Selected TEM images of LYAS samples annealed at 825°C for 60 min. The orange arrows point to gold nanoparticles. a) 1MQ, gold nanoparticles, approx. 10 nm in diameter, b) 2MQ, gold nanoparticle, c) 8MQ, phase separated glass matrix – spinodal decomposition, d) 9MQ gold nanoparticles in phase separated glass matrix.*

The results of the absorbance measurements of the LYAS samples are shown in **Figure 59** and are arranged as follows: columns represent different substitution rates in the glass matrix (from left to right: Y→Li, Si→Li, Al→Li); each row represents different Au concentrations (from top to bottom: highest, medium, lowest).

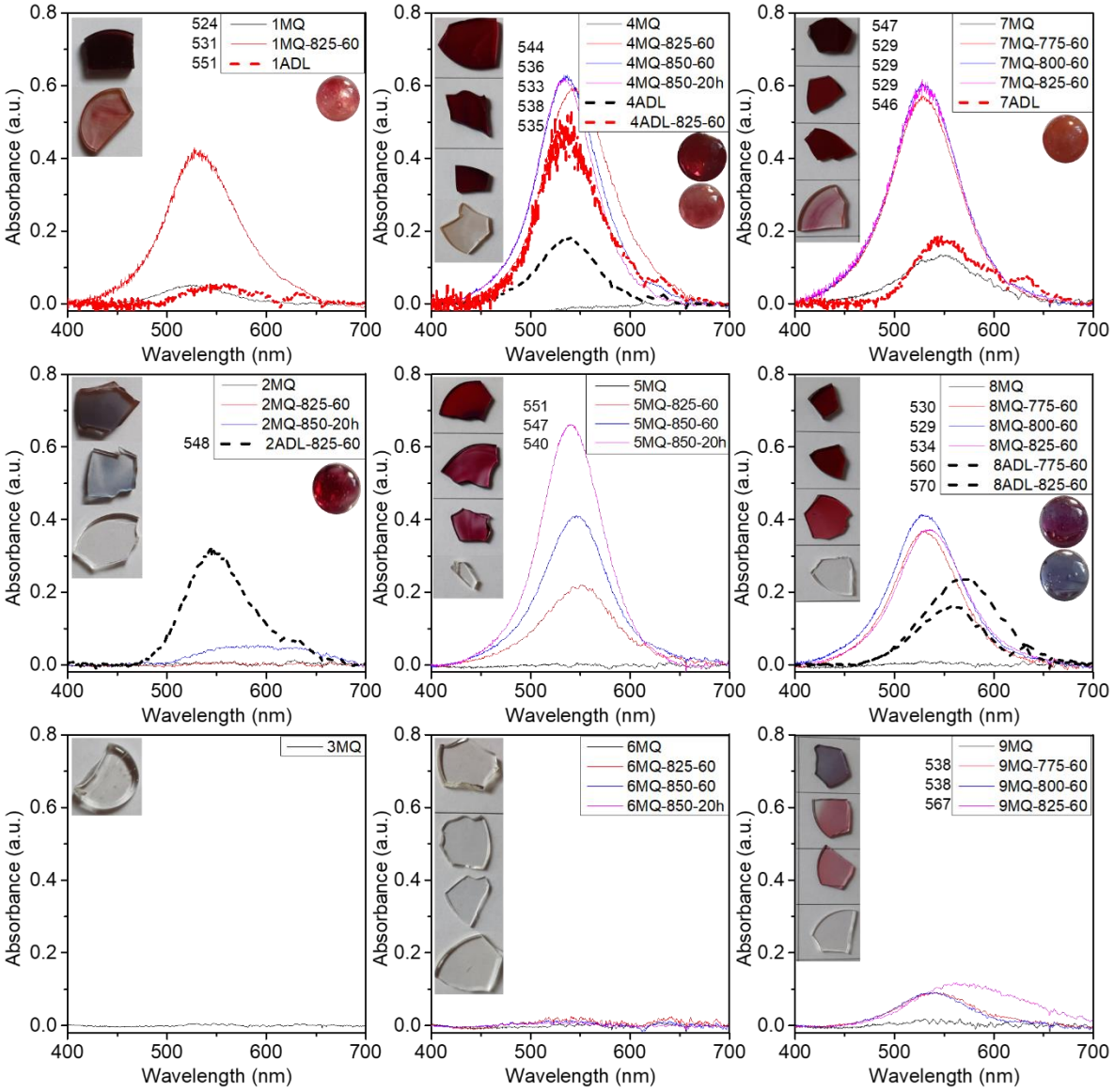

Figure 59 *Absorption spectra of Au:Sn LYAS samples. Columns represent different oxide substitution in the glass matrix. From left to right: Y→Li, Si→Li, Al→Li. Each row represents different Au concentration. From top to bottom: highest, medium, lowest. Photographs of the measured samples are also inserted in the graphs for easier visual orientation. Next to the legend are the values of the wavelengths in nm at which the absorption bands reach their maximum.*

In the absorption spectra, as expected, characteristic bands in the visible region of the spectrum appear in the region between 500 and 600 nm for most samples. Immediately, after preparation by both MQ and ADL, the samples are only weakly coloured, even at the highest Au concentration used, which is reflected in the spectra by a weak band intensity with a maximum in the 530-550 nm range. The shift of the maximum is related to the glass matrix used. On the other hand, annealing causes a distinct colouration in most samples. A characteristic Gaussian

absorption peak with a maximum around 530-550 nm. appears in samples with a high concentration of gold, which are dark red and brown in appearance. If the samples exhibit a dark red colour, the maximum of the band is around 530 nm, virtually independent of the matrix. If the samples appear to be ruby red the maximum is quite accurately at 547 nm. The shift of the band to higher wavelengths corresponds to a blue to blue-violet colour of the glass and is particularly noticeable in samples with the Al→Li substitution.

The absorbance measurements of selected bead samples prepared using the ADL method are shown by the dashed lines in the graphs in **Figure 59**. A new peak in the region around 630 nm on these lines corresponds to the absorption of the resin in which the samples were embedded for cutting and polishing. The characteristic bands corresponding to the colour change of the beads can be seen in these spectra, but with lower intensity. The wavelength maxima of the measured bands correspond very well to the colour and also to the maxima of the samples prepared by MQ technology in the different matrices with different compositions.

5.4.2 Summary and discussion

The results presented in this chapter can be summarized as follows:

1) The proposed LYAS system is a new suitable glass system for the preparation of glass enriched with Au NPs using ADL technology. In this system, it is possible to prepare homogeneous samples, where the colour corresponding to the presence of NPs can be tuned from brown to red to violet shades by changes in composition combined with subsequent annealing. However, according to Volf [239], we assume inferior mechanical and chemical properties of the glass in this system compared to YAS - not measured.
2) Among the systematically varying substitutions of Li for three different ions in the glass matrix, the substitution of Li for Al appears to be the most suitable in terms of the different variability of glass colour. The glasses exhibited the largest range of the observed absorption band maxima (from and thus take a correspondingly wide colour range).
3) Au NPs were relatively sparsely distributed in the glass and were spherical in shape, with an average size ranging from 3 to 22 nm, independently of the chosen

substitution and technology, yet the samples showed quite different absorption and therefore also colour. From these pilot results, it is concluded that the shape and distribution of the nanoparticles does not so much affect the colour as the phase separation of the glass, or the different combination of nanoparticle absorption and glass phases formed.

4) The maxima of the absorption spectral bands in the VIS region are between 524-570 nm, and it appears that the ruby red coloration corresponds to an absorption maximum at 540 nm.

The colour of the glass, the size of the AuNPs, the position of the absorption band and the composition of the glass matrix are closely linked. In silicate glasses of various compositions [102,103] , the absorption band ranges from 500 to 600 nm and is generally Gaussian in shape. In the literature, particle size estimation was performed either by Mie theory or [101,117,118,163] by calculation from XRD spectra according to the Scherrer equation [109,111]. Recently, the real size of AuNPs was investigated by TEM. However, as mentioned above, due to the challenging sample preparation, only a relatively small number of systematically observed changes or correlations of nanoparticle size, matrix chemistry, and gold nanoparticle size was described.

Currently, there are several freely available software programs to calculate absorption spectra according to Mie theory. As a pilot experiment, based on the recommendation of J.P. Blondeau [240], the BHMIE software [241] was used for simulation of absorption spectra of the ruby red sample of the LS system. For the given sample, the average size of the gold nanoparticle, the refractive index value of the glass matrix and several models, which the program includes, were selected. These models differ from each other in the values of the physical constants that are used in the calculations of the shape of absorption spectra. The models by Babar, Hagemann, Johnson, Palik and Rakic were compared with measured absorption spectra using this program. The simulation is shown in **Figure 60**. It is obvious that the Hagemann's model worked best. Why this is and whether this model can be used in general for e.g. all types of silicate glasses or for different types of AuNPs would require further comparisons, simulations and probably an additional set of experiments. Moreover, the BHMIE software assumes monodisperse

spherical nanoparticles and also that the nanoparticles do not cluster together, which is not achieved in prepared samples.

Figure 60

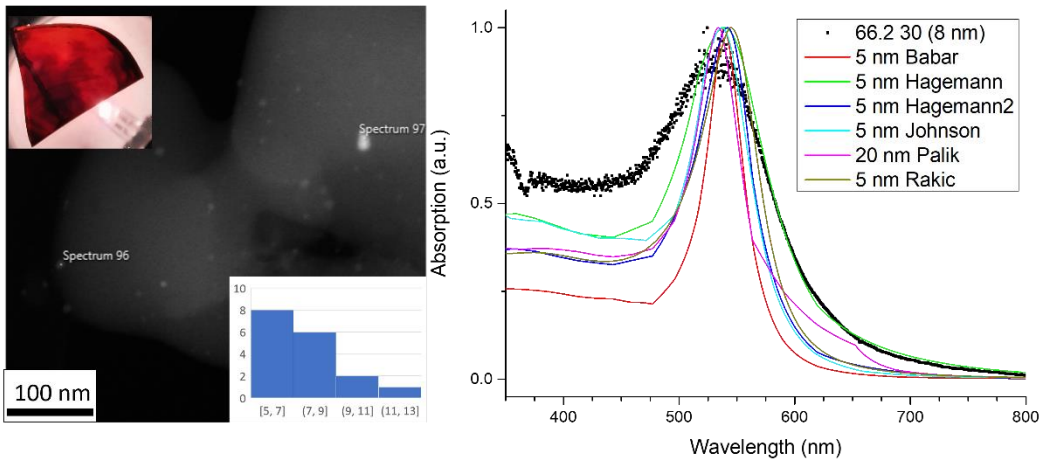

Figure 60 *Comparison of measured absorption spectra (black) with mathematical models – sample 10MQ, annealed at 500°C, 30 min. The Hagemann's model (light green) works best for our LS samples.*

However, in addition to the shape and distribution of the nanoparticles, the refractive index value can also have a significant effect on the position and shape of the absorption band, which shifts with changing composition of the glass matrix. Five different glass matrices were prepared. For each glass system, the dispersion by m-line spectroscopy was measured, and the refractive index value of the glass was calculated for a wavelength of 589 nm. The refractive index values and the observed position of the maximum of the absorption band are given in **Table 25** for the gold-enriched glasses or for the annealed glasses. It is clear from the table that, in general, the highest refractive index values correspond to high wavelengths of the absorption band maximum (LYAS A and YAS glass) and, conversely, low refractive index values to lower wavelengths of the absorption maximum (LYAS Y). This trend corresponds well to the trend predicted by, e.g., [71]. However, specific exact values deviate from this trend, e.g. in LYAS S glass, which may be due to the shape of the shape and number of NPs, or to the formation of new phases. Mathematical relationships have also been published to describe the relationship

between the wavelength of the absorption maximum and the refractive index value, but these have not yet been verified for the experiments reported in this thesis [109].

Table 25 *Comparison of the refractive index and the position of maximum of absorption peak of selected samples.*

Glass Matrix	**Sample**	**Refractive index (589 nm)**	**Maximum of absorption peak [nm]**
LS (*Au,Sn: L33-S67*)	**7, 8, 10 MQ**, as quenched	1.5415	533
YAS (*Au,Sn:Y13-A19-S68)*	**4,5 MQ**, 900°C, 60 min)	1.6168	554
LYAS Y (*Au,Sn:L10-Y3-A19-S68*)	**1MQ**,as quenched	1.5391	524
LYAS S (*Au,Sn:L10-Y13-A19-S58*)	**4MQ**, 825°C, 60 min	1.6435	544
LYAS A (*Au,Sn:L10-Y13-A9-S68*)	**7MQ**,as quenched	1.6142	547

In our opinion, the most interesting fact arising from our results is related to the fact that lithium-containing silicate glasses tend to crystallize. Thus, new phases are formed in the glass matrix as confirmed by TEM images of LYAS glass where lithium was substituted for aluminium. The formation of these phases clearly caused the greatest colour variability in these glasses. Therefore we believe that the formation of nanoscale crystals and/or amorphous phase separation greatly promotes the uniform nucleation of AuNPs and is the key to the uniform coloration of the glass samples doped with gold. Similar conclusions were published relatively recently when an admirable colour transformation was achieved in the ZnO-MgO-Al_2O_3-SiO_2 system due to the addition of TiO_2 and ZrO_2 phases to glass containing Au NPs [119,120]. Similarly, the variability of colours on the famous Lycurgus cup is also attributed to the formation of new glass phases present in the glass along with the gold nanoparticles, according to [85]. This opens up a very wide spectrum of possibilities for further controlling the coloration of glasses. The formation of nanoscale phase separation, nevertheless, proves to be crucial.

6 CONCLUSIONS

The thesis dealt with the preparation of AuNPs in silicate glass using ADL and MQ technologies. The effect of the technology used and the initial chemical composition on the distribution, shape and size of the AuNPs (mainly by TEM) and the absorption of the prepared glasses (by UV-VIS spectrophotometer) was investigated. In the case of ADL technology, the influence of a variety of input parameters (e.g. gas type and flow rate, laser power, melting time) on the properties of the prepared samples was also studied.

The first part of the work highlights some critical aspects of the ADL method for the synthesis of oxide glass beads, with the goal of extending its applicability to broader compositional landscapes, involving for example highly volatile components. From the point of view of mere glass formation, this technique exhibits unrivalled versatility: (1) its containerless conditions suppress heterogeneous nucleation of crystal phases and avoid contamination from crucible and refractory materials; (2) laser heating can attain up to ~3000 °C, above the melting temperature of any stable oxide material; (3) the setup enables fast cooling rates in the order of several hundreds of °C s^{-1} (depending on the levitation gas nature, the bead size and its composition), facilitating the quenching of melts prone to devitrification. Considering these advantageous features, it would appear that the ADL method should invariably represent the optimal choice for the obtainment of homogeneous, bubble-free beads of a desired stoichiometry. Nevertheless, the results obtained here signal that other key melt properties contribute to determination of the suitability of a given composition for ADL synthesis. Parameters r_{evap} a Δ_{evap} have been defined as

$$r_{evap} = \frac{T_{m,\Sigma}}{T_m} \qquad \text{Eq. 6.1}$$

$$\Delta_{evap} = r_{evap,max} - r_{evap,min} \qquad \text{Eq. 6.2}$$

where T_m is the melting point of a given oxide component, $T_{m,\Sigma}$ is the melting point of the target multicomponent glass (both obtainable from phase diagrams); $r_{evap,max}$ and $r_{evap,min}$ respectively stand for the highest and lowest r_{evap} values among all components of the target glass. These

parameters can be evaluated beforehand for a smart compositional design. It has been shown that when the achievement of low viscosity for bubble removal requires heating above the T_m of the target glass by hundreds of Kelvins, a non-negligible high-temperature evaporation should be expected for r_{evap} values significantly exceeding ~0.8, although this threshold may vary according to the chosen composition, ADL setup, levitation gas, desired final bead size and melting procedure. For instance, a shorter high-temperature dwell may limit volatilisation, though possibly preventing satisfactory homogenization and fining. Similarly, Δ_{evap} values above ~0.2 signalled a high risk of compositional drift for the prepared samples, stressing the general need to minimize this parameter during compositional design.

The second part of the thesis shed new light on liquid-liquid phase separation in the YAS system, specifically in the region with 65 mol% SiO_2 or more and simultaneously a maximum of 17.5 mol% Y_2O_3. In this region, SiO_2 amorphous nanoparticles are formed. As expected, the size and distribution of these nanoparticles can be controlled by the used synthesis technology, i.e., by the cooling rate. Slow cooling (melt-quenching) produces bigger nanoparticles than a very fast cooling (ADL). In addition, the formation and size of nanoparticles can also be fundamentally influenced by the composition. An increase in SiO_2 reduces the compositional contrast between nanoparticles and matrix, possibly due to a lower driving force towards phase separation. Conversely, increasing the glass modifier Y_2O_3 results in the formation of SiO_2 nanoparticles of different sizes, which can vary from tens to hundreds of nanometres depending on its content. With equal content of Y_2O_3 and Al_2O_3, an opalescent sample with very small, interconnected nanoparticles could be prepared. These results could be used as a guide for the tuneable fabrication of SiO_2 spherical nanoparticles in YAS glass for various potential applications.

The third part of the work was about preparation of AuNPs in YAS and LS glasses using ADL and MQ. A multi-step sample preparation process was developed for both technologies, which ensures better homogeneity and reduces the loss of volatile glass components (Au, SnO_2) by adding them up to the pre-melted glass powder. The basis of this process is the milling of the precursor materials, melting by MQ, a second milling, doping with the required amount of volatile components and final melting using the selected technology. A new procedure for the preparation of melting pellets using starch slurry and repetitive pipette has also been developed

for the ADL technology, which ensures constant weight of the prepared samples (15.84±0.24 mg for 50 µl LS pellets) and better reproducibility of the experiments performed. Due to the versatility of this procedure, it can be used in a wide range of other systems, not only in the investigated glasses.

Regarding the formation of nanoparticles in these two types of glass with different compositions, it was evident that by a suitable combination of technological conditions and subsequent annealing, it is possible to prepare mostly spherical-shaped nanoparticles in both types of glass (although triangular and vermicular particles were also prepared in some cases) and to control their size and distribution by subsequent annealing. In particular, it was found to be convenient to prepare clear transparent glasses containing only trace numbers of metallic nanoparticles and to control the parameters of the gold nanoparticles and hence the resulting glass colour by subsequent annealing. In the course of the work the beneficial effect of the addition of SnO_2 on the colour of the prepared glasses was experimentally verified.

If we compare the two techniques used, better results were achieved using MQ. Samples prepared by this technique were free of bubbles and more homogeneous in colour. Using ADL, any change in glass composition or sample size would require optimization and a change in the ADL input parameters to optimize the sample homogeneity. During this work, the same ADL parameters were always optimised first and then used for each bead in a sample set so that the prepared samples could be compared with each other.

In the fourth part of the thesis, based on the previous results, several glass compositions were designed and successfully prepared in the LYAS system using both technologies. These compositions were derived from the basic YAS glass composition by replacing 10 mol% of one of the oxides Y_2O_3, Al_2O_3 and SiO_2 with Li_2O. The main intention of this substitution was to benefit from the advantageous optical properties of YAS glass but reduce its viscosity and thus facilitate its preparation. From this point of view, the least successful substitution was Y→L. These glass samples were very difficult to prepare using MQ technology. Temperatures of up to 1700 °C were used for their melting, yet the glasses were very viscous and cracked during cooling. When melted by ADL, the high viscosity was reflected by a large number of bubbles in the samples that could not be removed. The A→L and S→L substitutions fulfilled their purpose, the temperature required to melt these glasses and their viscosity were reduced and the

glass was much easier to work with. Nanoscale phase separation was observed in the A→L exchange glass by TEM. We propose that this phase separation caused a uniform nucleation of AuNPs across the entire sample volume and thus the best colour homogeneity after additional heat treatment of the samples.

REFERENCES

[1] G. Tammann, Der glaszustand, L. Voss, Leipzig, 1933.
[2] J. Hlaváč, Základy technologie silikátů, SNTL, 1981.
[3] Standard Terminology of Glass and Glass Products, (n.d.). https://www.astm.org/c0162-05.html (accessed July 2, 2023).
[4] A.K. Varshneya, Fundamentals of inorganic glasses, Third edition, Elsevier, Amsterdam, Netherlands ; Cambridge, MA, 2019.
[5] R. Conradt, Thermodynamics and Kinetics of Glass, in: J.D. Musgraves, J. Hu, L. Calvez (Eds.), Springer Handbook of Glass, Springer International Publishing, Cham, 2019: pp. 51–77. https://doi.org/10.1007/978-3-319-93728-1_2.
[6] W.H. Zachariasen, THE ATOMIC ARRANGEMENT IN GLASS, J. Am. Chem. Soc. 54 (1932) 3841–3851. https://doi.org/10.1021/ja01349a006.
[7] G.N. Greaves, EXAFS and the structure of glass, Journal of Non-Crystalline Solids. 71 (1985) 203–217. https://doi.org/10.1016/0022-3093(85)90289-3.
[8] E.D. Zanotto, J.C. Mauro, The glassy state of matter: Its definition and ultimate fate, Journal of Non-Crystalline Solids. 471 (2017) 490–495. https://doi.org/10.1016/j.jnoncrysol.2017.05.019.
[9] J.D. Musgraves, J. Hu, L. Calvez, eds., Springer Handbook of Glass, Springer International Publishing, Cham, 2019. https://doi.org/10.1007/978-3-319-93728-1.
[10] H. Scholze, Glass: Nature, Structure, and Properties, Springer Science & Business Media, 2012.
[11] L. Lichtenstein, M. Heyde, H.-J. Freund, Atomic Arrangement in Two-Dimensional Silica: From Crystalline to Vitreous Structures, J. Phys. Chem. C. 116 (2012) 20426–20432. https://doi.org/10.1021/jp3062866.
[12] K.-H. Sun, Fundamental Condition of Glass Formation, Journal of the American Ceramic Society. 30 (2006) 277–281. https://doi.org/10.1111/j.1151-2916.1947.tb19654.x.
[13] G.N. Greaves, S. Sen, Inorganic glasses, glass-forming liquids and amorphizing solids, Advances in Physics. 56 (2007) 1–166. https://doi.org/10.1080/00018730601147426.
[14] F. Angeli, O. Villain, S. Schuller, S. Ispas, T. Charpentier, Insight into sodium silicate glass structural organization by multinuclear NMR combined with first-principles calculations, Geochimica et Cosmochimica Acta. 75 (2011) 2453–2469. https://doi.org/10.1016/j.gca.2011.02.003.
[15] P. Jóvári, A. Chrissanthopoulos, K.S. Andrikopoulos, I. Pethes, I. Kaban, S. Kohara, B. Beuneu, S.N. Yannopoulos, Short range order of glassy KSb5S8 by diffraction, EXAFS, vibrational spectroscopy and DFT calculations, Journal of Non-Crystalline Solids. 616 (2023) 122461. https://doi.org/10.1016/j.jnoncrysol.2023.122461.
[16] A. Pedone, G. Malavasi, A.N. Cormack, U. Segre, M.C. Menziani, Insight into Elastic Properties of Binary Alkali Silicate Glasses; Prediction and Interpretation through Atomistic Simulation Techniques, Chem. Mater. 19 (2007) 3144–3154. https://doi.org/10.1021/cm062619r.
[17] K. Baral, W.-Y. Ching, Electronic structures and physical properties of Na_2O doped silicate glass, Journal of Applied Physics. 121 (2017) 245103. https://doi.org/10.1063/1.4987033.
[18] S.D. Stookey, History of the Development of Pyroceram, Research Management. 1 (1958) 155–163. https://doi.org/10.1080/00345334.1958.11755484.

[19] J. Deubener, M. Allix, M.J. Davis, A. Duran, T. Höche, T. Honma, T. Komatsu, S. Krüger, I. Mitra, R. Müller, S. Nakane, M.J. Pascual, J.W.P. Schmelzer, E.D. Zanotto, S. Zhou, Updated definition of glass-ceramics, Journal of Non-Crystalline Solids. 501 (2018) 3–10. https://doi.org/10.1016/j.jnoncrysol.2018.01.033.
[20] B. Holand, Glass-Ceramic Technology, 3rd Edition | Wiley, Wiley.Com. (n.d.). https://www.wiley.com/en-us/Glass+Ceramic+Technology%2C+3rd+Edition-p-9781119423706 (accessed July 15, 2023).
[21] P. Yongsiri, S. Eitssayeam, G. Rujijanagul, S. Sirisoonthorn, T. Tunkasiri, K. Pengpat, Fabrication of transparent lead-free KNN glass ceramics by incorporation method, Nanoscale Res Lett. 7 (2012) 136. https://doi.org/10.1186/1556-276X-7-136.
[22] M. Nikl, D. Niž?anský, J. Ruzicka, C. Cannas, T. Yanagida, M. Nikl, D. Niž?anský, J. Ruzicka, C. Cannas, T. Yanagida, Silicate Glass-Based Nanocomposite Scintillators, in: Advances in Nanocomposite Technology, IntechOpen, 2011. https://doi.org/10.5772/19981.
[23] J.-P. Laval, J.-R. Duclère, V. Couderc, M. Allix, C. Genevois, V. Sarou-Kanian, F. Fayon, P.-E. Coulon, S. Chenu, M. Colas, J. Cornette, P. Thomas, G. Delaizir, Highly Transparent Fluorotellurite Glass-Ceramics: Structural Investigations and Luminescence Properties, Inorg. Chem. 58 (2019) 16387–16401. https://doi.org/10.1021/acs.inorgchem.9b01955.
[24] E.D. Zanotto, A bright future for glass-ceramics, Ceramics.Org. (2010). https://ceramics.org/wp-content/uploads/2010/09/bulletin_oct-nov2010.pdf (accessed August 30, 2023).
[25] W. Bragg, CHAPTER 2 - THE GLASSY STATE, in: K.J. Rao (Ed.), Structural Chemistry of Glasses, Elsevier Science Ltd, Oxford, 2002: pp. 13–76. https://doi.org/10.1016/B978-008043958-7/50020-0.
[26] L. Klein, M. Aparicio, A. Jitianu, Handbook of Sol-Gel Science and Technology: Processing, Characterization and Applications, Springer Nature, 2018.
[27] The Containerless Synthesis of Glass - Weber - 2010 - International Journal of Applied Glass Science - Wiley Online Library, (n.d.). https://ceramics.onlinelibrary.wiley.com/doi/10.1111/j.2041-1294.2010.00026.x (accessed September 2, 2023).
[28] P.C. Nordine, R.M. Atkins, Aerodynamic levitation of laser-heated solids in gas jets, Review of Scientific Instruments. 53 (1982) 1456–1464. https://doi.org/10.1063/1.1137196.
[29] L. Hennet, V. Cristiglio, J. Kozaily, I. Pozdnyakova, H.E. Fischer, A. Bytchkov, J.W.E. Drewitt, M. Leydier, D. Thiaudière, S. Gruner, S. Brassamin, D. Zanghi, G.J. Cuello, M. Koza, S. Magazù, G.N. Greaves, D.L. Price, Aerodynamic levitation and laser heating:, Eur. Phys. J. Spec. Top. 196 (2011) 151–165. https://doi.org/10.1140/epjst/e2011-01425-0.
[30] A.R. Oganov, C.J. Pickard, Q. Zhu, R.J. Needs, Structure prediction drives materials discovery, Nature Reviews Materials. 4 (2019) 331–348. https://doi.org/10.1038/s41578-019-0101-8.
[31] X. Wen, B. Zhang, W. Wang, F. Ye, S. Yue, H. Guo, G. Gao, Y. Zhao, Q. Fang, C. Nguyen, X. Zhang, J. Bao, J.T. Robinson, P.M. Ajayan, J. Lou, 3D-printed silica with nanoscale resolution, Nat. Mater. 20 (2021) 1506–1511. https://doi.org/10.1038/s41563-021-01111-2.

[32] H. Zhang, L. Huang, M. Tan, S. Zhao, H. Liu, Z. Lu, J. Li, Z. Liang, Overview of 3D-Printed Silica Glass, Micromachines. 13 (2022) 81. https://doi.org/10.3390/mi13010081.
[33] C. Zhang, D. Ouyang, S. Pauly, L. Liu, 3D printing of bulk metallic glasses, Materials Science and Engineering: R: Reports. 145 (2021) 100625. https://doi.org/10.1016/j.mser.2021.100625.
[34] Move aside, plastic: 3D printing conquers glass, Nature. 575 (2019) 419–419. https://doi.org/10.1038/d41586-019-03473-9.
[35] B. Singarapu, D. Galusek, A. Durán, M.J. Pascual, Glass-Ceramics Processed by Spark Plasma Sintering (SPS) for Optical Applications, Applied Sciences. 10 (2020) 2791. https://doi.org/10.3390/app10082791.
[36] M. Wang, Q. Zheng, A. Chen, Y. Li, X. Zhang, D. Zhang, S. Jin, D. Xiong, W. Deng, Crystallization, thermal expansion and hardness of Y2O3–Al2O3–SiO2 glasses, Ceramics International. 47 (2021) 25059–25066. https://doi.org/10.1016/j.ceramint.2021.05.236.
[37] M.J. Hyatt, D.E. Day, Glass Properties in the Yttria-Alumina-Silica System, Journal of the American Ceramic Society. 70 (1987) C-283-C–287. https://doi.org/10.1111/j.1151-2916.1987.tb04901.x.
[38] J. Marchi, D.S. Morais, J. Schneider, J.C. Bressiani, A.H.A. Bressiani, Characterization of rare earth aluminosilicate glasses, Journal of Non-Crystalline Solids. 351 (2005) 863–868. https://doi.org/10.1016/j.jnoncrysol.2005.01.078.
[39] A. Makehima, Y. Tamura, T. Sakaino, Elastic Moduli and Refractive Indices of Aluminosilicate Glasses Containing Y2O3, La2O3, and TiO2, Journal of the American Ceramic Society. 61 (1978) 247–249. https://doi.org/10.1111/j.1151-2916.1978.tb09291.x.
[40] J.K. Christie, A. Tilocca, Aluminosilicate Glasses As Yttrium Vectors for in situ Radiotherapy: Understanding Composition-Durability Effects through Molecular Dynamics Simulations, Chem. Mater. 22 (2010) 3725–3734. https://doi.org/10.1021/cm100847p.
[41] L. Bois, N. Barré, S. Guillopé, M.J. Guittet, M. Gautier-Soyer, J.P. Duraud, P. Trocellier, P. Verdier, Y. Laurent, Dissolution of lanthanide alumino-silicate oxynitride glasses, Journal of Nuclear Materials. 277 (2000) 57–66. https://doi.org/10.1016/S0022-3115(99)00137-3.
[42] S. Ahmad, M. Herrmann, M.M. Mahmoud, W. Lippmann, A. Hurtado, H.J. Seifert, Application of Nd2O3–Al2O3–SiO2 glass solder for joining of silicon carbide components, Journal of the European Ceramic Society. 36 (2016) 1559–1569. https://doi.org/10.1016/j.jeurceramsoc.2016.01.020.
[43] P. Dragic, Brillouin spectroscopy of YAG-derived optical fibers, (2010). https://opg.optica.org/oe/fulltext.cfm?uri=oe-18-10-10055&id=199174 (accessed August 30, 2023).
[44] R. Harrysson, P. Vomacka, Glass formation in the system Y2O3□Al2O3□SiO2 under conditions of laser melting, Journal of the European Ceramic Society. 14 (1994) 377–381. https://doi.org/10.1016/0955-2219(94)90075-2.
[45] S. Ahmad, T. Ludwig, M. Herrmann, M.M. Mahmoud, W. Lippmann, H.J. Seifert, Phase evaluation during high temperature long heat treatments in the Y2O3–Al2O3–SiO2 system, Journal of the European Ceramic Society. 34 (2014) 3835–3840. https://doi.org/10.1016/j.jeurceramsoc.2014.05.025.

[46] Z. Pan, O. Fabrichnaya, H. Seifert, R. Neher, K. Brandt, M. Herrmann, Thermodynamic evaluation of the Si-C-Al-Y-O system for LPS-SiC application, JPED. 31 (2010). https://doi.org/10.1007/s11669-010-9695-7.
[47] N.A. Toropov, I.A. Bondar', F.Ya. Galadhov, Kh.S. Nikogosyan, N.V. Vinogradova, Phase equilibria in the yttrium oxide-alumina system, Russ Chem Bull. 13 (1964) 1076–1081. https://doi.org/10.1007/BF00863104.
[48] Y. Zhang, A. Navrotsky, Thermochemistry of Glasses in the Y2O3-Al2O3-SiO2 System, Journal of the American Ceramic Society. 86 (2003) 1727–1732. https://doi.org/10.1111/j.1151-2916.2003.tb03547.x.
[49] U. Kolitsch, H.J. Seifert, T. Ludwig, F. Aldinger, Phase equilibria and crystal chemistry in the Y2O3–Al2O3–SiO2 system, Journal of Materials Research. 14 (1999) 447–455. https://doi.org/10.1557/JMR.1999.0064.
[50] H. Mao, M. Selleby, O. Fabrichnaya, Thermodynamic reassessment of the Y 2O3–Al2O3–SiO2 system and its subsystems, Calphad. 32 (2008) 399–412. https://doi.org/10.1016/j.calphad.2008.03.003.
[51] S.H. Risbud, J.A. Pask, Mullite Crystallization from SiO2-Al2O3 Melts, Journal of the American Ceramic Society. 61 (1978) 63–67. https://doi.org/10.1111/j.1151-2916.1978.tb09232.x.
[52] T. Takei, I. Kameshima, A. Yasumori, K. Okada, Crystallization kinetics of mullite in alumina–silica glass fibers, Journal of the American Ceramic Society. 21 (2004) 2487–2493.
[53] M. Hnatko, P. Šajgalík, Z. Lenčéš, D. Salamon, F. Monteverde, Carbon reduction reaction in the Y2O3–SiO2 glass system at high temperature, Journal of the European Ceramic Society. 21 (2001) 2797–2801. https://doi.org/10.1016/S0955-2219(01)00231-X.
[54] Z. Sun, M. Li, Y. Zhou, ChemInform Abstract: Recent Progress on Synthesis, Multi-Scale Structure, and Properties of Y—Si—O Oxides, ChemInform. 46 (2015). https://doi.org/10.1002/chin.201513295.
[55] N. Sadiki, J.P. Coutures, C. Fillet, J.L. Dussossoy, Crystallization of lanthanum and yttrium aluminosilicate glasses, Journal of Nuclear Materials. 348 (2006) 70–78. https://doi.org/10.1016/j.jnucmat.2005.09.003.
[56] O. Fabrichnaya, H.J. Seifert, R. Weiland, T. Ludwig, F. Aldinger, A. Navrotsky, Phase Equilibria and Thermodynamics in the Y2O3–Al2O3–SiO2 System, International Journal of Materials Research. 92 (2001) 1083–1097. https://doi.org/10.3139/ijmr-2001-0197.
[57] J. Groebner, Constitution Calculations in the System Y–Al–Si–C–O, University of Stuttgart, 1994.
[58] N.K. Nasikas, A. Retsinas, G.N. Papatheodorou, Y3Al5O12–SiO2 Glasses: Structure and Polyamorphism, Journal of the American Ceramic Society. 97 (2014) 2054–2060. https://doi.org/10.1111/jace.12999.
[59] Y. Hou, J. Yuan, J. Kang, J. Cui, J. Cheng, J. Cui, Effects of rare earth oxides on viscosity, thermal expansion, and structure of alkali-free boro-aluminosilicate glass, J. Wuhan Univ. Technol.-Mat. Sci. Edit. 32 (2017) 58–62. https://doi.org/10.1007/s11595-017-1558-1.
[60] A. Jaworski, B. Stevensson, B. Pahari, K. Okhotnikov, M. Edén, Local structures and Al/Si ordering in lanthanum aluminosilicate glasses explored by advanced 27Al NMR experiments and molecular dynamics simulations, Phys. Chem. Chem. Phys. 14 (2012) 15866–15878. https://doi.org/10.1039/C2CP42858J.

[61] K.E. Kelsey, J.F. Stebbins, D.M. Singer, G.E. Brown, J.L. Mosenfelder, P.D. Asimow, Cation field strength effects on high pressure aluminosilicate glass structure: Multinuclear NMR and La XAFS results, Geochimica et Cosmochimica Acta. 73 (2009) 3914–3933. https://doi.org/10.1016/j.gca.2009.03.040.
[62] T. Schaller, J.F. Stebbins, The Structural Role of Lanthanum and Yttrium in Aluminosilicate Glasses: A ^{27} Al and ^{17} O MAS NMR Study, J. Phys. Chem. B. 102 (1998) 10690–10697. https://doi.org/10.1021/jp982387m.
[63] P. Florian, N. Sadiki, D. Massiot, J.P. Coutures, 27Al NMR Study of the Structure of Lanthanum- and Yttrium-Based Aluminosilicate Glasses and Melts, J. Phys. Chem. B. 111 (2007) 9747–9757. https://doi.org/10.1021/jp072061q.
[64] J. Kalahe, M.P. Stone, P.D. Dragic, J. Ballato, J. Du, The structures and properties of yttrium aluminosilicate glasses with low, medium, and high silica contents, Journal of Non-Crystalline Solids. 614 (2023) 122394. https://doi.org/10.1016/j.jnoncrysol.2023.122394.
[65] M. Vert, Y. Doi, K.-H. Hellwich, M. Hess, P. Hodge, P. Kubisa, M. Rinaudo, F. Schué, Terminology for biorelated polymers and applications (IUPAC Recommendations 2012), Pure and Applied Chemistry. 84 (2012) 377–410. https://doi.org/10.1351/PAC-REC-10-12-04.
[66] Leitner J., Struktura nanomateriálů, (n.d.). http://old.vscht.cz/ipl/nanomaterialy/Skripta/Struktura_nanomaterialu_var_04.pdf (accessed July 19, 2023).
[67] N. Wang, S.I. Rokhlin, D.F. Farson, Nonhomogeneous surface premelting of Au nanoparticles, Nanotechnology. 19 (2008) 415701. https://doi.org/10.1088/0957-4484/19/41/415701.
[68] T.A. Taton, Nanoscale Materials in Chemistry Edited by Kenneth J. Klabunde (Kansas State University). Wiley-Interscience: New York. 2001. xi + 292 pp. $99.95. ISBN: 0-471-38395-3., J. Am. Chem. Soc. 124 (2002) 10629–10630. https://doi.org/10.1021/ja0252072.
[69] T. Wriedt, Mie Theory: A Review, in: W. Hergert, T. Wriedt (Eds.), The Mie Theory: Basics and Applications, Springer, Berlin, Heidelberg, 2012: pp. 53–71. https://doi.org/10.1007/978-3-642-28738-1_2.
[70] Mie G., Contribution to the optics of turbid meadia, particularly of coloidal metal solutions, Annalen Der Physik. 3 (1908) 377–445.
[71] C. Louis, O. Pluchery, Gold Nanoparticles for Physics, Chemistry and Biology, IMPERIAL COLLEGE PRESS, 2012. https://doi.org/10.1142/p815.
[72] P.K. Jain, K.S. Lee, I.H. El-Sayed, M.A. El-Sayed, Calculated Absorption and Scattering Properties of Gold Nanoparticles of Different Size, Shape, and Composition: Applications in Biological Imaging and Biomedicine, J. Phys. Chem. B. 110 (2006) 7238–7248. https://doi.org/10.1021/jp057170o.
[73] E. Ruska, The Development of the Electron Microscope and of Electron Microscopy (Nobel Lecture), Angewandte Chemie International Edition in English. 26 (1987) 595–605. https://doi.org/10.1002/anie.198705953.
[74] H. Mohammad-Beigi, S. Yaghmaei, R. Roostaazad, A. Arpanaei, Comparison of different strategies for the assembly of gold colloids onto Fe3O4@SiO2 nanocomposite particles, Physica E Low-Dimensional Systems and Nanostructures. 49 (2013) 30–38. https://doi.org/10.1016/j.physe.2013.01.004.

[75] J.E. Millstone, S. Park, K.L. Shuford, L. Qin, G.C. Schatz, C.A. Mirkin, Observation of a Quadrupole Plasmon Mode for a Colloidal Solution of Gold Nanoprisms, J. Am. Chem. Soc. 127 (2005) 5312–5313. https://doi.org/10.1021/ja043245a.
[76] H.-L. Wu, C.-H. Chen, M.H. Huang, Seed-Mediated Synthesis of Branched Gold Nanocrystals Derived from the Side Growth of Pentagonal Bipyramids and the Formation of Gold Nanostars, Chem. Mater. 21 (2009) 110–114. https://doi.org/10.1021/cm802257e.
[77] J. Zhang, M.R. Langille, M.L. Personick, K. Zhang, S. Li, C.A. Mirkin, Concave cubic gold nanocrystals with high-index facets, J Am Chem Soc. 132 (2010) 14012–14014. https://doi.org/10.1021/ja106394k.
[78] D. Alba-Molina, J. Giner-Casares, M. Cano, Bioconjugated Plasmonic Nanoparticles for Enhanced Skin Penetration, Topics in Current Chemistry. 378 (2019) 8. https://doi.org/10.1007/s41061-019-0273-0.
[79] S. Alex, A. Tiwari, Functionalized Gold Nanoparticles: Synthesis, Properties and Applications—A Review, Journal of Nanoscience and Nanotechnology. 15 (2015) 1869–1894. https://doi.org/10.1166/jnn.2015.9718.
[80] G. Walters, I.P. Parkin, The incorporation of noble metal nanoparticles into host matrix thin films: synthesis, characterisation and applications, J. Mater. Chem. 19 (2009) 574–590. https://doi.org/10.1039/B809646E.
[81] U. Kreibig, M. Vollmer, Optical Properties of Metal Clusters, Springer, Berlin, Heidelberg, 1995. https://doi.org/10.1007/978-3-662-09109-8.
[82] S. Basu, S.K. Ghosh, S. Kundu, S. Panigrahi, S. Praharaj, S. Pande, S. Jana, T. Pal, Biomolecule induced nanoparticle aggregation: effect of particle size on interparticle coupling, J Colloid Interface Sci. 313 (2007) 724–734. https://doi.org/10.1016/j.jcis.2007.04.069.
[83] D.J. Barber, I.C. Freestone, An Investigation of the Origin of the Colour of the Lycurgus Cup by Analytical Transmission Electron Microscopy, Archaeometry. 32 (1990) 33–45. https://doi.org/10.1111/j.1475-4754.1990.tb01079.x.
[84] J. Siegel, M. Staszek, V. Švorčík, Nanočástice ušlechtilých kovů připravené v kapalinách, Chemické listy. 108 (2014) 1102–1112.
[85] A. Drozdov, M. Andreev, M. Kozlov, D. Petukhov, S. Klimonsky, C. Pettinari, Lycurgus cup: the nature of dichroism in a replica glass having similar composition, Journal of Cultural Heritage. 51 (2021) 71–78. https://doi.org/10.1016/j.culher.2021.07.002.
[86] drinking-cup | British Museum, The British Museum. (n.d.). https://www.britishmuseum.org/collection/object/H_1958-1202-1 (accessed July 21, 2023).
[87] P. Chakraborty, Metal nanoclusters in glasses as non-linear photonic materials, Journal of Materials Science. 33 (1998) 2235–2249. https://doi.org/10.1023/A:1004306501659.
[88] S. Werner, J. Navaridas, M. Luján, A Survey on Optical Network-on-Chip Architectures, ACM Comput. Surv. 50 (2017) 89:1-89:37. https://doi.org/10.1145/3131346.
[89] W. Husinsky, A. Ajami, P. Nekvindova, B. Svecova, J. Pesicka, M. Janecek, Z-scan study of nonlinear absorption of gold nano-particles prepared by ion implantation in various types of silicate glasses, Optics Communications. 285 (2012) 2729–2733. https://doi.org/10.1016/j.optcom.2012.01.044.
[90] R. Ahmad, M.S. Rafique, A. Ahmed, A. Ajami, P. Nekvindova, B. Svecova, S. Bashir, S. Iqbal, Femtosecond laser induced two-photon absorption in Au-ion embedded glasses,

Laser and Particle Beams. 37 (2019) 61–66. https://doi.org/10.1017/S026303461900020X.
[91] P. Vařák, P. Nekvindová, S. Vytykáčová, A. Michalcová, P. Malinský, J. Oswald, Near-infrared photoluminescence enhancement and radiative energy transfer in RE-doped zinc-silicate glass (RE = Ho, Er, Tm) after silver ion exchange, Journal of Non-Crystalline Solids. 557 (2021) 120580. https://doi.org/10.1016/j.jnoncrysol.2020.120580.
[92] J. Zmojda, P. Miluski, M. Kochanowicz, Nanocomposite Antimony-Germanate-Borate Glass Fibers Doped with Eu3+ Ions with Self-Assembling Silver Nanoparticles for Photonic Applications, Applied Sciences. 8 (2018) 790. https://doi.org/10.3390/app8050790.
[93] H. Fares, H. Elhouichet, B. Gelloz, M. Férid, Surface plasmon resonance induced Er3+ photoluminescence enhancement in tellurite glass, Journal of Applied Physics. 117 (2015) 193102. https://doi.org/10.1063/1.4921436.
[94] K. Kneipp, H. Kneipp, H.G. Bohr, Single-Molecule SERS Spectroscopy, in: K. Kneipp, M. Moskovits, H. Kneipp (Eds.), Surface-Enhanced Raman Scattering: Physics and Applications, Springer, Berlin, Heidelberg, 2006: pp. 261–277. https://doi.org/10.1007/3-540-33567-6_13.
[95] S.M. Wells, S.D. Retterer, J.M. Oran, M.J. Sepaniak, Controllable Nanofabrication of Aggregate-like Nanoparticle Substrates and Evaluation for Surface-Enhanced Raman Spectroscopy, ACS Nano. 3 (2009) 3845–3853. https://doi.org/10.1021/nn9010939.
[96] P. Pal, A. Bonyár, M. Veres, L. Himics, L. Balázs, L. Juhász, I. Csarnovics, A generalized exponential relationship between the surface-enhanced Raman scattering (SERS) efficiency of gold/silver nanoisland arrangements and their non-dimensional interparticle distance/particle diameter ratio, Sensors and Actuators A: Physical. 314 (2020) 112225. https://doi.org/10.1016/j.sna.2020.112225.
[97] C. Gao, F. Lyu, Y. Yin, Encapsulated Metal Nanoparticles for Catalysis, Chem. Rev. 121 (2021) 834–881. https://doi.org/10.1021/acs.chemrev.0c00237.
[98] S. Majhi, K. Sharma, R. Singh, M. Ali, C.S.P. Tripathi, D. Guin, Development of Silver Nanoparticles Decorated on Functional Glass Slide as Highly Efficient and Recyclable Dip Catalyst, ChemistrySelect. 5 (2020) 12365–12370. https://doi.org/10.1002/slct.202002492.
[99] S.-J. Shih, W.-L. Tzeng, R. Jatnika, C.-J. Shih, K.B. Borisenko, Control of Ag nanoparticle distribution influencing bioactive and antibacterial properties of Ag-doped mesoporous bioactive glass particles prepared by spray pyrolysis, Journal of Biomedical Materials Research Part B: Applied Biomaterials. 103 (2015) 899–907. https://doi.org/10.1002/jbm.b.33273.
[100] J. Li, D. Zhai, F. Lv, Q. Yu, H. Ma, J. Yin, Z. Yi, M. Liu, J. Chang, C. Wu, Preparation of copper-containing bioactive glass/eggshell membrane nanocomposites for improving angiogenesis, antibacterial activity and wound healing, Acta Biomaterialia. 36 (2016) 254–266. https://doi.org/10.1016/j.actbio.2016.03.011.
[101] Y. Wei, Noble metal nanoparticles in glass: A universal pathway towards light modulation, Thesis, 2019. https://digital.library.adelaide.edu.au/dspace/handle/2440/124225 (accessed July 21, 2023).
[102] W.A. Weyl, Coloured Glasses, Society of Glass Technology, 1951.
[103] Fanderlík I., Barvení skla, Práh, 2009.

[104] S. Haslbeck, K.-P. Martinek, L. Stievano, F.E. Wagner, Formation of gold nanoparticles in gold ruby glass: The influence of tin, Hyperfine Interact. 165 (2005) 89–94. https://doi.org/10.1007/s10751-006-9246-0.
[105] J. Zhang, T. Sun, C. Zhang, Y. Yang, C. Lin, S. Dai, X. Zhang, W. Ji, F. Chen, Enhanced third-order optical nonlinearity and photon luminescence of Sn2+ in gold nanoparticles embedded chalcogenide glasses, J Mater Sci. 55 (2020) 15882–15893. https://doi.org/10.1007/s10853-020-05124-1.
[106] J. Fonseca, Nanoparticles embedded into glass matrices: glass nanocomposites, Front. Mater. Sci. 16 (2022) 220607. https://doi.org/10.1007/s11706-022-0607-7.
[107] P. Sciau, Nanoparticles in Ancient Materials: The Metallic Lustre Decorations of Medieval Ceramics, in: The Delivery of Nanoparticles, IntechOpen, 2012. https://doi.org/10.5772/34080.
[108] P. Colomban, The Use of Metal Nanoparticles to Produce Yellow, Red and Iridescent Colour, from Bronze Age to Present Times in Lustre Pottery and Glass: Solid State Chemistry, Spectroscopy and Nanostructure, Journal of Nano Research. 8 (2009) 109–132. https://doi.org/10.4028/www.scientific.net/JNanoR.8.109.
[109] T. Som, B. Karmakar, Plasmon tuning of nano-Au in dichroic devitrified antimony glass nanocomposites by refractive index control, Chemical Physics Letters. 479 (2009) 100–104. https://doi.org/10.1016/j.cplett.2009.07.109.
[110] F. Chen, S. Dai, T. Xu, X. Shen, C. Lin, Q. Nie, C. Liu, J. Heo, Surface-plasmon enhanced ultrafast third-order optical nonlinearities in ellipsoidal gold nanoparticles embedded bismuthate glasses, Chemical Physics Letters. 514 (2011) 79–82. https://doi.org/10.1016/j.cplett.2011.08.011.
[111] A. Jagannathan, R. Rajaramakrishna, K.M. Rajashekara, J. Gangareddy, V. Pattar K, V.R. S, E. B, J. Angadi V, J. Kaewkhao, S. Kothan, Investigations on nonlinear optical properties of gold nanoparticles doped fluoroborate glasses for optical limiting applications, Journal of Non-Crystalline Solids. 538 (2020) 120010. https://doi.org/10.1016/j.jnoncrysol.2020.120010.
[112] S. Singla, V.G. Achanta, O.P. Pandey, G. Sharma, Influence of the size of gold nanoparticles dispersed in glass matrix on optical properties, Ceramics International. 46 (2020) 9907–9912. https://doi.org/10.1016/j.ceramint.2019.12.267.
[113] S. Singla, Abhishek, N. Bansal, N. Chopra, G. Sharma, Analysis of gold nanoparticles dispersed bismuth borate glass: effect of size and concentration, J Mater Sci: Mater Electron. 34 (2023) 526. https://doi.org/10.1007/s10854-023-09964-w.
[114] K. Gurushantha, B.N. Swetha, S.B. Kolavekar, A.G. Pramod, A.H. Almuqrin, M.I. Sayyed, G. Jagannath, K. Keshavamurthy, Nonlinear optical properties of gold nanoparticles containing borate glasses at spectral region of surface plasmon resonance, Materials Today Communications. 35 (2023) 106032. https://doi.org/10.1016/j.mtcomm.2023.106032.
[115] K. Gurushantha, G. Jagannath, S.B. Kolavekar, A.G. Pramod, A.H. Almuqrin, M.I. Sayyed, N.L. Murthy, S. Venugopal Rao, K. Keshavamurthy, Gold nanoparticles enhanced femtosecond nonlinear optical properties of sodium borate oxide glasses, Infrared Physics & Technology. 131 (2023) 104663. https://doi.org/10.1016/j.infrared.2023.104663.
[116] K. Gurushantha, H. Patnala, S.B. Kolavekar, V.B. Tangod, D.A. Aloraini, A.H. Almuqrin, M.I. Sayyed, S.V. Rao, A.G. Pramod, G. Jagannath, D.R. Patwari, K.

Keshavamurthy, Annealing and intensity dependent femtosecond nonlinear optical studies of sodium zinc borate oxide glasses incorporated with gold nanoparticles, Journal of Non-Crystalline Solids. 617 (2023) 122484. https://doi.org/10.1016/j.jnoncrysol.2023.122484.
[117] D.A. Aloraini, A.H. Almuqrin, G. Jagannath, M.I. Sayyed, K. Keshavamurthy, A.G. Pramod, K. R Venkatesha Babu, S. Ibrahim Mohammed, S. Venugopal Rao, Annealing duration dependent optical, nonlinear optical, and optical limiting properties of rare-earth doped glasses embedded with gold nanoparticles, Journal of Non-Crystalline Solids. 597 (2022) 121921. https://doi.org/10.1016/j.jnoncrysol.2022.121921.
[118] Y. Al–Hadeethi, A.T. Kutbee, M. Ahmed, M.I. Sayyed, G. Jagannath, Tuning of third-order nonlinear optical susceptibility of Eu3+ doped alkali borate glasses in visible region by embedding gold nanoparticles, Eur. Phys. J. Plus. 137 (2022) 765. https://doi.org/10.1140/epjp/s13360-022-02992-1.
[119] G. Shakhgildyan, L. Avakyan, M. Ziyatdinova, G. Atroshchenko, N. Presnyakova, M. Vetchinnikov, A. Lipatiev, L. Bugaev, V. Sigaev, Tuning the plasmon resonance of gold nanoparticles in phase-separated glass via the local refractive index change, Journal of Non-Crystalline Solids. 566 (2021) 120893. https://doi.org/10.1016/j.jnoncrysol.2021.120893.
[120] G. Shakhgildyan, V. Durymanov, M. Ziyatdinova, G. Atroshchenko, N. Golubev, A. Trifonov, O. Chereuta, L. Avakyan, L. Bugaev, V. Sigaev, Effect of Gold Nanoparticles on the Crystallization and Optical Properties of Glass in ZnO-MgO-Al2O3-SiO2 System, Crystals. 12 (2022) 287. https://doi.org/10.3390/cryst12020287.
[121] K. Dzierżęga, A. Gorczyca, W. Zawadzki, W. Talik, N. Pellerin, B. Diallo, J.-P. Blondeau, S. Pellerin, Optical nonlinearities of silicate oxide glass with gold nanoparticles outside the spectral range of surface plasmon resonance, Optical Materials. 122 (2021) 111712. https://doi.org/10.1016/j.optmat.2021.111712.
[122] V.V. Srabionyan, M. Heinz, S.Y. Kaptelinin, L.A. Avakyan, G.B. Sukharina, A.V. Skidanenko, VasiliyV. Pryadchenko, K.G. Abdulvakhidov, AlexeyS. Mikheykin, VeniaminA. Durymanov, J. Meinertz, J. Ihlemann, M. Dubiel, L.A. Bugaev, Effect of thermal post-treatment on surface plasmon resonance characteristics of gold nanoparticles formed in glass by UV laser irradiation, Journal of Alloys and Compounds. 803 (2019) 354–363. https://doi.org/10.1016/j.jallcom.2019.06.263.
[123] H. Takebe, M. Okamoto, K. Mori, Fabrication of gold ruby glasses using solar panel glass cullet, Journal of the Ceramic Society of Japan. 129 (2021) 590–593. https://doi.org/10.2109/jcersj2.21087.
[124] S.M. Mârza, K. Magyari, S. Bogdan, M. Moldovan, C. Peștean, A. Nagy, A.F. Gal, F. Tăbăran, R.C. Purdoiu, E. Licărete, S. Suarasan, L. Baia, I. Papuc, The Impact of Composites with Silicate-Based Glasses and Gold Nanoparticles on Skin Wound Regeneration, Molecules. 26 (2021) 620. https://doi.org/10.3390/molecules26030620.
[125] S.M. Mârza, K. Magyari, S. Bogdan, M. Moldovan, C. Peștean, A. Nagy, F. Tăbăran, E. Licarete, S. Suarasan, A. Dreanca, L. Baia, I. Papuc, Skin wound regeneration with bioactive glass-gold nanoparticles ointment, Biomed. Mater. 14 (2019) 025011. https://doi.org/10.1088/1748-605X/aafd7d.
[126] D. Lebedev, M. Novomlinsky, V. Kochemirovsky, I. Ryzhkov, I. Anfimova, M. Panov, T. Antropova, Glass/Au Composite Membranes with Gold Nanoparticles Synthesized inside Pores for Selective Ion Transport, Materials. 13 (2020) 1767. https://doi.org/10.3390/ma13071767.

[127] A. Awang, S.K. Ghoshal, M.R. Sahar, R. Arifin, F. Nawaz, Non-spherical gold nanoparticles mediated surface plasmon resonance in Er3+ doped zinc–sodium tellurite glasses: Role of heat treatment, Journal of Luminescence. 149 (2014) 138–143. https://doi.org/10.1016/j.jlumin.2014.01.027.
[128] R.M. Gunji, E.V. de A. Santos, C.D.S. Bordon, J.A.M. Garcia, L.A. Gómez-Malagón, L.R.P. Kassab, Germanate glass layer containing Eu3+ ions and gold nanoparticles for enhanced silicon solar cell performance, Journal of Luminescence. 226 (2020) 117497. https://doi.org/10.1016/j.jlumin.2020.117497.
[129] M. Gajc, H.B. Surma, A. Klos, K. Sadecka, K. Orlinski, A.E. Nikolaenko, K. Zdunek, D.A. Pawlak, Nanoparticle Direct Doping: Novel Method for Manufacturing Three-Dimensional Bulk Plasmonic Nanocomposites, Advanced Functional Materials. 23 (2013) 3443–3451. https://doi.org/10.1002/adfm.201203116.
[130] M. Gajc, H.B. Surma, D.A. Pawlak, Optically-active metastable defects in volumetric nanoplasmonic composites, Sci Rep. 8 (2018) 13425. https://doi.org/10.1038/s41598-018-30803-0.
[131] P. Mazzoldi, C. Sada, A trip in the history and evolution of ion-exchange process, Materials Science and Engineering: B. 149 (2008) 112–117. https://doi.org/10.1016/j.mseb.2007.11.038.
[132] S. Berneschi, G.C. Righini, S. Pelli, Towards a Glass New World: The Role of Ion-Exchange in Modern Technology, Applied Sciences. 11 (2021) 4610. https://doi.org/10.3390/app11104610.
[133] G.C. Righini, J. Liñares, Active and Quantum Integrated Photonic Elements by Ion Exchange in Glass, Applied Sciences. 11 (2021) 5222. https://doi.org/10.3390/app11115222.
[134] R.M. Almeida, A.C. Marques, The potential of ion exchange in sol–gel derived photonic materials and structures, Materials Science and Engineering: B. 149 (2008) 118–122. https://doi.org/10.1016/j.mseb.2007.11.026.
[135] A. Quaranta, E. Cattaruzza, F. Gonella, Modelling the ion exchange process in glass: Phenomenological approaches and perspectives, Materials Science and Engineering: B. 149 (2008) 133–139. https://doi.org/10.1016/j.mseb.2007.11.016.
[136] S. Stanek, P. Nekvindova, B. Svecova, S. Vytykacova, M. Mika, J. Oswald, O. Barkmann, J. Spirkova, The influence of silver ion exchange on the luminescence properties of Er-Yb silicate glasses, Optical Materials. 72 (2017) 183–189. http://dx.doi.org/10.1016/j.optmat.2017.05.053.
[137] P. Tresnakova, H. Malichova, J. Spirkova, M. Mika, Fabrication of optical layers containing Er(III) and Cu(I) in silicate glasses, Journal of Physics and Chemistry of Solids. 68 (2007) 1276–1279. https://doi.org/10.1016/j.jpcs.2007.03.051.
[138] P. Vařák, S. Vytykáčová, P. Nekvindová, A. Michalcová, P. Malinský, The influence of copper and silver in various oxidation states on the photoluminescence of Ho3+/Yb3+ doped zinc-silicate glasses, Optical Materials. 91 (2019) 253–260. https://doi.org/10.1016/j.optmat.2019.03.029.
[139] L. Karvonen, J. Rönn, S. Kujala, Y. Chen, A. Säynätjoki, A. Tervonen, Y. Svirko, S. Honkanen, High non-resonant third-order optical nonlinearity of Ag–glass nanocomposite fabricated by two-step ion exchange, Optical Materials. 36 (2013) 328–332. https://doi.org/10.1016/j.optmat.2013.09.016.

[140] W. Xiang, H. Gao, L. Ma, X. Ma, Y. Huang, L. Pei, X. Liang, Valence State Control and Third-Order Nonlinear Optical Properties of Copper Embedded in Sodium Borosilicate Glass, ACS Appl. Mater. Interfaces. 7 (2015) 10162–10168. https://doi.org/10.1021/acsami.5b00218.
[141] P. Kumar, M.C. Mathpal, S. Hamad, S.V. Rao, J.H. Neethling, A.J. van Vuuren, E.G. Njoroge, R.E. Kroon, W.D. Roos, H.C. Swart, Cu nanoclusters in ion exchanged soda-lime glass: Study of SPR and nonlinear optical behavior for photonics, Applied Materials Today. 15 (2019) 323–334. https://doi.org/10.1016/j.apmt.2019.02.016.
[142] P. Mazzoldi, G.W. Arnold, G. Battaglin, R. Bertoncello, F. Gonella, Peculiarities and application perspectives of metal-ion implants in glasses, Nuclear Instruments and Methods in Physics Research Section B: Beam Interactions with Materials and Atoms. 91 (1994) 478–492. https://doi.org/10.1016/0168-583X(94)96273-1.
[143] P. Mazzoldi, G. w. Arnold, G. Battaglin, F. Gonella, R. f. Haglund, Metal nanocluster formation by ion implantation in silicate glasses: nonlinear optical applications, J. Nonlinear Optic. Phys. Mat. 05 (1996) 285–330. https://doi.org/10.1142/S0218863596000209.
[144] G. Battaglin, A. Boscolo-Boscoletto, P. Mazzoldi, C. Meneghini, G.W. Arnold, Gold nanocluster formation in silicate glasses by low fluence ion implantation and annealing, Nuclear Instruments and Methods in Physics Research Section B: Beam Interactions with Materials and Atoms. 116 (1996) 527–530. https://doi.org/10.1016/0168-583X(96)00101-2.
[145] A. Lin, D.H. Son, I.H. Ahn, G.H. Song, W.-T. Han, Visible to infrared photoluminescence from gold nanoparticles embedded in germano-silicate glass fiber, Opt. Express, OE. 15 (2007) 6374–6379. https://doi.org/10.1364/OE.15.006374.
[146] R.A. Wood, P.D. Townsend, N.D. Skelland, D.E. Hole, J. Barton, C.N. Afonso, Annealing of ion implanted silver colloids in glass, Journal of Applied Physics. 74 (1993) 5754–5756. https://doi.org/10.1063/1.354194.
[147] R.H. Magruder III, L. Yang, R.F. Haglund Jr., C.W. White, L. Yang, R. Dorsinville, R.R. Alfano, Optical properties of gold nanocluster composites formed by deep ion implantation in silica, Applied Physics Letters. 62 (1993) 1730–1732. https://doi.org/10.1063/1.109588.
[148] A. Stepanov, Nonlinear Optical Properties of Implanted Metal Nanoparticles in Various Transparent Matrixes: A Review, Rev. Adv. Mater. Sci. 27 (2011) 115–145.
[149] B. Svecova, P. Vindova, S. Stanek, S. Vytykacova, A. Mackova, P. Malinsky, R. Miksova, M. Janecek, J. Pesicka, J. Spirkova, The Effect of Various Silicate-Glass Matrixes on Gold-Nanoparticle Formation, Ceram.-Silik. 61 (2017) 52–58. https://doi.org/10.13168/cs.2016.0060.
[150] P. Malinský, A. Macková, J. Bočan, B. Švecová, P. Nekvindová, Au implantation into various types of silicate glasses, Nuclear Instruments and Methods in Physics Research Section B: Beam Interactions with Materials and Atoms. 267 (2009) 1575–1578. https://doi.org/10.1016/j.nimb.2009.01.161.
[151] S.D. Stookey, Photosensitive Glass, Ind. Eng. Chem. 41 (1949) 856–861. https://doi.org/10.1021/ie50472a042.
[152] M. Eichelbaum, K. Rademann, R. Müller, M. Radtke, H. Riesemeier, W. Görner, On the Chemistry of Gold in Silicate Glasses: Studies on a Nonthermally Activated Growth of

Gold Nanoparticles, Angew. Chem. Int. Ed. 44 (2005) 7905–7909. https://doi.org/10.1002/anie.200502174.
[153] N.F. Borrelli, Glass-Ceramics by Photosensitive Processes, International Journal of Applied Glass Science. 6 (2015) 268–274. https://doi.org/10.1111/ijag.12130.
[154] D. Ye, Q. Jian-Rong, The photosensitive effect of Ce on the precipitation of Ag nanoparticles induced by femtosecond laser in silicate glass, Chinese Phys. B. 18 (2009) 2858. https://doi.org/10.1088/1674-1056/18/7/039.
[155] A. Ruivo, C. Gomes, A. Lima, M.L. Botelho, R. Melo, A. Belchior, A. Pires de Matos, Gold nanoparticles in ancient and contemporary ruby glass, Journal of Cultural Heritage. 9 (2008) e134–e137. https://doi.org/10.1016/j.culher.2008.08.003.
[156] M. Epifani, C. Giannini, L. Tapfer, L. Vasanelli, Sol–Gel Synthesis and Characterization of Ag and Au Nanoparticles in SiO2, TiO2, and ZrO2 Thin Films, Journal of the American Ceramic Society. 83 (2000) 2385–2393. https://doi.org/10.1111/j.1151-2916.2000.tb01566.x.
[157] R.E.P. de Oliveira, N. Sjödin, M. Fokine, W. Margulis, C.J.S. de Matos, L. Norin, Fabrication and Optical Characterization of Silica Optical Fibers Containing Gold Nanoparticles, ACS Appl. Mater. Interfaces. 7 (2015) 370–375. https://doi.org/10.1021/am506327q.
[158] A. Ruivo, M.G. Ventura, M.D.R. Gomes da Silva, C.A.T. Laia, Synthesis of gold nanoparticles in sol–gel glass porogens containing [bmim][BF4] ionic liquid, J Sol-Gel Sci Technol. 68 (2013) 234–244. https://doi.org/10.1007/s10971-013-3159-6.
[159] J.C. Almeida, E.J.C. Davim, I.M.M. Salvado, M.H.V. Fernandes, F.M. Costa, F. Rey-García, L.M. Francisco, A.B. Lopes, Red ruby glass from gold nanoparticles obtained by LASiS – a new approach., Journal of Non-Crystalline Solids. 537 (2020) 119987. https://doi.org/10.1016/j.jnoncrysol.2020.119987.
[160] H. Lundén, A. Liotta, D. Chateau, F. Lerouge, F. Chaput, S. Parola, C. Bränlund, Z. Ghadyani, M. Kildemo, M. Lindgren, C. Lopes, Dispersion and self-orientation of gold nanoparticles in sol–gel hybrid silica – optical transmission properties, J. Mater. Chem. C. 3 (2015) 1026–1034. https://doi.org/10.1039/C4TC02353F.
[161] S. Kumar Medda, S. De, G. De, Synthesis of Au nanoparticle doped SiO 2 –TiO 2 films: tuning of Au surface plasmon band position through controlling the refractive index, Journal of Materials Chemistry. 15 (2005) 3278–3284. https://doi.org/10.1039/B506399J.
[162] Bring T., Red Glass Coloration–A Colorimetric and Structural Study, doctoral, Stockholm University, 2006.
[163] C. Saiyasombat, Preparation, structure and properties of gold-based "ruby" sodium silicate glass: A model metal-glass nano-composite, in: 2015. https://www.semanticscholar.org/paper/Preparation%2C-structure-and-properties-of-gold-based-Saiyasombat/476d7d4b0f298380ac1f71059cc4cddd3be440de (accessed July 24, 2023).
[164] L. HENNET, D. Moritz, J.K.R. Weber, A. Meyer, High-Temperature Levitated Materials, in: Experimental Methods in the Physical Sciences, 2017: pp. 583–636. https://doi.org/10.1016/B978-0-12-805324-9.00010-8.
[165] B. Gratuze, Glass Characterization Using Laser Ablation-Inductively Coupled Plasma-Mass Spectrometry Methods, in: L. Dussubieux, M. Golitko, B. Gratuze (Eds.), Recent Advances in Laser Ablation ICP-MS for Archaeology, Springer, Berlin, Heidelberg, 2016: pp. 179–196. https://doi.org/10.1007/978-3-662-49894-1_12.

[166] D. Taylor, Thermal expansion data: III. Sesquioxides, M_2O_3, with the corundum and the A-,B- and C-M_2O_3 structures., British Ceramic Transactions and Journal. 83 (1984) 92–98.
[167] A. Hrubý, Evaluation of glass-forming tendency by means of DTA, Czechoslovak Journal of Physics B. 22 (1972) 1187–1193. https://doi.org/10.1007/BF01690134.
[168] G.W. Scherer, Use of the Adam-Gibbs Equation in the Analysis of Structural Relaxation, Journal of the American Ceramic Society. 67 (1984) 504–511. https://doi.org/10.1111/j.1151-2916.1984.tb19643.x.
[169] Y. Yue, R. von der Ohe, S.L. Jensen, Fictive temperature, cooling rate, and viscosity of glasses, J. Chem. Phys. 120 (2004) 8053–8059. https://doi.org/10.1063/1.1689951.
[170] R. Al-Mukadam, D. Di Genova, H. Bornhöft, J. Deubener, High rate calorimetry derived viscosity of oxide melts prone to crystallization, Journal of Non-Crystalline Solids. 536 (2020) 119992. https://doi.org/10.1016/j.jnoncrysol.2020.119992.
[171] D. Di Genova, A. Zandona, J. Deubener, Unravelling the effect of nano-heterogeneity on the viscosity of silicate melts: Implications for glass manufacturing and volcanic eruptions, Journal of Non-Crystalline Solids. 545 (2020) 120248. https://doi.org/10.1016/j.jnoncrysol.2020.120248.
[172] R. Al-Mukadam, A. Zandona, J. Deubener, Kinetic fragility of pure TeO2 glass, Journal of Non-Crystalline Solids. 554 (2021) 120595. https://doi.org/10.1016/j.jnoncrysol.2020.120595.
[173] L. Shartsis, S. Spinner, W. Capps, Density, Expansivity, and Viscosity of Molten Alkali Silicates, Journal of the American Ceramic Society. 35 (1952) 155–160. https://doi.org/10.1111/j.1151-2916.1952.tb13090.x.
[174] J.C. Mauro, Y. Yue, A.J. Ellison, P.K. Gupta, D.C. Allan, Viscosity of glass-forming liquids, Proceedings of the National Academy of Sciences. 106 (2009) 19780–19784. https://doi.org/10.1073/pnas.0911705106.
[175] M.L.F. Nascimento, L.A. Souza, E.B. Ferreira, E.D. Zanotto, Can glass stability parameters infer glass forming ability?, Journal of Non-Crystalline Solids. 351 (2005) 3296–3308. https://doi.org/10.1016/j.jnoncrysol.2005.08.013.
[176] F.C. Kracek, The Binary System Li2O–SiO2, J. Phys. Chem. 34 (1930) 2641–2650. https://doi.org/10.1021/j150318a001.
[177] S.S. Kim, T.H. Sanders Jr., Thermodynamic Modeling of Phase Diagrams in Binary Alkali Silicate Systems, Journal of the American Ceramic Society. 74 (1991) 1833–1840. https://doi.org/10.1111/j.1151-2916.1991.tb07796.x.
[178] M. Blander, A.D. Pelton, Thermodynamic analysis of binary liquid silicates and prediction of ternary solution properties by modified quasichemical equations, Geochimica et Cosmochimica Acta. 51 (1987) 85–95. https://doi.org/10.1016/0016-7037(87)90009-3.
[179] R.H. Lamoreaux, D.L. Hildenbrand, L. Brewer, High-Temperature Vaporization Behavior of Oxides II. Oxides of Be, Mg, Ca, Sr, Ba, B, Al, Ga, In, Tl, Si, Ge, Sn, Pb, Zn, Cd, and Hg, Journal of Physical and Chemical Reference Data. 16 (1987) 419–443. https://doi.org/10.1063/1.555799.
[180] Leo. Brewer, Thermodynamic Properties of the Oxides and their Vaporization Processes., Chem. Rev. 52 (1953) 1–75. https://doi.org/10.1021/cr60161a001.

[181] R.H. Lamoreaux, D.L. Hildenbrand, High Temperature Vaporization Behavior of Oxides. I. Alkali Metal Binary Oxides, Journal of Physical and Chemical Reference Data. 13 (1984) 151–173. https://doi.org/10.1063/1.555706.
[182] P. Annamalai, N. Shankar, R. Cole, R.S. Subramanian, Bubble migration inside a liquid drop in a space laboratory, Applied Scientific Research. 38 (1982) 179–186. https://doi.org/10.1007/BF00385947.
[183] D. Brone, R. Cole, Bubble trajectories in rotating drops, Advances in Space Research. 11 (1991) 243–246. https://doi.org/10.1016/0273-1177(91)90290-Z.
[184] J.S. Ruggles, R.G. Cook, R. Cole, Microgravity bubble migration in rotating flows, Journal of Spacecraft and Rockets. 27 (1990) 43–47. https://doi.org/10.2514/3.26103.
[185] M. Hubert, Industrial Glass Processing and Fabrication, in: J.D. Musgraves, J. Hu, L. Calvez (Eds.), Springer Handbook of Glass, Springer International Publishing, Cham, 2019: pp. 1195–1231. https://doi.org/10.1007/978-3-319-93728-1_34.
[186] R.B. JUCHA, D. POWERS, T. McNEIL, R.S. SUBRAMANIAN, R. COLE, Bubble Rise in Glassmelts, Journal of the American Ceramic Society. 65 (1982) 289–292. https://doi.org/10.1111/j.1151-2916.1982.tb10446.x.
[187] R.W. RICKER, E.F. OSBORN, Additional Phase Equilibrium Data for the System CaO-MgO-SiO2, Journal of the American Ceramic Society. 37 (1954) 133–139. https://doi.org/10.1111/j.1151-2916.1954.tb14011.x.
[188] K. Kamiya, T. Yoko, Y. Hashimoto, S. Sakka, Crystallization behavior of xNa2O· (1−x)GeO2 glasses and melts with x of 0 to 0.30, Materials Research Bulletin. 23 (1988) 363–369. https://doi.org/10.1016/0025-5408(88)90010-4.
[189] R.M. SMART, F.P. GLASSER, Compound Formation and Phase Equilibria in the System PbO-SiO2, Journal of the American Ceramic Society. 57 (1974) 378–382. https://doi.org/10.1111/j.1151-2916.1974.tb11416.x.
[190] K.B. Kavaklıoğlu, S. Aydin, M. Çelikbilek, A.E. Ersundu, The TeO2-Na2O System: Thermal Behavior, Structural Properties, and Phase Equilibria, International Journal of Applied Glass Science. 6 (2015) 406–418. https://doi.org/10.1111/ijag.12103.
[191] V.J. Fratello, C.D. Brandle, Physical properties of a Y3Al5012 melt, Journal of Crystal Growth. 128 (1993) 1006–1010. https://doi.org/10.1016/S0022-0248(07)80087-X.
[192] A.K. Chatterjee, G.I. Zhmoidin, The phase equilibrium diagram of the system CaO-Al2O3-CaF2, Journal of Materials Science. 7 (1972) 93–97. https://doi.org/10.1007/BF00549555.
[193] G. Eriksson, A.D. Pelton, Critical evaluation and optimization of the thermodynamic properties and phase diagrams of the CaO-Al2O3, Al2O3-SiO2, and CaO-Al2O3-SiO2 systems, Metallurgical Transactions B. 24 (1993) 807–816. https://doi.org/10.1007/BF02663141.
[194] W. Schreyer, J.F. Schairer, Metastable solid solutions with quartz-type structures on the join SiO2–MgAl2O4, Zeitschrift Für Kristallographie - Crystalline Materials. 116 (1961) 60–82. https://doi.org/10.1524/zkri.1961.116.1-2.60.
[195] M.L.F. Nascimento, E. Dutra Zanotto, Does viscosity describe the kinetic barrier for crystal growth from the liquidus to the glass transition?, J. Chem. Phys. 133 (2010) 174701. https://doi.org/10.1063/1.3490793.
[196] M. Cassetta, D. Di Genova, M. Zanatta, T. Boffa Ballaran, A. Kurnosov, M. Giarola, G. Mariotto, Estimating the viscosity of volcanic melts from the vibrational properties of their

parental glasses, Scientific Reports. 11 (2021) 13072. https://doi.org/10.1038/s41598-021-92407-5.
[197] G. Urbain, Viscosité de liquides du système CaO-Al2O3, Rev. Int. Hautes Tempér. Réfract. Fr. 20 (1983) 135–139.
[198] V. Piacente, J. Matoušek, Alkali vapor pressures over some simple silicate melts, Collect. Czech. Chem. Commun. 48 (1983) 1528–1531. https://doi.org/10.1135/cccc19831528.
[199] R.G.C. Beerkens, Modeling the Kinetics of Volatilization from Glass Melts, Journal of the American Ceramic Society. 84 (2001) 1952–1960. https://doi.org/10.1111/j.1151-2916.2001.tb00942.x.
[200] R.J. CHARLES, Activities in Li2O-, Na2O, and K2O-SiO2 Solutions, Journal of the American Ceramic Society. 50 (1967) 631–641. https://doi.org/10.1111/j.1151-2916.1967.tb15018.x.
[201] P.A. Sossi, S. Klemme, H.St.C. O'Neill, J. Berndt, F. Moynier, Evaporation of moderately volatile elements from silicate melts: experiments and theory, Geochimica et Cosmochimica Acta. 260 (2019) 204–231. https://doi.org/10.1016/j.gca.2019.06.021.
[202] J. Badro, P.A. Sossi, Z. Deng, S. Borensztajn, N. Wehr, F.J. Ryerson, Experimental investigation of elemental and isotopic evaporation processes by laser heating in an aerodynamic levitation furnace, Comptes Rendus. Geoscience. 353 (2021) 101–114.
[203] R.A. Mendybaev, F.M. Richter, R.B. Georg, P.E. Janney, M.J. Spicuzza, A.M. Davis, J.W. Valley, Experimental evaporation of Mg- and Si-rich melts: Implications for the origin and evolution of FUN CAIs, Geochimica et Cosmochimica Acta. 123 (2013) 368–384. https://doi.org/10.1016/j.gca.2013.06.044.
[204] Z. Shan, S. Liu, H. Tao, Y. Yue, Mixed alkaline-earth effects on several mechanical and thermophysical properties of aluminate glasses and melts, Journal of the American Ceramic Society. 102 (2019) 1128–1136. https://doi.org/10.1111/jace.15975.
[205] Z. Zhang, Y. Xiao, J. Voncken, Y. Yang, R. Boom, N. Wang, Z. Zou, Phase Equilibria in the Na2O–CaO–SiO2 System, Journal of the American Ceramic Society. 94 (2011) 3088–3093. https://doi.org/10.1111/j.1551-2916.2011.04442.x.
[206] H. Yu, Z. Jin, Q. Chen, M. Hillert, Thermodynamic Assessment of the Lithium-Borate System, Journal of the American Ceramic Society. 83 (2000) 3082–3088. https://doi.org/10.1111/j.1151-2916.2000.tb01686.x.
[207] A.B. Meshalkin, A.B. Kaplun, B.I. Kidyarov, The influence of the compounds dissociation in melting point on melt supercooling, Journal of Crystal Growth. 310 (2008) 1362–1365. https://doi.org/10.1016/j.jcrysgro.2007.11.195.
[208] M.K. MURTHY, J. AGUAYO, Studies in Germanium Oxide Systems: II, Phase Equilibria in the System Na2O—GeO2, Journal of the American Ceramic Society. 47 (1964) 444–447. https://doi.org/10.1111/j.1151-2916.1964.tb14433.x.
[209] M.K. MURTHY, J. IP, Studies in Germanium Oxide Systems: I, Phase Equilibria in the System Li2O—GeO2, Journal of the American Ceramic Society. 47 (1964) 328–331. https://doi.org/10.1111/j.1151-2916.1964.tb12995.x.
[210] V.V. Safonov, V.V. Kravchenko, N.V. Filatkina, M.M. Bryksina-Lyamina, N.G. Chaban, Zh. Neorg. Khim. 34 (1989) 2920–2923.
[211] R.L. Cormia, J.D. Mackenzie, D. Turnbull, Viscous Flow and Melt Allotropy of Phosphorus Pentoxide, Journal of Applied Physics. 34 (1963) 2245–2248. https://doi.org/10.1063/1.1702721.

[212] J. Kropiwnicka, Phase equilibria in the system La2O3-Na2O-P2O5: Binary phase diagram La(PO3)3-NaPO3, Journal of Thermal Analysis. 34 (1988) 1405–1412. https://doi.org/10.1007/BF01914364.
[213] L. Muñoz-Senovilla, F. Muñoz, Behaviour of viscosity in metaphosphate glasses, Journal of Non-Crystalline Solids. 385 (2014) 9–16. https://doi.org/10.1016/j.jnoncrysol.2013.10.021.
[214] L. Shartsis, S. Spinner, W. Capps, Density, Expansivity, and Viscosity of Molten Alkali Silicates, Journal of the American Ceramic Society. 35 (1952) 155–160. https://doi.org/10.1111/j.1151-2916.1952.tb13090.x.
[215] E.M. Erbe, D.E. Day, Chemical durability of Y2O3-Al2O3-SiO2 glasses for thein vivo delivery of beta radiation, J. Biomed. Mater. Res. 27 (1993) 1301–1308. https://doi.org/10.1002/jbm.820271010.
[216] P. McMillan, A Raman spectroscopic study of glasses in the system CaO–MgO–SiO2, American Mineralogist. 69 (1984) 645–659.
[217] D.W. Matson, S.K. Sharma, J.A. Philpotts, The structure of high-silica alkali-silicate glasses. A Raman spectroscopic investigation, Journal of Non-Crystalline Solids. 58 (1983) 323–352. https://doi.org/10.1016/0022-3093(83)90032-7.
[218] C. O'Shaughnessy, G.S. Henderson, H.W. Nesbitt, G.M. Bancroft, D.R. Neuville, The influence of modifier cations on the Raman stretching modes of Qn species in alkali silicate glasses, Journal of the American Ceramic Society. 103 (2020) 3991–4001. https://doi.org/10.1111/jace.17081.
[219] C. Huang, E.C. Behrman, Structure and properties of calcium aluminosilicate glasses, Journal of Non-Crystalline Solids. 128 (1991) 310–321. https://doi.org/10.1016/0022-3093(91)90468-L.
[220] S. Petrescu, M. Constantinescu, E.M. Anghel, I. Atkinson, M. Olteanu, M. Zaharescu, Structural and physico-chemical characterization of some soda lime zinc alumino-silicate glasses, Journal of Non-Crystalline Solids. 358 (2012) 3280–3288. https://doi.org/10.1016/j.jnoncrysol.2012.09.001.
[221] D.R. Neuville, L. Cormier, V. Montouillout, P. Florian, F. Millot, J.-C. Rifflet, D. Massiot, Amorphous materials: Properties, structure, and durability: Structure of Mg- and Mg/Ca aluminosilicate glasses: 27Al NMR and Raman spectroscopy investigations, American Mineralogist. 93 (2008) 1721–1731. https://doi.org/10.2138/am.2008.2867.
[222] R.A. Barrio, F.L. Galeener, E. Martínez, R.J. Elliott, Regular ring dynamics in AX 2 tetrahedral glasses, Phys. Rev. B. 48 (1993) 15672–15689. https://doi.org/10.1103/PhysRevB.48.15672.
[223] A.G. KALAMPOUNIAS, IR and Raman spectroscopic studies of sol–gel derived alkaline-earth silicate glasses, Bull Mater Sci. 34 (2011) 299–303. https://doi.org/10.1007/s12034-011-0064-x.
[224] P. Colomban, A. Tournie, L. Bellot-Gurlet, Raman identification of glassy silicates used in ceramics, glass and jewellery: a tentative differentiation guide, J. Raman Spectrosc. 37 (2006) 841–852. https://doi.org/10.1002/jrs.1515.
[225] S. Chenu, E. Véron, C. Genevois, G. Matzen, T. Cardinal, A. Etienne, D. Massiot, M. Allix, Tuneable Nanostructuring of Highly Transparent Zinc Gallogermanate Glasses and Glass-Ceramics, Advanced Optical Materials. 2 (2014) 364–372. https://doi.org/10.1002/adom.201400007.

[226] E. Paul, Intrinsic Point Defects in Zinc Oxide: Modeling of Structural, Electronic, Thermodynamic and Kinetic Properties, Ph.D. Thesis, Technischen Universität Darmstadt, 2006.
[227] S. Fujita, S. Tanabe, Fabrication, microstructure and optical properties of Er3+:YAG glass–ceramics, Optical Materials. 32 (2010) 886–890. https://doi.org/10.1016/j.optmat.2010.01.014.
[228] H. Dong, Y. Chen, Y. Jiao, Q. Zhou, Y. Cheng, H. Zhang, Y. Lu, S. Wang, C. Yu, L. Hu, Nanocrystalline Yb:YAG-Doped Silica Glass with Good Transmittance and Significant Spectral Performance Enhancements, Nanomaterials. 12 (2022) 1263. https://doi.org/10.3390/nano12081263.
[229] Q. Zheng, Y. Liu, M. Li, Z. Liu, Y. Hu, X. Zhang, W. Deng, M. Wang, Crystallization behavior and IR structure of yttrium aluminosilicate glasses, Journal of the European Ceramic Society. 40 (2020) 463–471. https://doi.org/10.1016/j.jeurceramsoc.2019.09.044.
[230] S. Ahmad, M.M. Mahmoud, H.J. Seifert, Crystallization of two rare-earth aluminosilicate glass-ceramics using conventional and microwave heat-treatments, Journal of Alloys and Compounds. 797 (2019) 45–57. https://doi.org/10.1016/j.jallcom.2019.05.100.
[231] M.C. Paul, S. Bysakh, S. Das, S.K. Bhadra, M. Pal, S. Yoo, M.P. Kalita, A.J. Boyland, J.K. Sahu, Yb2O3-doped YAG nano-crystallites in silica-based core glass matrix of optical fiber preform, Materials Science and Engineering: B. 175 (2010) 108–119. https://doi.org/10.1016/j.mseb.2010.07.013.
[232] F. d'Acapito, W. Blanc, B. Dussardier, Different Er3+ environments in Mg-based nanoparticle-doped optical fibre preforms, Journal of Non-Crystalline Solids. 401 (2014) 50–53. https://doi.org/10.1016/j.jnoncrysol.2013.12.040.
[233] M. Cabié, T. Neisius, W. Blanc, Combined FIB/SEM tomography and TEM analysis to characterize high aspect ratio Mg-silicate particles inside silica-based optical fibres, Materials Characterization. 178 (2021) 111261. https://doi.org/10.1016/j.matchar.2021.111261.
[234] M. Vermillac, J.-F. Lupi, F. Peters, M. Cabié, P. Vennéguès, C. Kucera, T. Neisius, J. Ballato, W. Blanc, Fiber-draw-induced elongation and break-up of particles inside the core of a silica-based optical fiber, Journal of the American Ceramic Society. 100 (2017) 1814–1819.
[235] M.C. Paul, S. Bysakh, S. Das, A. Dhar, M. Pal, S.K. Bhadra, J.K. Sahu, A.V. Kir'yanov, F. d'Acapito, Recent Developments in Rare-Earths Doped Nano-Engineered Glass Based Optical Fibers for High Power Fiber Lasers, TRANSACTIONS OF THE INDIAN CERAMIC SOCIETY. 75 (2016) 195–208. https://doi.org/10.1080/0371750X.2016.1251852.
[236] V. Fuertes, N. Grégoire, P. Labranche, S. Gagnon, R. Wang, Y. Ledemi, S. LaRochelle, Y. Messaddeq, Engineering nanoparticle features to tune Rayleigh scattering in nanoparticles-doped optical fibers, Sci Rep. 11 (2021) 9116. https://doi.org/10.1038/s41598-021-88572-2.
[237] T. Cheng, M. Liao, X. Xue, J. Li, W. Gao, X. Li, D. Chen, S. Zheng, Y. Pan, T. Suzuki, Y. Ohishi, A silica optical fiber doped with yttrium aluminosilicate nanoparticles for supercontinuum generation, Optical Materials. 53 (2016) 39–43. https://doi.org/10.1016/j.optmat.2016.01.018.

[238] S. Moniri, M. Hantehzadeh, M. Ghoranneviss, M. Asadi Asadabad, Au-Pt alloy nanoparticles obtained by nanosecond laser irradiation of gold and platinum bulk targets in an ethylene glycol solution, The European Physical Journal Plus. 132 (2017) 318. https://doi.org/10.1140/epjp/i2017-11582-9.
[239] M.B. Volf, Chemie skla: Určeno [také] pro stud. vys. škol, SNTL, 1978.
[240] J.-P. Blondeau, Mathematical modelling of absorption spectra of AuNPs in glass, (n.d.).
[241] MiePlot, (n.d.). http://www.philiplaven.com/mieplot.htm (accessed October 1, 2023).

LIST OF USED ABBREVIATIONS

ADL	Aerodynamic levitation coupled to laser heating
AgAuNPs	Nanoparticles of a silver-gold alloy
AIMD	Ab initio molecular dynamics
AuNP(s)	Gold nanoparticle(s)
BOx	Bridging oxygens
CEMHTI	Extreme Conditions and Materials: High Temperature and Irradiation
CNRS	French National Centre for Scientific Research
CVD	Chemical vapour deposition method
DFT	Density functional theory
DSC	Differential scanning calorimetry
DTA	Differential thermal analysis
EDS	Energy dispersive X-ray spectrometer
EDX	Energy-dispersive X-ray spectroscopy
EMPA	Electron probe micro-analysis
EXAFS	Extended x-ray absorption fine structure
FEG	Field emission gun
FWHM	Full width at half maximum
LA-ICP-MS	Laser ablation inductively coupled plasma mass spectrometry
LS	Lithium silicate
LSPR	Localized Surface Plasmon Resonance
LYAS	Lithium yttrium aluminosilicate
MAS-NMR	Magic angle spinning nuclear magnetic resonance
MNP(s)	Metal nanoparticle(s)
MQ	Melt-quenching
NBOx	Non-bridging oxygens
NIR	Near-infrared
NLO	Non-linear optics
NMR	Nuclear magnetic resonance
NP(s)	Nanoparticle(s)
OLCAO	Orthogonalized linear combination of atomic orbitals
OM	Optical microscopy
PIPS	Precision ion polishing system
rpm	Revolutions per minute
SCL	Supercooled liquid
SEM	Scanning electron microscopy
SERS	Surface-enhanced Raman spectroscopy
SPR	Surface Plasmon Resonance
SPS	Spark Plasma Sintering
STA	Simultaneous thermal analysis
STEM	scanning transmission electron microscopy
STM	Scanning tunnelling microscope
TEC	Thermal expansion coefficient

TEM	Transmission electron microscopy
TG	Thermogravimetric analysis
UCT	University of Chemistry and Technology
VT-XRD	Variable temperature X-ray diffraction
WDS	Wave dispersive X-ray spectrometers
XAFS	X-ray absorption fine structure
XRD	X-ray diffraction
YAG	Yttrium-aluminium garnet
YAP	Yttrium-aluminium perovskite
YAS	Yttrium aluminosilicate

LIST OF SYMBOLS

Symbol	Meaning	Unit
D	diameter	m
E_b	bonding energy	J mol^{-1}
I	nucleation rate	number m^{-3} s^{-1}
K_{gl}	glass stability parameter according to Hrubý	-
Q_{abs}	efficiency of absorption	-
Q_{ext}	efficiency of extinction	-
Q_n	Q-units, Q=1,2,3,4	-
Q_{sca}	efficiency of scattering	-
T	temperature	°C
T_c	glass crystallization onset	°C
T_g	glass transition temperature	°C
T_l	liquidus temperature	°C
T_m	melting temperature	°C
$T_{m,\Sigma}$	melting point of the target multicomponent glass	°C
V	crystal growth rate	m s^{-1}
k	Scherrer's constant	-
n	refractive index	-
r_{evap}	rate of evaporation; experimental parameter	-
β	full width at half maximum (FWHM) of the diffraction peak	m
Δ_{evap}	difference between highest and lowest revap in studied glass	-
η	viscosity	Pa s
$\eta(T_x)$	viscosity at temperature x	Pa s
θ	diffraction angle	°
λ	wavelength	m

LIST OF TABLES

LIST OF FIGURES

APPENDICES

Table 26 *Overview of samples prepared by ADL*

Sample	System	SiO_2	Al_2O_3	Y_2O_3	CaO	Li_2O	Na_2O	K2O	Au	SnO_2
JB1	Y-Al-Si	35.211	49.798	14.991	-	-	-	-	-	-
JB2	Y-Al-Si	53.929	35.411	10.660	-	-	-	-	-	-
JB3	Y-Al-Si	68.493	24.217	7.290	-	-	-	-	-	-
JB4	Y-Al-Si	80.148	15.259	4.593	-	-	-	-	-	-
JB5	Y-Al-Si	89.686	7.928	2.386	-	-	-	-	-	-
JB6	Y-Al-Si	45.744	32.347	21.909	-	-	-	-	-	-
JB7	Y-Al-Si	54.139	22.332	23.529	-	-	-	-	-	-
JB8	Y-Al-Si	61.950	13.559	24.490	-	-	-	-	-	-
JB9	Y-Al-Si	68.169	19.212	12.620	-	-	-	-	-	-
LDS	Li-Si	66.670	-	-	-	33.330	-	-	-	-
LSPOD	Li-Al-Si	57.766	7.765	-	-	34.469	-	-	-	-
SL 1	Na-Ca-Si	74.809	-	-	10.687	-	14.504	-	0.303	-
SL 0,1	Na-Ca-Si	74.809	-	-	10.687	-	14.504	-	0.030	-
JB2 0,125	Y-Al-Si	53.929	35.411	10.660	-	-	-	-	0.059	-
JB2 0,25	Y-Al-Si	53.929	35.411	10.660	-	-	-	-	0.117	-
JB2 0,5	Y-Al-Si	53.929	35.411	10.660	-	-	-	-	0.234	-
JB2 1	Y-Al-Si	53.929	35.411	10.660	-	-	-	-	0.468	-
JB2 2	Y-Al-Si	53.929	35.411	10.660	-	-	-	-	0.938	-
JB9 0,125	Y-Al-Si	68.169	19.212	12.620	-	-	-	-	0.056	-
JB9 0,25	Y-Al-Si	68.169	19.212	12.620	-	-	-	-	0.113	-

Table 26 *- continuation*

Sample	System	SiO_2	Al_2O_3	Y_2O_3	CaO	Li_2O	Na_2O	K_2O	Au	SnO_2
JB9 0,5	Y-Al-Si	68.169	19.212	12.620	-	-	-	-	0.226	-
JB9 1	Y-Al-Si	68.169	19.212	12.620	-	-	-	-	0.450	-
JB9 2	Y-Al-Si	68.169	19.212	12.620	-	-	-	-	0.905	-
LDS 0,125	Li-Si	66.670	-	-	-	33.330	-	-	0.032	-
LDS 0,5	Li-Si	66.670	-	-	-	33.330	-	-	0.127	-
LDS 1	Li-Si	66.670	-	-	-	33.330	-	-	0.253	-
LSPOD 0,125	Li-Al-Si	57.766	7.765	-	-	34.469	-	-	0.034	-
LSPOD 0,5	Li-Al-Si	57.766	7.765	-	-	34.469	-	-	0.134	-
LSPOD 1	Li-Al-Si	57.766	7.765	-	-	34.469	-	-	0.268	-
JB10	Y-Al-Si	75.410	10.628	13.962	-	-	-	-	-	-
JB11	Y-Al-Si	80.000	12.071	7.929	-	-	-	-	-	-
JB12	Y-Al-Si	85.000	9.053	5.947	-	-	-	-	-	-
JB13	Y-Al-Si	90.000	6.035	3.965	-	-	-	-	-	-
JB14	Y-Al-Si	95.000	3.018	1.982	-	-	-	-	-	-
JB15	Na-Y-Al-Si	80.000	10.000	10.000	-	-	2.500	-	-	-
JB16	Y-Al-Si	80.000	5.000	15.000	-	-	-	-	-	-
JB17	Na-Y-Al-Si	80.000	5.000	15.000	-	-	2.500	-	-	-
JB18	Y-Al-Si	80.000	2.500	17.500	-	-	-	-	-	-
JB19	Na-Y-Al-Si	80.000	2.500	17.500	-	-	2.500	-	-	-
JB20	Na-Y-Al-Si	95.000	3.018	1.982	-	-	2.500	-	-	-
JB21	Na-Y-Al-Si	95.000	3.018	1.982	-	-	5.000	-	-	-
JB22	Y-Al-Si	80.000	10.000	10.000	-	-	-	-	-	-

Table 26 *- continuation*

Sample	System	SiO_2	Al_2O_3	Y_2O_3	CaO	Li_2O	Na_2O	K_2O	Au	SnO_2
JB23	Y-Al-Si	80.000	17.500	2.500	-	-	-	-	-	-
JB24	Li-Si	66.667	-	-	-	33.333	-	-	-	-
JB25	Na-Si	66.667	-	-	-	-	33.333	-	-	-
JB26	K-Si	66.667	-	-	-	-	-	33.333	-	-
JB27	Li-Si	80.000	-	-	-	20.000	-	-	-	-
JB28	Li-Si	88.889	-	-	-	11.111	-	-	-	-
JB29	Na-Si	80.000	-	-	-	-	20.000	-	-	-
JB30	Na-Si	88.889	-	-	-	-	11.111	-	-	-
JB31	K-Si	80.000	-	-	-	-	-	20.000	-	-
JB32	K-Si	88.889	-	-	-	-	-	11.111	-	-
JB33	Y-Al-Si	65.820	22.000	12.180	-	-	-	-	-	-
JB34	Y-Al-Si	74.000	25.000	1.000	-	-	-	-	-	-
JB35	Y-Al-Si	72.000	25.000	3.000	-	-	-	-	-	-
JB36	Y-Al-Si	84.000	15.000	1.000	-	-	-	-	-	-
JB37	Li-Si	66.667	-	-	-	33.333	-	-	0.253	-
JB38	Li-Si	66.667	-	-	-	33.333	-	-	0.127	-
JB39	Li-Si	66.667	-	-	-	33.333	-	-	0.032	-
JB40	Li-Si	66.667	-	-	-	33.333	-	-	0.253	2.000
JB41	Li-Si	66.667	-	-	-	33.333	-	-	0.127	2.000
JB42	Li-Si	66.667	-	-	-	33.333	-	-	0.032	2.000
JB43	Y-Al-Si	65.820	22.000	12.180	-	-	-	-	0.127	-
JB44	Y-Al-Si	65.820	22.000	12.180	-	-	-	-	0.127	2.000
JB45	Li-Si	66.667	-	-	-	33.333	-	-	0.127	0.500

Table 26 *- continuation*

Sample	System	SiO_2	Al_2O_3	Y_2O_3	CaO	Li_2O	Na_2O	K_2O	Au	SnO_2
JB46	Li-Si	66.667	-	-	-	33.333	-	-	0.127	1.000
JB47	Li-Si	66.667	-	-	-	33.333	-	-	0.127	0.100
JB48 (old)	Li-Si	66.667	-	-	-	33.333	-	-	0.127	0.250
JB49 (2g)	Li-Si	66.667	-	-	-	33.333	-	-	0.127	0.250
JB50 (10g)	Li-Si	66.670	-	-	-	33.330	-	-	-	-
JB48 (5g)	Li-Si	66.667	-	-	-	33.333	-	-	0.127	0.250
JB51 (3g)	Na-Si	66.667	-	-	-	-	33.333	-	0.127	0.250
JB52 (3g)	K-Si	66.667	-	-	-	-	-	33.333	0.127	0.250
JB53 (3g)	Li-Si	66.667	-	-	-	33.333	-	-	0.127	0.250
JB60	Y-Al-Si	68.169	19.212	12.620	-	-	-	-	0.127	0.250
JB62	Li-Si	66.667	-	-	-	33.333	-	-	0.127	0.250
JB82	Li-Si	66.667	-	-	-	33.333	-	-	0.127	0.250
JB83	Li-Si	66.667	-	-	-	33.333	-	-	0.127	-
JB84	Li-Si	66.667	-	-	-	33.333	-	-	0.013	0.250
JB85	Li-Si	66.667	-	-	-	33.333	-	-	0.013	-
JB86	Li-Si	66.667	-	-	-	33.333	-	-	0.001	0.250
JB87	Li-Si	66.667	-	-	-	33.333	-	-	0.001	-
JB88	Y-Al-Si	68.169	19.212	12.620	-	-	-	-	0.127	0.250
JB89	Y-Al-Si	68.169	19.212	12.620	-	-	-	-	0.127	-
JB90	Y-Al-Si	68.169	19.212	12.620	-	-	-	-	0.013	0.250
JB91	Y-Al-Si	68.169	19.212	12.620	-	-	-	-	0.013	-
JB92	Y-Al-Si	68.169	19.212	12.620	-	-	-	-	0.001	0.250
JB93	Y-Al-Si	68.169	19.212	12.620	-	-	-	-	0.001	-
JB94	LYAS	68.16941	19.21233	12.62		0				

Table 26 *- continuation*

Sample	System	SiO_2	Al_2O_3	Y_2O_3	CaO	Li_2O	Na_2O	K_2O	Au	SnO_2
JB95	LYAS	68.16941	19.21233	10.096	-	2.524	-	-	-	-
JB96	LYAS	68.16941	19.21233	7.572	-	5.048	-	-	-	-
JB97	LYAS	68.16941	19.21233	5.048	-	7.572	-	-	-	-
JB98	LYAS	68.16941	19.21233	2.524	-	10.096	-	-	-	-
JB99	LYAS	68.169	19.212	0.000	-	12.620	-	-	-	-
JB100	LYAS	68.169	19.212	10.096	-	2.524	-	-	0.127	0.250
JB101	LYAS	68.169	19.212	7.572	-	5.048	-	-	0.127	0.250
JB102	LYAS	68.169	19.212	2.524	-	10.096	-	-	0.127	0.250
JB103	LYAS	68.169	19.212	10.096	-	2.524	-	-	0.127	-
JB104	LYAS	68.169	19.212	7.572	-	5.048	-	-	0.127	-
JB105	LYAS	68.169	19.212	2.524	-	10.096	-	-	0.127	-
JB106	LYAS	58.169	19.210	12.620	-	10.000	-	-	0.127	0.250
JB107	LYAS	68.169	9.210	12.620	-	10.000	-	-	0.127	0.250
JB120	LYAS	68.169	19.212	2.524	-	10.000	-	-	0.013	0.250
JB121	LYAS	58.169	19.210	12.620	-	10.000	-	-	0.013	0.250
JB122	LYAS	68.169	9.210	12.620	-	10.000	-	-	0.013	0.250

Table 27 *Overview of samples prepared by melt-quenching*

Sample	System	SiO_2	Al_2O_3	Y_2O_3	Li_2O	Au	SnO_2
JB9 Pt	Y-Al-Si	68.169	19.212	12.620	-	-	-
JB10	Y-Al-Si	75.410	10.628	13.962	-	-	-
LDS	Li-Si	66.670	-	-	33.330	-	-
LDS 0,5	Li-Si	66.670	-	-	33.330	0.127	-
LSPOD	Li-Al-Si	57.766	7.765	-	34.469	-	-
LSPOD 0,5	Li-Al-Si	57.766	7.765	-	34.469	0.134	-
JB55	Y-Al-Si	68.169	19.212	12.620	-	-	-
JB56	Y-Al-Si	65.820	22.000	12.180	-	-	-
JB57	Y-Al-Si	68.169	19.212	12.620	-	-	-
JB58	Y-Al-Si	65.820	22.000	12.180	-	-	-
JB59	Li-Si	66.667	-	-	33.333	-	-
JB61	Y-Al-Si	65.820	22.000	12.180	-	0.127	0.250
JB63	Y-Al-Si	68.169	19.212	12.620	-	-	-
JB64	Li-Si	66.667	0.000	0.000	33.333	-	-
JB65	Y-Al-Si	68.169	19.212	12.620	-	0.127	0.250
JB65.2	Y-Al-Si	68.169	19.212	12.620	-	0.127	0.250
JB66	Li-Si	66.667	-	-	33.333	0.127	0.250
JB67	Li-Si	66.667	-	-	33.333	-	-
JB68	Li-Si	66.667	-	-	33.333	-	-
JB69	Li-Si	66.667	-	-	33.333	0.127	-
JB70	Li-Si	66.667	-	-	33.333	-	-
JB71	Li-Si	66.667	-	-	33.333	0.013	0.250
JB72	Li-Si	66.667	-	-	33.333	0.013	-
JB73	Li-Si	66.667	-	-	33.333	0.001	0.250
JB74	Li-Si	66.667	-	-	33.333	0.001	-

Table 27 *- continuation*

Sample	System	SiO_2	Al_2O_3	Y_2O_3	Li_2O	Au	SnO_2
JB75	Y-Al-Si	68.169	19.212	12.620	-	0.127	-
JB76	Y-Al-Si	68.169	19.212	12.620	-	0.013	0.250
JB77	Y-Al-Si	68.169	19.212	12.620	-	0.013	-
JB78	Y-Al-Si	68.169	19.212	12.620	-	0.001	0.250
JB79	Y-Al-Si	68.169	19.212	12.620	-	0.001	-
JB80	Y-Al-Si	68.169	19.212	12.620	-	-	-
JB81	Y-Al-Si	68.169	19.212	12.620	-	-	0.350
LDS rinse	Li-Si	66.667	-	-	33.333	-	0.350
JB108	LYAS	68.169	19.212	2.524	10.000	0.127	0.250
JB109	LYAS	58.169	19.210	12.620	10.000	0.127	0.250
JB110	LYAS	68.169	9.210	12.620	10.000	0.127	0.250
JB111	LYAS	68.169	19.212	2.524	10.000	0.013	0.250
JB112	LYAS	58.169	19.210	12.620	10.000	0.013	0.250
JB113	LYAS	68.169	9.210	12.620	10.000	0.013	0.250
JB114	LYAS	68.169	19.212	2.524	10.000	0.127	0.250
JB115	LYAS	58.169	19.210	12.620	10.000	0.127	0.250
JB116	LYAS	68.169	9.210	12.620	10.000	0.127	0.250
JB117	LYAS	68.169	19.212	2.524	10.000	0.001	0.250
JB118	LYAS	58.169	19.210	12.620	10.000	0.001	0.250
JB119	LYAS	68.169	9.210	12.620	10.000	0.001	0.250

AUTHOR PUBLICATIONS AND RESEARCH

List of peer-reviewed papers

[1] **J. Baborák**, M. Yembele, P. Vařák, S. Ory, E. Véron, M.J. Pitcher, M. Allix, P. Nekvindová, A. Zandonà, Key melt properties for controlled synthesis of glass beads by aerodynamic levitation coupled to laser heating, International Journal of Applied Glass Science. 14 (2023) 455–467. https://doi.org/10.1111/ijag.16627.

[2] **J. Baborák**, P. Vařák, A. Canizarès, M. Rada, C. Genevois, M.J. Pitcher, E. Véron, A. Zandonà, M. Allix, P. Nekvindová, The morphology and composition of nanosized amorphous-phase separation in the Y_2O_3–Al_2O_3–SiO_2 glass system, Ceramics International. (2023). https://doi.org/10.1016/j.ceramint.2023.10.067.

[3] P. Vařák, P. Nekvindová, **J. Baborák**, J. Oswald, Near-infrared photoluminescence properties of Er/Yb- and Ho/Yb-doped multicomponent silicate glass – The role of GeO_2, Al_2O_3 and ZnO, Journal of Non-Crystalline Solids. 582 (2022) 121457. https://doi.org/10.1016/j.jnoncrysol.2022.121457.

List of conference proceedings

[1] P. Varak, **J. Baborak**, J. Cajzl, P. Nekvindova, Photoluminescence of Er/Yb-doped zinc-silicate glass and glass ceramics with ZnO and Zn_2SiO_4 nanoparticles, in: Fiber Lasers and Glass Photonics: Materials through Applications III, SPIE, 2022: pp. 257–262. https://doi.org/10.1117/12.2620488.

List of conference contributions (as presenting author)

[1] **Jan Baborak**, Alessio Zandona, Mathieu Allix, Emmanuel Veron, Mike Pitcher, Pavla Nekvindova, Preparation of Y_2O_3-Al_2O_3-SiO_2 glasses using aerodynamic levitation, Journées Françaises du verre: journées plénières de l'USTV, 17-19 nov. 2021 Rennes, France (POSTER)

[2] **J. Baborak**, P. Varak, A. Zandona, C. Genevois, M. Pitcher, M. Allix, E. Veron, P. Nekvindova, Preparation of glasses with gold nanoparticles using aerodynamic levitation coupled to laser heating, Anorganické nekovové materiály, Feb 2022, VŠCHT Praha – online (ORAL)

[3] **Jan Baborak**, Alessio Zandona, Petr Varak, Maureen Yembele, Mathieu Allix, Emmanuel Veron, Mike Pitcher, Cécile Genevois, Pavla Nekvindova, Evaluation of aerodynamic levitation laser heating technique for synthesis of silicate glasses with gold nanoparticles, SPIE Photonics 3.-7.04. 2022, Strasbourg, France (POSTER)

[4] **J. Baborak**, P. Varak, A. Zandona, J. P. Blondeau, M. Pitcher, M. Allix, E. Veron, P. Nekvindova, Preparation of glasses with gold nanoparticles using melt-quenching and aerodynamic levitation coupled to laser heating, Joint meeting DGG-USTV, 22.-25.05. Orléans, France (ORAL)

[5] **J. Baborak**, P. Varak, A. Zandona, M. Pitcher, M. Allix, E. Veron, P. Nekvindova, Preparation and characterization of gold nanoparticles in silicate glass matrices using aerodynamic levitation coupled to laser heating, DMSRE 04.-08.09. 2023 Pavlov, Czechia (ORAL)

[6] **J. Baborak**, P. Varak, A. Zandona, M. Pitcher, M. Allix, E. Veron, P. Nekvindova, Gold nanoparticles in lithium yttrium aluminosilicate glass prepared using aerodynamic levitation coupled to laser heating and melt quenching, Le Studium 04.-06.10. 2023 Orléans, France (POSTER)

RÉSUMÉ EN FRANÇAIS

La longue histoire du verre contenant des nanoparticules d'or, apprécié notamment pour sa belle couleur rouge, trouve aujourd'hui des applications modernes. Ces matériaux sont par exemple utilisés dans les domaines de la photonique, de la détection, de la catalyse, de la biomédecine et de la joaillerie. Ces applications motivent la poursuite de recherches afin de comprendre en détail les liens entre la technologie de préparation, la composition et les propriétés de la matrice de verre et les paramètres des nanoparticules d'or.

Le sujet de ce travail était de comparer la possibilité de préparer du verre contenant des nanoparticules d'or par la technique conventionnelle de fusion-trempe avec une technologie innovante, la lévitation aérodynamique couplée au chauffage laser (ADL).

Cette thèse est le résultat d'une collaboration entre deux laboratoires : le Laboratoire des matériaux pour la photonique de l'Université de chimie et de technologie de Prague (UCT) en République tchèque et le Laboratoire des conditions extrêmes et des matériaux : Haute température et irradiation (CEMHTI) du Centre national de la recherche scientifique (CNRS) à Orléans, en France. Le laboratoire de photonique de l'UCT de Prague a utilisé la technologie conventionnelle de préparation du verre par trempe par fusion. Au laboratoire du CEMHTI à Orléans, les échantillons vitreux ont été synthétisés par lévitation aérodynamique couplée à un chauffage laser, technique toujours en développement dans cette institution.

La thèse est structurée de manière conventionnelle. Tout d'abord, une partie théorique est présentée avec une revue de l'état de l'art dans les domaines du verre, des vitrocéramiques et des nanoparticules d'or. Ensuite, une partie expérimentale est présentée, décrivant les méthodes de préparation et de caractérisation des échantillons, suivie des objectifs de recherche. Le cœur de la thèse est constitué de la partie résultats / discussion qui est divisée en quatre sous-sections dont les résultats les plus importants sont présentés dans les pages suivantes. A la fin de la thèse, un résumé des résultats les plus importants est présenté.

Le premier sous-chapitre des résultats met en lumière certains aspects critiques de la méthode ADL pour la synthèse de billes de verre d'oxyde, dans le but d'étendre son applicabilité à des

compositions plus larges, impliquant par exemple des composants hautement volatils. Du point de vue de la simple formation de verre, cette technique présente une polyvalence inégalée : (1) ses conditions sans creuset évitent la nucléation hétérogène des phases cristallines lors du refroidissement ainsi que la contamination par le creuset et les matériaux réfractaires ; (2) le chauffage laser peut atteindre jusqu'à ~3000 °C, au-dessus de la température de fusion de tout matériau oxyde stable ; (3) la configuration permet des vitesses de refroidissement rapides de l'ordre de plusieurs centaines de degrés Celsius par seconde (en fonction de la nature du gaz de lévitation, de la taille des billes et de leur composition), ce qui facilite la formation de verre par trempe des compositions liquides sujettes à la dévitrification. Compte tenu de ces caractéristiques avantageuses, il pourrait sembler que la méthode ADL devrait invariablement représenter le choix optimal pour l'obtention de billes homogènes, sans bulles, d'une stœchiométrie souhaitée. Néanmoins, les résultats obtenus ici indiquent que d'autres propriétés clés du fondu contribuent à déterminer l'adéquation d'une composition donnée pour la synthèse ADL. Les paramètres revap a Δevap ont été définis comme suit

$$r_{evap} = \frac{T_{m,\Sigma}}{T_m} \qquad \text{Eq. 6.1}$$

$$\Delta_{evap} = r_{evap,max} - r_{evap,min} \qquad \text{Eq. 6.2}$$

où Tm est la température de fusion d'un composant d'oxyde donné, Tm,Σ la température de fusion du verre multicomposant cible (tous deux obtenus à partir des diagrammes de phase) ; revap,max et revap,min représentent respectivement les valeurs de revap les plus élevées et les plus basses parmi tous les composants du verre cible. Ces paramètres peuvent être évalués à l'avance pour une conception intelligente de la composition. Il a été démontré que lorsque l'obtention d'une faible viscosité pour l'élimination des bulles nécessite un chauffage supérieur à la Tm du verre cible par des centaines de Kelvins, une évaporation à haute température non négligeable devrait être attendue pour des valeurs revap dépassant largement ~0,8, bien que ce seuil puisse varier en fonction de la composition choisie, de la configuration ADL, du gaz de lévitation, de la taille finale souhaitée des billes et de la procédure de fonte. Par exemple, un temps de séjour à haute température plus court peut limiter la volatilisation, bien qu'il puisse empêcher une homogénéisation et une finition satisfaisantes. De même, des valeurs de Δevap supérieures à ~0,2 ont signalé un risque élevé de dérive de la composition pour les échantillons

préparés, soulignant la nécessité générale de minimiser ce paramètre lors de la conception de la composition.

Le deuxième sous-chapitre se concentre sur la possibilité de préparer du verre d'aluminosilicate d'yttrium en utilisant la lévitation aérodynamique couplée au chauffage laser. La possibilité de préparer le verre YAS (Y_2O_3-Al_2O_3-SiO_2) par la méthode ADL a été étudiée expérimentalement. La région à haute température de ce système ternaire, jusqu'alors inexplorée, a été décrite expérimentalement, en particulier la région avec 65 % de SiO_2 ou plus et simultanément un maximum de 17,5 % de Y_2O_3. Dans cette région nous avons observé des séparations de phase et des nanoparticules amorphes de SiO_2 sont formées. Comme prévu, la taille et la distribution de ces nanoparticules peuvent être contrôlées par la technologie de synthèse utilisée, c'est-à-dire par la vitesse de refroidissement. Un refroidissement lent (four commercial) produit des nanoparticules plus grosses qu'un refroidissement très rapide (ADL). En outre, la formation et la taille des nanoparticules peuvent également être fondamentalement influencées par la composition. Une augmentation de SiO_2 réduit le contraste de composition entre les nanoparticules et la matrice, probablement en raison d'une force motrice plus faible vers la séparation des phases. Inversement, l'augmentation du modificateur vitreux Y_2O_3 entraîne la formation de nanoparticules de SiO_2 de différentes tailles, qui peuvent varier de quelques dizaines à quelques centaines de nanomètres en fonction de sa teneur. À teneur égale en Y_2O_3 et Al_2O_3, un échantillon opalescent avec de très petites nanoparticules interconnectées a pu être préparé. Ces résultats pourraient servir de guide pour la fabrication de nanoparticules sphériques de SiO_2 dans le verre YAS pour diverses applications potentielles.

Le troisième sous-chapitre traite de la préparation des nanoparticules d’or (AuNPs) dans les verres YAS et LS en utilisant les techniques de synthèse par lévitation aérodynamique (ADL) fusion trempe dans un four commercial (MQ). Un processus de préparation d'échantillons en plusieurs étapes a été développé pour les deux technologies, qui assure la meilleure homogénéité et réduit la perte de composants volatils du verre (Au, SnO_2) en les ajoutant à la poudre de verre pré-fondue. Ce processus repose sur le broyage des matériaux précurseurs, la

fusion par MQ, un second broyage, le dopage avec la quantité requise de composants volatils et la fusion finale à l'aide de la technologie choisie. Une nouvelle procédure de préparation des pastilles de fusion à l'aide d'une boue d'amidon et d'une pipette répétitive a également été mise au point pour la technologie ADL, ce qui garantit un poids constant des échantillons préparés (15,84±0,24 mg pour 50 µl de pastilles LS) et une meilleure reproductibilité des expériences réalisées. En raison de la polyvalence de cette procédure, elle peut être utilisée dans une large gamme d'autres systèmes, et pas seulement dans les verres étudiés.

En ce qui concerne la formation de nanoparticules dans ces deux types de verre de compositions différentes, il est évident qu'en combinant de manière appropriée les conditions technologiques et le recuit ultérieur, il est possible de préparer des nanoparticules de forme essentiellement sphérique dans les deux types de verre (bien que des particules triangulaires et vermiculaires aient également été préparées dans certains cas) et de contrôler leur taille et leur distribution par un recuit ultérieur. En particulier, il s'est avéré pratique de préparer des verres transparents ne contenant que des traces de nanoparticules métalliques et de contrôler les paramètres des nanoparticules d'or et donc la couleur du verre qui en résulte par un recuit ultérieur. Au cours de ce travail, l'effet bénéfique de l'ajout de SnO_2 sur la couleur des verres préparés a été vérifié expérimentalement.

Si l'on compare les deux techniques utilisées, de meilleurs résultats ont été obtenus avec la m éthode MQ. Les échantillons préparés par cette technique étaient exempts de bulles et de couleur plus homogène. Avec ADL, toute modification de la composition du verre ou de la taille de l'échantillon nécessite une optimisation et une modification des paramètres d'entrée d'ADL afin d'optimiser l'homogénéité de l'échantillon. Au cours de ce travail, les mêmes paramètres ADL ont toujours été optimisés en premier lieu, puis utilisés pour chaque bille d'un ensemble d'échantillons afin que les échantillons préparés puissent être comparés les uns aux autres.

Les résultats de ce chapitre permettent de tirer les conclusions suivantes :

1) La technologie ADL peut être utilisée pour préparer des particules d'or métallique dans le verre, dont les dimensions sont de l'ordre du µm ou du nm. La structure fcc commune de l'or métallique a été démontrée pour ces nanoparticules. Les conditions sélectionnées de la

technologie, ainsi que le recuit ultérieur, peuvent ensuite influencer leur nombre, leur forme, leur distribution et donc la couleur du verre.

2) Il a été démontré que pendant le processus ADL, l'or se volatilise de la matrice du verre. Sa volatilisation dépend des conditions sélectionnées de la technologie, et il est confirmé que plus la température et le temps de préparation sont élevés, plus la concentration en Au est faible. En comparant les deux technologies utilisées, nous avons observé une perte d'Au plus importante avec la technologie ADL qu'avec la technologie MQ.

3) Il est difficile de contrôler la reproductibilité des échantillons préparés qui présenteraient la même couleur. Lors de ce travail, nous avons réussi à préparer des échantillons homogènes et reproductibles de même taille grâce à la nouvelle conception de la technologie de préparation des pastilles et au contrôle strict des paramètres de l'ADL. Cependant, un échantillon de couleur uniforme n'a pas pu être préparé de manière reproductible. Un exemple de la meilleure série d'échantillons jusqu'à présent est illustré à la figure 1. La préparation d'échantillons incolores dont la couleur peut être contrôlée ultérieurement par un recuit semble plus appropriée.

Figure 1. *1Meilleur example de billes homogènes préparées (10ADL).*

4) Il a été démontré que l'ajout d'étain favorisait de manière significative la formation d'AuNPs dans les deux technologies utilisées. L'étain présente un pourcentage de perte lors de la fusion du verre inférieur à celui de l'or.

5) La formation de nanoparticules a été fortement influencée par la composition de la matrice de verre. Un facteur important a été l'ajout d'ions réduisant le degré de polymérisation de la matrice vitreuse et favorisant la formation de NBO, ce qui conduit probablement à la nucléation des nanoparticules d'or. En raison de la plus faible viscosité associée au plus faible degré de polymérisation, les nanoparticules d'or se sont formées plus facilement dans le système LS que dans le système YAS. En outre, de grosses nanoparticules sphériques, dont la taille est quasiment de l'ordre du μm et qui n'affectent pas la couleur du verre, ont été observées beaucoup plus fréquemment dans le système YAS. Les échantillons LS montrent des couleurs beaucoup plus attrayantes en raison de la présence de nanoparticules d'or de dimensions nanométriques.

6) De grosses particules d'or sphériques, d'un diamètre de 1 à 10 μm, ont été observées dans les deux types de systèmes de verre, mais elles étaient réparties de manière trop éparse pour permettre une analyse statistique des images. La formation de ces particules n'était guère affectée par la composition du verre et n'était pas liée à la couleur des échantillons. En utilisant la technologie ADL, ces grosses particules étaient distribuées de manière très hétérogène et formaient des grappes ressemblant à des chaînes.

7) La formation de nanoparticules d'or de dimensions nanométriques et de formes différentes (vermiculaire anisométrique, triangulaire, sphérique) a été détectée dans les deux systèmes de verre à l'aide de la MET. Dans le système de verre YAS, les formes irrégulières correspondent à l'apparition d'une coloration brune ou brun-rouge des échantillons. En outre, la couleur de ces échantillons de verre ne pouvait pas être facilement affectée par un recuit ultérieur. Dans le système LS, les formes irrégulières correspondent à une coloration rouge du verre.

8) Un recuit ultérieur du verre avec des nanoparticules de forme irrégulière a transformé la forme en sphère dans les systèmes LS et YAS.

Si nous nous concentrons sur les technologies utilisées pour la préparation des AuNPs dans le verre, il est clair que la MQ est la technologie la plus utilisée et la plus industrielle, qui est également associée à la couleur du verre. Les échantillons de verre dopé en vrac sont préparés par cette technologie. Les nanoparticules d'or en couches minces sont probablement les plus préparées par la technique sol-gel [124,125] ou par la technologie d'implantation ionique [122]. Dans ces cas, cependant, leur préparation est principalement associée à leur bioactivité, à des

réactions catalytiques, à la résonance plasmonique de surface, à des phénomènes optiques non linéaires ou à d'autres effets. Nous n'avons trouvé aucune trace de l'utilisation de la technologie ADL pour la préparation d'échantillons de verre contenant des AuNPs.

Si nous comparons la forme, la quantité, la taille et la distribution des nanoparticules d'or préparées par différentes technologies à partir de la littérature actuelle, il semble que dans la plupart des cas des nanoparticules d'or sphériques aient été préparées, leur quantité et leur distribution étant liées aux conditions de préparation de l'échantillon sélectionnées. Pour le sol-gel, la concentration de nanoparticules dans le gel est cruciale et peut être très bien contrôlée. Pour l'implantation ionique, c'est principalement la fluence qui détermine le nombre de NP formées et c'est l'énergie du faisceau d'ions qui est critique pour la distribution et surtout la profondeur à laquelle les NP sont implantées sous la surface. Quelques images d'AuNPs en couches minces variant systématiquement ont été prises par TEM.

Si nous nous concentrons sur la composition chimique des matrices de verre dans lesquelles les NP d'or ont été préparées, les compositions principalement étudiées sont les verres de borate [109-118], de silicate [119-126,162,163] et également de chalcogénure [101,105,127] sur la base des conclusions de la littérature récente. Les verres à haute teneur en bore et en chalcogénures ont des propriétés mécaniques et chimiques inférieures à celles des verres silicatés et sont difficiles à utiliser pour des applications commerciales. La procédure de préparation des échantillons de verre (en particulier les borates et les chalcogénures) utilisée par d'autres auteurs diffère par la fusion du verre à une température plus basse et pendant une durée plus courte. Par exemple, les verres à haute teneur en bore sont fondus à 850-1200°C pendant 10 à 60 min [109-118]. Dans la littérature, les informations sur la teneur réelle en Au de l'échantillon après la fusion ne sont pratiquement jamais rapportées et la question de la volatilisation de l'Au n'est pas abordée. Cela est probablement dû à la très faible concentration d'or, qui est généralement inférieure à la limite de détection des méthodes analytiques. L'ajout de nanoparticules d'or uniformes de taille définie dans le verre a également été tenté dans ces systèmes à bas point de fusion (le verre a un point de fusion plus bas que l'or), mais les nanoparticules se sont dissoutes et se sont réassemblées [112,113]. Les images TEM des AuNPs dans le verre sont très rarement publiées et les nanoparticules sont généralement de forme sphérique. La taille moyenne des particules varie de 10 à 100 nm - le plus souvent autour de 10

nm ou 40 nm. Cependant, certaines nanoparticules n'apparaissent pas clairement sur les images et sont très densément distribuées, la plupart du temps sans analyse XRD ou EDS, de sorte que l'on peut se demander s'il ne s'agit que de NPs d'or et non d'une séparation d'autres phases du verre (par ex. [113,118]).

Bien plus souvent, les conditions technologiques sont associées à une absorption optique dans la région visible correspondant à la couleur rouge. La couleur typique des verres contenant des AuNPs est dans certains cas obtenue immédiatement après la trempe du verre, dans d'autres cas seulement après un recuit thermique ultérieur [102,103]. Si un traitement thermique supplémentaire est utilisé, la température utilisée est proche de la Tg de la matrice du verre [103]. Ces publications montrent clairement que la formation de nanoparticules, leur forme, leur distribution et la coloration des échantillons sont étroitement liées à leur histoire thermique.

Dans notre cas, il est possible de comparer les deux verres, c'est-à-dire les verres YAS et LS, car la température des billes a été enregistrée pendant la fusion et le refroidissement ADL (pour la technologie MQ, une telle comparaison n'est pas possible). Les enregistrements mentionnés sont présentés sur deux échantillons de même masse, comme le montre la figure 2. Si nous faisons la moyenne de la vitesse de refroidissement pour les cinq échantillons YAS et les cinq échantillons LS, nous obtenons des valeurs de 135 $°C.s^{-1}$ et 226 $°C.^{s-1}$ pour YAS et LS, respectivement. Ces valeurs montrent clairement que le refroidissement du verre au lithium est plus rapide.

La raison pour laquelle la couleur rouge est plus facile à développer et à contrôler dans le système LS que dans le système YAS n'est pas tout à fait claire. Selon Weyl [102], le paramètre clé est la dépendance de la température de la solubilité de l'or dans un verre donné, mais ce paramètre est difficile à quantifier. Nous pensons que ce fait peut également être lié à la densité du réseau de verre et donc à la mobilité des particules d'Au en son sein. Bien qu'avec la technologie ADL, le refroidissement contrôlé des échantillons directement après la fusion soit plus facile qu'avec la MQ, et que les échantillons colorés puissent donc être obtenus directement sans traitement thermique supplémentaire, pour obtenir une coloration uniforme de manière contrôlée, il est préférable de commencer avec du verre incolore après ADL ou MQ et d'obtenir la couleur souhaitée par un traitement thermique secondaire des échantillons. Enfin, on peut

noter que seul un petit nombre d'auteurs montrent l'apparence des échantillons et discutent de leur homogénéité et de leur reproductibilité.

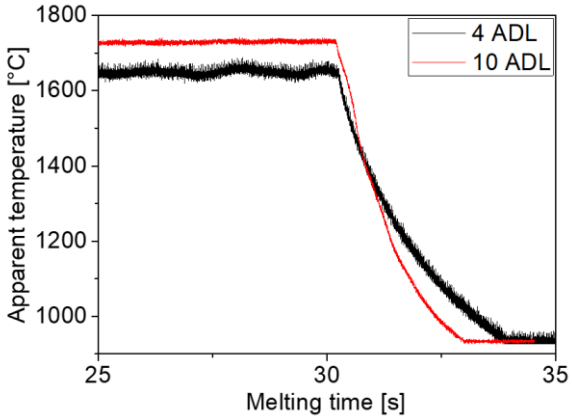

Figure 2. *Comparaison des vitesses de refroidissement des compositions vitreuses YAS (4ADL) et LS (10ADL).*

Le quatrième sous-chapitre se concentre sur la préparation de nanoparticules d'or dans des matrices de verre nouvellement conçues. La thèse explore la possibilité d'utiliser une nouvelle technologie de fusion sans récipient pour la préparation de nanoparticules d'or dans le verre. Nous supposons que la beauté du verre préparé pourrait être utilisée à des fins décoratives ou dans la joaillerie et la modification des propriétés physiques dans la photonique, par exemple.

Dans la quatrième partie de la thèse, sur la base des résultats précédents, plusieurs compositions de verre ont été conçues et préparées avec succès dans le système LYAS en utilisant les deux technologies. Ces compositions dérivent de la composition de base du verre YAS en remplaçant 10 mol% de l'un des oxydes Y_2O_3, Al_2O_3 et SiO_2 par Li_2O. L'intention principale de cette substitution était de bénéficier des propriétés optiques avantageuses du verre YAS tout en réduisant sa viscosité et donc de faciliter sa préparation. De ce point de vue, la substitution la moins réussie était Y→L. Ces échantillons de verre ont été très difficiles à préparer avec la technologie MQ. Des températures allant jusqu'à 1700 °C ont été utilisées pour leur fusion, mais les verres étaient très visqueux et se fissuraient pendant le refroidissement. Lors de la fusion par ADL, la viscosité élevée s'est traduite par un grand nombre de bulles dans les échantillons qui ne pouvaient pas être éliminées. Les substitutions A→L et S→L ont rempli leur rôle, la température requise pour fondre ces verres et leur viscosité ont été réduites et le verre était beaucoup plus facile à travailler. Une séparation de phase à l'échelle nanométrique a été observée dans le verre d'échange A→L par TEM. Nous pensons que cette séparation de

phase a entraîné une nucléation uniforme des AuNPs dans tout le volume de l'échantillon et donc une meilleure homogénéité de la couleur après un traitement thermique supplémentaire des échantillons.

1) Le système LYAS proposé est un nouveau système de verre adapté à la préparation de verre enrichi en nanoparticules d'or à l'aide de la technologie ADL. Dans ce système, il est possible de préparer des échantillons homogènes, où la couleur correspondant à la présence de nanoparticules peut être ajustée du brun au rouge et au violet par des changements de composition combinés à un recuit ultérieur. Cependant, selon Volf [239], nous supposons que les propriétés mécaniques et chimiques du verre dans ce système sont inférieures à celles du YAS - non mesurées.

2) Parmi les substitutions systématiquement variables de Li pour trois ions différents dans la matrice du verre, la substitution de Li pour Al semble être la plus appropriée en termes de variabilité de la couleur du verre. Les verres présentaient la plus grande gamme de maxima de bandes d'absorption observées (de et donc une gamme de couleurs correspondante).

3) Les nanoparticules d'or étaient relativement peu distribuées dans le verre et étaient de forme sphérique, avec une taille moyenne allant de 3 à 22 nm, indépendamment de la substitution et de la technologie choisies, mais les échantillons présentaient une absorption et donc une couleur très différentes. Ces résultats préliminaires permettent de conclure que la forme et la distribution des nanoparticules n'affectent pas tant la couleur que la séparation des phases du verre ou la combinaison différente de l'absorption des nanoparticules et des phases vitreuses formées.

4) Les maxima des bandes spectrales d'absorption dans la région visible se situent entre 524 et 570 nm. Il semble que la coloration rouge rubis corresponde à un maximum d'absorption à 540 nm.

La couleur du verre, la taille des AuNPs, la position de la bande d'absorption et la composition de la matrice du verre sont étroitement liées. Dans les verres de silicate de diverses compositions [102,103], la bande d'absorption s'étend de 500 à 600 nm et est généralement de forme gaussienne. Dans la littérature, l'estimation de la taille des particules a été réalisée soit par la théorie de Mie, soit [101,117,118,163] par calcul à partir des spectres DRX selon l'équation de Scherrer [109,111]. Récemment, la taille réelle des AuNPs a été étudiée par MET. Cependant, comme mentionné ci-dessus, en raison de la difficulté de préparation des échantillons, seul un nombre relativement faible de changements observés systématiquement ou de corrélations entre

la taille des nanoparticules, la chimie de la matrice et la taille des nanoparticules d'or, a été décrit.

Il existe actuellement plusieurs logiciels gratuits permettant de modéliser les spectres d'absorption selon la théorie de Mie. À titre d'expérience pilote, sur la base des recommandations de J.P. Blondeau [240], le logiciel BHMIE [241] a été utilisé pour simuler les spectres d'absorption de l'échantillon rouge rubis du système LS. Pour l'échantillon donné, la taille moyenne des nanoparticules d'or, la valeur de l'indice de réfraction de la matrice de verre et plusieurs modèles, que le programme inclut, ont été sélectionnés. Ces modèles diffèrent les uns des autres par les valeurs des constantes physiques utilisées dans les calculs de la forme des spectres d'absorption. Les modèles de Babar, Hagemann, Johnson, Palik et Rakic ont été comparés aux spectres d'absorption mesurés à l'aide de ce programme. La simulation est illustrée à la figure 3. Il est évident que c'est le modèle de Hagemann qui fonctionne le mieux. La raison de ce résultat et la question de savoir si ce modèle peut être utilisé en général, par exemple pour tous les types de verres silicatés ou pour différents types d'AuNPs, nécessiteraient d'autres comparaisons, simulations et probablement une série supplémentaire d'expériences. En outre, le logiciel BHMIE suppose des nanoparticules sphériques monodispersées et que les nanoparticules ne se regroupent pas, ce qui n'est pas le cas dans les échantillons préparés.

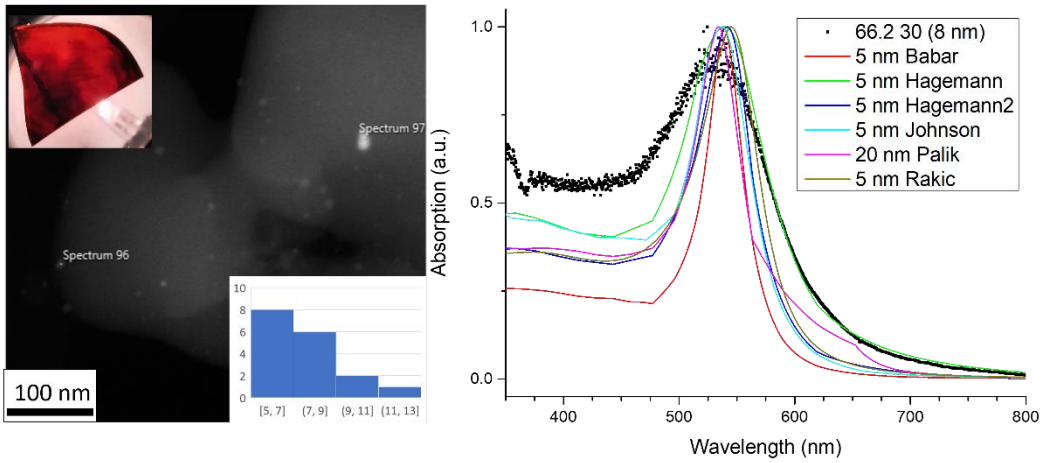

Figure 3 *Comparaison des spectres d'absorption mesurés (en noir) avec différentes modèles mathématiques – échantillon 10MQ, recuit à 500°C 30 min. Le modèle Hagemann (en vert clair) est le plus approprié pour nos échantillons LS.*

Toutefois, outre la forme et la distribution des nanoparticules, la valeur de l'indice de réfraction peut également avoir un effet significatif sur la position et la forme de la bande d'absorption, qui se déplace en fonction de la composition de la matrice de verre. Cinq matrices de verre

différentes ont été préparées. Pour chaque système de verre, la dispersion a été mesurée par spectroscopie et la valeur de l'indice de réfraction du verre a été calculée pour une longueur d'onde de 589 nm. Les valeurs de l'indice de réfraction et la position observée du maximum de la bande d'absorption sont données dans le tableau 1 pour les verres enrichis en or ou pour les verres recuits. Il ressort clairement du tableau qu'en général, les valeurs d'indice de réfraction les plus élevées correspondent à des longueurs d'onde élevées du maximum de la bande d'absorption (verre LYAS A et YAS) et, inversement, les valeurs d'indice de réfraction faibles à des longueurs d'onde plus faibles du maximum d'absorption (LYAS Y). Cette tendance correspond bien à celle prédite par exemple par [71]. Cependant, des valeurs exactes spécifiques s'écartent de cette tendance, par exemple dans le verre LYAS S, ce qui peut être dû à la forme et au nombre de NPs, ou à la formation de nouvelles phases. Des relations mathématiques ont également été publiées pour décrire la relation entre la longueur d'onde du maximum d'absorption et la valeur de l'indice de réfraction, mais elles n'ont pas encore été vérifiées pour les expériences rapportées dans cette thèse [109].

Table 1 *Comparaison de l'indice de refraction et de la position du maximum d'absorption des échantillons sélectionnés.*

Matrice vitreuse	**Echantillon**	**Indice de réfraction (589 nm)**	**Maximum D'absorption [nm]**
LS (*Au,Sn: L33-S67*)	**7, 8, 10 MQ**, trempé	1.5415	533
YAS (*Au,Sn:Y13-A19-S68)*	**4,5 MQ**, recuit à 900°C 60 min)	1.6168	554
LYAS Y (*Au,Sn:L10-Y3-A19-S68*)	**1MQ**, trempé	1.5391	524
LYAS S (*Au,Sn:L10-Y13-A19-S58*)	**4MQ**, recuit à 825°C 60 min	1.6435	544
LYAS A (*Au,Sn:L10-Y13-A9-S68*)	**7MQ**,trempé	1.6142	547

À notre avis, le fait le plus intéressant découlant de nos résultats est lié au fait que les verres silicatés contenant du lithium ont tendance à cristalliser. Ainsi, de nouvelles phases se forment dans la matrice du verre, comme le confirment les images MET du verre LYAS où le lithium a été remplacé par l'aluminium. La formation de ces phases est clairement à l'origine de la plus

grande variabilité de couleur dans ces verres. Nous pensons donc que la formation de cristaux nanométriques et/ou la séparation des phases amorphes favorisent grandement la nucléation uniforme des AuNPs et sont la clé de la coloration uniforme des échantillons de verre dopés à l'or. Des conclusions similaires ont été publiées relativement récemment lorsqu'une transformation admirable de la couleur a été obtenue dans le système ZnO-MgO-Al_2O_3-SiO_2 grâce à l'ajout de phases TiO_2 et ZrO_2 au verre contenant des NP d'or [119,120]. De même, la variabilité des couleurs sur la célèbre coupe de Lycurgue est également attribuée à la formation de nouvelles phases présentes dans le verre avec les nanoparticules d'or, selon [85]. Cela ouvre un très large éventail de possibilités pour contrôler davantage la coloration des verres. La formation d'une séparation de phase à l'échelle nanométrique s'avère néanmoins cruciale.

Jan BABORÁK

Nanoparticules métalliques à nanostructuration ajustable dans les verres et les vitrocéramiques : chimie de l'état solide, propriétés optiques et nanostructure

Résumé :

La longue histoire du verre contenant des nanoparticules d'or, apprécié notamment pour sa belle couleur rouge, trouve aujourd'hui des applications modernes. Il est notamment utilisé dans les domaines de la photonique, de la détection, de la catalyse, de la biomédecine et des bijoux. Ces applications motivent la poursuite de recherches afin de comprendre en détail les liens entre les méthodes de préparation, la composition et les propriétés de la matrice vitreuse et les paramètres des nanoparticules d'or.

L'objet de ce travail était de comparer la possibilité de préparer du verre contenant des nanoparticules d'or par la technique conventionnelle de trempe par fusion avec une technologie innovante, la lévitation aérodynamique couplée au chauffage laser (ADL). En termes de formation de verre, cette technique présente une polyvalence inégalée : (1) la fusion sans creuset supprime la nucléation hétérogène des phases cristallines pendant le refroidissement et évite la contamination par le creuset et les matériaux réfractaires ; (2) le chauffage laser peut atteindre jusqu'à ~3000 °C, ce qui est supérieur à la température de fusion de tout matériau oxyde stable ; (3) la technique permet un refroidissement rapide de l'ordre de plusieurs centaines de °C par seconde, ce qui facilite le refroidissement des matières fondues sujettes à la dévitrification.

Ce travail porte sur la recherche d'un système d'oxyde vitreux adapté à la technologie ADL et, en même temps, sur un modèle général permettant de déterminer les précurseurs les plus appropriés. En outre, la possibilité de préparer le verre YAS (Y_2O_3-Al_2O_3-SiO_2) par la méthode ADL a été étudiée expérimentalement. La région nécessitant de hautes températures de fusion de ce système ternaire, jusqu'alors inexplorée, a été décrite expérimentalement. Des verres transparents, opalescents et blancs ont été préparés dans ce système, qui diffèrent par leur nanostructure. En outre, ce travail présente la possibilité de préparer des nanoparticules d'or dans les systèmes de verre YAS, LS (Li_2O-SiO_2) et LYAS (Li_2O-Y_2O_3-Al_2O_3-SiO_2) avec différentes teneurs en Au et SnO_2 à l'aide de la technologie ADL. En particulier, l'absorption optique et les paramètres des nanoparticules d'or ont été étudiés par microscopie électronique en transmission MET pour les verres préparés. Il a été constaté que l'absorption, et donc la couleur du matériau, peut être contrôlée non seulement par la taille et la distribution des nanoparticules, mais aussi par la composition du verre environnant, et qu'il est également préférable d'utiliser une séparation de phase à l'échelle nanométrique pour obtenir une meilleure homogénéité de la couleur.

Mots clés : nanoparticules métalliques, propriétés optiques, vitrocéramique, verre

Jan BABORÁK

Metal nanoparticles tunable nanostructuring in glasses and glass ceramics: solid state chemistry, optical properties and nanostructure

Summary :

The long history of glass containing gold nanoparticles, which is appreciated especially for its beautiful red colour, is now facing modern applications. They are used in photonics, sensing, catalysis, biomedicine and jewellery. These applications motivate further research to gain detailed understanding of the links between the preparation technology, the composition and properties of the glass matrix and the parameters of the gold nanoparticles.

The subject of this work was to compare the possibility of preparing glass containing gold nanoparticles by the conventional melt-quenching technique with an innovative technology, aerodynamic levitation coupled to laser heating (ADL). In terms of glass formation, this technique shows unrivalled versatility: (1) containerless melting suppresses heterogeneous nucleation of crystal phases during cooling and avoids contamination from crucible and refractory materials; (2) laser heating can attain up to ~3000 °C, which is above the melting temperature of any stable oxide material; (3) the technique allows rapid cooling on the order of several hundred °C per second, facilitating cooling of melts prone to devitrification.

This work covers the search for a glassy oxide system suitable for ADL technology and, at the same time, a general model for determining the most suitable precursors. Furthermore, the possibility of preparing YAS (Y2O3-Al2O3-SiO2) glass by the ADL method was experimentally investigated. Previously unexplored high temperature region of this ternary system was newly experimentally described. Transparent, opalescent and white glasses were prepared in this system, which differed in their nanostructure. Furthermore, the work presents the possibility of preparation of gold nanoparticles in YAS, LS (Li_2O-SiO_2) and LYAS (Li_2O-Y_2O_3-Al_2O_3-SiO_2) glass systems with different Au and SnO_2 contents using ADL technology. In particular, the optical absorption and parameters of gold nanoparticles were investigated for the prepared glasses by transmission electron microscopy (TEM). It was found that the absorption, and thus the colour of the material, can be controlled not only by the size and distribution of the nanoparticles but also by the composition of the surrounding glass, and that it is also advisable to use nanoscale phase separation to achieve better colour homogeneity.

Keywords : metal nanoparticles, optical properties, glass-ceramics, glass

Materials for Photonics Laboratory, Department of Inorganic Chemistry,
University of Chemistry and Technology Prague, Technicka 5, 166 28 Prague 6, Czech Republic

Conditions Extrêmes et Matériaux : Haute Température et Irradiation (CEMHTI), CNRS UPR 3079,

1D Avenue de la Recherche Scientifique, 45071 Orléans Cedex 2, France